Metal-Organic Framework Hybrid Materials: Developing Tailored Synthesis Approaches for Biology and Medicine

Zur Erlangung des akademischen Grades eines

DOKTORS DER NATURWISSENSCHAFTEN

(Dr. rer. nat.)

von der KIT-Fakultät für Chemie und Biowissenschaften

des Karlsruher Instituts für Technologie (KIT)

genehmigte

DISSERTATION

von

M.Sc. Ilona Wagner

aus

Freiamt, Germany

1. Referent: PD. Dr. Manuel Tsotsalas

2. Referent: Prof. Dr. Patrick Théato

Tag der mündlichen Prüfung: 09.02.2024

Honesty Declaration

This work was carried out from February 1st, 2021, to February 29th, 2024, at the Institute of Functional Interfaces (IFG), Faculty of Chemistry and Biosciences at the Karlsruhe Institute of Technology (KIT) under the supervision of PD. Dr. MANUEL TSOTSALAS.

Die vorliegende Arbeit wurde im Zeitraum vom 01. Februar 2021 bis 29. Februar 2024 am Institut für Funktionelle Grenzflächen (IFG) an der Fakultät für Chemie und Biowissenschaften am Karlsruher Institut für Technologie (KIT) unter der Leitung von PD. Dr. MANUEL TSOTSALAS angefertigt.

Hiermit versichere ich, ILONA WAGNER, die vorliegende Arbeit selbstständig verfasst und keine anderen als die angegebenen Hilfsmittel verwendet, sowie Zitate kenntlich gemacht zu haben. Die Dissertation wurde bisher an keiner anderen Hochschule oder Universität eingereicht.

Hereby, I, ILONA WAGNER, declare that I completed the work independently, without any improper help, and that all material published by others is adequately cited. This thesis has not been submitted to any other university before.

Preface

Parts of this thesis were published or submitted during the writing process. The relevant contents are correctly cited and printed with the publishing journal's permission.

Content

Abstract (English) 11
Abstract (German) 13
List of Figures 15
List of Tables 26
List of Equations 27
1. Motivation 1
2. Theory and Background 3
2.1 Metal-Organic Frameworks 3
2.1.1 SBUs and Linkers 4
2.1.2 MOF Thin Film Synthesis 5
2.1.3 Applications of MOFs 6
2.2 Tailored MOF Biomaterials 9
2.2.1 Enzyme Nanoencapsulation in MOF Materials 9
2.2.2 MOF/Polymer Nanomaterials 14
2.2.3 Machine Learning with MOF Materials 20
3. Characterization Techniques 24
3.1 X-Ray Diffraction (XRD) 24
3.1.1 Theoretical Background 24
3.1.2 Instrument and Method 26
3.2 Dynamic Light Scattering (DLS) 27
3.2.1 Theoretical Background 28
3.2.2 Instrument and Method 29
3.3 Infrared Spectroscopy (IR) 29
3.3.1 Theoretical Background 29
3.3.2 Attenuated Total Reflection (ATR) Infrared Spectroscopy (IR) 31
3.3.3 Instrument and Method 33
3.4 Scanning Electron Microscopy (SEM) 33
3.4.1 Theoretical Background 33
3.4.2 Instrument and Method 35

3.5 Nuclear Magnetic Resonance (NMR) 35
3.5.1 Theoretical Background 35
3.5.2 Instrument and Method 38
3.6 Time-of-Flight Secondary Ion Mass Spectrometry (ToF-SIMS) 38
3.6.1 Theoretical Background 38
3.6.2 Instrument and Method 40
3.7 Gel Permeation Chromatography (GPC) 40
3.7.1 Theoretical Background 40
3.7.2 Instrument and Method 42
3.8 Ultraviolet and Visible Spectroscopy (UV-Vis) 43
3.8.1 Theoretical Background 43
3.8.2 Instrument and Method 45
4. MOF-Shell Protection of Enzymes 46
4.1 Introduction 46
4.2 Results and Discussion 49
4.2.1 MOF Characterization 49
4.2.2 Enzyme Activity after Incorporation 54
4.2.3 Proof of Enzyme Encapsulation 59
4.2.4 Enzymatic Activity Behavior by MOF Protection in Different Solvents 61
4.3 Summary 66
5. MOF/Polymer Nanoparticles for Drug Delivery 68
5.1 Introduction 68
5.2 Results and Discussion 71
5.2.1 Grafting-from Polymerization of the Surface of UiO-66-NH_2 Nanoparticles 71
5.2.2 Increasing Dispersibility and Reducing the Protein Adsorption - Proofing the “Stealth Effect” 74
5.2.3 Nitroxide Exchange Reaction for the Attachment of Targeting Proteins to the MOF Surface 77
5.2.4 Testing the Suitability of MOF/Polymers for Drug Delivery 79
5.2.4.1 Applying the MOF/NMP Strategy on Other Monomers 79
5.2.4.2 Drug Loading Efficiency in MOF/Polymer Nanoparticles 94

5.2.4.3 Cell Viability Studies of MOF/Polymers on Breast Cancer Cells 97
5.3 Summary 100
6. Machine Learning supporting MOF Synthesis 104
6.1 Introduction 104
6.2 Results and Discussions 107
6.2.1 Genetic Algorithm vs. Bayesian Optimization: A Comparative Study 107
6.2.2 Reproducing the Optimized Reactions 109
6.2.3 Scientific Application Potentials 110
6.3 Summary 112
7. Summary and Outlook 113
8. Experimental Section 120
8.1 MOF-Shell Protection of Enzymes 120
8.1.1 ZIF-8 (ZIF-CO_3-1) – Synthesis 120
8.1.2 ZIF-90 – Synthesis 121
8.1.3 Disodium Terephthalate Synthesis 121
8.1.4 MIL-53(Al) – Synthesis 121
8.1.5 Ca(BDC) – Synthesis 122
8.1.6 Ca(BDC) – Tests in Different Solvents 122
8.2 MOF/Polymer Nanoparticles for Drug Delivery 123
8.2.1 UiO-66-NH_2 – Synthesis 123
8.2.2 TEMPO-Alkoxyamine – Synthesis 123
8.2.3 MOF Surface Modification 124
8.2.4 Nitroxide-Mediated Polymerization on the MOF Surface 126
8.2.5 Protein Adsorption Test 130
8.2.6 Nitroxide Exchange Reaction of TEMPO with RGD-Nitroxide 130
8.2.7 Drug Loading 131
8.2.8 Cell Cytotoxicity Tests 131
8.3 Machine Learning supporting MOF Synthesis 132
8.3.1 MOF Thin Film Synthesis – Chemical Vapor-Assisted Conversion 132
8.3.2 Machine Learning Setup 134
8.3.3 Fitness Calculation 135

9. Abbreviations 136
10. References 139
11. Appendix 149
Acknowledgment 162

Abstract (English)

Metal-organic frameworks (MOFs) are highly customizable and adaptable and can be developed and improved for applications in various research fields, such as medicine and biology. In this thesis, I developed several new strategies to synthesize, modify, and apply MOF materials in biology or medicine.

In the first project, I encapsulated enzymes in MOFs to protect them from the harmful effects of organic solvents or other environmental influences. Through testing various MOFs, I determined the Ca(BDC) as the best protection for the phenacrylate decarboxylase (PAD) enzyme. The PAD@MOF particles even preserve the enzymatic activity in organic solvents such as ethanol (EtOH) or cyclohexane (Cyc).

In the second project, I modified MOF materials with polymers to enhance their biocompatibility for delivering drugs into cells. Pristine MOF nanocarriers often aggregate quickly, adsorb blood proteins on their surface, and are eventually eliminated by the body's immune response before they reach the desired site. To address these limitations and make the MOFs more biocompatible, I implemented a nitroxide-mediated polymerization (NMP) method and modified the surface of UiO-66-NH_2 (Universitetet i Oslo) nanoparticles (NPs) with hydrophilic polymers. This customization allowed the crystallinity and size of the NPs to be maintained while increasing dispersibility and reducing non-specific protein adsorption. In addition, the polymer-modified UiO-66-NH_2 NPs showed a 10-fold lower cytotoxicity and, therefore, higher biocompatibility in a model body cell environment than the unmodified UiO-66-NH_2 NPs.

In the third project, I used machine learning (ML) techniques to find optimized synthesis parameters for MOF film synthesis. Identifying optimal synthesis parameters for a specific application can be very time-consuming. In this context, ML algorithm tools have proven valuable and allow the optimization of multiple parameters simultaneously. Here, I demonstrated the successful application of the genetic (GA) and Bayesian optimization (BO) algorithms for the complete and uniform coating of a glass wafer with UiO-66-NH_2.

Abstract (German)

Metallorganische Gerüstverbindungen (MOFs) sind in hohem Maße anpassbar und können für Anwendungen in verschiedenen Forschungsbereichen, wie z. B. Medizin und Biologie, entwickelt und verbessert werden. In dieser Arbeit habe ich mehrere neue Strategien zur Synthese, Modifizierung und Anwendung von MOF-Materialien in Biologie und Medizin entwickelt.

Im ersten Projekt habe ich Enzyme in MOFs eingekapselt, um sie vor den schädlichen Auswirkungen von organischen Lösungsmitteln oder anderen Umwelteinflüssen zu schützen. Durch Testen verschiedener MOFs habe ich Ca(BDC) als besten Schutz für das Enzym Phenacrylat-Decarboxylase (PAD) ermittelt. Die PAD@MOF-Partikel bewahren die enzymatische Aktivität sogar in organischen Lösungsmitteln wie Ethanol (EtOH) oder Cyclohexan (Cyc).

Im zweiten Projekt habe ich MOF-Materialien mit Polymeren modifiziert, um ihre Biokompatibilität für die Verabreichung von Medikamenten in Zellen zu verbessern. Unveränderte MOF Nanocarrier aggregieren oft schnell, adsorbieren Blutproteine an ihrer Oberfläche und werden schließlich von der körpereigenen Immunreaktion eliminiert, bevor sie den gewünschten Wirkungsort erreichen. Um diese Einschränkungen zu überwinden und die MOFs biokompatibler zu machen, habe ich eine Nitroxid-vermittelte Polymerisationsmethode (NMP) angewandt und die Oberfläche von UiO-66-NH_2 (Universitetet i Oslo) Nanopartikeln (NPs) mit hydrophilen Polymeren modifiziert. Durch diese Anpassung konnten die Kristallinität und die Nanogröße der NPs beibehalten werden, während die Dispergierbarkeit erhöht und die unspezifische Proteinadsorption verringert wurde. Darüber hinaus zeigten die polymermodifizierten UiO-66-NH_2 NPs eine 10-fach geringere Zytotoxizität und damit eine höhere Biokompatibilität in einer modellhafen Körperzellenumgebung als die unmodifizierten UiO-66-NH_2 NPs.

Im dritten Projekt verwendete ich Techniken des maschinellen Lernens (ML), um optimierte Syntheseparameter für die MOF-Filmsynthese zu finden. Die Identifizierung optimaler Syntheseparameter für eine bestimmte Anwendung kann sehr zeitaufwändig sein. In diesem Zusammenhang haben sich ML-Algorithmen bewährt, die die

gleichzeitige Optimierung mehrerer Parameter ermöglichen. Hier habe ich die erfolgreiche Anwendung des Genetischen (GA) und des Bayes'schen Optimierungs (BO) Algorithmus für die vollständige und gleichmäßige Beschichtung eines Glaswafers mit UiO-66-NH_2 demonstriert.

List of Figures

Figure 1: Common secondary building units (SBU) to construct MOF materials. Carbon (black), oxygen (red), and polyhedra metal (blue). [Reprinted and adapted with permission from {A. Schoedel, S. Rajeh, “Why design matters: From decorated metal-oxide clusters to functional metal-organic frameworks”, Top. Curr. Chem. 2020, 378, 19, p. 4, http://dx.doi.org/10.1007/978-3-030-47340-2_1}. Copyright {2020} Springer Nature].[24] 5

Figure 2: General procedure for the growth of a metal-organic framework (MOF) on a substrate. Here, the substrate is first modified with a self-assembled monolayer (SAM), and then the metal and linker are grown step-by-step on the surface. [Figure based on {O. Shekhah, H. Wang, S. Kowarik, F. Schreiber, M. Paulus, M. Tolan, C. Sternemann, F. Evers, D. Zacher, R. A. Fischer et al., “Step-by-Step Route for the Synthesis of Metal−Organic Frameworks”, J. Am. Chem. Soc. 2007, 129, p. 15118}].[26] 6

Figure 3: Synthesis of ZIF-8 frameworks. ZIF-8 consists of 2-methylimidazole (HmIM) and a tetrahedral metal cluster of Zn(II). [Reprinted and adapted with permission from {M. Gao, J. Wang, Z. Rong, Q. Shi, J. Dong, “A combined experimental-computational investigation on water adsorption in various ZIFs with the SOD and RHO topologies”, RSC Adv. 2018, 8, p. 39628, https://doi.org/10.1039/C8RA08460B}. Copyright {2018} The Royal Society of Chemistry].[57] 11

Figure 4: Synthesis of ZIF-90 frameworks. ZIF-90 consists of 2-imidazolecarboxaldehyde (HICA) and a tetrahedral metal cluster of Zn(II). [Reprinted and adapted with permission from {M. Gao, J. Wang, Z. Rong, Q. Shi, J. Dong, “A combined experimental-computational investigation on water adsorption in various ZIFs with the SOD and RHO topologies”, RSC Adv. 2018, 8, p. 39628, https://doi.org/10.1039/C8RA08460B}. Copyright {2018} The Royal Society of Chemistry].[57] 12

Figure 5: Synthesis of MIL-53(Al) frameworks. MIL-53(Al) consists of terephthalic acid (BDC) and octahedral $AlO_4(H_2O)$. [Reprinted and adapted with permission from {H. T. Nguyen, L. H. Thuy Nguyen, T. Le Hoang Doan, P. H. Tran, “A mild and efficient method for the synthesis of pyrroles using MIL-53(Al) as a catalyst under solvent-free sonication”, RSC Adv. 2019, 9, p. 9097, https://doi.org/10.1039/C9RA01071H}. Copyright {2019} The Royal Society of Chemistry].[65] 13

Figure 6: Synthesis of Ca(BDC) frameworks. Ca(BDC) consists of terephthalic acid (BDC) and Ca(II) metals. The carboxy groups of the linker connect these two building blocks, and the hydrogen bonds link the metal and linker blocks to span up the framework. [Figure based on {S. H. Dale, M. R. J. Elsegood, “catena-Poly-[[di-aqua-calcium(II)]-μ3-terephthalato-μ2-aqua] at 150 K”, Acta Crystallogr., Sect. E: Struct. Rep. Online 2003, 59,

m586, https://doi.org/10.1107/S1600536803015071} with permission of the International Union of Crystallography. Copyright{2003} International Union of Crystallography].[67]. 14

Figure 7: Using UiO-66 with different linkers makes it possible to increase the pore size. The linkers differ in the number of benzene rings, which influences the pore width of the formed metal-organic framework (MOF). Together with the Zr_6-cluster, terephthalic acid (BDC) creates UiO-66, biphenyl-4,4'-dicarboxylate (BPDC) UiO-67, and terphenyl-4,4′-dicarboxylate (TPDC) UiO-68. [Reprinted and adapted with permission from {J. H. Cavka, S. Jakobsen, U. Olsbye, N. Guillou, C. Lamberti, S. Bordiga, K. P. Lillerud, “A New Zirconium Inorganic Building Brick Forming Metal Organic Frameworks with Exceptional Stability”, J. Am. Chem. Soc., 2008, 130, p. 13851, https://doi.org/10.1021/ja8057953}. Copyright {2008} American Chemical Society].[75]..... 17

Figure 8: Three distinct terephthalic acid (BDC) linkers, each with a unique set of functional groups. All of these linkers can be used to synthesize UiO-66 derivatives. .. 18

Figure 9: Three distinct PEGylation modification techniques for nanoparticles (NPs). Adsorption, covalent coupling, and self-assembly result in a surface-modified PEG NP. [Figure based on {L. Shi, J. Zhang, M. Zhao, S. Tang, X. Cheng, W. Zhang, W. Li, X. Liu, H. Peng, Q. Wang, “Effects of polyethylene glycol on the surface of nanoparticles for targeted drug delivery”, Nanoscale 2021, 13, p. 10750}].[81]..... 19

Figure 10: Determining the ideal reaction conditions for a specific chemical reaction using two distinct approaches. The top of the chart displays the typical chemical manual or random reaction optimization for a certain parameter space. This approach usually involves numerous experiments and requires the expertise of a scientist. The bottom of the chart displays the machine learning (ML) method for the same parameter space. ML techniques acquire knowledge through training an algorithm on a provided dataset. As a result, it mimics scientific understanding and frequently makes connections more quickly for an accelerated synthesis optimization..... 21

Figure 11: X-ray diffraction (XRD) on a crystalline lattice. The incoming X-rays are scattered on crystal atoms in the material. d_{hkl} is the lattice distance, and θ the incident angle.[88] 25

Figure 12: Examples of lattice planes with the indicated Miller Indices in a cubic system.[90] In green, the planes (100), (110), and (111) are shown. [Figure based on {T. Oeser, “Kristallstrukturanalyse durch Röntgenbeugung. Spektroskopiekurs kompakt“, Springer Spektrum, Wiesbaden, Germany, 2019, p. 20}].[90] 26

Figure 13: Principal setup of a dynamic light scattering (DLS) experiment. The particles in suspension scatter the laser light, and the scattered intensity is recorded under defined

scattering angles.[97–99] With this, it is possible to detect the particle behaviors in the solvent and the hydrodynamic radius of the particles.[97] 28

Figure 14: Simple model system for a molecule and its bonds. In (A), a classical mechanic model for a two-atom molecule, in this case, HCl and their vibrations are shown. (B) displays the harmonic oscillator, the ideal case if a molecule has no dissipation, and (C) shows the real energy transition states for a molecule in an inharmonic oscillator.[102] [Figure based on {M. Hesse, S. Bienz, H. Meier, L. Bigler, T. Fox, “Spektroskopische Methoden in der organischen Chemie“, Georg Thieme Verlag KG, Stuttgart, Germany, New York, NY, USA, 2016, p. 38-40}].[102] 30

Figure 15: Principle setup of an attenuated total reflection infrared spectroscopy (ATR-IR) experiment: total reflection from the internal reflection element (IRE) into a sample with A) simple reflection and B) multiple reflections. n_1 = refraction index of the IRE, n_2 = refraction index of the sample, whereas $n_2 < n_1$, θ = incident angle and d_p = penetration depth.[100,103] The beam provides vibrational stimulations that give information about the chemical composition of a material. [Figure based on {H. Günzler, H.-U. Gremlich, “IR-Spektroskopie. Eine Einführung“, WILEY-VCH Verlag GmbH & Co. KGaA, Weinheim, 2003, p. 123}].[100] 32

Figure 16: Basic illustration of a scanning electron microscopy (SEM) experiment. An incoming beam hitting the sample with electrons excites secondary and backscattered electrons.[108] These electrons can give information about the surface texture, size, shape, and particle distribution on a surface.[108] [Figure based on {K. Akhtar, S. A. Khan, S. B. Khan, A. M. Asiri, “Handbook of Materials Characterization” (Ed.: S. K. Sharma), Springer Nature Switzerland AG, Cham, Switzerland, 2018, p. 120}].[108] 34

Figure 17: Energy level system and possible transitions for a nucleus with I=1/2 (for example, in a chloroform ($CHCl_3$) solution). Irradiation of $h\nu_1$ can cause absorption or emission. [Figure based on {H. Friebolin, J. K. Becconsall, “Basic one- and two-dimensional nuclear magnetic resonance (NMR) spectroscopy”, WILEY-VCH Verlag GmbH & Co. KGaA, Weinheim, Germany, 2011, p. 7}].[113] 37

Figure 18: General procedure of a time-of-flight secondary ion mass spectrometry (ToF-SIMS) measurement. The high-energy beam of primary ions knocks fragment ions off the surface of a substrate.[102,120] These ions are accelerated and detected based on their mass-to-charge ratio (m/z) in a ToF detector.[102] 39

Figure 19: Basic illustration of a gel permeation chromatography (GPC) experiment. The GPC separates a given polymer sample according to its molecular size.[123,125] Swollen polymer particles of different sizes are given into the column. While passing through the column, smaller particles diffuse in the cavities of the column material, while bigger ones

cannot access them.[123,125] This results in the size-dependent separation of the polymer particles passing through the column.[125] 41

Figure 20: The energy diagram with a HOMO and LUMO state of a molecule. By irradiating light into the sample, an electron is excited from the HOMO into the LUMO.[115] The molecule enters an excited state.[115] [Figure based on {J. B. Lambert, S. Gronert, H. F. Shurvell, “Spektroskopie. Strukturaufklärung in der organischen Chemie”, Pearson Education Deutschland GmbH, München, Germany, 2012, p. 595}].[115] 43

Figure 21: The displayed Jablonski diagram shows the energy absorption of a molecule and possible distributions of the electrons. For a radiation process, fluorescence (F), absorbance (A), and phosphorescence (Ph) are possible, whereas for a nonradiation process, internal conversion (IC) and intersystem crossing (ISC) are possible.[102,127] [Figure based on {M. Hesse, S. Bienz, H. Meier, L. Bigler, T. Fox, “Spektroskopische Methoden in der organischen Chemie“, Georg Thieme Verlag KG, Stuttgart, Germany, New York, NY, USA, 2016, p. 7}].[102] 44

Figure 22: Catalyzed synthesis reaction of p-coumaric acid (pCA) (1) to p-hydroxystyrene (pHS) (2) with the use of a phenacrylate decarboxylase (EsPAD). The reaction is conducted in a flow reactor at room temperature (RT) for 70 h.[130] [Figure based on {M. Peng, E. Mittmann, L. Wenger, J. Hubbuch, M. K. M. Engqvist, C. M. Niemeyer, K. S. Rabe, “3D-Printed Phenacrylate Decarboxylase Flow Reactors for the Chemoenzymatic Synthesis of 4-Hydroxystilbene”, Chem. - Eur. J. 2019, 25, p. 15999}].[130] 46

Figure 23: The formation of a metal-organic framework (MOF) with phenacrylate decarboxylase (PAD) enzymes leads to the encapsulated enzymes. In green, the PAD wild type (wT) and in purple, the PAD mutant (m) are shown. 47

Figure 24: The precipitated metal-organic framework (MOF) particles after the MOF formation without (woE) and with the phenacrylate decarboxylase enzyme (PAD) (wild type (wT) and mutant (m)). The four MOFs tested were the ZIF-8 (ZIF-CO_3-1), ZIF-90, MIL-54(Al), and Ca(BDC) from left to right. The reactions are shown after the respective reaction time in water at room temperature (RT). 50

Figure 25: The X-ray diffraction (XRD) characterization for the four distinct metal-organic framework (MOF) systems - ZIF-8 (ZIF-CO_3-1), ZIF-90, MIL-53(Al), and Ca(BDC) synthesized with or without the phenacrylate decarboxylase enzyme (PAD). Two samples from one MOF system contained either the PAD (wild type (wT) or mutant (m)) or no enzyme (woE) as a reference to trace the crystallization process for pure particles. Along with the reference sample for the MOFs (red), the diffractogram of the respective metals and linkers used for the MOF synthesis are included. The XRD determines the crystalline

phases and verifies whether the MOFs have formed by matching the patterns with the reference.[63,67,95,96] 51

Figure 26: Size and morphology analysis of the four different metal-organic framework (MOF) systems: ZIF-8 (ZIF-CO_3-1), ZIF-90, MIL-53(Al), and Ca(BDC) used for the enzyme encapsulation of the phenacrylate decarboxylase enzymes (PAD) (wild type (wT) and mutant (m)). Additionally, the MOFs without enzymes (woE) are shown. 54

Figure 27: The enzymatic activity of 1 µm phenacrylate decarboxylase enzyme (PAD) (wild type (wT)) monitored together with different concentrations of the metal and linker of ZIF-8 (ZIF-CO_3-1); $Zn(OAc)_2$×$2H_2O$ with 2-methylimidazole (HmIM) and ZIF-90; $Zn(NO_3)_2$×$6H_2O$ with 2-imidazolecarboxaldehyde (HICA). The conversion of p-coumaric acid (pCA) [1.25 mM] (yellow) to p-hydroxystyrene (pHS) [mM] (blue) in an aqueous solution was measured for over 15 minutes at 30 °C. [Parts of this figure were reproduced with permission from {M. Gao, J. Wang, Z. Rong, Q. Shi, J. Dong, “A combined experimental-computational investigation on water adsorption in various ZIFs with the SOD and RHO topologies” RSC Adv. 2018, 8, p. 39628, https://doi.org/10.1039/C8RA08460B}. Copyright {2018} The Royal Society of Chemistry].[57] 55

Figure 28: The enzymatic activity of the phenacrylate decarboxylase enzyme (PAD) (wild type (wT)), monitored together with different concentrations of the metal and linker of MIL-53(Al) and Ca(BDC) ($Al(NO_3)_3$×$9H_2O$ (MIL-53(Al)) and $CaCl_2$ (CaBDC) and disodium terephthalate (Na_2BDC)). The conversion of p-coumaric acid (pCA) [1.25 mM] (yellow) to p-hydroxystyrene (pHS) [mM] (blue) in an aqueous solution was measured for over 15 minutes at 30 °C. [Parts of this figure were reproduced or adapted with permission from {H. T. Nguyen, L. H. Thuy Nguyen, T. Le Hoang Doan, P. H. Tran, “A mild and efficient method for the synthesis of pyrroles using MIL-53(Al) as a catalyst under solvent-free sonication”, RSC Adv. 2019, 9, p. 9097, https://doi.org/10.1039/C9RA01071H}. Copyright {2019} The Royal Society of Chemistry and {S. H. Dale, M. R. J. Elsegood, “catena-Poly-[[di-aqua-calcium(II)]-µ3-terephthalato-µ2-aqua] at 150 K”, Acta Crystallogr., Sect. E: Struct. Rep. Online 2003, 59, m586, https://doi.org/10.1107/S1600536803015071}. Copyright{2003} International Union of Crystallography].[65,67] 56

Figure 29: Phenacrylate decarboxylase enzyme (PAD) (wild type (wT) and mutant (m)) activity measurement after the encapsulation in ZIF-8 (ZIF-CO_3-1), ZIF-90, MIL-53(Al), and Ca(BDC) particles. The p-hydroxystyrene (pHS) [mM] production from p-coumaric acid (pCA) [1.25 mM] is illustrated over 25 h. The different enzymes, PAD (wT and m), are displayed in green and violet. [Parts of this figure were reproduced or adapted with permission from {M. Gao, J. Wang, Z. Rong, Q. Shi, J. Dong, “A combined experimental-

computational investigation on water adsorption in various ZIFs with the SOD and RHO topologies" RSC Adv. 2018, 8, p. 39628, https://doi.org/10.1039/C8RA08460B}. Copyright {2018} The Royal Society of Chemistry, {H. T. Nguyen, L. H. Thuy Nguyen, T. Le Hoang Doan, P. H. Tran, "A mild and efficient method for the synthesis of pyrroles using MIL-53(Al) as a catalyst under solvent-free sonication", RSC Adv. 2019, 9, p. 9097, https://doi.org/10.1039/C9RA01071H}. Copyright {2019} The Royal Society of Chemistry, and {S. H. Dale, M. R. J. Elsegood, "catena-Poly-[[di-aqua-calcium(II)]-μ3-terephthalato-μ2-aqua] at 150 K", Acta Crystallogr., Sect. E: Struct. Rep. Online 2003, 59, m586, https://doi.org/10.1107/S1600536803015071}. Copyright{2003} International Union of Crystallography].[57,65,67] 57

Figure 30: The compatibility of the Ca(BDC) particles with the reactant (p-coumaric acid (pCA)) [1.25 mM] and the product (p-hydroxystyrene (pHS)) [1.25 mM], measured throughout 25 h. The pHS concentration is on the left, and the pCA concentration is on the right. 59

Figure 31: The western blot with the results from the enzyme activity in the Ca(BDC) particles. The used samples were Ca(BDC) without (woE) and with phenacrylate decarboxylase enzyme (PAD) (wild type (wT) and mutant (m)). Furthermore, the washing solution gives information about the successful incorporation of the enzymes into the metal-organic framework (MOF) structure. We used 50 µg MOF with or without enzyme (woE) (rows 1-3), the centrifuged supernatant of the Ca(BDC) samples resuspended in SDS and filtered afterward with a 0.2 µm filter (rows 4-6), a marker (row 7), free enzyme (rows 8-9), the solution from the washing step (row 10-12) and the filtered washing solution with a 0.2 µl filter (row 13-15). All experiments were conducted overnight at 8 °C. The substrate concentration was 1.25 mM..... 60

Figure 32: The X-ray diffraction (XRD) of Ca(BDC) particles, dispersed for two weeks in various solvents or at various pHs without the phenacrylate decarboxylase enzyme (PAD) (woE, blue), with PAD wild type (wT, green), and with PAD mutant (m, purple) are shown. All diffractograms show intact crystalline structures, with the exception of the aqueous solution of pH 4. The repetition, shown in light blue (woE), light green (wT), and light purple (m), confirms this finding. 63

Figure 33: After exposing the phenacrylate decarboxylase enzyme (PAD) (wild type (wT) and mutant (m)) encapsulated in Ca(BDC) to different organic solvents for two weeks, the preserved enzymatic activity of the encapsulated enzymes in the metal-organic framework (MOF) particles is measured. The PAD (wT (green) and m (purple)) encapsulated in Ca(BDC) continue to show enzymatic activity after two weeks in all solvents except methanol (MeOH) and in an aqueous solution with pH 4. The repetition of the experimental series shown in light green and light pink displays similar results. The

conversion of the analyte p-coumaric acid (pCA) [1.25 m]) to p-hydroxystyrene (pHS) [mM] was measured over 24 h at 30 °C. We used 10.0 mg/ml PAD@MOF (wT and m). 65

Figure 34: Polymerization on the UiO-66-NH_2 surface via nitroxide-mediated polymerization (NMP). After the metal-organic framework (MOF) is synthesized, the initiator (either the TEMPO-alkoxyamine (AA) or MAMA-SG1) for the polymerization is applied, and the polymerization happens on this new surface functionalization. The different polymers used for the modification are shown below. 70

Figure 35: The basic principle of the nitroxide-mediated polymerization (NMP) on the surface of UiO-66-NH_2. First, the UiO-66-NH_2 was synthesized, then the TEMPO-alkoxyamine initiator (AA) was attached via the formation of an amide bond on the linker, and finally, the styrene-PEG derivative (poly(ethylene oxide) methyl-p-vinylbenzyl-ether (SPEGA)) polymers were grown on the surface. [Reprinted with permission from {I. Wagner, S. Spiegel, J. Brückel, M. Schwotzer, A. Welle, M. H. Stenzel, S. Bräse, S. Begum, M. Tsotsalas, ”Biofunctionalization of Metal–Organic Framework Nanoparticles via Combined Nitroxide-Mediated Polymerization and Nitroxide Exchange Reaction“, Macromol. Mater. Eng. 2023, p. 3, https://doi.org/10.1002/mame.202300048}. Copyright {2023} The Authors, Macromolecular Materials and Engineering published by Wiley-VCH GmbH].[141] 72

Figure 36: Overview of the reaction scheme for the nitroxide-mediated polymerization (NMP) with poly(ethylene oxide) methyl-p-vinylbenzyl-ether (SPEGA) on the surface of UiO-66-NH_2 nanoparticles (NPs) (A). Attenuated total reflection infrared spectroscopy (ATR-IR) (B) and time-of-flight secondary ion mass spectrometry (ToF-SIMS) normalized on the Zr-signal (C) measurements verify the successful polymerization on the NP surface. Meanwhile, X-ray diffraction (XRD) measurements prove that the crystallinity is preserved after the modification steps on the NP's surface (D). [Reprinted and adapted with permission from {I. Wagner, S. Spiegel, J. Brückel, M. Schwotzer, A. Welle, M. H. Stenzel, S. Bräse, S. Begum, M. Tsotsalas, ”Biofunctionalization of Metal–Organic Framework Nanoparticles via Combined Nitroxide-Mediated Polymerization and Nitroxide Exchange Reaction“, Macromol. Mater. Eng. 2023, p. 3, https://doi.org/10.1002/mame.202300048}. Copyright {2023} The Authors, Macromolecular Materials and Engineering published by Wiley VCH GmbH].[141] 73

Figure 37: Scanning electron microscope (SEM) (A) and dynamic light scattering (DLS) (C) measurements to analyze the pristine, the TEMPO-alkoxyamine (AA)-modified, and the poly(ethylene oxide) methyl-p-vinylbenzyl-ether (SPEGA)-modified nanoparticles (NPs). The NP size is maintained after polymerization. A dispersibility experiment of the pristine and SPEGA-modified NPs in ethanol (EtOH) shows the increased dispersibility

of the metal-organic framework (MOF)/polymer NPs (B). Furthermore, the decreased human serum albumin (HSA) protein adsorption on the MOF/polymer NPs is displayed (D). [Reprinted and adapted with permission from {I. Wagner, S. Spiegel, J. Brückel, M. Schwotzer, A. Welle, M. H. Stenzel, S. Bräse, S. Begum, M. Tsotsalas, ”Biofunctionalization of Metal–Organic Framework Nanoparticles via Combined Nitroxide-Mediated Polymerization and Nitroxide Exchange Reaction“, Macromol. Mater. Eng. 2023, p. 3, https://doi.org/10.1002/mame.202300048}. Copyright {2023} The Authors, Macromolecular Materials and Engineering published by Wiley VCH GmbH]. [141] 76

Figure 38: Nitroxide exchange reaction (NER) of the TEMPO-nitroxide (green) with the RGD-nitroxide (orange). The R-group connects the TEMPO- or the RGD-nitroxide to the polymer chain on the metal-organic framework (MOF) surface. The reaction is conducted under the exclusion of oxygen to avoid side reactions. [Figure based on {I. Wagner, S. Spiegel, J. Brückel, M. Schwotzer, A. Welle, M. H. Stenzel, S. Bräse, S. Begum, M. Tsotsalas, ”Biofunctionalization of Metal–Organic Framework Nanoparticles via Combined Nitroxide-Mediated Polymerization and Nitroxide Exchange Reaction“, Macromol. Mater. Eng. 2023, p. 5}].[141]..... 77

Figure 39: The time-of-flight secondary ion mass spectrometry (ToF-SIMS) measurement verifies the successful nitroxide exchange reaction (NER). The characteristic fragments for the arginine (in the RGD sequence), the $TEMPO^+$ group, and the intact RGD sequence are shown. [Reprinted and adapted with permission from {I. Wagner, S. Spiegel, J. Brückel, M. Schwotzer, A. Welle, M. H. Stenzel, S. Bräse, S. Begum, M. Tsotsalas, ”Biofunctionalization of Metal–Organic Framework Nanoparticles via Combined Nitroxide-Mediated Polymerization and Nitroxide Exchange Reaction“, Macromol. Mater. Eng. 2023, p. 3, https://doi.org/10.1002/mame.202300048}. Copyright {2023} The Authors, Macromolecular Materials and Engineering published by Wiley VCH GmbH].[141] 78

Figure 40: Reaction scheme for the two-step polymerization on the surface of UiO-66-NH_2 nanoparticles (NPs) with poly(ethylene glycol) methyl ether acrylate (APEG), N-hydroxyethylacrylamide (HEAA), and N,N-dimethylacrylamide (DMAA). For the polymerization with MAMA-SG1, the initiator was applied on the surface of UiO-66-NH_2 via an amide bond. In the next step, the polymerization was started in dimethylformamide (DMF) by heating the mixture to 110 °C in the presence of the respective monomers. In the scope of this thesis, the shown process is called two-step synthesis. 80

Figure 41: Attenuated total reflection infrared spectroscopy (ATR-IR) results verifying the successful two-step surface polymerization for the UiO-66-NH_2 nanoparticles (NPs) with poly(ethylene glycol) methyl ether acrylate (APEG), N-hydroxyethylacrylamide (HEAA), and N,N-dimethylacrylamide (DMAA). The polymerization reactions were conducted in

two steps after a previous initiator (MAMA-SG1) attachment on the surface. The polymerization was carried out at 110 °C in dimethylformamide (DMF). 81

Figure 42: Time-of-flight secondary ion mass spectrometry (ToF-SIMS) results verifying the successful two-step surface polymerization for the UiO-66-NH_2 nanoparticles (NPs) with poly(ethylene glycol) methyl ether acrylate (APEG), N-hydroxyethylacrylamide (HEAA), and N,N-dimethylacrylamide (DMAA). The polymerization reactions were conducted in a two-step procedure after a previous initiator (MAMA-SG1) attachment on the surface. The polymerization was carried out at 110 °C in dimethylformamide (DMF). 83

Figure 43: X-ray diffraction (XRD) (left) and dynamic light scattering (DLS) (right) measurements proving the conserved crystallinity and nano-size of the UiO-66-NH_2 nanoparticles (NPs) modified with poly(ethylene glycol) methyl ether acrylate (APEG), N-hydroxyethylacrylamide (HEAA), and N,N-dimethylacrylamide (DMAA) in a two-step synthesis procedure. The polymerization reactions were conducted in a two-step procedure after a previous initiator (MAMA-SG1) attachment on the surface. The polymerization was carried out at 110 °C in dimethylformamide (DMF). 84

Figure 44: Reaction scheme for the one-step polymerization on the surface of UiO-66-NH_2 nanoparticles (NPs) with poly(ethylene glycol) methyl ether acrylate (APEG), N-hydroxyethylacrylamide (HEAA), and N,N-dimethylacrylamide (DMAA). For the polymerization, the initiator (MAMA-SG1), UiO-66-NH_2, and different amounts of the monomers (APEG, HEAA, and DMAA) were heated at 110 °C in dimethylformamide (DMF) for a specific amount of time. The shown process is called one-step synthesis. The copolymers shown here represent a simple visualization and do not reflect the actual distribution in the polymer. 86

Figure 45: Attenuated total reflection infrared spectroscopy (ATR-IR) verifying the successful surface polymerization of the UiO-66-NH_2 nanoparticles (NPs) with different polymer chain lengths and/or copolymer combinations of poly(ethylene glycol) methyl ether acrylate (APEG), N-hydroxyethylacrylamide (HEAA), and N,N-dimethylacrylamide (DMAA). The polymerization reactions were conducted in a one-step procedure after mixing MAMA-SG1, UiO-66-NH_2 NPs, and the respective monomers (APEG, HEAA, and DMAA) and heating them to 110 °C in dimethylformamide (DMF). 87

Figure 46: Time-of-flight secondary ion mass spectrometry (ToF-SIMS) results verifying the successful one-step surface modification for the UiO-66-NH_2 nanoparticles (NPs) modified with poly(ethylene glycol) methyl ether acrylate (APEG), N-hydroxyethylacrylamide (HEAA), and N,N-dimethylacrylamide (DMAA) polymers with different chain lengths or copolymers on their surface. The polymerization reactions were conducted in a one-step procedure after mixing MAMA-SG1, UiO-66-NH_2 NPs, and the

respective monomers (APEG, HEAA, and DMAA) and heating them to 110 °C in dimethylformamide (DMF). 90

Figure 47: X-ray diffraction (XRD) (left) and dynamic light scattering (DLS) (right) confirm the conserved crystallinity and maintained nano-size of the one-step synthesized metal-organic framework (MOF)/polymer nanoparticles (NPs). The polymerization reactions were conducted in one-step procedures after mixing MAMA-SG1, UiO-66-NH_2 NPs, and the respective monomers (poly(ethylene glycol) methyl ether acrylate (APEG), N-hydroxyethylacrylamide (HEAA), and/or N,N-dimethylacrylamide (DMAA)) and heating them to 110 °C in dimethylformamide (DMF). 91

Figure 48: Gel permeation chromatography (GPC) measurement of the polymers grown on the UiO-66-NH_2 nanoparticles (NP) (one- or two-step process). The GPC measurement shows the molecular mass distribution of the individual polymer chains formed in situ in the reaction solution of the polymer-modified metal-organic framework (MOF) NPs and provides information about the molar mass dispersity ($Đ_M$). The GPC experiment was conducted in H_2O+0.5 g/L NaN_3 and a mixture of 40 % acetonitrile (MeCN) and 0.1 % trifluoroacetic acid (TFA). 92

Figure 49: Kinetic study of the curcumin uptake into pristine UiO-66-NH_2 nanoparticles (NPs) over 180 h. Different solvent combinations: chloroform ($CHCl_3$), $CHCl_3$/cyclohexane (Cyc) (2:1, v:v), and $CHCl_3$/Cyc (1:1, v:v) are displayed to determine the highest uptake and correlate different solvent environments with the uptaken drug amount. After 180 h, the NPs in $CHCl_3$/Cyc (1:1, v:v) have the highest uptake. The reaction time is displayed at the bottom, and the concentration is given in mg curcumin per g metal-organic framework (MOF). 95

Figure 50: Measuring the curcumin uptake for the different polymer-modified UiO-66-NH_2 nanoparticles (NPs) after 24 h. All NPs show an uptake after 24 h. The curcumin was previously dissolved in chloroform/cyclohexane ($CHCl_3$/Cyc) (1:1, v:v). The time is displayed at the bottom, and the concentration is given in mg curcumin per g metal-organic framework (MOF)/polymer. 96

Figure 51: Experimental method for determining the cytotoxicity of drug-free polymer-modified and pristine UiO-66-NH_2 nanoparticles (NPs) for cells. MCF-7 breast cancer cells are used to model the cell environment in the body and provide information on the compatibility of the metal-organic framework (MOF) NPs used with body cells and in the medium. The cells were previously cultured at 37 °C, and the sulforhodamine B (SRB) cytotoxicity assay was used for the analysis. 99

Figure 52: The fitness values of the three generations for the Synthesis Condition Finder (SyCoFinder) with the genetic algorithm (GA) (left) and the Bayesian optimization (BO)

(right). All generations consist of ten experiments, and the average fitness was calculated from all the successful reactions. The scanning electron microscopy (SEM) pictures at the bottom show one surface picture of the single best results in each generation for both algorithms..... 108

Figure 53: Repetition of the reactions with the best fitness values found by the two machine learning (ML) algorithms over three generations. The fitness values of the Synthesis Condition Finder (SyCoFinder) with the genetic algorithm (GA) are on the right, and the Bayesian optimization (BO) algorithm is on the left. Both experiments show comparably good fitness values concerning the original results. The fitness for the optimized results is shown in black, and the fitness of the repeated reactions is shown in blue. 110

Figure 54: Reaction scheme of nitroxide-mediated polymerization (NMP) on the surface of UiO-66-NH_2 nanoparticles (NP). After the initiator (TEMPO-alkoxyamine) has been applied to the NP, the molecule (1) is heated. The heating of the surface-bound initiator results in a bond break between C and O. The resulting carbon radical can react with the double bond of the monomer, forming the polymer chain on the surface (2). The reaction was carried out in toluene (Tol) under the exclusion of oxygen..... 126

Figure 55: Reaction scheme of the nitroxide-mediated polymerization (NMP) on the surface of UiO-66-NH_2 nanoparticles (NPs) with the initiator MAMA-SG1. After the initiator has been applied to the NPs, the molecule (1) is heated. The heating of the surface-bound initiator results in a bond break between C and O. The resulting carbon radical can react with the double bond of the monomer, forming the polymer chain (2) (two-step synthesis). Additionally, the UiO-66-NH_2 NPs are heated in the presence of the initiator MAMA-SG1 and the respective monomer. In this case, the bond formation on the metal-organic framework (MOF) surface happens simultaneously with polymerization (one-step synthesis). The reaction was carried out in dimethylformamide (DMF) under the exclusion of oxygen..... 127

Figure 56: General principle of the chemical vapor-assisted method (VAC). A substrate is placed on top of Raschig rings over a vapor source. Carefully, a drop of the precursor solution (containing metal, linker, and modulator) is placed on top of the wafer. The reaction vessel is closed and heated up for a defined time. During that time, a metal-organic framework (MOF) film forms on the wafer's surface. 133

Figure 57: Scanning electron microscopy (SEM) evaluation of the experiments predicted with the two machine learning (ML) algorithms. The illustration in A shows the positions on which SEM images were taken to evaluate the surface coverage on a glass wafer. Additionally, B shows the process of determining the particle ratio in the pictures. A Python script was used to calculate the particle coverage on the surface [%]. 135

List of Tables

Table 1: This work utilizes reference literature to identify the X-ray diffraction (XRD) pattern of UiO-66, ZIF-8 (ZIF-CO_3-1), ZIF-90, MIL-53(Al), and Ca(BDC). 27

Table 2: Two-step procedure for three different metal-organic framework (MOF)/polymer nanoparticles (NPs) using poly(ethylene glycol) methyl ether acrylate (APEG), N-hydroxyethylacrylamide (HEAA), or N,N-dimethylacrylamide (DMAA). The synthesis was carried out with the pristine UiO-66-NH-MAMA modified MOF NP and the free MAMA-SG1 nitroxide-mediated polymerization (NMP) initiator in a dimethylformamide (DMF) solution. The table gives an overview of the monomer amounts used [equiv.] and the polymerization time. 128

Table 3: One-step procedure for four different metal-organic framework (MOF)/polymer or MOF/copolymer nanoparticles (NPs) using poly(ethylene glycol) methyl ether acrylate (APEG), N-hydroxyethylacrylamide (HEAA), and/or N,N-dimethylacrylamide (DMAA). The synthesis was carried out with the pristine UiO-66-NH_2 NP and the free MAMA-SG1 nitroxide-mediated polymerization (NMP) initiator in a dimethylformamide (DMF) solution. The table gives an overview of the monomer amounts used [equiv.] and the polymerization time. 129

Table 4: The parameter sets for the optimization strategy with the two machine learning (ML) algorithms. The parameters were adjusted according to the user-provided range values. 134

List of Equations

Equation 1: Braggs-Law determines the plane distance in a single crystal or a crystal powder.[89] d_{hkl} is the lattice distance, θ the incident angle, λ the wavelength, and n the integer. 25

Equation 2: Connection between the Miller indices and the Bragg equation in a cubic system. a is the lattice parameter, d_{hkl} the lattice distance, and h,k,l the Miller indices.[89] 26

Equation 3: The energy of a given molecule can be calculated with the harmonic oscillator. Therefore, V is the potential energy, k is the force constant, x is the deflection, μ the reduced mass, and ν_{osc} is the vibration frequency of the oscillator.[102] 30

Equation 4: A function of the refractive indices from the sample (n_2) and the internal reflection element (IRE) (n_1) describes the incident angle θ_C.[100,103] 32

Equation 5: Intrinsic angular moment of a nuclei. I is the nuclear spin, and ħ consists of Planck's constant (ħ=h/2π)..... 35

Equation 6: The effective magnetic field on the nucleus depends on the shielding capacity of the electrons. σ is the shielding constant.[102,116] 37

Equation 7: The Lambert-Beer law describes the correlation of the incident light (I_0) to the outgoing light (I) and the concentration of the sample.[102,117] With A, the extinction measured with ultraviolet and visible spectroscopy (UV-Vis), k the absorption coefficient, l the thickness of the sample holder, and ε the molar extinction coefficient.[102,117]..... 45

Equation 8: The shown fitness formula reflects the criteria for the quality of a produced sample. All produced samples were classified with the fitness formula, and the experiments and their fitness were used to train the algorithms..... 135

1. Motivation

In the last 20 years, metal-organic frameworks (MOFs) have become an important class of porous materials, predominately known for their high porosity and ideal application in gas storage or gas separation. Nowadays, over 100,000 MOFs are known with the potential to expand in the following years.[1] But what makes MOFs interesting? A valuable property is their high porosity. With Langmuir surface areas of up to 10,000 m^2/g, MOFs exceed porosity compared to porous materials, like zeolites and activated carbons.[2,3] In addition, the adjustable pore size, surface functionalization, and chemical robustness offer great potential for applications in various research fields.[2,4,5]

MOFs are especially interesting for extending the scope of traditional chemical methods, and nowadays, applications in biology and medicine become prominent. Although MOF materials are generally useful for these two application areas, they must often be modified for specific purposes. For example, the very robust 3D network structure led to the development of many water-stable MOF materials.[6–9] Although they can be used for applications in enzyme encapsulation, they often have to be adjusted to a specific enzyme to preserve the enzymatic activity. Similarly, modifying or choosing specific MOF materials used as drug carriers is often necessary. MOF metals like Fe, Zn, Ca, Mg, etc, may be nontoxic, and together with nontoxic linkers, a biocompatible MOF for drug delivery or other medical applications is promising.[10] Nevertheless, the application of MOFs in drug delivery requires a stable, good dispersed nanoparticle (NP) for long circulation times in the bloodstream. For this biocompatibility, MOFs must often be adjusted to the specific drug or cell type targeted in the body.

Fortunately, MOFs are versatile, and many different linkers and metals allow for synthesizing unique systems or adapting existing systems to specific applications. All these modifications and adjustments help to expand the range of applications of MOF materials. Particularly for applications in biology and medicine, it is essential to develop customized materials for a specific purpose. Therefore, this work focuses on modifying, synthesizing, and adapting synthesis approaches for MOF materials for specific applications.

In the first project, I tried to find a suitable MOF system to protect the phenacrylate decarboxylase (PAD). I tested several MOF systems and evaluated which best allowed the encapsulation of the enzyme while simultaneously protecting the enzymatic activity. Furthermore, I tested the stability of the MOF bond enzyme in different organic solvents and evaluated the long-term stability and activity preservation of the enzyme.

The second project aimed to modify the MOF NP surface with polymers to increase the blood circulation time and biocompatibility for drug delivery. Therefore, I established a new modification strategy based on nitroxide-mediated polymerization (NMP) for surface polymerization with hydrophilic polymers. I then tested whether the polymer modification increases the dispersibility, prolongs the suspension of the particles in polar solvents, and reduces non-specific protein adsorption. Additionally, I introduced a bioactive group to enhance biocompatibility. Furthermore, I transferred the NMP method to verify its success for other MOF/polymer systems. Afterward, I proved the conserved drug uptake into the NPs and tested the suitability of the modified MOF/polymer NPs as drug carriers in a model body cell environment.

The third project targeted machine learning (ML) supported parameter optimization of a given synthesis for producing a uniformly coated MOF film on a surface. Finding optimized synthesis parameters in a multiparameter space can be very time-consuming. In this context, ML algorithm tools have proven valuable and allow the optimization of multiple parameters simultaneously. To assess how well two distinct ML methods optimize the synthesis of a uniformly covered glass wafer with crystalline UiO-66-NH_2 particles, I compared the genetic (GA) and the Bayesian optimization (BO) algorithm

2. Theory and Background

This chapter focuses on the development of metal-organic framework (MOF) compounds from their occurrence to today's research interests. I will identify essential MOFs for this thesis and describe their components and synthesis. In addition, I outline new developments and application areas in biology and medicine, plus possible modification strategies for tailored MOF materials.

2.1 Metal-Organic Frameworks

Metal-organic frameworks (MOFs) consist of a metal or metal cluster as the node and an organic ligand as the linker.[11,12] Together, they build up a 3D network known for its robust structures, high surface areas, big and adjustable pore sizes, and versatile modification possibilities.[11] Coming from zeolites, Omar Yaghi first reported about a new class of materials to link metal atoms with organic ligands in 1995.[13] In 1999, he released studies about his work focusing on a stable MOF called MOF-5, which can retain its porosity and exist without stabilizing gas molecules.[14] After that, MOF research increased drastically, and within the next couple of years, many MOF structures with different metal nodes and linkers for various applications were produced.[11]

MOFs originally belonged to a class called coordinative polymers (CPs), in which coordinative bonds connect the metals and linkers.[15,16] One- two- or three-dimensional networks can be built up, and currently, CPs with porous properties are called PCPs or porous MOFs.[15]

The high surface of MOFs was first reported in 1999 with MOF-5 and a surface area of 2900 m^2/g (Langmuir).[14] These values were already better than the ones for zeolites and activated carbon.[17] Nonetheless, MOF structures with even higher surface areas were found over the years, with NU-110 and a surface area of around 7000 m^2/g (Brunauer–Emmett–Teller (BET)) and MOF-177 with a surface area of 4500 m^2/g (Langmuir).[18,19] Computer simulations even predict possible surface areas for MOFs around 14600 m^2/g.[18]

2.1.1 SBUs and Linkers

The high surface areas raise the question of how we can generate and adjust the porosity in a MOF structure. As formerly described, the MOF consists of metals and organic linker molecules. The synthesis is generally a one-pot reaction, and the metal-ligand bond is formed in situ.[20] The most prominent reaction method, the solvothermal synthesis, is usually conducted at relatively low temperatures (<300 °C).[21] Other possible synthesis methods include mechanochemical, electrochemical, microwave-assisted, and sonochemical methods.[22]

The organic linkers consist of bi- or multivalent carboxylic acids (or other nucleophilic groups), which form M-O-C clusters with the metals, referred to as secondary building units (SBU).[23] The linker molecules use these SBUs as rigid vertices and crosslink them to an extended MOF network.[23] The linkers between the SBUs define how the resulting framework will look. Different functional groups, ligand lengths, bulkiness, chirality, etc., are crucial in designing MOF materials with specified characteristics.[21] The adjustable pore size and structure are additionally essential for tailored synthesis approaches.

The SBU concept can help predict different framework structures and porosities. [22] The SBUs are classified by their points of extension (POE). The minimum number of POEs is 3 (triangular-shaped SBU), and the maximum is 18 (polyhedron).[24] Some common SBUs are basic zinc acetate $Zn_4O(\text{-}COO)_6$, square paddlewheel: $Cu_2(\text{-}COO)_4$ (for HKUST-I, for example), and trigonal prismatic: $M_3O(\text{-}COO)_6$ clusters.[24] These building units helped build new structures using the “heterogeneity within order” concept to synthesize structures with more than two metal ions and/or linkers.[24] Figure 1 displays some newer building units, which became interesting a couple of years ago, like $Zr_6O_4(OH)_4(\text{-}COO)_{12}$, ring-like SBUs $Al_2(OH)_8(\text{-}COO)_{16}$, $UO_2(\text{-}COO)_3$, or rare earth metals.[24]

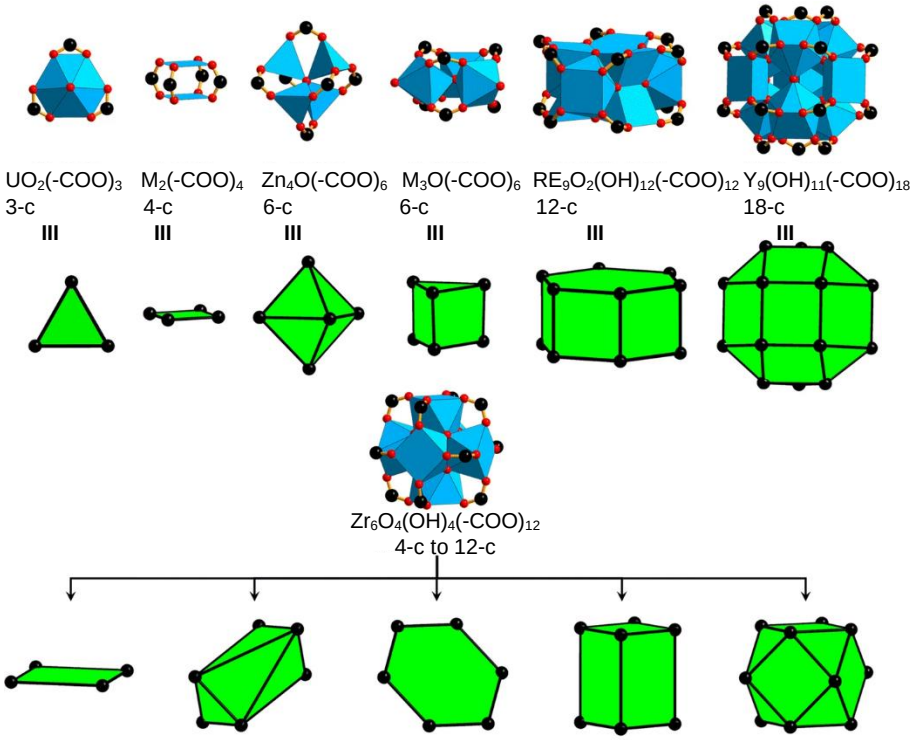

Figure 1: Common secondary building units (SBU) to construct MOF materials. Carbon (black), oxygen (red), and polyhedra metal (blue). [Reprinted and adapted with permission from {A. Schoedel, S. Rajeh, "Why design matters: From decorated metal-oxide clusters to functional metal-organic frameworks", Top. Curr. Chem. 2020, 378, 19, p. 4, http://dx.doi.org/10.1007/978-3-030-47340-2_1}. Copyright {2020} Springer Nature].[24]

2.1.2 MOF Thin Film Synthesis

The previously mentioned high surface area, adjustable pore size, and topology did not only raise interest in MOF applications as powders. Furthermore, the described synthesis method with SBUs made room for ideas for MOF coatings on surfaces for sensor applications.[25] The first significant milestone for that was reached in 2007 with the growth of HKUST-1. [26] After that, growing a thin MOF film with defined porosity and tunable chemical functionality became possible.[25] Surface-anchored metal-organic frameworks (SURMOFs) can be employed on various substrates, for example, gold, silica, or glass wafers. A well-known synthesis method for SURMOFs is the layer-by-layer (LBL) method. Unlike the solvothermal method, where two or more building blocks are mixed, the LBL method uses a step-by-step approach to grow MOF materials (see Figure 2).

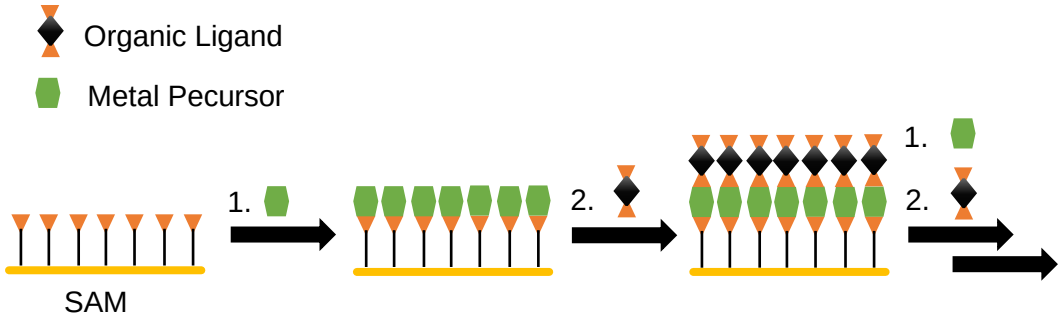

Figure 2: General procedure for the growth of a metal-organic framework (MOF) on a substrate. Here, the substrate is first modified with a self-assembled monolayer (SAM), and then the metal and linker are grown step-by-step on the surface. [Figure based on {O. Shekhah, H. Wang, S. Kowarik, F. Schreiber, M. Paulus, M. Tolan, C. Sternemann, F. Evers, D. Zacher, R. A. Fischer et al., "Step-by-Step Route for the Synthesis of Metal−Organic Frameworks", J. Am. Chem. Soc. 2007, 129, p. 15118}].[26]

Different LBL methods have been established, for example, the spray[27] and the dipping method.[28] Over the years, other methods of forming MOF thin films on surfaces were developed. For an easy and fast approach, an interesting one is the 2018 developed chemical vapor-assisted conversion (VAC). In the VAC, a precursor solution containing metal and linker is placed on top of a substrate. The substrate is placed in a glass bottle equipped with a vapor source. The closed bottle is heated in an oven, and the metal and linker in the precursor solution form a MOF film on the substrate by interacting with the created atmosphere. In a case study, the UiO-66, -67, and -68(NH_2) (Universitetet i Oslo) growth was effectively employed on gold wafers.[29]

2.1.3 Applications of MOFs

Initially, considerable research focused on implementing MOF materials for gas sorption or storage. And also, nowadays, many researchers focus on developing MOFs for even better results in this field. Mainly, the tunable pore geometry and the diversity of MOF structures have gained interest in absorbing and storing gas molecules.[21] Systems for storing hydrogen and methane can provide an alternative to fossil fuels.[21] Current storage systems involve high-pressure tanks, chemisorption, physisorption, and cryogenic tanks.[21] The first MOF synthesized and described for hydrogen storage was introduced in 2003.[30] After that, several more MOFs were tested and evaluated for their

hydrogen storage capability.[31,32] Higher surface areas play a crucial role in higher uptake.[21,31] Since then, many researchers have focused on tailoring the pore sizes of MOF materials to maximize the interaction with hydrogen.[21]

Gas sorption, another prominent field in MOF applications, emphasizes selective gas adsorption and separation.[21] MOFs stand out for these applications primarily because of their selectivity and tunable properties.[21,33] Since the invention of MOFs, a wide range of MOF structures have been shown to exhibit selective gas adsorption.[34]

MOF properties of tunable pore sizes, post-modification strategies, high surface areas, and selectivity have also gained interest in catalysis, sensing, and biological applications.[21,35] The last became especially interesting since MOF materials could be applied to protect catalytic enzymes from harsh conditions, store or deliver drugs as nanocarriers, or be adapted as MOF thin films for biosensors.[21,35,36]

Enzyme encapsulation or immobilization on MOF materials focuses on the catalytic properties of many enzymes. As natural catalysts, enzymes are highly selective and efficient.[37] To use them under harsh conditions, they must be protected and stabilized.[37] Because of the high chemical and thermal stability, MOF systems proved highly useful for enzyme stabilization against environmental and incidental influences.[37] For instance, ZIF-8 (zeolitic imidazole framework) was employed to enclose cytochrome C while preserving and boosting enzymatic activity.[38]

In another system, ZIF-90 was used to embed catalase.[39] While the catalase activity could be preserved for a synthesis approach in water, the normal ethanol (EtOH) based synthesis for ZIF-90@catalase yielded inactivity of the enzyme.[39] These demonstrate the significance of choosing the proper synthesis strategy when using bioactive MOF materials. It also demonstrates how, by modifying the synthesis conditions, we may modify a MOF system to suit a particular application.

Two possible ways for drug delivery and storage existed in the past. On the one hand, the polymeric route, via polymers or macromolecules, has strong biocompatibility but lacks a controlled release mechanism. On the other hand, the inorganic route, via zeolites or porous solids, has enormous potential for controlled drug release but has a decreased

loading capacity.[21,40,41] Combining both advantages with the hybrid features of MOFs with their organic (excellent for biocompatibility) and inorganic components (suitable for controlled drug release) is particularly convincing for medical applications.[21]

Possible representatives for such MOFs are MIL-100 (Matériaux de l'Institut Lavoisier) or MIL-101.[41] They especially persuade with their well-defined and ordered porosity.[21] Another representative of medical and biological approaches is UiO-66. For UiO-66, modifying the linkers to tailor them to a given application is, for example, possible. This modification can also be of use in biological or medical applications. In particular, the encapsulation and control of a released substance make MOF materials suitable for the delivery of therapeutics.[10] Here, a carrier is often required to ensure that appropriate therapeutic amounts reach the site of action or increase the drug's half-life or efficacy without rapid biodegradation.[10] With this, recent developments in the field have shown that MOF materials can be used for encapsulating drugs like ibuprofen,[41] procainamide HCl,[42] curcumin,[43] and more.

In biology, MOF thin films can be of immense influence. One article in 2020 stated, for example, the application of SURMOFs on quartz crystal microbalance and dissipation (QCM-D) wafers to detect plant oil scents.[36] Essential oils can be helpful for their antibacterial properties and potential applications in food.[44] The exact composition of essential oils in plants is challenging to determine, and SURMOF sensors can be engaged to help detect the mixtures.[36] Another valuable tool for MOF thin films in biology is their conversion to SURGELS, a surface-grafted gel.[45] For in vitro studies on cell cultures, SURGELs can be loaded with bioactive substances and used as bioactive coatings to release drugs.[45]

The previous paragraphs described some promising application areas for MOF materials in biology and medicine. Still, before using MOF materials in these areas, we must consider some general concerns regarding toxicity, stability, efficiency, simplicity, and reproducibility.[10] MOFs have shown great potential here, especially in developing mild synthesis routes, post-modification methods with functional groups on linker molecules, or converting MOF thin films to SURGELs. These modifications make them great for further development in biological and medical applications.

2.2 Tailored MOF Biomaterials

Initially, inorganic chemists focused on developing MOF materials.[20] Still, in recent years, organic chemists conducted the predominant studies in the field, focusing on developing new linkers or post-synthetic linker modification.[20] Over the years, different newly designed linkers were synthesized, and new MOF structures were introduced. Some had high potential for applications in biology and medicine since they are chemically stable against pH, temperature, and organic solvents.

Regarding toxicology and biocompatibility of the used MOF materials, customization of the MOF material for a specific application is often necessary. Fortunately, the tunability and diversity of MOFs with different linkers, metals, and post-modifications make it possible to adjust them, especially for biological or medical purposes. In the following part, I will show possible modifications and adjustments for MOF materials in biology and medicine.

2.2.1 Enzyme Nanoencapsulation in MOF Materials

Enzymes consist of amino acids with complex structures and specific catalytically active sites.[37] With their high selectivity, efficiency, and environmentally friendly characteristics, enzymes have found application in large-scale processes for producing fine and pharmaceutical chemicals.[37,46,47] The company Degussa, for example, tried to use enzymatic processes to obtain fatty acid esters for skin care applications.[46] The environmental aspect is especially interesting since we can reduce energy usage and waste disposal with an enzymatic catalyzation process.[46] Furthermore, because enzymes may be designed for a specific chemical transformation, they are particularly attractive for industrial processes.[37,48]

However, the main drawbacks and limitations of enzyme application in industrial processes are reduced long-term stability and poor recyclability and recovery rates.[49] Different approaches are known to protect the enzymes while maintaining their substrate production. One idea to overcome this is the immobilization of enzymes with porous solids, for example, mesoporous silica,[50] silicate glass,[51] carbon nanotubes,[52] and

MOF particles.[53,54] These immobilization approaches can enhance enzyme stabilities and recovery rates while simultaneously reducing costs.[37]

MOF materials are appealing for immobilizing biological materials due to their properties, including adjustable porosity, desirable functionality, high surface area, and chemical/thermal stability.[53,54] They offer great potential since different interactions between the MOF and the enzymes are possible, including hydrogen bonds, salt-bridges, covalent or coordinative bonds, or van-der-Waals forces.[37] The versatility of MOF materials allows for their complete customization, with a particular surface volume and pore size, shape, and size for a specific enzyme.[37] As an example, immobilizing an enzyme with a MOF material provides the benefit of shielding it from harsh reaction conditions.[37] Denaturation can, for example, be prevented by enclosing the enzymes in a MOF and not just immobilizing them on the surface.[37]

Despite the high variability of MOF materials, selecting a suitable framework for incorporating and protecting an enzyme is not easy. Running numerous tests using various MOF structures is frequently necessary to find a system that works. One approach, when searching a MOF for enzyme encapsulation, is, for example, to focus on some general synthesis parameters. The solvent used to prepare the MOFs is one example. For instance, MOFs with water-based synthesis pathways should be considered if the enzyme is unstable in organic solvents, which is the case for most enzymes. For this purpose, below the MOFs ZIF-8, ZIF-90, MIL-53(Al), and Ca(BDC) are presented. All of them have mild synthesis routes in water. Since most biological groups do not survive harsh conditions, the synthesis in water is a primary advantage for using MOF materials to encapsulate enzymes.

ZIF-8 (ZIF-CO_3-1)

ZIF-8 is a representant of the class of zeolitic imidazolate frameworks (ZIFs).[55] In ZIF MOFs, tetrahedral metal ions (e.g., Zn or Co) are linked by imidazolate molecules (Im).[55] The typical angle of the M-Im-M bond is close to 145°, similar to the preferred Si-O-Si angle in zeolites.[56] Different ZIF systems are known, and a study in 2006 compared ZIF-1 to ZIF-4, -6, -8, -10, and -11 (Zn(II)) by their chemical and thermal stability.[56] They describe the stability tested in boiling benzene, methanol (MeOH), water, and aqueous sodium hydroxide.[56] ZIF-8 showed exceptional structural stability in all solvents and survived seven days in boiling water.

The different ZIF structures have different topologies due to different linkages of the metal centers with the ligands.[12] A tetrahedral metal center connected with linear bridging ligands gives the common diamondoid network (dia) topology, while ZIF-8, for example, crystallizes in the sodalite (sod) topology.[12]

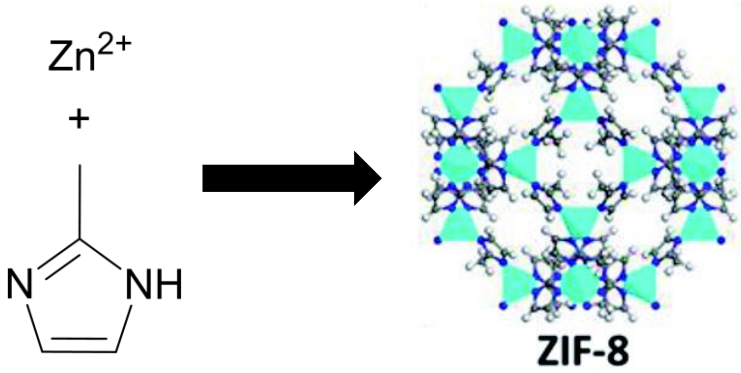

Figure 3: Synthesis of ZIF-8 frameworks. ZIF-8 consists of 2-methylimidazole (HmIM) and a tetrahedral metal cluster of Zn(II). [Reprinted and adapted with permission from {M. Gao, J. Wang, Z. Rong, Q. Shi, J. Dong, "A combined experimental-computational investigation on water adsorption in various ZIFs with the SOD and RHO topologies", RSC Adv. 2018, 8, p. 39628, https://doi.org/10.1039/C8RA08460B}. Copyright {2018} The Royal Society of Chemistry].[57]

2-Methylimidazole (HmIM) and a tetrahedral metal cluster of Zn(II) make up ZIF-8 (see Figure 3).[57,58] It exhibits the same excellent chemical stability as other ZIFs, thanks to the stable Zn(II)/Co(II) and ligand compound, as well as the hydrophobic pore and surface structure, which prevents the accumulation of water molecules and thus the dissolution of the framework.[12,56]

Although ZIF-8 can crystallize in the sod form, several topologies are feasible, some of which may form different structures despite sharing the same chemical connections. In 2019, a study investigated the variation of linker, metal, and enzyme concentrations for encapsulating an enzyme in ZIF-8 structures.[59] Depending on the concentration, different topologies: sod, dia, amorphous, two unidentified topologies named U12 and U13,[60] and ZIF-CO_3-1 were received.[59] It became evident that the structure of ZIF-8 could be altered by varying the concentration of one of the reaction parameters.[59] Therefore, confirming the structure of the produced ZIF crystals using X-ray diffraction (XRD) is crucial.

ZIF-90

Another ZIF representative is ZIF-90. It consists of Zn(II) metals and 2-imidazolecarboxaldehyde (HICA) linkers and crystallizes in the same sod structure as ZIF-8 (see Figure 4).[57,58]

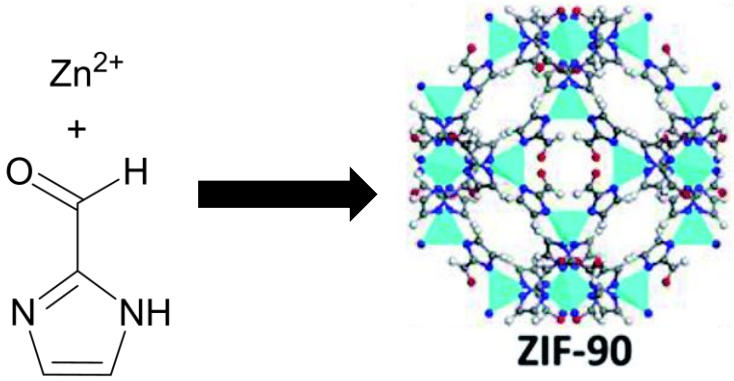

Figure 4: Synthesis of ZIF-90 frameworks. ZIF-90 consists of 2-imidazolecarboxaldehyde (HICA) and a tetrahedral metal cluster of Zn(II). [Reprinted and adapted with permission from {M. Gao, J. Wang, Z. Rong, Q. Shi, J. Dong, "A combined experimental-computational investigation on water adsorption in various ZIFs with the SOD and RHO topologies", RSC Adv. 2018, 8, p. 39628, https://doi.org/10.1039/C8RA08460B}. Copyright {2018} The Royal Society of Chemistry].[57]

While ZIF-8 is highly hydrophobic, the linker of ZIF-90 has polar groups, shows hydrophilic properties, and thus has a high water uptake.[58,61] In MOF materials, ZIFs have high thermal and chemical stability while containing permanent porosity. Together

with the possibility to synthesize them in water, they became ideal candidates for application in enzyme encorporations.

MIL-53(Al)

Ocahedral metal (III) ions, like Al^{3+}, Cr^{3+}, and $Fe^{3+,}$ together with terephthalic acid (BDC), form MIL-53(Al, Cr, or Fe).[62] MIL-53(Al) (MIL = (Matériaux de l'Institut Lavoisier) is built up from $AlO_4(H_2O)$ octahedral structures and connected with BDC, creating rhombic-shaped tunnels (see Figure 5).[63] Given that it only decomposes at temperatures over 500 °C, it has the best thermal stability of the three MIL-53 materials.[63] As in ZIF, the uptake of a guest molecule in MIL-53 can widen the pores and, therefore, change the structure. In this case, the temperature, pressure, or guest molecule encapsulated in the MOF determines if the pores are open or closed.[64]

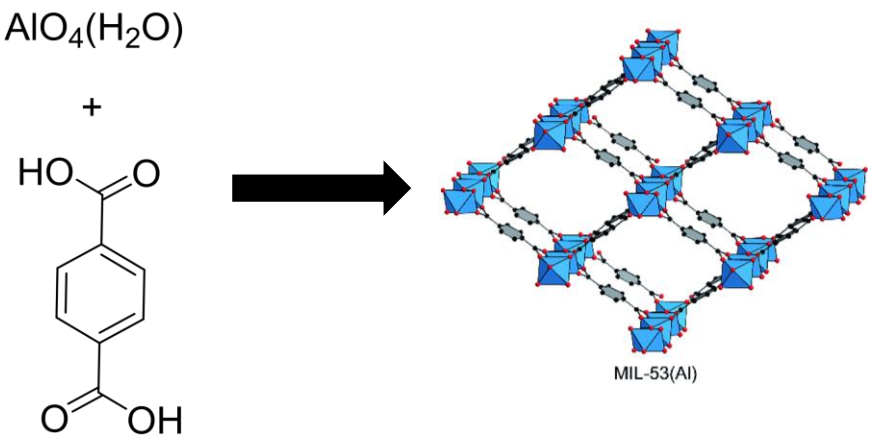

Figure 5: Synthesis of MIL-53(Al) frameworks. MIL-53(Al) consists of terephthalic acid (BDC) and octahedral $AlO_4(H_2O)$. [Reprinted and adapted with permission from {H. T. Nguyen, L. H. Thuy Nguyen, T. Le Hoang Doan, P. H. Tran, "A mild and efficient method for the synthesis of pyrroles using MIL-53(Al) as a catalyst under solvent-free sonication", RSC Adv. 2019, 9, p. 9097, https://doi.org/10.1039/C9RA01071H}. Copyright {2019} The Royal Society of Chemistry].[65]

Ca(BDC)

Ca(BDC) consists of Ca^{2+} and BDC as a linker.[66] The carboxyl groups in the linker and free H_2O groups connect to the Ca^{2+} over hydrogen bonds and build up the fan-shaped structure (see Figure 6).

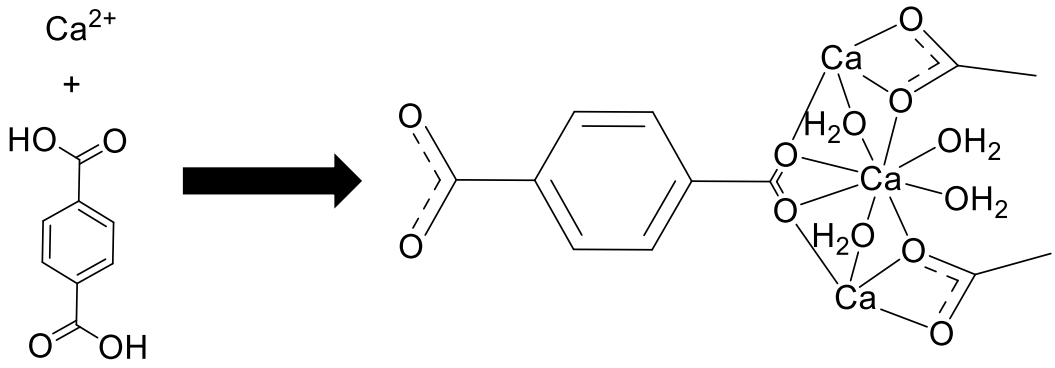

Figure 6: Synthesis of Ca(BDC) frameworks. Ca(BDC) consists of terephthalic acid (BDC) and Ca(II) metals. The carboxy groups of the linker connect these two building blocks, and the hydrogen bonds link the metal and linker blocks to span up the framework. [Figure based on {S. H. Dale, M. R. J. Elsegood, "catena-Poly-[[di-aqua-calcium(II)]-μ3-terephthalato-μ2-aqua] at 150 K", Acta Crystallogr., Sect. E: Struct. Rep. Online 2003, 59, m586, https://doi.org/10.1107/S1600536803015071} with permission of the International Union of Crystallography. Copyright{2003} International Union of Crystallography].[67]

Its stability in an aqueous solution and the strong biocompatibility of the linker favor the application of Ca(BDC) in biology and medicine.[66,68]

Even though the water synthesis is a significant advantage of ZIF-8, ZIF-90, MIL-53(Al), and Ca(BDC), the complete incorporation procedure must still be carried out for an enzyme with each MOF. Only then it is clear whether a specific MOF permits the integration of a particular enzyme without restricting its reactivity.

2.2.2 MOF/Polymer Nanomaterials

Another exciting area for customizing MOF materials for a desired application is the possibility of miniaturizing them.[69] Combining porous materials with nanostructures makes MOF nanoparticles (NPs) an interesting material class for sensing or drug delivery.[69] It is especially significant for the transport of active ingredients that a suitable

nanocarrier is found. This carrier has to protect the active ingredient from degradation by the immune response.[10] The carrier should be non-toxic and deliver sufficient quantities of the active ingredient to the desired site.[10]

Currently, polymers and lipids are typically used as drug delivery carriers.[70] Unfortunately, they often lack a controlled drug release and chemical or mechanical stability.[71] Due to their great versatility and stability, recent work in applying silica-based mesoporous materials as drug carriers was undertaken.[71] Their tunability using different chemical strategies makes them helpful in designing customized carriers for particular drugs and clinical approaches.[71] Nevertheless, achieving good biodistribution, circulation properties, or targeting efficiency is often difficult.[72] Here, MOFs are ideal candidates to accomplish both advantages.[41] Recent progress has proven the successful utilization of MOFs to encapsulate ibuprofen[41] or antitumor drugs like busulfan, cidofovir, and azidothymidine triphosphate.[10]

Essential for a biomedical application is the toxicology and stability of the MOF in a biological environment.[10] So far, in vitro studies showed no toxicity for MOF materials, and intravenous administrations in rats with MIL-88A, MIL-88B_4CH_3, and MIL-100 yielded good results.[73] Medications with structures similar to MIL-88A, like iron fumarate, have been approved as a medicine so far.[10]

Another critical factor for applying MOF materials in biology is their stability. The carrier must maintain stability for the duration of the intended use for drug delivery to be successful.[10] Simultaneously, a certain level of chemical instability is necessary for medical applications to prevent endogenous accumulation.[10] It is crucial that the body's natural immune system can remove the decomposition products after the delivery.[10]

By using MOF materials, we significantly profit from their wide selection of different linkers and metals. Just like from a construction kit, building up a structure suited for a particular case is possible. We can, for example, choose a nontoxic metal (Fe, Zn, Ca, Mg, etc.) and low-toxicity carboxylic or phosphoric acids in drug delivery.[10] Due to their hydrophilic-hydrophobic core, MOFs can accommodate various active molecules with different chemistry.[10] Finally, not only is it easy to customize the MOF network geometry system for better biocompatibility, but we can also tune the organic linker in the MOF with

different polar or nonpolar functional groups to fit an incorporated molecule better.[10] Furthermore, functional groups on the linker can help to attach additional groups or functional molecules. With UiO-66, the following paragraph describes a model MOF for the functionalization and adaptation as a drug delivery carrier.

UiO-66

The MOF named after the University of Oslo (Universitetet i Oslo) called UiO-66 shows excellent chemical stability in pH ranges from 2-10.[74,75] UiO-66 is built from BDC and Zr_6 clusters. The inorganic component is 12-coordinated in a closed-packed metal structure.[75] The initially high stability helps the MOF to withstand temperatures up to 540 °C.[75] The inner core consists of $Zr_6O_4(OH)_4(CO_2)_{12}$ clusters capped with O or OH groups, and the carboxylate groups of the linker connect all of the edges.[75]

The pore size of UiO-66 can be extended by elongating the linker molecules. Therefore, Figure 7 shows BDC and the two and three benzene ring analog linkers: biphenyl-4,4'-dicarboxylate (BPDC) and terphenyl-4,4′-dicarboxylate (TPDC). [75] The solvent stability against water, dimethylformamide (DMF), benzene, and acetone for 24 h without structural decomposition is critical for MOFs and makes UiO-66 worth investigating.

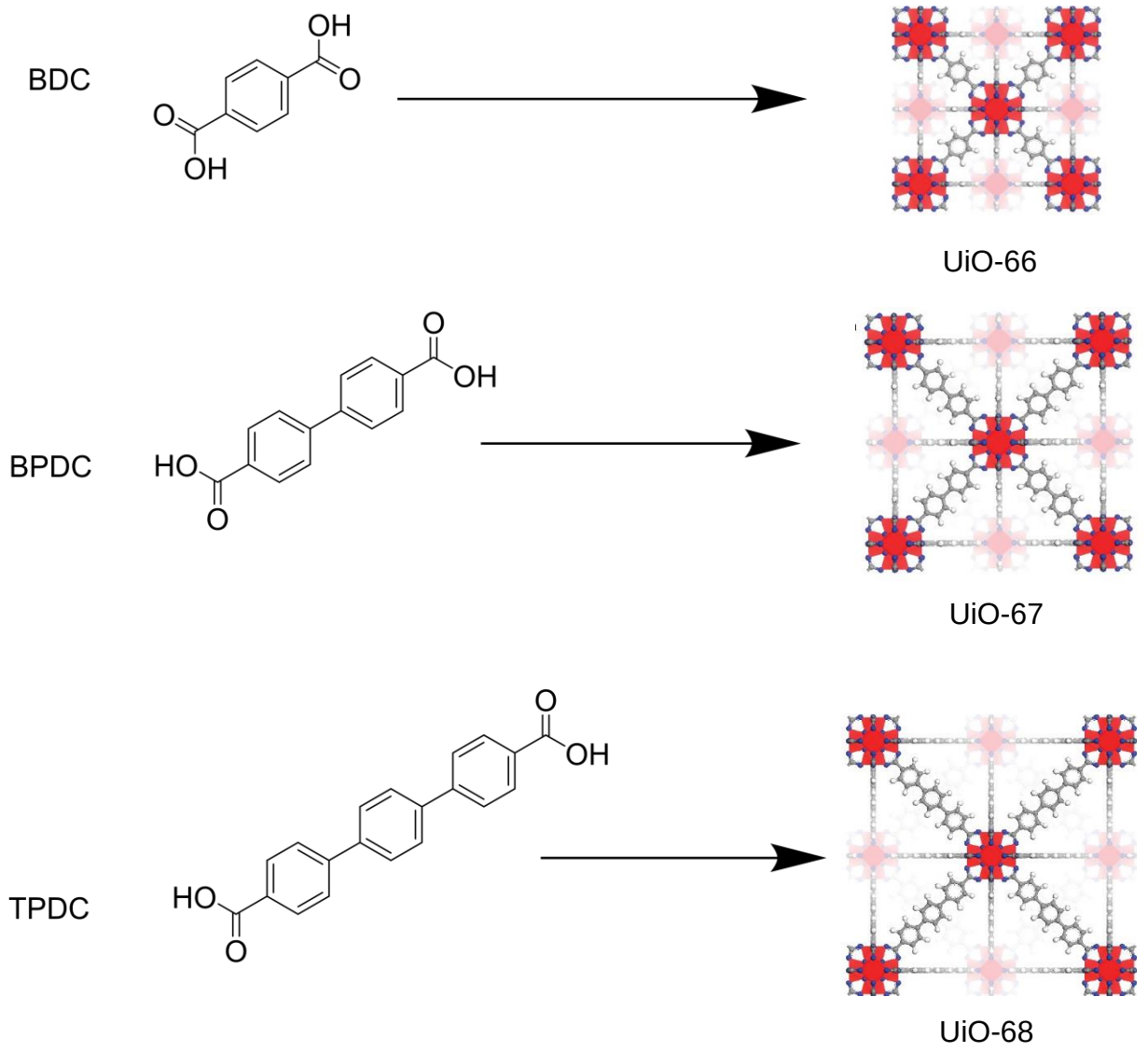

Figure 7: Using UiO-66 with different linkers makes it possible to increase the pore size. The linkers differ in the number of benzene rings, which influences the pore width of the formed metal-organic framework (MOF). Together with the Zr_6-cluster, terephthalic acid (BDC) creates UiO-66, biphenyl-4,4'-dicarboxylate (BPDC) UiO-67, and terphenyl-4,4'-dicarboxylate (TPDC) UiO-68. [Reprinted and adapted with permission from {J. H. Cavka, S. Jakobsen, U. Olsbye, N. Guillou, C. Lamberti, S. Bordiga, K. P. Lillerud, "A New Zirconium Inorganic Building Brick Forming Metal Organic Frameworks with Exceptional Stability", J. Am. Chem. Soc., 2008, 130, p. 13851, https://doi.org/10.1021/ja8057953}. Copyright {2008} American Chemical Society].[75]

Additionally, linkers possessing functional groups have extended the scope of UiO-66, and new applications with new derivatives were found. Maintaining the original topology of UiO-66 has already been demonstrated with commercially available linkers, like

2-aminoterephthalic acid (BDC-NH_2), 2-nitroterephthalic acid (BDC-NO_2), and 2-bromoterephthalic acid (BDC-Br) (see Figure 8).[76] The reaction procedure for these UiO-66 analogs differs only slightly from the original synthesis. A significant advantage of the newly synthesized UiO-66 compounds is the possibility of high-temperature thermal evacuation process.[76] Microporous availability is a primary interest in different application areas of MOF materials. Previously, solvent exchange was used to access a MOF system's entire internal surface area.[77] Unfortunately, this method is not always successful and can result in a topology loss or change.[77,78] The new UiO-66-NH_2, UiO-66-NO_2, and UiO-66-Br can survive an evacuation procedure at low temperatures while retaining their structure.[76] Finally, high robustness to organic solvents and high resistance to acidic conditions could also be achieved for the new UiO-66 materials.[76]

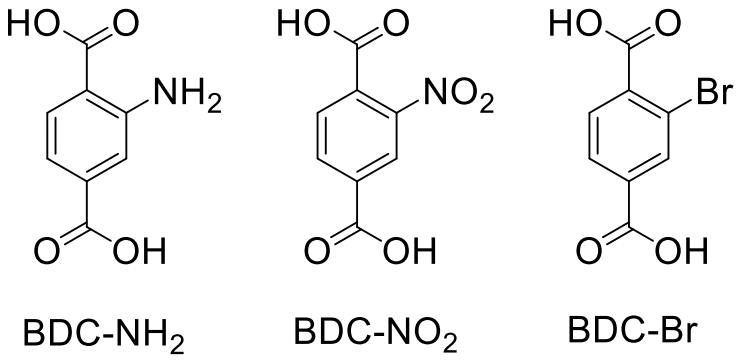

Figure 8: Three distinct terephthalic acid (BDC) linkers, each with a unique set of functional groups. All of these linkers can be used to synthesize UiO-66 derivatives.

As a result of its high resistance to pH, organic solvents, and temperatures, UiO-66 makes a good choice for various applications. A possible surface coating on functional groups in the UiO-66 derivatives extends their application area, and especially for medical and biological purposes, the possibility of attaching tailored bioactive groups is an advantage.

This last modification strategy is particularly interesting for modifying the MOF's outer surface. Especially in drug delivery in the body, NPs must circulate in the blood for a prolonged time. In addition, blood proteins should not adhere to the surface (protein corona) to prevent blood clogging.[79] Applying a hydrophilic polymer on the outer surface of the NP, known as the “stealth effect”, can help circumvent that.[80] The newly attached polymer decreases the protein adsorption and increases the in vivo stability. [80]

The polymer polyethylene glycol (PEG) is frequently utilized for the “stealth effect” on NPs due to its good biocompatibility,[5] high inertness,[5] strong hydrophilicity, electrical neutrality, and spatial repulsion.[81] PEG can be applied to NP surfaces using various techniques (see Figure 9). The most traditional method is the physisorption. Additionally, it is possible to bind PEG by forming a chemical bond. The last method is the self-assembling of a copolymer chain with hydrophobic and hydrophilic compounds.

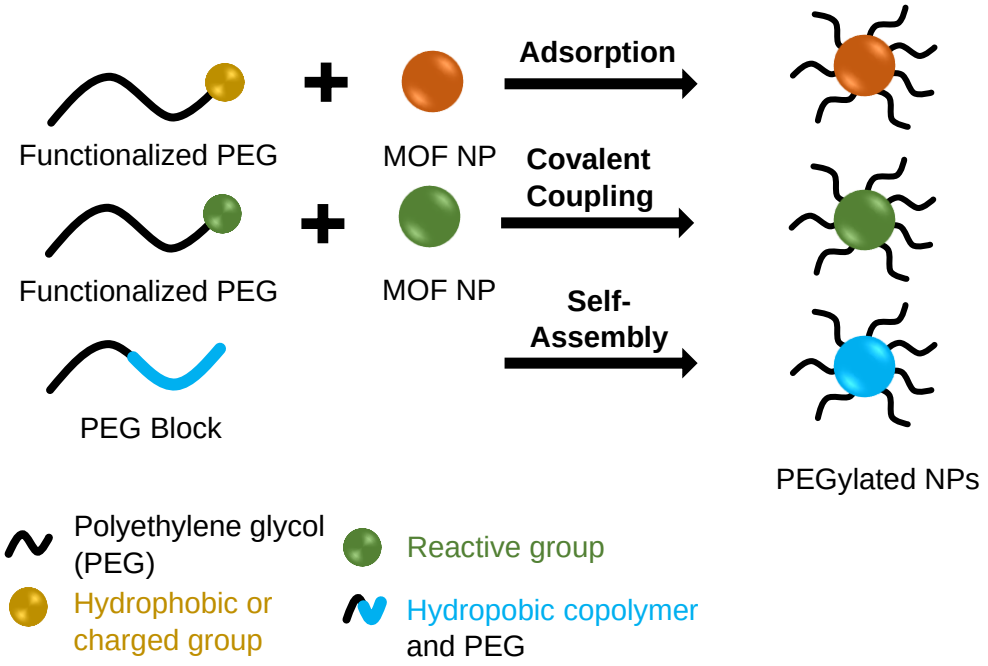

Figure 9: Three distinct PEGylation modification techniques for nanoparticles (NPs). Adsorption, covalent coupling, and self-assembly result in a surface-modified PEG NP. [Figure based on {L. Shi, J. Zhang, M. Zhao, S. Tang, X. Cheng, W. Zhang, W. Li, X. Liu, H. Peng, Q. Wang, “Effects of polyethylene glycol on the surface of nanoparticles for targeted drug delivery”, Nanoscale 2021, 13, p. 10750}].[81]

In the adsorption step, the hydrophobic or charged group on the PEG polymer's end chain adsorbs on the NPs' surfaces.[81] A main drawback of the physisorption approach is that the bond strength is relatively low, and PEG chains can easily detach. To avoid this separation, PEG can be covalently attached to the NPs.[81] Therefore, the active group on the NP must be exposed for the reaction to occur.[81] The third variant is the molecule self-assembly of a hydrophilic-hydrophobic copolymer. It happens through nanoprecipitation or emulsification.[81]

In particular, experts are focusing on the covalent attachment of a PEG polymer chain to synthesize a robust and durable MOF/polymer material. Generally, two main modification strategies are known: the grafting-to and -from approach.[5] While the grafting-to approach focuses on modifying MOFs with pre-synthesized polymer chains, the grafting-from approach tries to polymerize from or on the surface of MOF NPs. In the grafting-to approach, the polymers are synthesized, end-functionalized, and then bonded to the NP via the applied functional group.[5] This approach allows complete characterization of the polymer chain before the attachment.[5] A downside is the poor density of the polymer on the surface.[5] In contrast, the grafting-from approach overcomes this problem by directly synthesizing on an attached initiator group on the surface of the NP.[5] Because the initiator molecule is smaller than the polymer chains, a denser polymer coating can be reached when the initiator is first applied to the surface.[5]

Polymer grafting-from the surface was successfully demonstrated in 2015 when UiO-66-NH_2 was modified with an atom transfer radical polymerization (ATRP) initiator.[82] After attaching bromoisobutyryl bromide as the initiator, poly(ethylene glycol) methyl ether methacrylate was polymerized from the MOF surface.[82] Like ATRP, any other controlled radical polymerization (CRP) methods, such as the reversible addition-fragmentation chain-transfer polymerization (RAFT) or nitroxide-mediated polymerization (NMP), may also be a possibility for polymerization from the surface of MOF particles.

With the grafting-from polymerization from the MOF surface, it is possible to increase the biocompatibility of MOF materials. It is then feasible to further functionalize and modify the surface to enhance MOF usage in biology and medicine. Surface polymerization is one variant of how MOF materials can be specifically adapted, for example, for drug transport in the body.

2.2.3 Machine Learning with MOF Materials

Customizing MOF materials can be challenging, especially when numerous factors in a synthetic route can be altered to determine the most suitable reaction parameters. A high degree of material diversity and adjustability is essential for the above-listed applications, especially in biology. Extensive testing and research are often needed to find an optimal

synthesis or modification route. Therefore, chemists have begun using machine learning (ML) techniques to identify a suitable synthesis pathway quickly and effectively.

ML is a subclass of artificial intelligence that became interesting for a potential application in science and engineering.[83] The heart of ML methods for optimizing synthetic reactions is the algorithms that, like a chemist, predict reactions and can be improved with training.[83] In contrast to humans, algorithms can handle a whole bunch of data simultaneously and address complex problems with enormous combinatorial space or nonlinear processes.[83] Therefore, it is possible to solve complex problems or to find an appropriate reaction strategy for a particular chemical substance more quickly and easily. (see Figure 10).

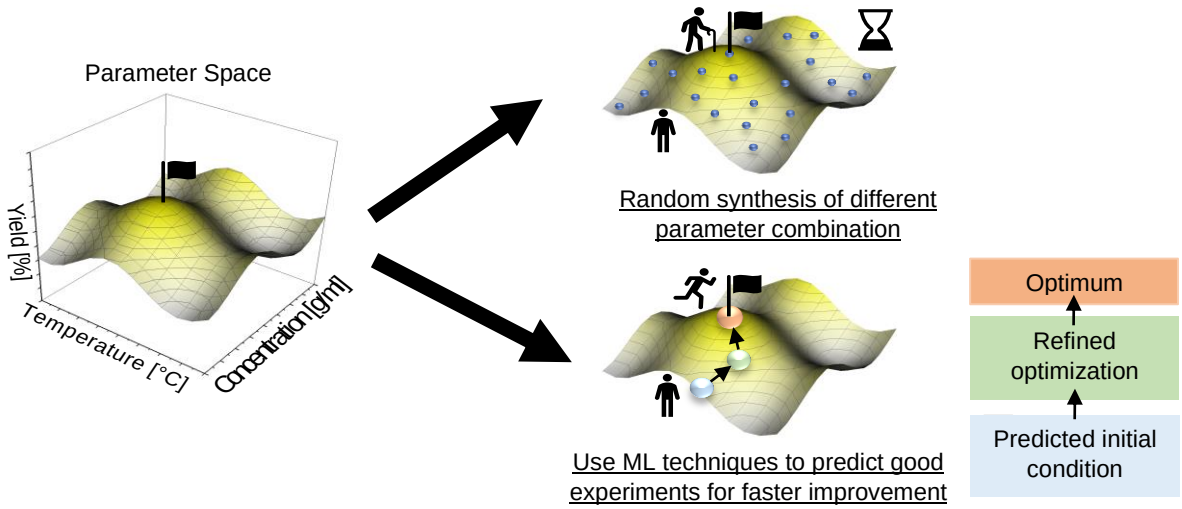

Figure 10: Determining the ideal reaction conditions for a specific chemical reaction using two distinct approaches. The top of the chart displays the typical chemical manual or random reaction optimization for a certain parameter space. This approach usually involves numerous experiments and requires the expertise of a scientist. The bottom of the chart displays the machine learning (ML) method for the same parameter space. ML techniques acquire knowledge through training an algorithm on a provided dataset. As a result, it mimics scientific understanding and frequently makes connections more quickly for an accelerated synthesis optimization.

For an ML approach to correctly predict reactions, it needs data to be trained.[83] The training can be supervised, semi-supervised, or unsupervised.[83] Supervised learning requires a set of input values and associated marked output values.[83] Semi-supervised

learning is when lots of input data is present but not an equal amount of output data, and unsupervised learning lacks output data altogether.[83] All ML approaches aim to train an algorithm with a given data set to predict output values for a new synthesis approach.[83] Unsupervised training often requires a large amount of data, making optimizing synthesis for unknown or unpopular chemical reactions challenging. On the other hand, supervised learning can work with small amounts of data and promises to be a valuable and powerful tool for optimizing chemical reactions.

Depending on the question posed or the data type, the next step is to choose an appropriate learning model for the problem.[83] Many learners or model types are known, and it is essential to know whether the problem to be solved is a classification or regression problem.[83] Classification problems model discrete values, such as the categorization of a material or a metal, whereas regression problems model continuous values, such as polarizability.[83]

Once a suitable model has been selected, it must be tested. To test an applied model, unseen data that were withheld from the training set can be used.[83] The accuracy of the model's predicted output compared to the validation in the test set indicates the effectiveness of the training.[83] The test set must have been recorded for the same material and cover the entire response space. Often, over- or under-fitted models can be detected in this step.[83] Overfitting primarily occurs when too many parameters are involved and the model is too complex.[83] Conversely, underfitting occurs when the data is not detailed enough to find a suitable pattern or when the model is inflexible and can no longer describe the relationship between input and output values.[83]

With ML, it is possible to predict new output values. Chemists have already benefited from computer-aided synthesis planning by increasing the output of their reactions.[84] Reaction databases with millions of reactions, like Reaxys or SciFinder, can be utilized for this purpose.[84] In particular, experimental ML algorithms for prioritization can be a helpful tool for the examination of many various predictions, such as regio- and enantioselectivity.[84]

Several teams have already effectively included ML algorithms in their daily synthesis procedure for the synthesis of MOF materials.[85,86] As a case study, a project that

exploited real failed experiments to improve the synthesis conditions for HKUST-1 (Hong Kong University [$Cu_3(btc)_2$]) was presented by S. M. Moosavi *et al.* in 2019.[85] With the applied ML optimization approaches, they discovered optimized reaction conditions for HKUST-1 and obtained HKUST-1 with the highest surface area discovered until 2019.[85] In 2022, researchers used the same ML method to optimize HKUST-1 films on a SURMOF structure.[87] Initial results showed that the ML approach could identify optimized synthesis parameters for the crystal and uniform growth of HKUST-1 on a gold surface. In 2022, MOF synthesis data were extracted from literature research in a database and integrated into a tool for predicting new MOF structures and their synthesis reactions.[86] The model showed good initial performance, exceeding even the predictions of the human experts.[86]

I anticipate the ML technique becoming more significant in chemistry in the upcoming years. It provides a practical and efficient strategy to accelerate and simplify synthesis planning and optimization. The method of computer-based synthesis planning has benefits for biological and medical applications as well. ML-based techniques could help reduce the reaction effort for targeted materials, frequently requiring synthesis for a specific process or application. With an ML technique used throughout the synthesis, reactions might be designed for a specific use case and quickly directed in a particular way. Ultimately, ML approaches would reduce the time and materials used.

3. Characterization Techniques

In the following chapter, I describe the utilized measurement techniques and their theoretical principles. Additionally, I will go into detail about the sample treatment before the analysis.

3.1 X-Ray Diffraction (XRD)

X-ray diffraction (XRD) is based on the discovery of X-rays by Wilhelm Conrad Röntgen in 1895.[88,89] In 1912, with the work of M. Laue, W. Friedrich, and P. Knipping, X-rays were developed to determine crystalline structures.[88,89] X-rays are electromagnetic radiation with wavelengths between 10^{-9} to 5×10^{-12} m and higher energy than visible light.[89]

3.1.1 Theoretical Background

Generating monochromatic X-rays, a cathode (often a tungsten filament) is heated.[88] The emerging electrons from the cathode are accelerated (10-60 kV), and the beam is focused on the anode surface to knock out electrons in inner shells (ionization).[88–90] Atoms on outer shells fill the vacant places (relaxation), and the energy thus released is emitted through X-rays.[88–90] The spectra of the released X-rays depend on the accelerating voltage, the type of anode material, and the shells involved.[88,90] The energy-richest X-rays are produced by the K-shell and are therefore called K-radiation.[88] Different typical anode materials are chromium (Cr), iron (Fe), cobalt (Co), nickel (Ni), copper (Cu), gallium (Ga), molybdenum (Mo), and indium (In).[88]

The produced electromagnetic beam is irradiated onto a single crystal or powder sample to analyze the structure of a crystalline material. When irradiating on the surface, the electrons in a material start a forced oscillation, and the beam is scattered.[89] A part of the waves is scattered directly at the surface, while some beams penetrate the sample and are scattered at lower scattering planes (see Figure 11).[88]

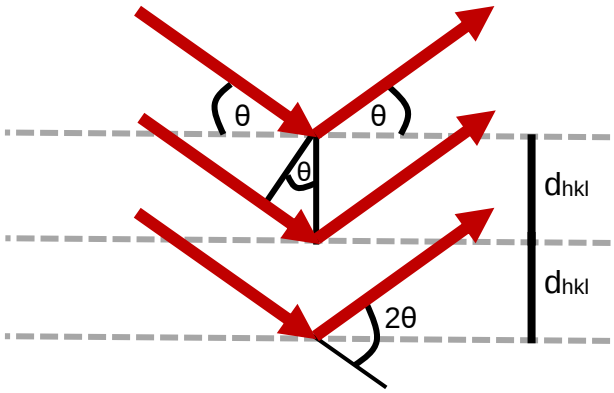

Figure 11: X-ray diffraction (XRD) on a crystalline lattice. The incoming X-rays are scattered on crystal atoms in the material. d_{hkl} is the lattice distance, and θ the incident angle.[88]

If the path difference between two waves scattered on adjacent planes is a multiple of the wavelength λ, constructive interference occurs; otherwise, destructive interference occurs.[89] While destructive waves cancel each other out, constructive waves can be detected, and the condition for reflection is represented in Bragg's law, Equation 1.[90,91]

$$2d_{hkl}sin(\theta) = n\lambda$$

Equation 1: Braggs-Law determines the plane distance in a single crystal or a crystal powder.[89] *d_{hkl} is the lattice distance, θ the incident angle, λ the wavelength, and n the integer.*

Braggs-Law consists of d_{hkl} as the lattice distance in the crystal, θ as the (incident) angle, λ as the wavelength of the electromagnetic radiation, and n as the order of interferences (reflection orders).[88–90] The angle between the incident beam and the reflected beam is known as the deflection angle and is 2 θ.[89] After obtaining a diffractogram, an unknown substance can be determined with the help of a database such as the ICDD.[89]

Crystalline materials consist of atoms arranged in a regular periodic pattern.[88] This arrangement leads to lattice-like structures and creates lattice planes between the individual atoms. The Miller indices (h, k, l) describe these different lattice planes in a crystalline system.[88] Figure 12 shows an example of three different lattice planes (100, 110, and 111) in a cubic system.[90]

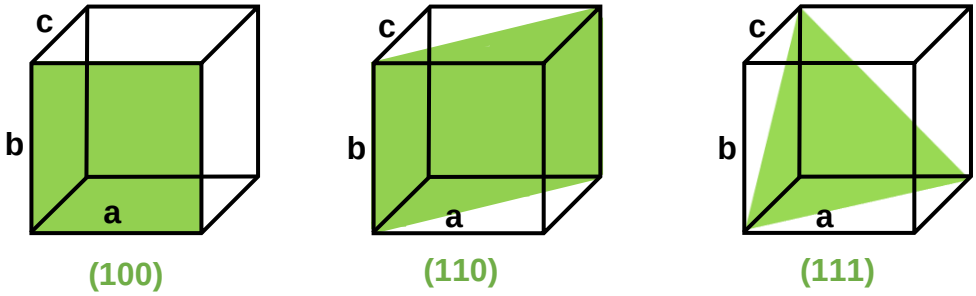

Figure 12: Examples of lattice planes with the indicated Miller Indices in a cubic system.[90] In green, the planes (100), (110), and (111) are shown. [Figure based on {T. Oeser, "Kristallstrukturanalyse durch Röntgenbeugung. Spektroskopiekurs kompakt", Springer Spektrum, Wiesbaden, Germany, 2019, p. 20}].[90]

Utilizing the measured lattice spacings d_{hkl} from the Bragg equation, the corresponding Miller indices for a crystalline sample can be calculated. With this information and assuming the appropriate crystal system, calculating the cell parameters is possible. Equation 2 shows an example of this for a cubic system.

$$\frac{h^2+k^2+l^2}{a^2} = \frac{1}{{d_{hkl}}^2}$$

Equation 2: Connection between the Miller indices and the Bragg equation in a cubic system. a is the lattice parameter, d_{hkl} the lattice distance, and h,k,l the Miller indices.[89]

Standard XRD devices consist of an X-ray tube, often Cu-anode, a sample stage, and a dectector[88]. The sample stage can be adapted to the type of sample, i.e., single crystal or powder. The detector, most common for general use, is a gas proportional counters, scintillation counters, intrinsic germanium detectors, or Si(Li) detector diode.[92]

3.1.2 Instrument and Method

The following paragraph describes the sample preparation for powder samples and metal-organic framework (MOF) films in this thesis. All of the later described characterizations were conducted with the so-prepared samples.

Powder samples: About 20.0 mg of the powder to be determined was placed on a gold wafer (1 cm x 1 cm). Then, a Bruker D8 Advance with Si strip detector (PSD Lynxeye ©)

in θ-θ geometry with Cu K-alpha radiation (WL = 1.54060 Å) at a temperature of 298 K, with the software DIFFRAC.Measurement Center, version 4.0, was used to examine the synthesized MOF particles. The Au (111) peak was measured as an internal height correction peak to obtain correct peak positions.

In addition, powder samples have also been examined on an X'Pert Philips Panalytical XRD with Cu K-alpha radiation (WL = 1.54060 Å) equipped with the software X'Pert Data Collector Version 2.2d at 298 K. The software PowDLL Converter was used to convert the measured powder diffractogram into a raw format. The data from both XRDs were analyzed with the Bruker AXS DIFFRAC.EVA V5.2 software.

MOF film samples: Small cover glasses made of pure white glass (1 mm thick with a diameter of 1.3 cm) coated with MOF films were measured with a Bruker D8 Advance with Si strip detector (PSD Lynxeye ©) in θ-θ geometry at a temperature of 298 K. The received XRD data were analyzed with the software DIFFRAC.EVA V5.2.

The obtained XRD spectra were compared to the data of the following authors:

Table 1: This work utilizes reference literature to identify the X-ray diffraction (XRD) pattern of UiO-66, ZIF-8 (ZIF-CO_3-1), ZIF-90, MIL-53(Al), and Ca(BDC).

MOF pattern	Author
UiO-66	Q. Yang *et al.* (2018)[93]
ZIF-8 (ZIF-CO_3-1)	Z. Huang *et al.* (2021)[94,95]
ZIF-90	C. L. Hobday *et al.* (2008)[96]
MIL-53(Al)	T. Loiseau *et al.* (2004)[63]
Ca(BDC)	S. H. Dale & M. R. J. Elsegood (2003)[67]

3.2 Dynamic Light Scattering (DLS)

Dynamic light scattering (DLS) is a helpful tool for studying specific properties of molecules and particles or aggregates suitable for DLS analysis.[97] One of the first light scattering experiments on particles in suspension was conducted by Tyndall in 1869, and the first theoretical work by Rayleigh in 1871 and 1881.[98]

3.2.1 Theoretical Background

Macromolecules in solution can be analyzed with a monochromatic light beam scattered when striking the sample.[97] The scattering depends on the size and shape of the molecules.[97] Solvent molecules can hit particles dispersed in a solution, known as Brownian motion, leading to random movement throughout the solvent.[97] With DLS, the diffusion coefficient and the hydrodynamic size of the macromolecule can be determined.[97] Temperature influences the viscosity of the solvent and, therefore, the movement of the particles, and a temperature control in DLS is required.[97]

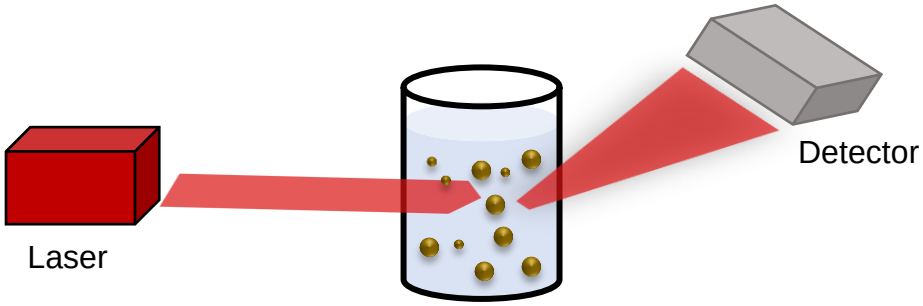

Figure 13: Principal setup of a dynamic light scattering (DLS) experiment. The particles in suspension scatter the laser light, and the scattered intensity is recorded under defined scattering angles.[97–99] With this, it is possible to detect the particle behaviors in the solvent and the hydrodynamic radius of the particles.[97]

A monochromatic laser beam is sent through the particle's suspension to measure particle sizes and distributions.[98] A digital autocorrelator can capture the movement of the particles, which leads to fluctuations in the intensity of the scattered light, which either result in destructive phases, canceling each other out, or in constructive phases.[97] Here, the intensity fluctuations are correlated with the time to determine how fast the intensity fluctuates.[97] This information can calculate the diffusion behavior of macromolecules ($D\tau$).[97] The particle motion highly depends on the size of the particle.[97] While smaller particles move fast and do not take on a specific position, bigger ones show a slower motion due to their higher mass and show similar positions at different times.[97]

In DLS, the detector is generally placed at a 90° angle to the light source.[97] DLS is a versatile tool to measure particle sizes. However, micro-processes like sedimentation, convection, and aggregation lead to fluctuation in the light beam and must be absent for

a reliable measurement.[99] Therefore, DLS is limited to stable and highly diluted suspensions and emulsions.[99]

3.2.2 Instrument and Method

The same protocol was used for all MOF nanoparticles (NPs). Around 20 µl of a 7.00 mg/ml MOF suspension was dispersed in 1 ml of the respective solvent. The particles were then washed three times with 1 ml of the solvent (water or ethanol (EtOH)) and sonicated for around 5 minutes before the measurement. Particle sizes and distributions were measured with a Zetasizer Nano ZS device from Malvern Panalytical, equipped with the ZETASIZER software version 7.13. The measurement was carried out at 25 °C, and the exact solvent and refractive index of the sample were selected in the instrument. For evaluation, I used the Zetasizer family software v8.20.

3.3 Infrared Spectroscopy (IR)

Sir William Herschel developed infrared spectroscopy (IR) around 1800 while he looked at the energy distribution in a solar spectrum.[100,101] In his studies, he investigated the energy of the sunlight.[100,101] He found that the temperature maxima lie outside the red spectra, in the invisible region.[100,101] Applying the newly gained knowledge, it was possible to define the chemical composition using IR radiation to stimulate molecular rotations and vibrations in a molecule.[102]

3.3.1 Theoretical Background

In IR spectra, the absorption bands can be assigned to a molecule's characteristic vibration and rotation bands.[7] The IR area lies between 780 nm and 1 mm behind the visible light.[102] The most valuable bands for IR are in the area between 2.5 µm to 15 µm. The commonly used unit in IR spectroscopy is the reciprocal wavelength v.[7] The reciprocal wavelength v is inversely proportional to the wavelength λ and is primarily used in the range of 4000 to 400 cm^{-1}.[7]

A classical mechanical model can describe a molecule's rotational and vibrational states.[7] In this, all atoms are approximated as point masses.[7] Figure 14 shows, for example, the approach for an H-Cl molecule. Giving energy in the system would result in a vibration of the two atoms in HCl (see Figure 14 (A)).

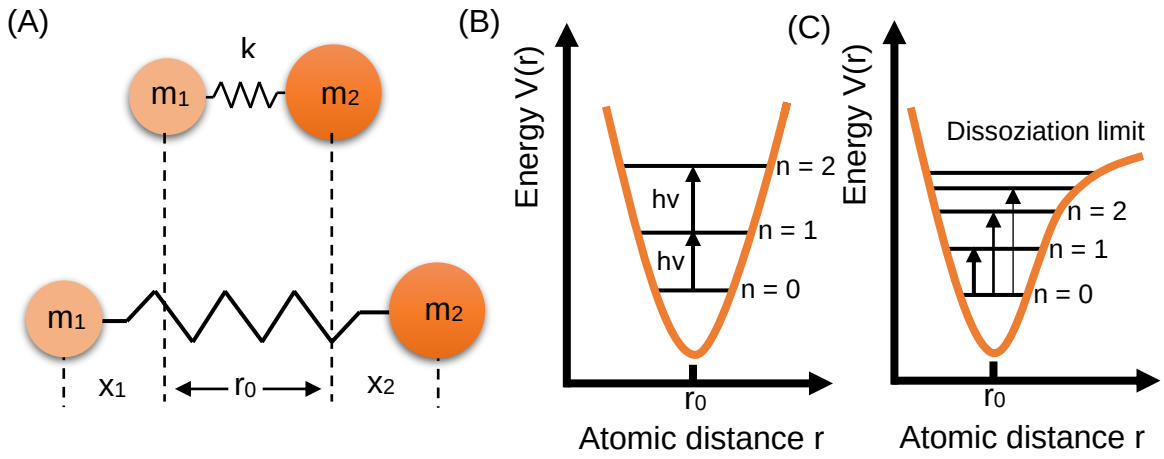

Figure 14: Simple model system for a molecule and its bonds. In (A), a classical mechanic model for a two-atom molecule, in this case, HCl and their vibrations are shown. (B) displays the harmonic oscillator, the ideal case if a molecule has no dissipation, and (C) shows the real energy transition states for a molecule in an inharmonic oscillator.[102] [Figure based on {M. Hesse, S. Bienz, H. Meier, L. Bigler, T. Fox, "Spektroskopische Methoden in der organischen Chemie", Georg Thieme Verlag KG, Stuttgart, Germany, New York, NY, USA, 2016, p. 38-40}].[102]

Figure 14 (B) shows that the harmonic oscillator model can roughly estimate the vibrational energy.[102] Therefore, the function of its core *r* can represent the potential energy (see Equation 3).[102]

$$V(r) = \frac{1}{2}k * x^2 = 2\pi^2\mu v_{osc}^2 x^3 \; ; \; v_{osc} = \frac{1}{2\pi}\sqrt{\frac{k}{\mu}} \; ; \; \mu = \frac{m_1 * m_2}{m_1 + m_2}$$

Equation 3: The energy of a given molecule can be calculated with the harmonic oscillator. Therefore, V is the potential energy, k is the force constant, x is the deflection, μ the reduced mass, and v_{osc} is the vibration frequency of the oscillator.[102]

Since the vibration energy increases with increasing force constant, the molecular vibrational energy increases with increasing bond strength.[102] In addition, the relationship indicates that frequency increases with decreasing atom size.[102] With that, IR analysis can help to evaluate the direct relations of atoms in molecules.[102] So, for example, the bond strength decreases for carbon atoms from triple to single bonds ($k_{C\equiv C} > k_{C=C} > k_{C-C}$).[102] With the mentioned relation, it is known that the absorption frequency should decrease in the same manner, and we obtain

$\nu(C\equiv C)$ = 2260-2190 cm^{-1}, $\nu(C=C)$ = 1680-1620 cm^{-1}, and $\nu(C-C)$ = 1350-750 cm^{-1}.[100,102]

The harmonic oscillator model gets increasingly inaccurate with higher energy levels, and a better model, including the relation between the higher energy level and the weakened molecular bond, had to be found. Here, the inharmonic oscillator, showing the bond weakening with increasing energy until the dissipation of the molecule at the top, can be used (see Figure 14 (C)).[102]

In the beginning, the molecule vibrates in the ground state.[102] With the energy supplied by the IR radiation, the molecule absorbs a light quantum to transit from a lower vibrational state into a higher one.[102] The energy difference equals the absorbed light quantum (resonance), and the energy needed to transit into a higher state decreases with increasing energy states up until the dissociation of the molecule. [102] Although it is possible to induce a double or triple quantum transition over two or three energy states, it is less likely and mostly happens for smaller atoms.[102] Also, the frequency is lower than for a single quantum transition.[102] The selection rules for an IR experiment are not only that the absorption frequency of the light quantum has to match the energy transition state but also that the molecule's dipole moment has to change during a vibration, which depends on the molecule's symmetry.[102]

Nowadays, the most commonly used IR spectrometers are Fourier-Transformation (FT) devices.[7] The basic principle is that the radiation of a light source is directed on the sample and attenuated by the vibration and rotation of the sample. [7] Then, the time-dependent intensities are detected in an interferogram, which has to be translated with a mathematical operation in a frequency-dependent spectra.[7]

3.3.2 Attenuated Total Reflection (ATR) Infrared Spectroscopy (IR)

There are different sampling techniques for IR investigations. One crucial technique for powders is the attenuated total reflection infrared spectroscopy (ATR-IR). With ATR-IR, it is possible to investigate the IR absorption bands of a solid powder or liquid sample quickly and typically non-destructive.[103] It is also a primary investigation method for samples that are usually too thick or absorb too much in transmission experiments.[100,103]

ATR-IR goes back to Goos and Lindeberg-(Hänchen), who studied the light phenomena at the interfaces of different media in 1943.[104,105] They experimentally concluded that even at total reflection, the incident beam on the interface between two media will penetrate the media with a lower refraction index some wavelength deep before reemerging into the optical thicker media.[104,105] Therefore, the sample has to have contact with the internal reflection element (IRE) (see Figure 15).[100]

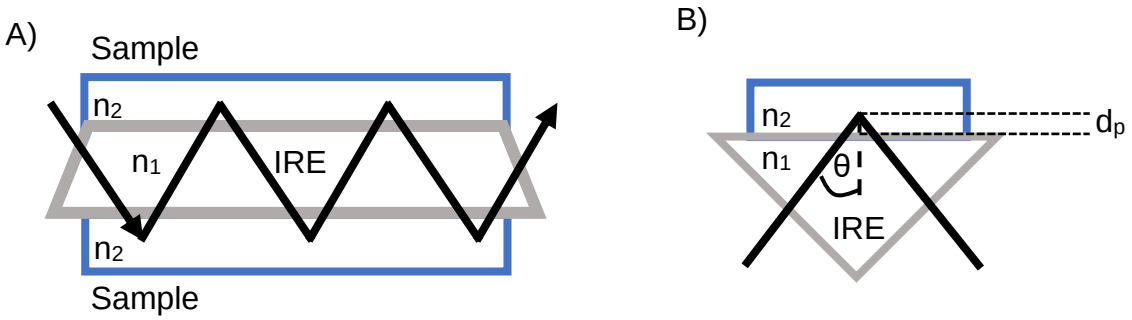

Figure 15: Principle setup of an attenuated total reflection infrared spectroscopy (ATR-IR) experiment: total reflection from the internal reflection element (IRE) into a sample with A) simple reflection and B) multiple reflections. n_1 = refraction index of the IRE, n_2 = refraction index of the sample, whereas $n_2 < n_1$, θ = incident angle and d_p = penetration depth.[100,103] The beam provides vibrational stimulations that give information about the chemical composition of a material. [Figure based on {H. Günzler, H.-U. Gremlich, "IR-Spektroskopie. Eine Einführung", WILEY-VCH Verlag GmbH & Co. KGaA, Weinheim, 2003, p. 123}].[100]

To obtain total internal reflectance, the incident angle of the radiation on the interface had to be bigger than the critical angle, see Equation 4.[103] To accomplish this, standard IREs are Ge, ZnSe, or diamond, with much higher refraction indices than the common organic molecules under investigation.[103]

$$\theta_C = sin^{-1}\left(\frac{n_1}{n_2}\right)$$

Equation 4: A function of the refractive indices from the sample (n_2) and the internal reflection element (IRE) (n_1) describes the incident angle θ_C.[100,103]

3.3.3 Instrument and Method

The samples were dried in a high vacuum under reduced pressure for several hours and then directly analyzed with ATR-IR. The used device was a TENSOR27 from Bruker with a diamond crystal. The incident angle was 45° in single reflection mode. The software used was OPUS, version 8.5. Additionally, samples were analyzed using a Nicolet iS5 FTIR spectrometer, version 2.03, equipped with a diamond crystal. The sample was analyzed in single reflection mode. The software used was OMNIC 9 version 9.7.7. The software for evaluating the data was OPUS, version 7.8.

3.4 Scanning Electron Microscopy (SEM)

The German scientist Max Knoll demonstrated the principle behind scanning electron microscopy (SEM) in 1935, and in 1938, Manfred von Ardenne was the first to develop an SEM device.[106,107] With their high magnification, SEMs can determine surface features, texture, size, shape, and particle distribution on a surface.[108]

3.4.1 Theoretical Background

The human eye can see structures down to 200 µm.[108,109] Everything smaller is invisible to it. To enlarge small materials up to 10-2000 times, we can use optical microscopy (OM).[108] Although OMs have been improved in the last years, they have only one lens, and organics or small solid pieces are challenging to magnify. Therefore, researchers developed SEMs that can resolute objects down to 1 nm with electrons instead of normal light.[109,110]

The electrons for the SEM are produced by an electron gun, sitting on top of the device, connected to a high voltage.[111] After accelerating, the electrons hit the sample in a sample chamber. The acceleration speed can be manually chosen (up to 30 kEv) and depends on the sample.[107,111] Since air molecules can disturb the electron beam, the electron gun and the sample chamber of the SEM are operated under vacuum.[108]

Different processes occur after the beam hits the sample (see Figure 16).[108] Two of these, namely the emission of backscattered (BSE) or secondary electrons (SE), are routinely used for sample image creation in SEM. BSE are produced by primary electrons reflected on the surface. Because BSE depends on the surface's atom density, they are

frequently used to visualize the contrast change in surface compositions. SE are considered the most important for checking the samples' morphology and topography.[108] They are produced when primary electrons hit the sample and knock out electrons. While magnifying structures down to 1 nm, SEM is a valuable tool for investigating small particles or surface-attached structures.[109,110]

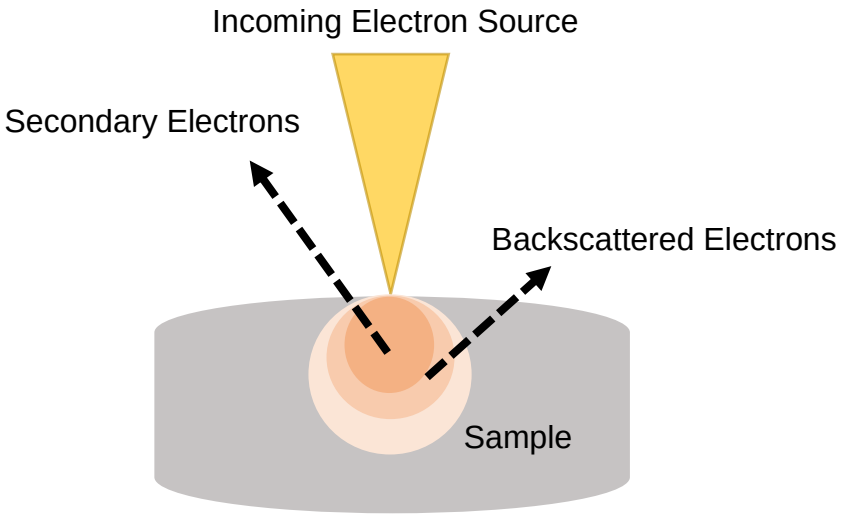

Figure 16: Basic illustration of a scanning electron microscopy (SEM) experiment. An incoming beam hitting the sample with electrons excites secondary and backscattered electrons.[108] These electrons can give information about the surface texture, size, shape, and particle distribution on a surface.[108] [Figure based on {K. Akhtar, S. A. Khan, S. B. Khan, A. M. Asiri, "Handbook of Materials Characterization" (Ed.: S. K. Sharma), Springer Nature Switzerland AG, Cham, Switzerland, 2018, p. 120}].[108]

An electron gun, consisting of a cathode and an anode connected by a high voltage, produces the electron beam of an SEM device.[111] Materials for the electron gun should be reliable in producing an electron beam with high brightness, fine source sizing, beam stability, and a small energy spread.[111] Possible types are a tungsten filament, LaB_6 emitter, Schottky field emission, and cold field emission.[111] Since the substance must be electrically conductive, a thin layer of conductive material is applied on the material's surface.[112]

3.4.2 Instrument and Method

An ESEM Quattro S from ThermoScientific and a VEGA3 from TESCAN were used to determine the particle sizes. The following paragraph describes the preparation of the different specimens.

MOF Nanoparticles powder samples:
All MOF NP powder samples were treated the same. A 1 cm x 1 cm gold wafer was prepared by washing it three times with EtOH. Meanwhile, the NPs were dispersed in EtOH and then drop-cast onto the gold wafer. The specimen was then sputtered with a platinum layer of around 1.5 nm using a MED-020 from Baltec high-vacuum coating system.

MOF films:
MOF films were prepared according to the procedures in Chapter 8.3.1. Afterward, they were sputtered with a platinum layer of around 5 nm using a Baltec MED-020 high-vacuum coating system.

3.5 Nuclear Magnetic Resonance (NMR)

The 1946 developed nuclear magnetic resonance (NMR) spectroscopy is a noninvasive method used for characterizing and determining liquid and solid materials structure.[113] In a magnetic field, it gives information about the position, interaction, and correlation of atoms inside a molecule. Especially in chemistry and biochemistry, it is very popular due to its easy and fast usability.

3.5.1 Theoretical Background

The NMR method is based on the principle that most atom nuclei have an intrinsic angular moment (*P)* and a magnetic moment (μ).[102,113] *P* is quantized and can be calculated from the nuclear spin (*I*) (see Equation 5).[113]

$$P = \sqrt{I(I+1)}\hbar$$

Equation 5: Intrinsic angular moment of a nuclei. I is the nuclear spin, and ħ consists of Planck's constant (ħ=h/2π).

I can have half or whole-numbered values reaching from 0 to 6, and only nuclei with a momentum different from 0 can be evaluated with NMR.[102,114] The most investigated nuclei in organic chemistry are ^{1}H, ^{7}Li, ^{11}B, ^{13}C, ^{15}N, ^{17}O, ^{19}F, ^{29}Si, ^{31}P, and ^{77}Se.[102,115] For inorganic chemists, metal atom cores, such as ^{109}Ag or ^{111}Cd also became important.[102]

Without applying a static magnetic field, all spin states have the same energy. [116] They are degenerate.[116] By giving the sample into a static field (B_0), *P* takes up an orientation along the direction of the field.[113] For the orientation, the magnetic quantum number (*m*) plays a role and takes values from $m = +I, I-1, I-2, \ldots, -I+1, -I$.[102] They have exact $2I+1$ possible orientations.[114] This behavior is called quantization of direction.[114] The $2I+1$ energy states, formerly degenerated, are energetically split in the external magnetic field B_0, which is called the Zeeman effect.[102]

Classically, the nuclei precesses toward the magnetic field around an invisible axis.[113] This precession frequency is called Lamour frequency.[113] In an energetically lower state, μ precede with the Lamour frequency around B_0 and in a higher state with $-B_0$.[102] Transitions between different energy levels are induced by irradiating the nuclei with a magnetic field (B_1) of a certain suitable frequency (*v1*).[113] To obtain this resonance, the frequency *v1* must correspond exactly to the Lamour frequency of the nuclei.[113] As an example, Figure 17 shows the energy levels of the protons in a solution of chloroform ($CHCl_3$).[113]

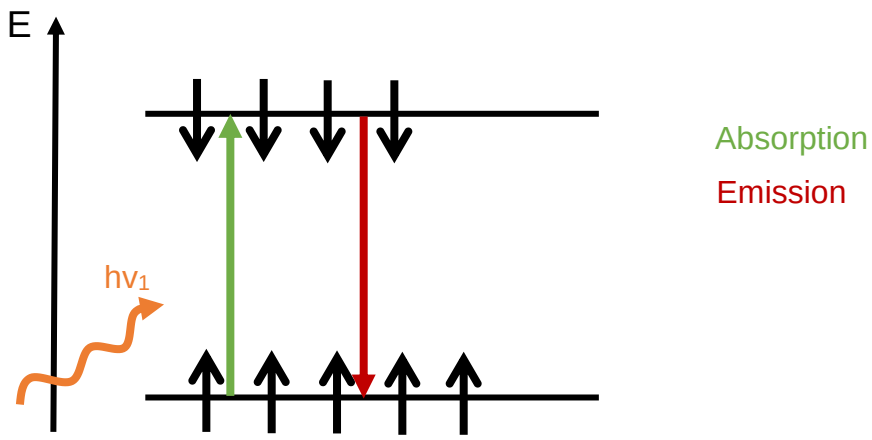

Figure 17: Energy level system and possible transitions for a nucleus with I=1/2 (for example, in a chloroform ($CHCl_3$) solution). Irradiation of hv_1 can cause absorption or emission. [Figure based on {H. Friebolin, J. K. Becconsall, "Basic one- and two-dimensional nuclear magnetic resonance (NMR) spectroscopy", WILEY-VCH Verlag GmbH & Co. KGaA, Weinheim, Germany, 2011, p. 7}].[113]

When irradiated with the frequency v_1, absorption or emission processes can occur.[113] There is an equal chance for both transitions.[113] In the example above, a high population at a lower energy level leads to a dominant absorption process.[113] This adsorption is detected as a signal and provides information about the population difference and, thus, about the total number of spins in the sample.[113]

The strength of the magnetic field B_0 strongly depends on the shielding capacity of the surrounding electrons and the gyromagnetic ratio (γ).[116] For instance, the electrons surrounding the nucleus weaken the magnetic field (see Equation 6).[116]

$$B_{eff} = B_0 - \sigma B_0$$

Equation 6: The effective magnetic field on the nucleus depends on the shielding capacity of the electrons. σ is the shielding constant.[102,116]

That means not all nuclei have the same resonance frequency depending on the surrounding electrons.[116] For example, the hydrogen atoms in an EtOH molecule have different resonance frequencies due to their different surroundings.[116] This validation enables us to identify different signals for atoms in various chemical environments.

Modern NMR devices work with the pulse method (pulse-fourier-transform-technique), in which all nuclei of a specific sample are excited simultaneously by a radiofrequency pulse.[102,113] The material is dissolved using deuterated solvents.[102] The deuterating ensures that no solvent hydrogen atoms could interfere with the sample's analysis.[102] Usually, an additional reference substance, such as tetramethyl silane (peak at 0 ppm), is introduced as an internal standard or in a separate sample tube as an external standard.[102]

3.5.2 Instrument and Method

Samples were dissolved in a commonly used deuterated NMR solvent. ^{1}H and ^{13}C NMR spectra in $CDCl_3$ were recorded on a Bruker Advanced 400 spectrometer equipped with the software Bruker IconNMR 5.0.12 and Ascend 400 from Bruker with the software Bruker Icon NMR 5.0.6. The analyzation software used was MestReNova 14.1.2-25024. Chemical shifts (δ) were expressed in parts per million (ppm) referenced to the NMR solvent residual peak.

3.6 Time-of-Flight Secondary Ion Mass Spectrometry (ToF-SIMS)

Mass spectrometry originated around 1910 and became popular around 1960 for evaluating the relative molar mass of even the smallest quantities of substance and for gathering information on the molecular structure from the fragmentation pattern of the substance.[102] One specific mass spectrometry method that is especially important for analyzing surface compositions is the time-of-flight secondary ion mass spectrometry (ToF-SIMS).[102]

3.6.1 Theoretical Background

In mass spectrometry, the first step is the ionization of the substances.[102] In SIMS, bombarding a sample with primary ions sets free a cascade of neutral and charged fragments.[117] In a high vacuum chamber, the generated ion fragments of a sample are separated according to their mass-to-charge (*m/z*) ratio in an analyzer.[102,118] In a mass spectrum, signal intensity, as a measure of the relative abundance, is plotted over the mass-to-charge ratio *m/z*. Now, the relative abundance sometimes referred to as the

intensity of the peak, of the masses obtained can be matched with typical theoretical mass fragments of the substance under investigation.

A possible ionization method is the secondary ion mass spectrometry (SIMS). Together with a time-of-flight (ToF) analyzer, the mass spectrometric method is called ToF-SIMS. Here, primary ions, for example, Cs^+, Ar^+, Ga^+, or Bi^+, are irradiated on the sample surface, generating positively and negatively charged secondary ions.[102,119–121] The primary beam normally has energies around 2 to 20 keV.[102] Typical fragment ions emerging are M^{+*} and M^{-*}, $[M + H]^+$, $[M - H]^-$, $[M + Na]^+$, and $[M + \text{metal ion}]^+$, in which Na is from impurity and the metal ions from the metal substrates, if present.[102] The characteristic ions are then accelerated and detected in a ToF setting. The ToF detectors separate the produced ions by their different masses.[102] Because of this, the secondary ions are accelerated to a constant energy level, and the time required for each ion to travel a certain distance can be measured.[102] Figure 18 shows a typical setup of a ToF-SIMS device.

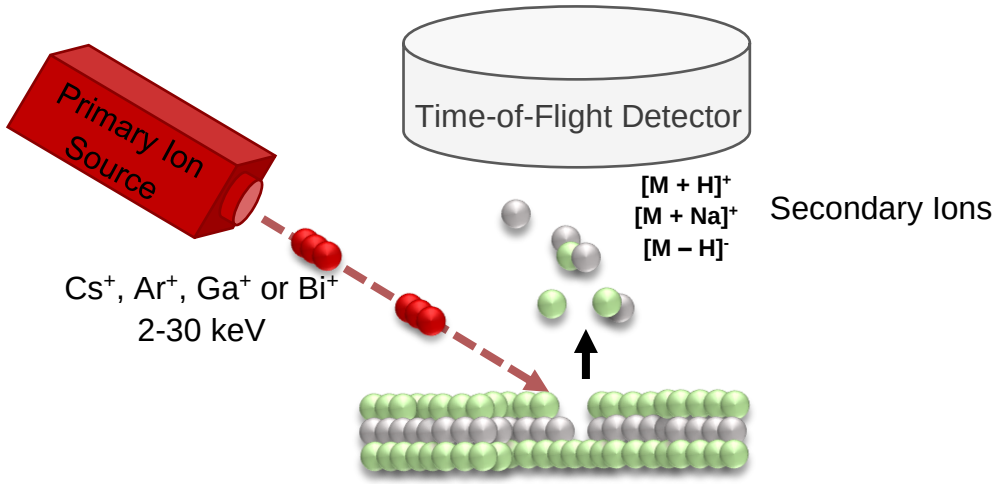

Figure 18: General procedure of a time-of-flight secondary ion mass spectrometry (ToF-SIMS) measurement. The high-energy beam of primary ions knocks fragment ions off the surface of a substrate.[102,120] These ions are accelerated and detected based on their mass-to-charge ratio (m/z) in a ToF detector.[102]

Because all ions are monitored, ToF analyzers are extremely sensitive compared to quadrupole mass filters.[102,120] ToF-SIMS only irradiates on a small sample spot with an extremely low dose of primary ions.[120] This low dosage of ions has the advantage that

the surface is approximately unaffected, and the sample is undamaged.[120] ToF-SIMS can also be used in different modes during the measurement, and it is generally possible to use it for surface spectroscopy, surface imaging, and depth profiling.[121]

3.6.2 Instrument and Method

The samples were dried under reduced pressure and fixed with carbon tape. The ToF-SIMS measurement was performed on a ToFSIMS5 instrument (IONTOF GmbH, Münster, Germany). The spectrometer is equipped with a Bi cluster primary ion source and a reflection-type time-of-flight analyzer. UHV base pressure during analysis was $< 3\times10^{-8}$ mbar. The Bi source was operated in bunched mode for high mass resolution, providing short Bi_3^+ primary ion pulses at 25 keV energy, a lateral resolution of approx. 4 µm, a target current of 0.35 pA at 10 kHz repetition rate, and 1.1 ns pulse length. Data acquisition was stopped at the quasi-static limit (2×10^{11} ions/cm^2). Charge compensation was performed by applying a 21 eV. electron flood gun and tuning the reflection accordingly. Mass scale calibration was based on low Mw hydrocarbon signals together with ZrO_2^-, ZrO_3H^-, or Zr^+ signals, respectively. The primary ion beam was screened across a 500×500 µm^2 field of view on the sample, and 128×128 data points were recorded.

3.7 Gel Permeation Chromatography (GPC)

Developed in the mid-1960s, gel permeation chromatography (GPC) characterizes polymers and can give the molecular weight distribution of a polymer mixture.[122,123] It is a relative method and determines the molecular weight indirectly from a calibration.[122,124] Therefore, it strongly depends on the quality of the calibration.

3.7.1 Theoretical Background

Like most chromatographic separation procedures, GPC contains a stationary and a mobile phase. Rigid porous beads of 10-10^5 nm of a cross-linked swelling polymer are filled in a separation column (stationary phase) in the GPC.[124] To accomplish the diffusion of the polymers in the pores on the stationary phase and to achieve separation, the polymer's molecular size and distribution must be the same as the stationary phase's pore size and distribution.[125] The transient or mobile phase forms the eluant.[124] When

the dissolved sample travels through the column, small molecules diffuse into the particle beads (illustrated in yellow and green), while bigger molecules pass through (in blue) (see Figure 19).[122,124] The detection takes place at the end of the column by measuring the refraction index or the UV absorption, and the more elution volume a molecule needs to exit, the smaller it is.[124] The retention volume V_e is the volume a molecule needs to pass the column, whereas the retention time t_R is the time needed for the process.[122,123,125,126]

The exclusion size limit $M_u > M$ gives the maximal possible size for the molecules to be measured.[123] Therefore, larger molecules cannot diffuse into the pores. The separation threshold $M_l < M$ describes the minimal molecular size below which the molecules can enter a sample.[123] That column separates the polymers with masses between $M_l < M < M_u$.[123] Since absorption or adsorption on the column material might affect the measurement findings, there should be no interaction between the column and the molecules.[122]

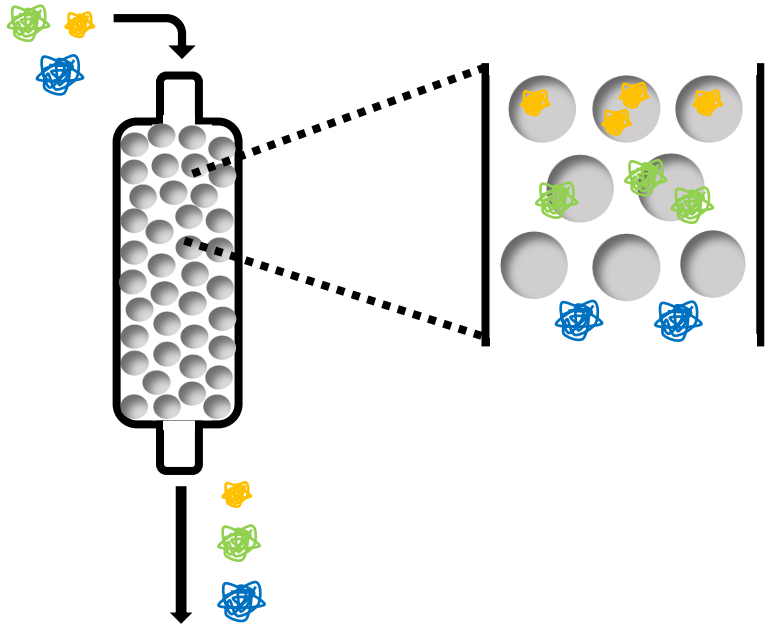

Figure 19: Basic illustration of a gel permeation chromatography (GPC) experiment. The GPC separates a given polymer sample according to its molecular size.[123,125] Swollen polymer particles of different sizes are given into the column. While passing through the column, smaller particles diffuse in the cavities of the column material, while bigger ones cannot access them.[123,125] This results in the size-dependent separation of the polymer particles passing through the column.[125]

Before starting an experiment, the GPC column has to be calibrated.[122] Therefore, narrowly distributed polymer standards are passed through the column, their molecular masses are detected, and V_e is obtained.[122] The so-received relation between V_e and the known polymer masses is used to measure other polymer samples in the same column and under the same conditions.[125] If any conditions change, a new calibration curve must be created.[125]

GPC devices used with organic solvents are usually filled with rigid porous beads of crosslinked polystyrene or surface-treated silica.[122] Aqueous GPC systems work with water-swollen crosslinked polyacrylamides, glass, or silica.[122] To obtain the different resolutions of the different sizes of polymer chains, either a series of columns with different pore sizes are connected, or a long column with mixed gels is used.[122] The eluent is important as well. The polymer has to be entirely dissolved in the solvent, and the most common eluents are toluene (Tol) and tetrahydrofuran (THF) for nonpolar eluents at room temperature (RT).[122] For hydrophilic polymers, water or dimethylacetamide (DMAc) are possible. Most GPCs consist of the column or columns, the solvent pump, and a differential refractometer for analyzation.[122]

3.7.2 Instrument and Method

The polymer samples were precipitated with a combination of dimethylformamide (DMF) and diethyl ether until no polymer remained in the supernatant. They were then dried in a vacuum oven for 24 h at 100 °C. Afterward, they were swollen in the mobile phase (water and 10 % Isopropanol) for 5 h and then measured with a GPC system from Agilent. The injection volume was 50 µl. The calibration standard was PEG for the water GPC. As the mobile phase, a solvent based on $H_2O+NaN_3\backslash H_2O+0.5$ g/L NaN_3 and a mixture of 40 % acetonitrile (MeCN) and 0.1 % trifluoroacetic acid (TFA) was used. The columns used were PSS SUPREMA linS (5 µm). The used detector was an IR and ultraviolet and visible spectroscopy (UV-Vis) detector. The measurement and analysis were carried out with the LabSolutions software, version 5.96.

3.8 Ultraviolet and Visible Spectroscopy (UV-Vis)

The method of ultraviolet and visible spectroscopy (UV-Vis) is one of the most famous electron spectroscopic methods.[115] The UV area from 400-320 nm (UV-A), 320-380 nm (UV-B), and 280-10 nm (UV-C) directly follows the visible light from 400 nm to 750 nm.[102] The absorption of visible and UV irradiation by passing a sample is detected using UV-Vis, and this information can be used to discover distinct conjugations in a molecule or the concentration and kinetics of an unknown material.[115]

3.8.1 Theoretical Background

Spectroscopic investigations can reveal the kind, oxidation state, and distance or strength of a bond.[117] In UV-Vis, the irradiation with light leads to the absorption of electrons.[117] To measure UV-Vis, the energy of the irradiated wavelength must be similar to the energy difference between two electronic states in a molecule.[102,115] If the energetically higher state is not occupied, an electronic excitation of the molecule can take place.[102,115] Most of the time in organic chemistry, this means an electron transition between the highest occupied molecular orbital (HOMO) and the lowest unoccupied molecular orbital (LUMO) occurs (see Figure 20).[115]

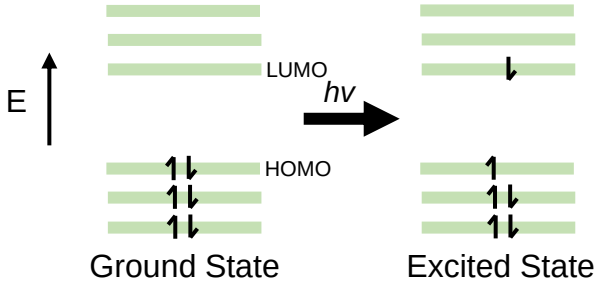

Figure 20: The energy diagram with a HOMO and LUMO state of a molecule. By irradiating light into the sample, an electron is excited from the HOMO into the LUMO.[115] The molecule enters an excited state.[115] [Figure based on {J. B. Lambert, S. Gronert, H. F. Shurvell, "Spektroskopie. Strukturaufklärung in der organischen Chemie", Pearson Education Deutschland GmbH, München, Germany, 2012, p. 595}].[115]

Even if the excitation and the transition between orbitals happen for the whole molecule, the transition can often be traced back to individual functional groups (called chromophores) with valence electrons.[115,117] An example is non-binding *n*-electrons or

π-electrons in carbonyl groups or C=C double bounds.[115] In general, four kinds of electronic transitions are possible ($\pi \rightarrow \pi^*$, $n \rightarrow \sigma^*$, $n \rightarrow \pi^*$, and $\sigma \rightarrow \sigma^*$). Due to their excitation in the wavelength range between 200 and 700 nm, the $n \rightarrow \pi^*$ and $\pi \rightarrow \pi^*$ transitions are particularly significant for UV/Vis.[117] This revelation also means only molecules with free electron pairs or double bounds can be investigated with UV-Vis.[117]

After the excitation, spontaneous emission can cause the molecule to fall back to the ground state.[102] The possibility of this happening is called the transition probability.[102] Radiation processes such as absorption, fluorescence, phosphorescence, or non-radiation processes such as internal conversion and intersystem crossing can occur, as illustrated in the Jablonski diagram (see Figure 21).[115]

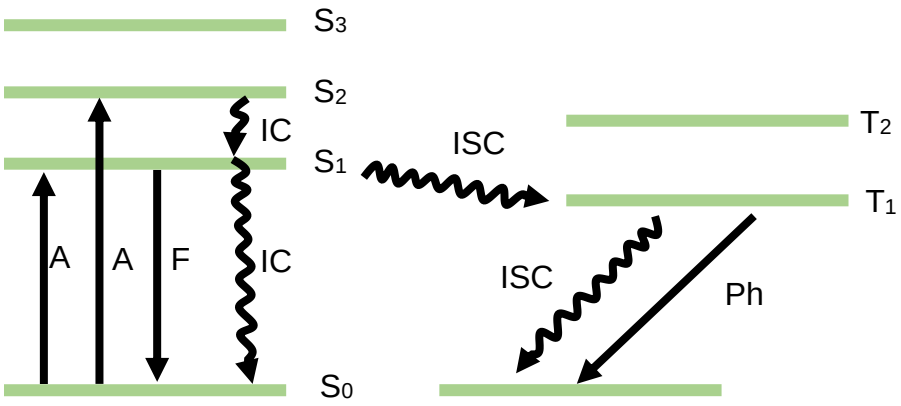

Figure 21: The displayed Jablonski diagram shows the energy absorption of a molecule and possible distributions of the electrons. For a radiation process, fluorescence (F), absorbance (A), and phosphorescence (Ph) are possible, whereas for a nonradiation process, internal conversion (IC) and intersystem crossing (ISC) are possible.[102,127] [Figure based on {M. Hesse, S. Bienz, H. Meier, L. Bigler, T. Fox, "Spektroskopische Methoden in der organischen Chemie", Georg Thieme Verlag KG, Stuttgart, Germany, New York, NY, USA, 2016, p. 7}].[102]

Several rules influence the transition. Thus, the total spin S and the multiplicity ($M = 2S+1$) may not change during the transition.[102] Furthermore, an electron transition between two orbitals with the same parity is forbidden, also called symmetry or Laporte prohibition.[102] And the transition can only occur if the orbital angular-momentum quantum number ($\Delta l = 0$ *or* ± 1) changes.

To measure the quantitative absorption of a sample, the Lambert-Beer law is introduced.[117] Bouguer, Lambert, and Beer investigated the relationship between the weakening of the irradiated beam (*I*), the concentration of the sample (*c*), the optical path length (*l*), and the molar extinction coefficient (***ε***), resulting in the Lambert-Beer law, see Equation 7.[102,117] Important for the measurement is that the irradiated light is monochromatic, the absorbed molecules must be uniform in distribution, there must be no scattering of the molecules, and there can be no interaction with the solvent.[117]

$$I = I_0 e^{-kl} \rightarrow I = I_0 10^{-\varepsilon cl} \rightarrow A = log\frac{I_0}{I} = \varepsilon cl$$

Equation 7: The Lambert-Beer law describes the correlation of the incident light (I_0) to the outgoing light (I) and the concentration of the sample.[102,117] With A, the extinction measured with ultraviolet and visible spectroscopy (UV-Vis), k the absorption coefficient, l the thickness of the sample holder, and ε the molar extinction coefficient.[102,117]

Usually, UV-Vis devices consist of a radiation source (a mercury or deuterium lamp for UV and a tungsten-halogen lamp for Vis), a monochromator, two chambers for the sample and the solvent cuvette, and a detector.[102,117] Normally, the sample is dissolved in an optical pure solvent, which shows no absorption in the measurement area.[102] The absorbance is then recorded and displayed as a function of the wavelength for the following analysis.[102]

3.8.2 Instrument and Method

For the UV-Vis measurement, a TECAN Plate reader from TECAN Spark with the software SPARKCONTROL version 3.3 and Multiskan Ascent 354, software version 2.6, a Varian Cary 50 Bio, software Cary WinUV version 3.00(182)UV-Vis, and a Varian Cary 60 UV-Vis, software Cary WinUV version 5.1.3.1042 was used.

The samples were dissolved in the respective solvent, and the absorbance was read. A background spectrum of the solvent alone was performed in the beginning. For the measurement, a quartz glass cuvette with a diameter of 1 cm and 96-well plates made of polypropylene and polystyrene were used.

4. MOF-Shell Protection of Enzymes

As described in Chapter 2.1.3, enzymes are crucial in catalyzing reactions and replacing harsh chemical reaction routes, especially in biological or medical applications. In the following, I will present my research about incorporating two prokaryotic phenacrylate decarboxylases (PAD, EC 4.1.1.102) in different metal-organic frameworks (MOFs) while preserving the enzymatic activity. Afterward, I will describe how we tested the enzymatic activity of the incorporated MOF/PADs after dispersion in different organic solvents.

4.1 Introduction

PADs are enzymes found in bacteria[128] and plants,[129] catalyzing the elimination of carbon dioxide from p-coumaric acid (pCA) to p-hydroxystyrene (pHS) without the need for a cofactor.[130,131] Figure 22 shows an example of a reaction process from pCA to pHS catalyzed by the PAD.

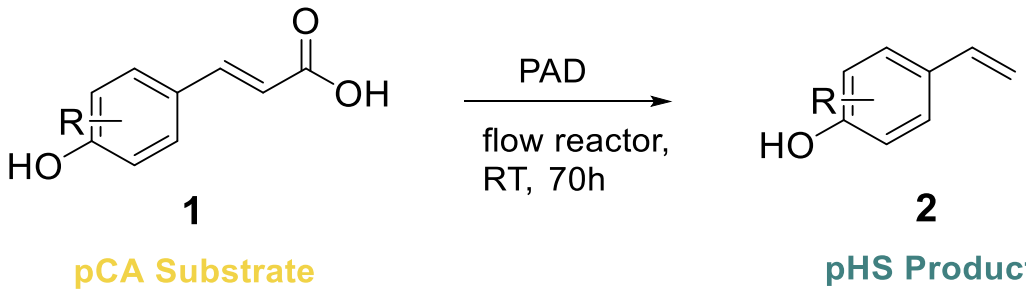

*Figure 22: Catalyzed synthesis reaction of p-coumaric acid (pCA) (**1**) to p-hydroxystyrene (pHS) (**2**) with the use of a phenacrylate decarboxylase (EsPAD). The reaction is conducted in a flow reactor at room temperature (RT) for 70 h.[130] [Figure based on {M. Peng, E. Mittmann, L. Wenger, J. Hubbuch, M. K. M. Engqvist, C. M. Niemeyer, K. S. Rabe, "3D-Printed Phenacrylate Decarboxylase Flow Reactors for the Chemoenzymatic Synthesis of 4-Hydroxystilbene", Chem. - Eur. J. 2019, 25, p. 15999}].[130]*

The monomer pHS can be synthesized into a polymer that is applied in resins, elastomers, and adhesives.[131,132] Chemically synthesized pHS is often produced under high temperatures in thermal processes or expensive base catalysis and microwave heating.[132,133] The conversion with the PAD is a convenient way to reduce costs and harsh conditions while simultaneously reducing waste during the synthesis of pHS.[131]

Unfortunately, a common problem with enzymes is their sensitivity to pH, temperature, and mechanical stressors.[50] With all of these influences, the enzyme activity is reduced or eliminated.[50] In addition, reproduction is often time-intensive and pricey. Protecting the enzymes is, therefore, a promising goal for applying enzymes in high-throughput synthesis.

In recent studies, MOFs have emerged as potential carriers protecting enzymes.[50] Due to their high crystallinity and adjustable pore size, they can be precisely adjusted and modified to encapsulate different enzymes.[50] In this collaborative study, I show how choosing a MOF system for the PAD enzymes works by comparing four distinct MOF systems. In doing so, I searched for the ideal MOF system to maintain the crystallinity of the MOF structure and preserve the enzymatic activity of the enzymes. Figure 23 shows the process of incorporating the PAD into the MOF system.

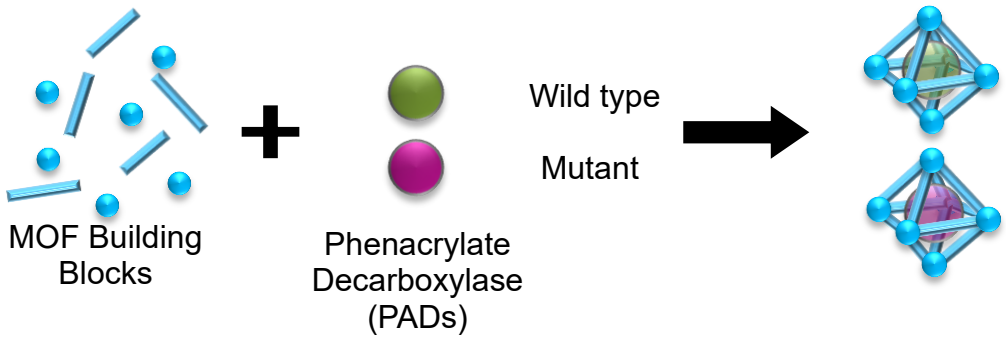

Figure 23: The formation of a metal-organic framework (MOF) with phenacrylate decarboxylase (PAD) enzymes leads to the encapsulated enzymes. In green, the PAD wild type (wT) and in purple, the PAD mutant (m) are shown.

The enzymes used were the wild type (wT) and a mutant (m) form of the PAD, both provided by Esther Mittmann and Kersten Rabe from the Institute for Biological Interfaces 1 (IBG-1) at KIT. After choosing the most compatible MOF, I exposed the enzyme/MOF biocomposite to different mechanical, thermal, and pH stressors and tested the effectiveness of the encapsulation.

Parts of this chapter were produced in a collaborative study for the Bachelor Thesis of Emily Bevier and with Kersten Rabe and Esther Mittmann from the Institute for Biological

Interfaces 1 (IBG-1). Additionally, Esther Mittmann kindly performed and provided the enzyme activity tests before and after the MOF formation and the enzyme gel tests.

4.2 Results and Discussion

We tested four different MOFs for their ability to incorporate the PAD enzymes while maintaining the enzymatic activity and MOF crystallinity. The different MOFs tested were ZIF-8 (ZIF-CO_3-1), ZIF-90, MIL-53(Al), and Ca(BDC). They all showed high potential for incorporating enzymes and could be synthesized in water. [6–9] I tested the PAD (wT and m), and additionally, I created a batch of each of the MOFs without enzyme (woE). Afterward, I tested the protection and preserved enzymatic activity of the encapsulated PAD enzymes (wT and m) in different organic solvents for two weeks.

4.2.1 MOF Characterization

Since the enzymatic activity should not be affected during the MOF synthetization process, the PAD had to be in the same solvent for the synthesis. Therefore, I decided on MOFs that could be synthesized in water and had previously been successfully used to incorporate other enzymes.[6–9] Promising MOFs were ZIF-8 (ZIF-CO_3-1), ZIF-90, MIL-53(Al), and Ca(BDC) (see Chapter 2.2.1), and I tested all four of them together with the PAD enzymes (wT and m). I used the reaction protocols mentioned in Chapter 8.1 for the MOF synthesis and the enzyme encapsulation. During the reaction, precipitations of white powders fell out for all the synthesized materials. Figure 24 shows the precipitated MOF powders.

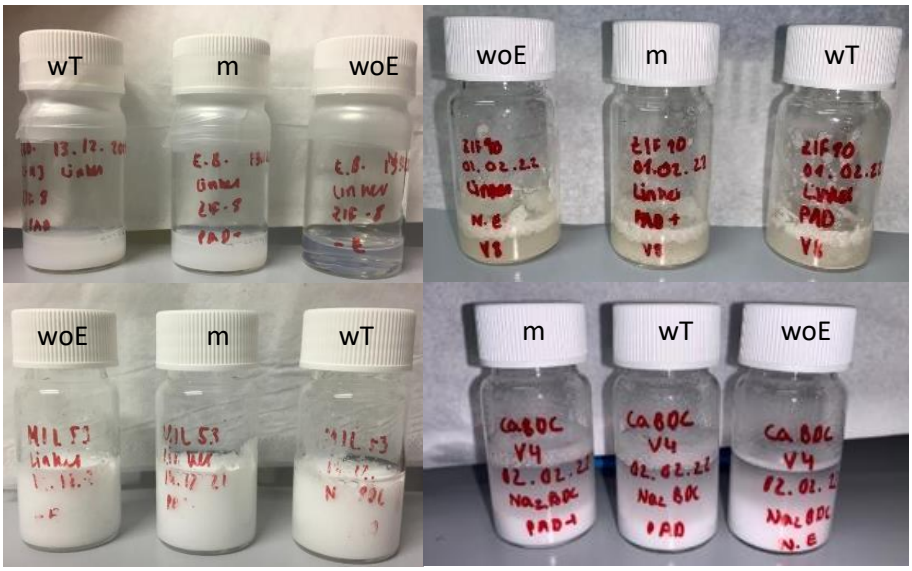

Figure 24: The precipitated metal-organic framework (MOF) particles after the MOF formation without (woE) and with the phenacrylate decarboxylase enzyme (PAD) (wild type (wT) and mutant (m)). The four MOFs tested were the ZIF-8 (ZIF-CO_3-1), ZIF-90, MIL-54(Al), and Ca(BDC) from left to right. The reactions are shown after the respective reaction time in water at room temperature (RT).

Except for the ZIF-8 (ZIF-CO_3-1) particles (woE), each reaction resulted in a white powder of precipitated particles (see Figure 24). The enzyme-free ZIF-8 (ZIF-CO_3-1) particles show less precipitation than the ZIF-8 (ZIF-CO_3-1) particles containing the enzyme. The low precipitated amount indicates that we require a seed crystal to synthesize ZIF-8 (ZIF-CO_3-1) (woE). After purification, I measured the X-ray diffraction (XRD) of all MOF powders (see Figure 25).

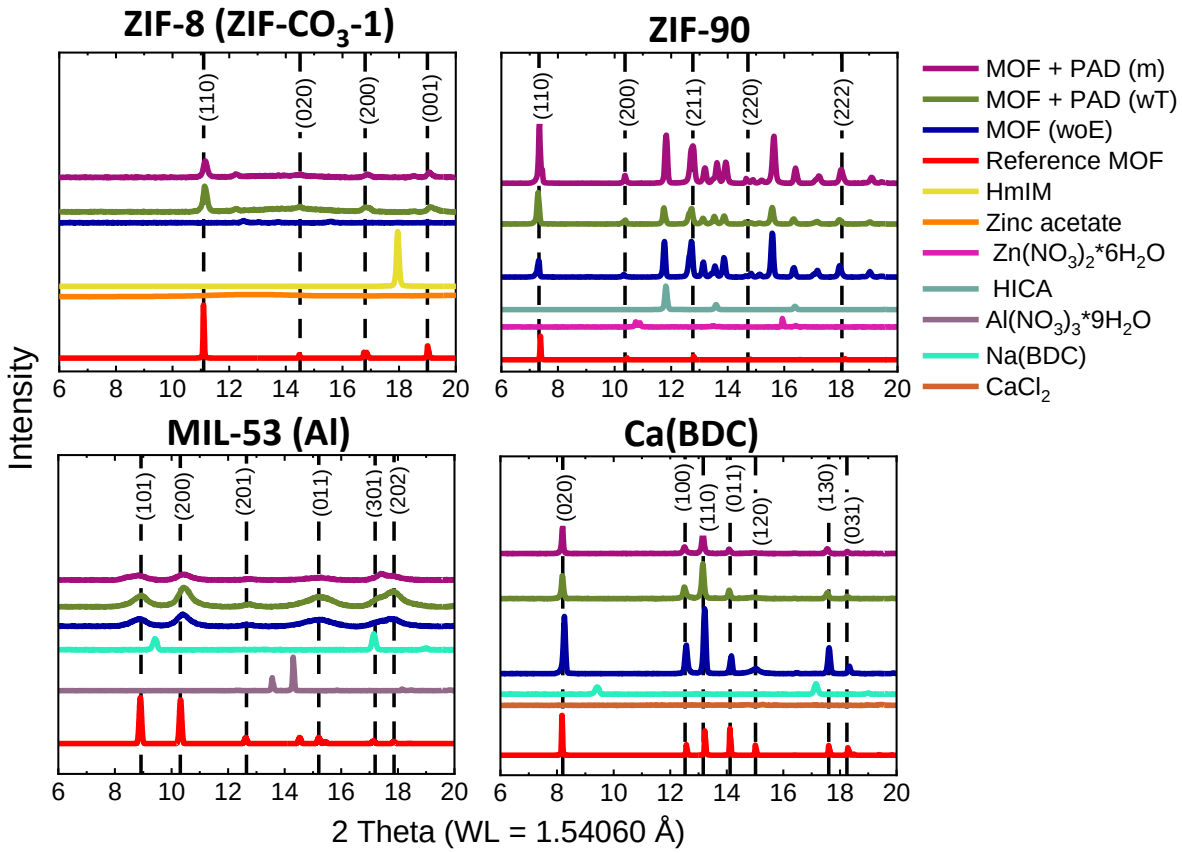

Figure 25: The X-ray diffraction (XRD) characterization for the four distinct metal-organic framework (MOF) systems - ZIF-8 (ZIF-CO_3-1), ZIF-90, MIL-53(Al), and Ca(BDC) synthesized with or without the phenacrylate decarboxylase enzyme (PAD). Two samples from one MOF system contained either the PAD (wild type (wT) or mutant (m)) or no enzyme (woE) as a reference to trace the crystallization process for pure particles. Along with the reference sample for the MOFs (red), the diffractogram of the respective metals and linkers used for the MOF synthesis are included. The XRD determines the crystalline phases and verifies whether the MOFs have formed by matching the patterns with the reference.[63,67,95,96]

Figure 25 shows all the different MOF patterns and their references. Additionally, it displays the pure metal and linker diffractograms of every MOF. While ZIF-8@PAD (wT and m) show a crystalline pattern and are consistent with the reference, ZIF-8 (woE) shows no pattern at all. A primary reason could be that the crystallization rate was low (see Figure 24), and the amount of particles was too small to be measured.

Interestingly, the crystalline structure of ZIF-8@PAD (wT and m) does not coincide with the actual ZIF-8 structure but with another related structure with the same reactants, the ZIF-CO_3-1. The new structure of ZIF is reported to be received with different reaction parameters and concentrations.[59,134] Since I synthesized in water and at RT, the structural change could result from the enzyme incorporation. Recent studies in this field also showed that the enzyme, metal, and linker concentration can influence the structure of the received ZIF.[59] The reference in Figure 25 also holds bovine serum albumin enclosed in the pores.[94,95] The ZIF-CO_3-1 crystallizes in the orthorhombic crystal system with the space group Pba2.[94]

ZIF-90 crystallizes in a cubic crystal system with the space group I-43m.[96] All synthesized ZIF-90@PAD particles (woE, wT, and m) show the characteristic pattern for the structure, and I could confirm the successful crystallization. Limitations occurred for the purification process with the ZIF-90 particles. Since the linkers' solubility was reduced in water, the remaining linker precipitated during the reaction and could not be removed afterward. Therefore, Figure 25 shows additional peaks matching the free linker (2-imidazolecarboxaldehyde (HICA)) in ZIF-90.

All the received diffractograms for MIL-53(Al) with or without the PAD (wT and m) show equally broad peaks (see Figure 25). The first two peaks (101 and 200) concur with the reference peak (red), but the other peaks show a shift, and I could not allocate them. The used reference for MIL-53(Al) held the linker terephthalic acid (BDC) captured in its pores.[63] Since the first two reference peaks fit the measured XRD of our synthesized MIL-53(Al), I assume incorporating PAD (wT and m) also leads to similar structural changes. Although the first peaks indicate the successful creation of MIL-53(Al), I miss conclusive evidence of the success of the synthesis. MIL-53(Al) crystallizes in the orthorhombic crystal structure with the space group Pnma.[63]

The Ca(BDC) samples with and without PAD (wT and m) show clear and pure diffractograms. All received peaks match the reference (red), confirming the successful synthesis. Ca(BDC) crystallizes in a monoclinic crystal system with the space group $P2_1/c$ ($P12_1/c1$).[67]

The XRD demonstrates that all iterations of ZIF-8 (ZIF-CO_3-1), ZIF-90, and Ca(BDC) (woE, wT, and m) lead to crystalline products. ZIF-8 (ZIF-CO_3-1) (woE) and MIL-53(Al) are the only reactions in which the formation of a crystalline product is unclear. However, I used MIL-53(Al) in additional investigations to see how it impacts and possibly protects the PAD enzymes.

In the next step, I tested the influences of the enzyme encapsulation on the particle size and shape. Therefore, I examined the synthesized particles with scanning electron microscopy (SEM) (see Figure 26).

In Figure 26, ZIF-8 (ZIF-CO_3-1) (woE) shows fan-like arranged squares of 5 to 10 µm, whereas ZIF-8 (ZIF-CO_3-1) (wT and m) shows small bead size particles under 1 µm. The disparity in the SEM images makes sense, given that the ZIF-8 (ZIF-CO_3-1) (woE) amount was too low to obtain a crystalline diffractogram and that I could not clearly state that a crystalline material formed (see Figure 25). The ZIF-90 particles (woE, wT, and m) all show big particles in the 10 to 50 µm range. They all have rectangular structures and crystalline structures (see Figure 26). For MIL-53(Al), all synthesized products show small particles ranging from 1 to 30 µm. Given their proximity, I could not establish the shape of the particles. The Ca(BDC) particles in all variations gave nice big particles (25 to 30 µm) with a clear rectangular structure.

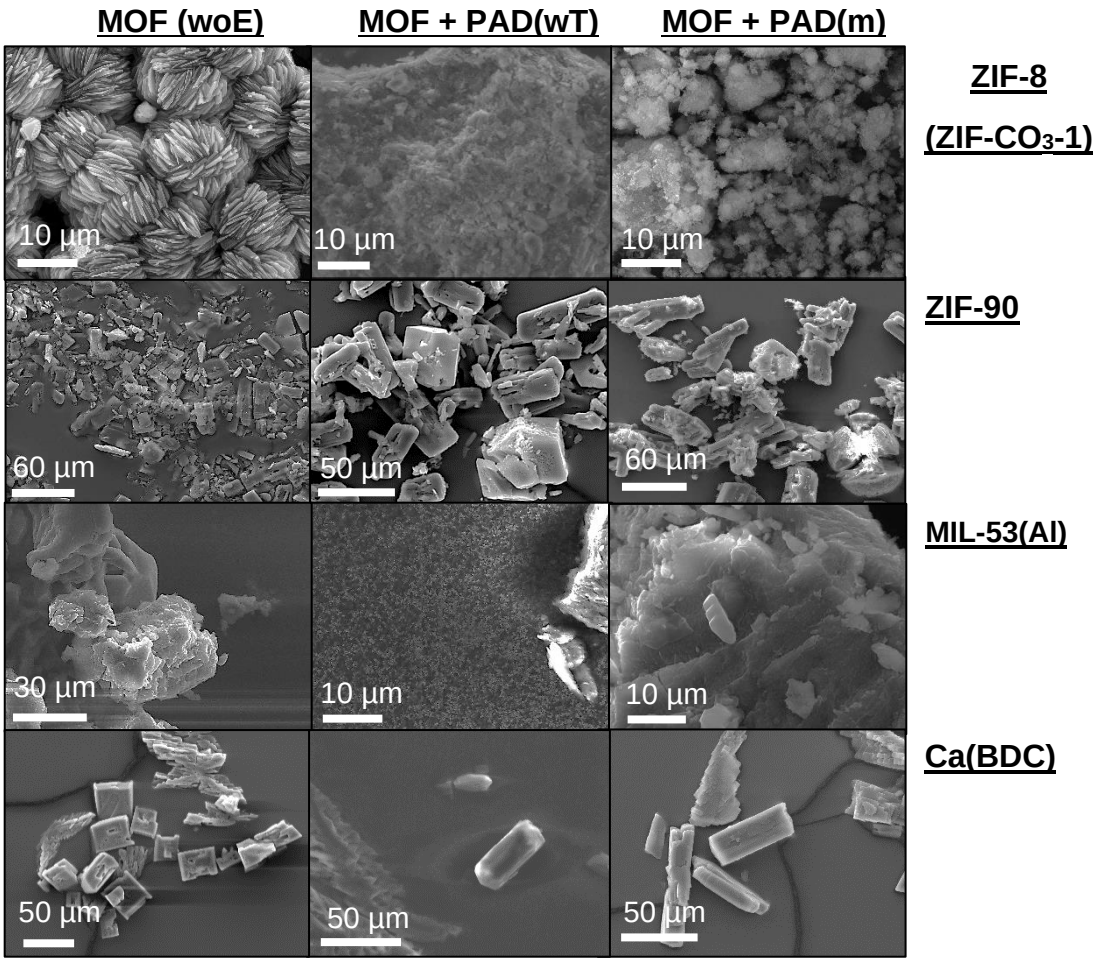

Figure 26: Size and morphology analysis of the four different metal-organic framework (MOF) systems: ZIF-8 (ZIF-CO_3-1), ZIF-90, MIL-53(Al), and Ca(BDC) used for the enzyme encapsulation of the phenacrylate decarboxylase enzymes (PAD) (wild type (wT) and mutant (m)). Additionally, the MOFs without enzymes (woE) are shown.

As shown in the previous chapter and Figure 26, the enzyme incorporation did not influence the size or shape of the particles. However, it did benefit ZIF-8 (ZIF-CO_3-1) as a seed crystal and allowed the production of crystalline particles.

4.2.2 Enzyme Activity after Incorporation

Different stressors can compromise enzyme activity. In the first step, we evaluated the behavior of the metal and linker solution and the substrate conversion of the PAD enzyme (wT). Therefore, we measured the conversion of pCA to pHS in the presence of the different linkers and metals (see Figure 27 and Figure 28).

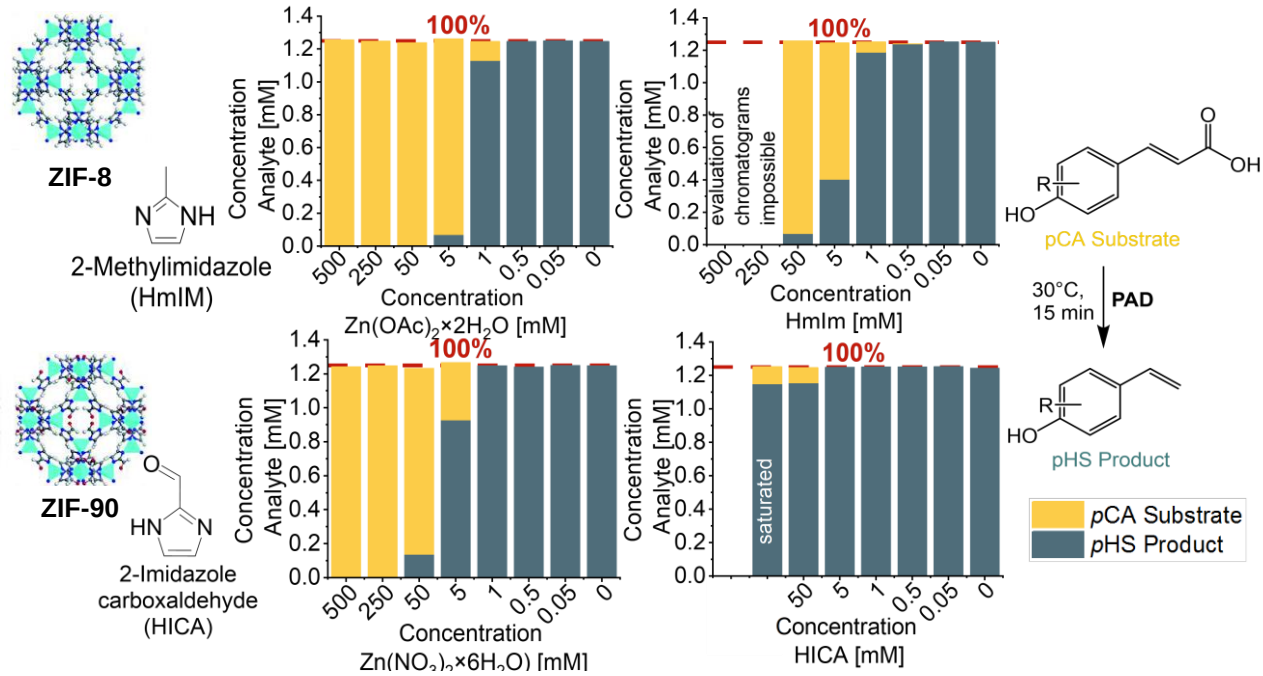

Figure 27: The enzymatic activity of 1 µm phenacrylate decarboxylase enzyme (PAD) (wild type (wT)) monitored together with different concentrations of the metal and linker of ZIF-8 (ZIF-CO_3-1); $Zn(OAc)_2×2H_2O$ with 2-methylimidazole (HmIM) and ZIF-90; $Zn(NO_3)_2×6H_2O$ with 2-imidazolecarboxaldehyde (HICA). The conversion of p-coumaric acid (pCA) [1.25 mM] (yellow) to p-hydroxystyrene (pHS) [mM] (blue) in an aqueous solution was measured for over 15 minutes at 30 °C. [Parts of this figure were reproduced with permission from {M. Gao, J. Wang, Z. Rong, Q. Shi, J. Dong, "A combined experimental-computational investigation on water adsorption in various ZIFs with the SOD and RHO topologies" RSC Adv. 2018, 8, p. 39628, https://doi.org/10.1039/C8RA08460B}. Copyright {2018} The Royal Society of Chemistry].[57]

For ZIF-8 (ZIF-CO_3-1), the PAD performs less efficiently when combined with 2-methylimidazole (HmIM) and $Zn(OAc)_2×H_2O$ at concentrations greater than 1 to 5 mM. For ZIF-90, $Zn(NO_3)_2×H_2O$ costs enzymatic activity loss beyond a concentration of 5 mM. On the contrary, the HICA linker can be employed up to a concentration of 50 mM.

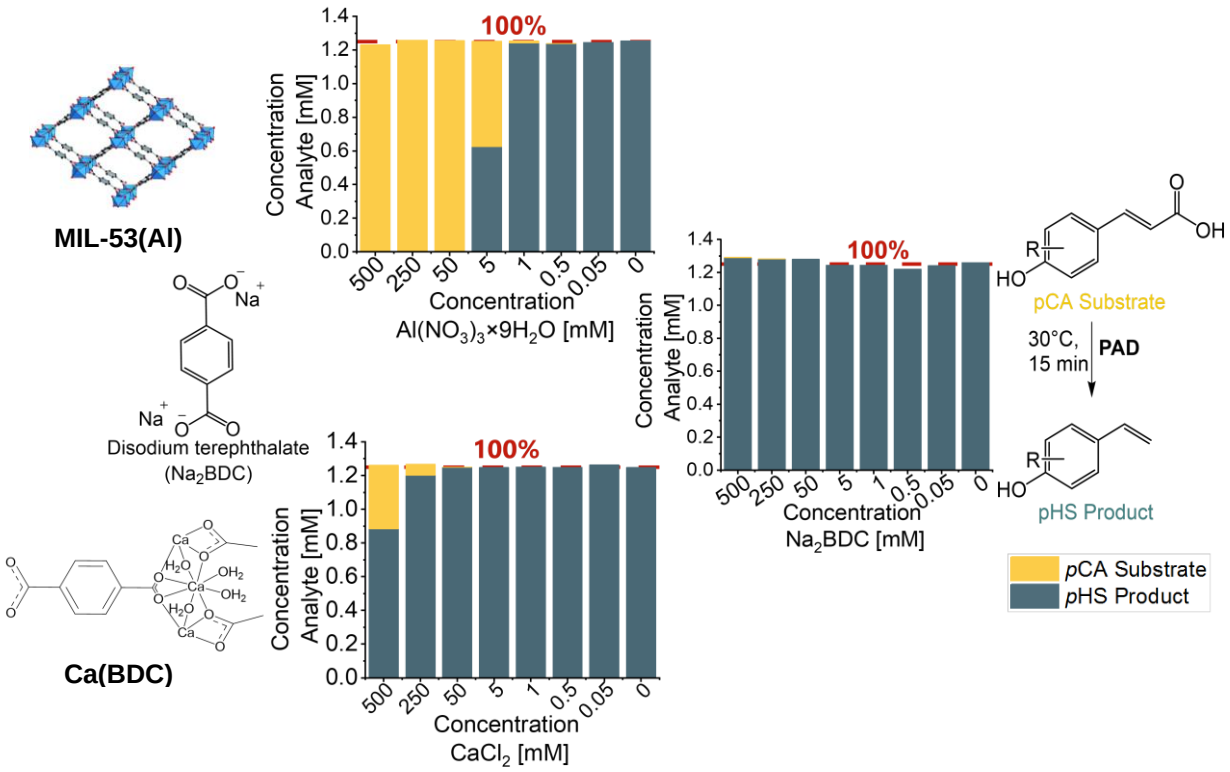

Figure 28: The enzymatic activity of the phenacrylate decarboxylase enzyme (PAD) (wild type (wT)), monitored together with different concentrations of the metal and linker of MIL-53(Al) and Ca(BDC) ($Al(NO_3)_3×9H_2O$ (MIL-53(Al)) and $CaCl_2$ (CaBDC) and disodium terephthalate (Na_2BDC)). The conversion of p-coumaric acid (pCA) [1.25 mM] (yellow) to p-hydroxystyrene (pHS) [mM] (blue) in an aqueous solution was measured for over 15 minutes at 30 °C. [Parts of this figure were reproduced or adapted with permission from {H. T. Nguyen, L. H. Thuy Nguyen, T. Le Hoang Doan, P. H. Tran, "A mild and efficient method for the synthesis of pyrroles using MIL-53(Al) as a catalyst under solvent-free sonication", RSC Adv. 2019, 9, p. 9097, https://doi.org/10.1039/C9RA01071H}. Copyright {2019} The Royal Society of Chemistry and {S. H. Dale, M. R. J. Elsegood, "catena-Poly-[[di-aqua-calcium(II)]-μ3-terephthalato-μ2-aqua] at 150 K", Acta Crystallogr., Sect. E: Struct. Rep. Online 2003, 59, m586, https://doi.org/10.1107/S1600536803015071}. Copyright{2003} International Union of Crystallography].[65,67]

For MIL-53(Al), it is evident that the metal $Al(NO_3)_2×9H_2O$ produces a 50 % loss of activity as early as 5 mM, whereas the linker disodium terephthalate (Na_2BDC) has no effect. The enzyme's activity is also not influenced by $CaCl_2$. Even in a high concentration of 50 mM, we maintain the enzymatic activity for the Ca(BDC) metal.

In conclusion, of all the metal and linkers tested, only Ca(BDC) can be used or synthesized with a high concentration of metal and linker. For all other metals, the concentration must be reduced to such an extent that no reduction in enzyme activity occurs during the MOF synthesis.

Nevertheless, the essential part is retaining the enzymatic activity after the encapsulation. Therefore, we tested the conversion of the substrate pCA to pHS with the encapsulated PAD@MOF enzymes (wT and m) for the different MOF systems (see Figure 29).

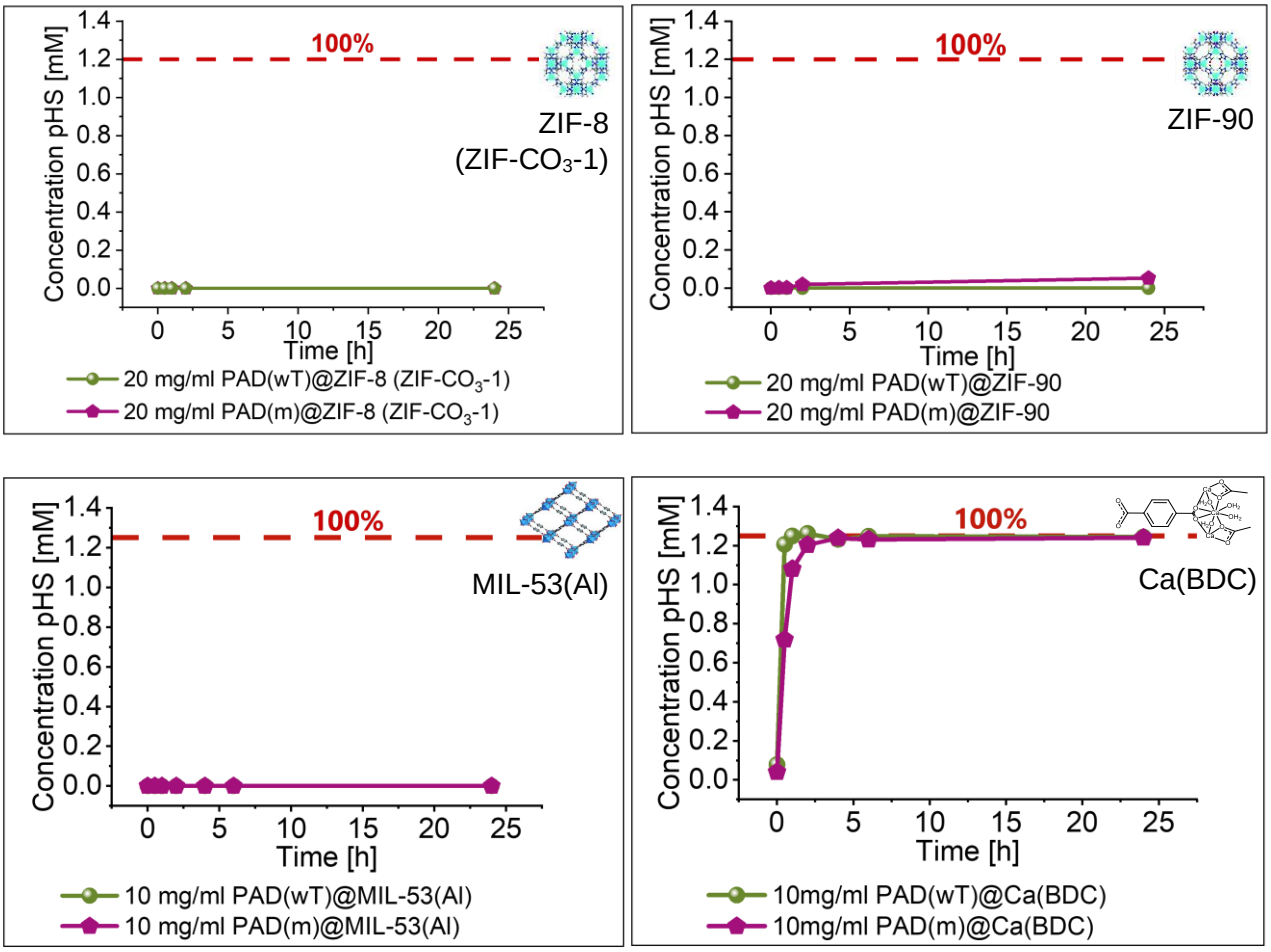

Figure 29: Phenacrylate decarboxylase enzyme (PAD) (wild type (wT) and mutant (m)) activity measurement after the encapsulation in ZIF-8 (ZIF-CO₃-1), ZIF-90, MIL-53(Al), and Ca(BDC) particles. The p-hydroxystyrene (pHS) [mM] production from p-coumaric acid (pCA) [1.25 mM] is illustrated over 25 h. The different enzymes, PAD (wT and m), are displayed in green and violet. [Parts of this figure were reproduced or adapted with permission from {M. Gao, J. Wang, Z. Rong, Q. Shi, J. Dong, "A combined experimental-computational investigation on water adsorption in

various ZIFs with the SOD and RHO topologies" RSC Adv. 2018, 8, p. 39628, https://doi.org/10.1039/C8RA08460B}. Copyright {2018} The Royal Society of Chemistry, {H. T. Nguyen, L. H. Thuy Nguyen, T. Le Hoang Doan, P. H. Tran, "A mild and efficient method for the synthesis of pyrroles using MIL-53(Al) as a catalyst under solvent-free sonication", RSC Adv. 2019, 9, p. 9097, https://doi.org/10.1039/C9RA01071H}. Copyright {2019} The Royal Society of Chemistry, and {S. H. Dale, M. R. J. Elsegood, "catena-Poly-[[di-aqua-calcium(II)]-μ3-terephthalato-μ2-aqua] at 150 K", Acta Crystallogr., Sect. E: Struct. Rep. Online 2003, 59, m586, https://doi.org/10.1107/S1600536803015071}. Copyright{2003} International Union of Crystallography].[57,65,67]

Figure 29 shows no substrate conversion for the PADs (wT and m) encapsulated in ZIF-8 (ZIF-CO_3-1), ZIF-90, and MIL-53(Al). The low compatibility of the metal and linker shown in Figure 27 and Figure 28 could be a reason for the decreased enzymatic activity in the three MOF systems. In contrast, the pHS conversion of the PADs (wT and m) encapsulated in Ca(BDC) reaches 100 %. This fact is supported by Figure 28, which shows the preserved PAD activity (wT and m) with Na_2BDC and $CaCl_2$.

Additionally, we investigated whether a PAD (PAD(m)) with amino acid substitutions that change the surface charge distribution on the enzyme would influence the incorporation of the enzyme into the MOF. Figure 29 shows that both PADs (wT and m) display the same enzymatic activity for all systems. I conclude that the PAD (m) did not significantly influence the incorporation in MOFs or their protection.

Following the identification of Ca(BDC) as a potential MOF shell, we also examined the compatibility of the pure MOF with the product (pHS) and reactant (pCA). Therefore, I tested whether pristine Ca(BDC) influences the pHS and pCA concentration. For this reason, we mixed the pristine Ca(BDC) with the pHS and pCA in two separate reaction vials and measured each concentration for 25 h (see Figure 30).

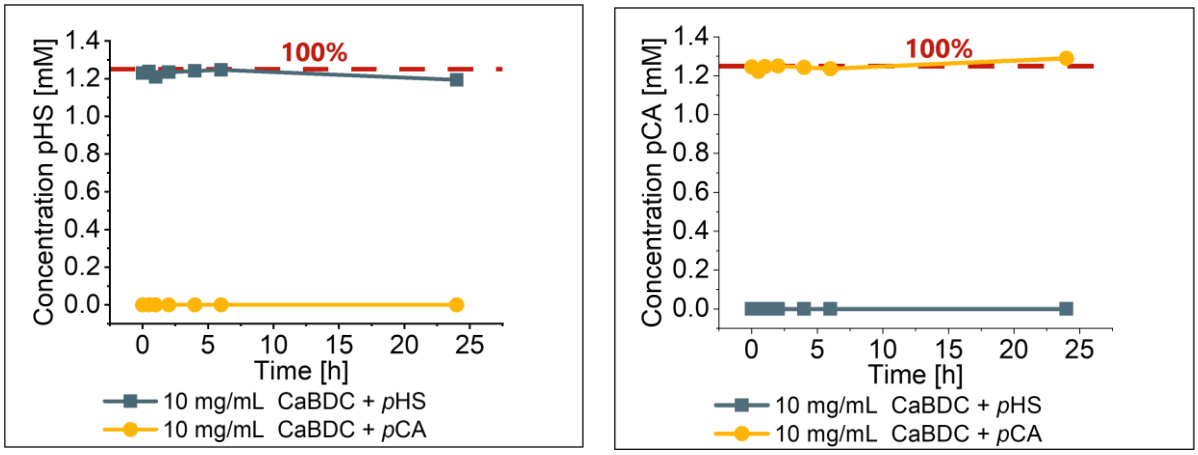

Figure 30: The compatibility of the Ca(BDC) particles with the reactant (p-coumaric acid (pCA)) [1.25 mM] and the product (p-hydroxystyrene (pHS)) [1.25 mM], measured throughout 25 h. The pHS concentration is on the left, and the pCA concentration is on the right.

Even after 25 h, the pristine Ca(BDC) does not influence pHS or pCA. While no reduction or increase occurred, pHS and pCA stayed in high concentration all the time. Therefore, I confirm that Ca(BDC) successfully encapsulates the PADs (wT and m) without affecting their catalytic activity.

4.2.3 Proof of Enzyme Encapsulation

After determining Ca(BDC) as the most promising protection for PAD enzymes, we used a western blot to test whether the enzymes are incorporated into the MOF or physisorbed on the surface. For this, different combinations of Ca(BDC), untreated (PAD@CaBDC(woE, wT, and m)) (rows 1-3), dissolved in SDS, filtered, and centrifuged (PAD@CaBDC(woE, wT, and m)) (rows 4-6), the free enzymes (wT and m) without Ca(BDC) (rows 8-9), the washing solution following the PAD (wT and m) encapsulation in Ca(BDC) (rows 10–12), and the washing solution after filtration and centrifugation (rows 13–15), were tested in a western blot. In row 7, the marker was placed (see Figure 31).

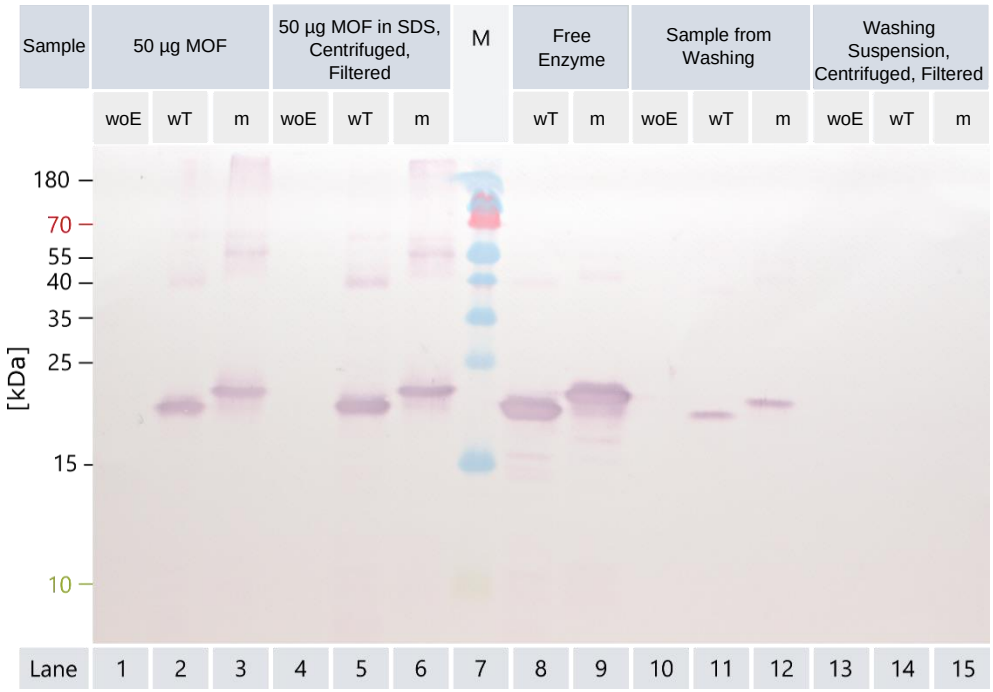

Figure 31: The western blot with the results from the enzyme activity in the Ca(BDC) particles. The used samples were Ca(BDC) without (woE) and with phenacrylate decarboxylase enzyme (PAD) (wild type (wT) and mutant (m)). Furthermore, the washing solution gives information about the successful incorporation of the enzymes into the metal-organic framework (MOF) structure. We used 50 µg MOF with or without enzyme (woE) (rows 1-3), the centrifuged supernatant of the Ca(BDC) samples resuspended in SDS and filtered afterward with a 0.2 µm filter (rows 4-6), a marker (row 7), free enzyme (rows 8-9), the solution from the washing step (row 10-12) and the filtered washing solution with a 0.2 µl filter (row 13-15). All experiments were conducted overnight at 8 °C. The substrate concentration was 1.25 mM.

With the western blot, I confirm the Ca(BDC) particles in rows 2 to 3 exhibit enzyme activity, as opposed to pristine Ca(BDC) in row 1. Equally, rows 5 and 6, with PAD (wT and m), show evidence of enzyme activity even after centrifugation and SDS treatment. The enzymatic activity in the washing solution in rows 10 to 12 first indicates free enzyme. A possible explanation lies in the washing process, which had to be very mild so as not to destroy the enzyme. Therefore, the centrifugation was slow, and the washing solution may still contain Ca(BDC particles with encapsulated PAD enzymes (wT and m).

Consequently, we filtrated and centrifuged the washing solution and measured the activity again (rows 13 to 14). Following this, we detected no enzymatic activity and concluded

that there was no free enzyme left in the solution. This indicates that the enzymes found in rows 1-6 are encapsulated inside the MOF particles.

4.2.4 Enzymatic Activity Behavior by MOF Protection in Different Solvents

In the previous paragraph, I incorporated the (wT) and (m) PAD into Ca(BDC) while maintaining the enzyme's function. Next, I examined how effectively the MOF system protects enzymatic activity from extreme heat, various organic solvents, and fluctuations in pH. Therefore, I dispersed the Ca(BDC) with PAD (wT and m) and the pristine Ca(BDC) in methanol (MeOH), cyclohexane (Cyc), dimethylformamide (DMF), Milli-Q water (H_2O), tetrahydrofuran (THF), toluene (Tol), ethanol (EtOH), aqueous solutions with pH 4, pH 6, and pH 7, acetonitrile (MeCN), ethyl acetate (EtOAc), and H_2O (100 °C). Additionally, I prepared a control sample on air. After two weeks under the respective conditions, we washed the MOF particles with water, dried them, and measured the enzymatic activity. Besides the enzymatic activity, I tested the XRD pattern of the MOF particles before and after the treatment with the solvents to see if I could maintain the crystallinity over time. I repeated all experiments a second time to verify our results.

Following XRD analysis, I discovered that all Ca(BDC) particles, except those in pH 4, exhibit diffractograms consistent with the reference (see Figure 32). This finding indicates that these MOFs still have their original crystalline structure. However, the particles at pH 4 do not exhibit characteristic Ca(BDC) peaks, leading us to believe that the acid environment destroys the MOF structure (see Figure 32).

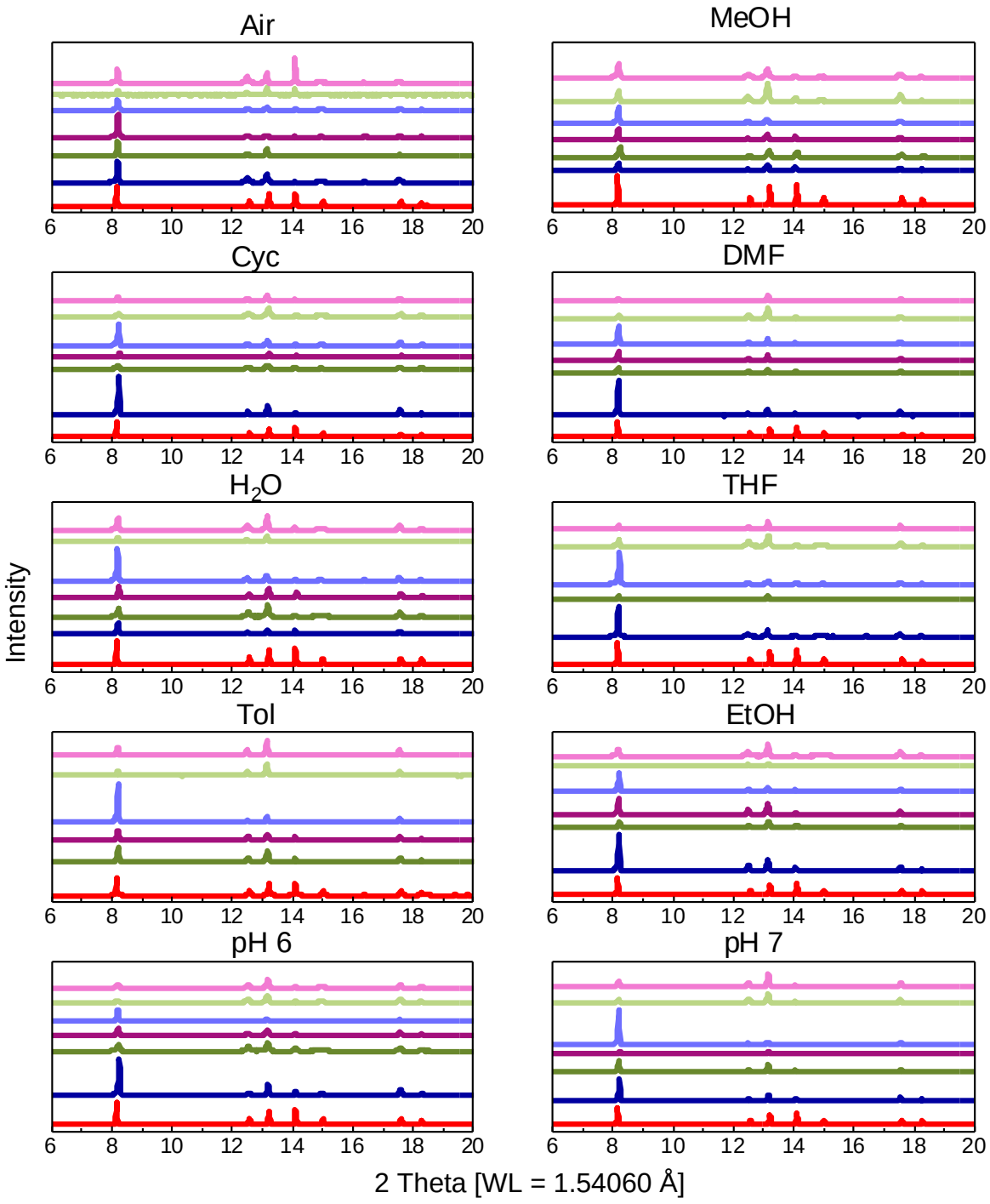
Air
MeOH
Cyc
DMF
H2O
THF
Tol
EtOH
pH 6
pH 7
Intensity
6 8 10 12 14 16 18 20
2 Theta [WL = 1.54060 Å]

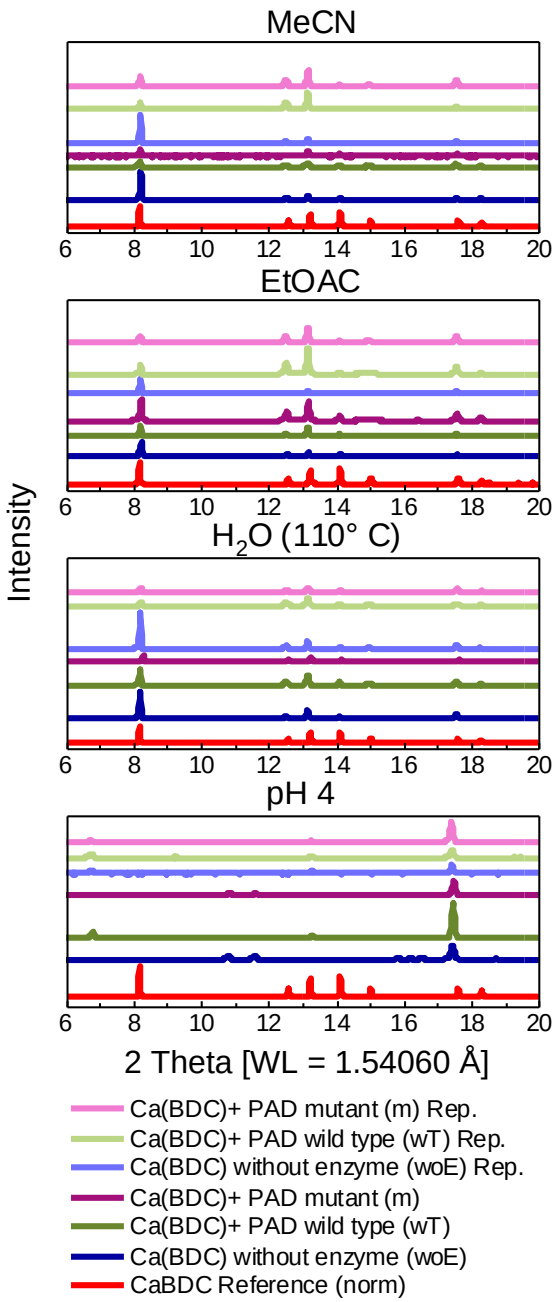

Figure 32: The X-ray diffraction (XRD) of Ca(BDC) particles, dispersed for two weeks in various solvents or at various pHs without the phenacrylate decarboxylase enzyme (PAD) (woE, blue), with PAD wild type (wT, green), and with PAD mutant (m, purple) are shown. All diffractograms show intact crystalline structures, with the exception of the aqueous solution of pH 4. The repetition, shown in light blue (woE), light green (wT), and light purple (m), confirms this finding.

After confirming the intact crystalline structure of all particles except pH 4, we tested the enzymatic activity (see Figure 33). Thermal and other stressors typically result in structural and bioactivity loss.[135] As a result, MOFs to encapsulate and protect the biological activity were searched and synthesized. ZIF-8 can, for example, protect the horseradish peroxidase (HRP) against pH changes, high temperatures, and organic solvents like DMF.[135] Recent progress shows that MOF particles can protect enzymes from different stressors. However, they often only test the protection for a few minutes or

even days. By testing the influence and the protection for two weeks, I focused on a later application in high throughput studies for high substrate conversions over weeks.

Even after two weeks, we found good enzymatic activity for the PAD (wT and m) on air (see Figure 33). Even the PAD@Ca(BDC) (wT and m) in the different organic solvents, like Cyc, Tol, THF, EtOAc, DMF, MeCN, and EtOH, show a reduced but still existing enzymatic activity. Also, the samples in water at pH 7 and 6 show a conserved activity. Solely the samples in water at pH 4 and MeOH show no activity. Since the Ca(BDC) structure shows no diffractogram in water at pH 4, I assume the acid environment destroyed the MOF structure, and the enzymatic activity was lost. Although MeOH does not influence the MOF structure, the enzymatic activity is lost after two weeks. It is possible that MeOH, as the smallest molecule, could more quickly enter the pores of the MOF and interfere with the enzyme structure inside.

The enzymatic activity of the two different PAD enzymes (wT and m) exhibits modest variations in different solvents like Cyc or Tol. However, most other solvents show similar activities for both PADs, and I find that protection with Ca(BDC) gives similar results for both enzymes.

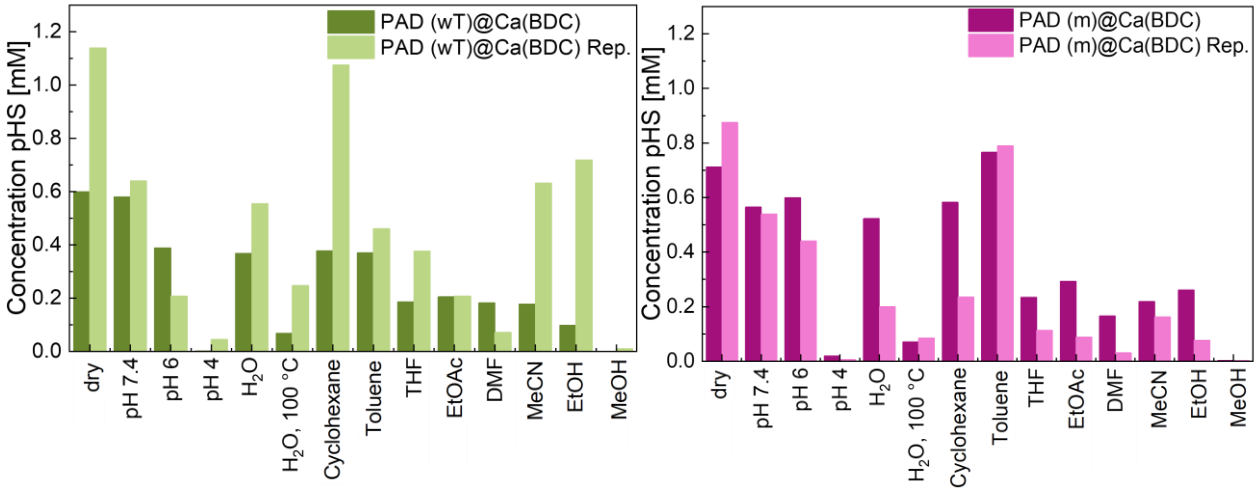

Figure 33: After exposing the phenacrylate decarboxylase enzyme (PAD) (wild type (wT) and mutant (m)) encapsulated in Ca(BDC) to different organic solvents for two weeks, the preserved enzymatic activity of the encapsulated enzymes in the metal-organic framework (MOF) particles is measured. The PAD (wT (green) and m (purple)) encapsulated in Ca(BDC) continue to show enzymatic activity after two weeks in all solvents except methanol (MeOH) and in an aqueous solution with pH 4. The repetition of the experimental series shown in light green and light pink displays similar results. The conversion of the analyte p-coumaric acid (pCA) [1.25 m]) to p-hydroxystyrene (pHS) [mM] was measured over 24 h at 30 °C. We used 10.0 mg/ml PAD@MOF (wT and m).

The results show that encapsulating PAD (wT and m) in Ca(BDC) is a promising protective approach against harsh reaction conditions. The shown MOF protection is valuable for applications in flow reactors to guarantee high throughput substrate conversion.

4.3 Summary

In the previous paragraph, I tested incorporating PAD (wT and m) into different MOF particles. While I could not definitively confirm that I successfully synthesized the MOF structures ZIF-8 (ZIF-CO_3-1) (woE) and MIL-53(Al) (woE, wT, and m), all the other MOFs (ZIF-8 (ZIF-CO_3-1), ZIF-90, and Ca(BDC)) yielded crystalline products. Interestingly, there was a structural change by the incorporated PAD (wT and m) enzymes in ZIF-8. Their crystalline structure does not coincide with the actual ZIF-8 structure but with another related structure with the same reactants, the ZIF-CO_3-1. The structural change probably results from the encapsulated enzymes in the pores of the structure.

The SEM pictures showed different patterns and sizes for all MOF structures. The SEM pictures of ZIF-8 (ZIF-CO_3-1) (woE) showed some crystals, but since the XRD did not yield a diffractogram, I excluded them from the study. The other ZIF-8 (ZIF-CO_3-1) showed fan-like arranged squares of 5 to 10 µm. ZIF-90, on the other side, showed rectangular particles (woE, wT, and m) in the range of 10 to 50 µm. The particles for MIL-53(Al) were very small, around 1 to 30 µm. I could not determine a shape since the particles were small and difficult to obtain. The Ca(BDC) particles in all variations gave excellent big particles (25-30 µm) with a straightforward rectangular structure.

Checking the enzymatic activity for all different MOF systems, I found that only the linker and metal for Ca(BDC): Na_2BDC and $CaCl_2$ are compatible with the PAD (wT) and did not influence the substrate conversion (pCA → pHS). All the other metals and linkers were only applicable up to a concentration of 5 mM. Otherwise, the high concentration would inhibit the substrate conversion. The metal and linker influence was also detectable in the enzymatic activity tests after the encapsulation. Only the PAD (wT and m) in Ca(BDC) resulted in substrate conversion. Therefore, I identified Ca(BDC) as the most suitable PAD@MOF (wT and m) system.

Afterward, the PAD@Ca(BDC) (wT and m) particles were tested in various organic solvents and under extreme conditions, including temperature and pH changes. The PAD@Ca(BDC) (wT and m) were stored for two weeks at RT, in EtOAc, Tol, EtOH, MeCN, MeOH, H_2O, DMF, THF, H_2O (100 °C), Cyc, and aqueous solutions of pH 4, pH 6,

and pH 7. Additionally, the pristine particles were dispersed in every solvent to see the influence on the Ca(BDC) particles alone.

Except for the Ca(BDC) particles (wT, m, and woE) in pH 4, all the particles showed a crystalline pattern after two weeks. The acid environment at pH 4 destroyed the Ca(BDC) structure, and I did not obtain a diffractogram after two weeks. The impairment of the Ca(BDC) structure leads to an enzymatic activity loss at pH 4. All other enzymatic activities except for MeOH were reduced but remained after two weeks. Even PAD@Ca(BDC) (wT and m) particles in harsh solvents (DMF, MeCN, THF) still showed enzymatic activity. The enzymatic activity of the two distinct PADs (wT and m) did not differ substantially.

In summary, I demonstrated how to tailor and adjust a MOF system to shield a specific enzyme, the PAD, from chemical and physical stressors for up to two weeks. The efficient protection of an enzyme is a beneficial finding, particularly for flow catalysis applications, since it allows us to extend the lifetime of enzymes and, hence, lower their cost through the integration of a customized MOF system.

5. MOF/Polymer Nanoparticles for Drug Delivery

Parts of this chapter are published in Macromolecular Materials and Engineering under https://doi.org/10.1002/mame.202300048. The publication title is Biofunctionalization of Metal–Organic Framework Nanoparticles via Combined Nitroxide-Mediated Polymerization and Nitroxide Exchange Reaction.

5.1 Introduction

Metal-organic framework (MOF) materials have a lot of potential for biological and medical applications (see Chapter 2.2.2). Especially the surface modification and adaptability of MOF materials to a specific application make MOFs interesting, for example, as drug carriers for the administration of drugs. MOFs must meet particular criteria to be qualified as a nanocarrier, such as being highly biocompatible, non-toxic, and stable enough to stay in the bloodstream for a prolonged time.[136]

Given the modification possibilities on MOF materials, applying a hydrophilic polymer on the MOF surface can improve this biocompatibility by increasing circulation time in blood and dispersion stability.[80,137] The attached hydrophilic polymers also help to reduce nonspecific protein adsorption of blood proteins on the surface. Grafting polymers onto the MOF surface can be accomplished in several ways (see Chapter 2.2.2). While the "grafting-to" method is generally very simple, we chose the "grafting-from" method because it results in a higher polymer density on the surface.[5]

Several controlled radical polymerization (CRP) processes are identified for the polymerization method. Atom transfer radical polymerization (ATRP), reversible addition-fragmentation chain-transfer polymerization (RAFT), and nitroxide-mediated polymerization (NMP) are the three most well-known. Due to the controlled nature of the polymerization, achieving equal chain lengths of the polymer chains on the surface is possible. Since ATRP works with heavy metals, which are detrimental to biological applications, and RAFT often uses smelly sulfur-containing substances, we focused on the third method, NMP.[138]

Another advantage of NMP is that a so-called nitroxide exchange reaction (NER) at the end-group of the polymer chain is possible.[139,140] Thus, for example, a biologically active

group can be applied subsequently to the nanoparticle (NP). In 2021, we first published a polymerization approach from the surface of UiO-66-NH_2 with NMP.[140]

In this work, I describe the grafting-from approach with hydrophilic polymers on the surface of UiO-66-NH_2 NP using the NMP method. The four hydrophilic monomers that were used are the Poly(ethylene oxide) methyl-p-vinylbenzyl-ether (SPEGA), the poly(ethylene glycol) methyl ether acrylate (APEG), the N-hydroxyethylacrylamide (HEAA), and the N,N-dimethylacrylamide (DMAA).

In a model experiment, I first applied the SPEGA to UiO-66-NH_2 NPs and then tested them concerning the successful polymer addition and conserved particle size and crystallinity with attenuated total reflection infrared spectroscopy (ATR-IR), time-of-flight secondary ion mass spectrometry (ToF-SIMS), X-ray diffraction (XRD), scanning electron microscopy (SEM) and dynamic light scattering (DLS). Afterward, I tested the reduced protein adsorption and then performed a NER to modify the polymer end chain with a bioactive RGD sequence (Arg-Gly-Asp peptide).

Furthermore, I tested the transfer of the NMP grafting-from strategy with various other monomers. With the NMP approach, I wanted to show that the implemented NMP strategy can also be used for different polymers and that I can synthesize and modify different MOF/polymer NPs for later applications in particular areas of biology and medicine.

To prove this versatility of the NMP modification strategy, I used the same synthesis approach to produce seven other MOF/polymer or MOF/copolymer NPs with the hydrophilic polymers APEG, HEAA, and DMAA. In addition, I tested these new MOF/polymer or MOF/copolymer materials for their compatibility for drug uptake and their suitability for drug delivery in cancer research using MCF-7 breast cancer cells. To this end, I have conducted experiments in collaboration with Prof. Martina H. Stenzel at the University of New South Wales (UNSW) in Sydney. Figure 34 displays the general principle of the MOF/polymer synthesis strategy using NMP.

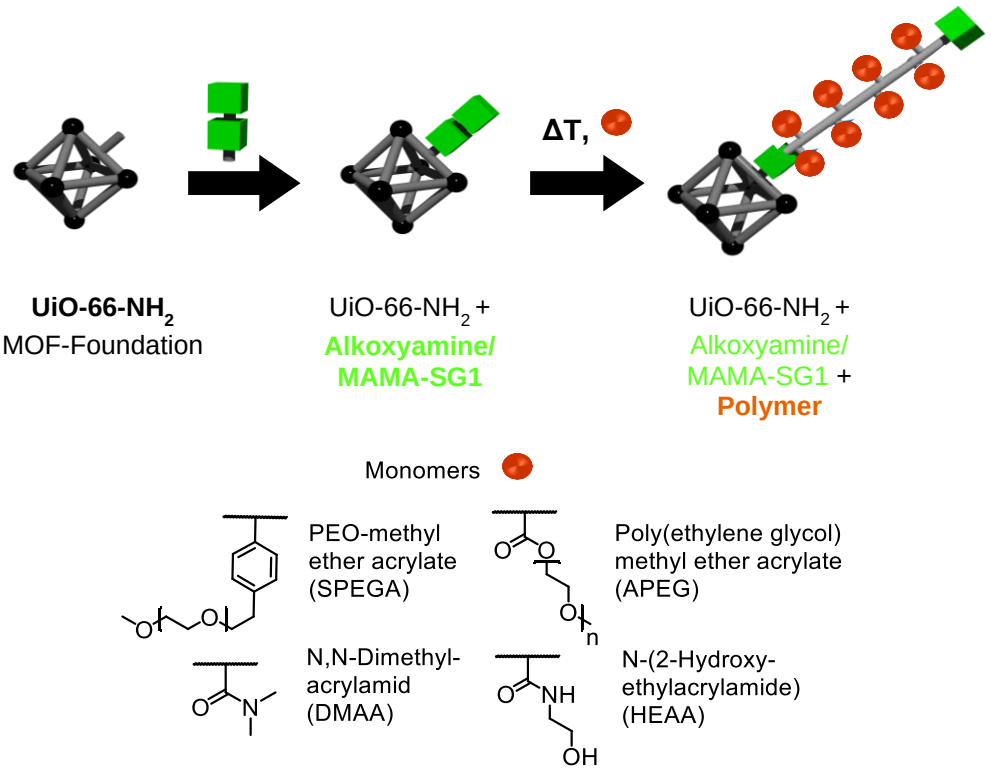

Figure 34: Polymerization on the UiO-66-NH_2 surface via nitroxide-mediated polymerization (NMP). After the metal-organic framework (MOF) is synthesized, the initiator (either the TEMPO-alkoxyamine (AA) or MAMA-SG1) for the polymerization is applied, and the polymerization happens on this new surface functionalization. The different polymers used for the modification are shown below.

5.2 Results and Discussion

The following chapter describes the results and insights into MOF/polymer composites and strategies for their synthesis and modification. I will show a suitable modification strategy for outer surface modification and the influence of polymers on the MOF surface. Additionally, I will demonstrate the application of the polymerization strategy on different polymers and show their suitability for drug delivery by testing their initial cytotoxicity in a model cell environment.

5.2.1 Grafting-from Polymerization of the Surface of UiO-66-NH_2 Nanoparticles

I first synthesized the UiO-66-NH_2 NP for the grafting-from experiment (see Chapter 8.2.1). Then, I modified the surface with a TEMPO-alkoxyamine initiator (AA) via an amide bond formation on the amine of the UiO-66-NH_2 linker and then polymerized in solution with the styrene-PEG derivative (SPEGA) (see Chapter 8.2.3 and 8.2.4). Figure 35 shows the general reaction scheme.

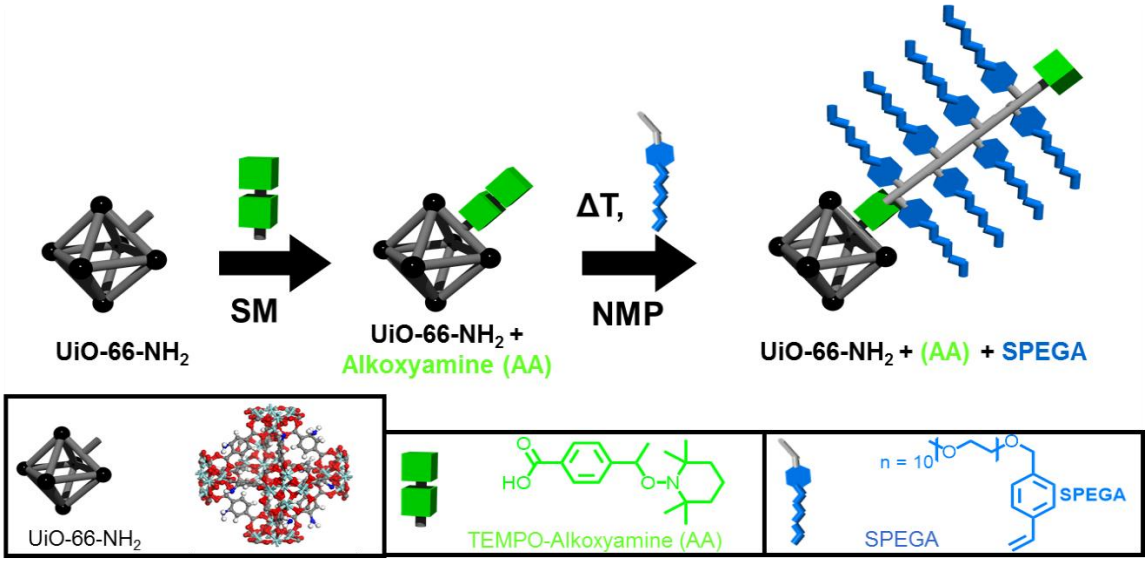

Figure 35: The basic principle of the nitroxide-mediated polymerization (NMP) on the surface of UiO-66-NH_2. First, the UiO-66-NH_2 was synthesized, then the TEMPO-alkoxyamine initiator (AA) was attached via the formation of an amide bond on the linker, and finally, the styrene-PEG derivative (poly(ethylene oxide) methyl-p-vinylbenzyl-ether (SPEGA)) polymers were grown on the surface. [Reprinted with permission from {I. Wagner, S. Spiegel, J. Brückel, M. Schwotzer, A. Welle, M. H. Stenzel, S. Bräse, S. Begum, M. Tsotsalas, "Biofunctionalization of Metal–Organic Framework Nanoparticles via Combined Nitroxide-Mediated Polymerization and Nitroxide Exchange Reaction", Macromol. Mater. Eng. 2023, p. 3, https://doi.org/10.1002/mame.202300048}. Copyright {2023} The Authors, Macromolecular Materials and Engineering published by Wiley-VCH GmbH].[141]

After the reaction, I proved the successful polymerization and conserved crystallinity with ATR-IR, ToF-SIMS, and XRD measurements. The results are represented in Figure 36. Figure 36 (A) illustrates the overall reaction scheme for the SPEGA-modification on the UiO-66-NH_2 surface.

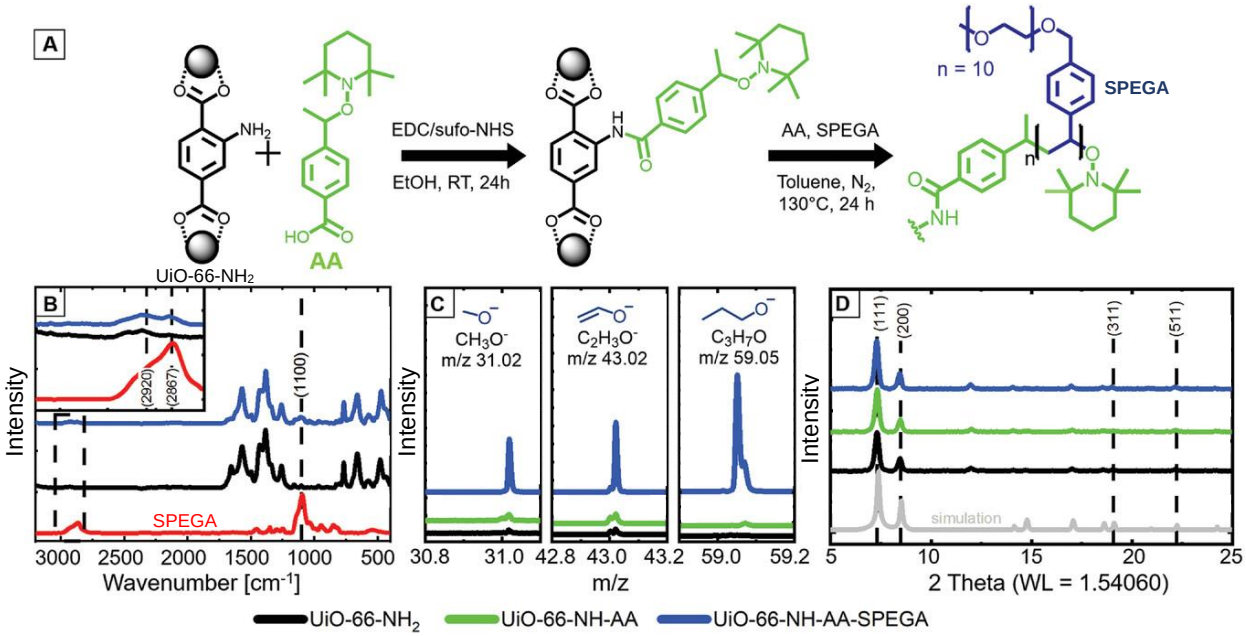

Figure 36: Overview of the reaction scheme for the nitroxide-mediated polymerization (NMP) with poly(ethylene oxide) methyl-p-vinylbenzyl-ether (SPEGA) on the surface of UiO-66-NH_2 nanoparticles (NPs) (A). Attenuated total reflection infrared spectroscopy (ATR-IR) (B) and time-of-flight secondary ion mass spectrometry (ToF-SIMS) normalized on the Zr-signal (C) measurements verify the successful polymerization on the NP surface. Meanwhile, X-ray diffraction (XRD) measurements prove that the crystallinity is preserved after the modification steps on the NP's surface (D). [Reprinted and adapted with permission from {I. Wagner, S. Spiegel, J. Brückel, M. Schwotzer, A. Welle, M. H. Stenzel, S. Bräse, S. Begum, M. Tsotsalas, "Biofunctionalization of Metal–Organic Framework Nanoparticles via Combined Nitroxide-Mediated Polymerization and Nitroxide Exchange Reaction", Macromol. Mater. Eng. 2023, p. 3, https://doi.org/10.1002/mame.202300048}. Copyright {2023} The Authors, Macromolecular Materials and Engineering published by Wiley VCH GmbH].[141]

For verifying the successful polymerization with IR, especially the bands, characteristics for the PEG polymer from 900 to 670 cm^{-1} and 2866 and 1100 cm^{-1} are essential. The band around 699 cm^{-1} results from the mono-substituted benzene vibrations from the monomer styrene-PEG, while the bands around 1100 and 2866 cm^{-1} are typical for the

O=C-O-C and the C-H stretching vibration. I found all of the respective PEG bands in the polymer reference (red) and the UiO-66-NH-AA-SPEGA NPs (blue), confirming the success of the polymerization on the surface (Figure 36 (B)).

ToF-SIMS measurements, normalized on the Zr-signal, further validate the successful polymerization. The usual PEG fragments can be discovered at 31.02 (CH_3O^-), 43.02 ($C_2H_3O^-$), and 59.05 (C_3H_7O) *m/z* (Figure 36 (C)). While they are not present in the pristine or the TEMPO-alkoxyamine-modified (AA-modified) MOF NPs, I found all those fragments in the SPEGA-modified ones.

The ATR-IR and ToF-SIMS results are reliable signs that the surface NMP reaction succeeded. Furthermore, XRD patterns confirmed the conserved crystallinity of the NPs even after polymerization. In Figure 36 (D), all the diffractograms show the characteristic UiO-66-NH_2 pattern, which all matches the simulation.

5.2.2 Increasing Dispersibility and Reducing the Protein Adsorption - Proofing the “Stealth Effect”

The SEM images in Figure 37 (A) show octahedral crystals with sizes around 150 nm. Homogenous dispersibility and avoiding aggregation are a central part of drug delivery. Therefore, I needed to increase the dispersibility of the MOF NPs in polar solvents. Consequently, I conducted a dispersibility test by adding pristine and SPEGA-modified NPs in ethanol (EtOH) and letting them stand for two days (Figure 37 (B)). While the pristine particles settled down in hours, the polymer-modified ones are well dispersed even after two days, indicating increased dispersibility. Reduced agglomeration tendency might correlate with the solvent’s polarity and the polymer composition. During our previous studies, we found a reduced agglomeration tendency for polystyrene(PS)-modified MOF NPs in toluene (Tol).[140] With this finding, I state that MOF NPs have different agglomeration tendencies depending on their surface composition. While the PS-modified NPs are more stable in nonpolar solvents, the SPEGA-modified ones show less aggregation in polar solvents, like EtOH (Figure 37 (B)). The PEG derivative on the surface helps the NPs maintain a well-dispersed, stable solution even after days.

Additionally, the DLS measurement shows small NP sizes in water, around 195 ± 63.7 nm for the pristine MOF and 191 ± 73.3 nm for the SPEGA-modified MOF NPs. In EtOH, the SPEGA-modified NPs show lower particle sizes, around 163 ± 55.0 nm, compared to the pristine NPs, with 177 ± 54.5 nm. In distinct from the pristine and the SPEGA-modified NPs, the AA-modified NPs in water show a wide range of particle distribution with two peaks (761 ± 359 and 236 ± 66.6 nm), indicating the aggregation of the particles.

Increasing the dispersibility and reducing the non-specific immune clearance for a biomedical application was our main goal for synthesizing PEG-modified MOF NPs. To enhance the blood circulation time and to increase the effectiveness of MOF NPs as drug delivery carriers, the adsorption of unspecific blood proteins has to be reduced ("stealth effect"). To test the influence of the surface modification in this matter, I tested the protein adsorption of human serum albumin (HSA), a common blood protein, on the pristine and polymer-modified MOF NPs. After 4 h at 37 °C, the particles were centrifuged, and the non-adsorbed HSA in the supernatant was quantified using a bicinchoninic acid (BCA) treatment. The pristine particles adsorbed 329 µg/mg, while the SPEGA-modified NPs adsorbed only 211 µg/mg (Figure 37 (D)). The verified lower unspecific protein adsorption in the measurement directly translates to an increased biological application scope for future drug delivery applications.

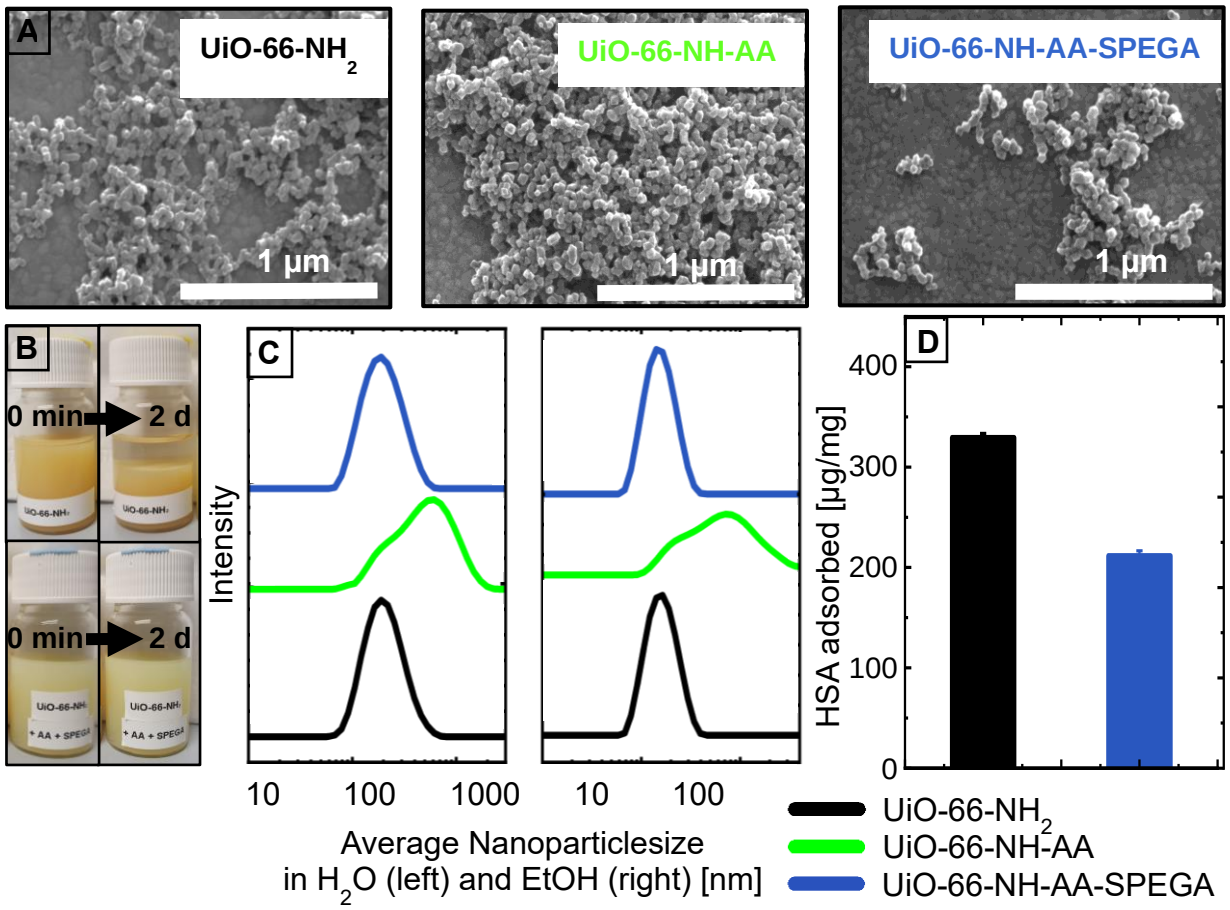

Figure 37: Scanning electron microscope (SEM) (A) and dynamic light scattering (DLS) (C) measurements to analyze the pristine, the TEMPO-alkoxyamine (AA)-modified, and the poly(ethylene oxide) methyl-p-vinylbenzyl-ether (SPEGA)-modified nanoparticles (NPs). The NP size is maintained after polymerization. A dispersibility experiment of the pristine and SPEGA-modified NPs in ethanol (EtOH) shows the increased dispersibility of the metal-organic framework (MOF)/polymer NPs (B). Furthermore, the decreased human serum albumin (HSA) protein adsorption on the MOF/polymer NPs is displayed (D). [Reprinted and adapted with permission from {I. Wagner, S. Spiegel, J. Brückel, M. Schwotzer, A. Welle, M. H. Stenzel, S. Bräse, S. Begum, M. Tsotsalas, "Biofunctionalization of Metal–Organic Framework Nanoparticles via Combined Nitroxide-Mediated Polymerization and Nitroxide Exchange Reaction", Macromol. Mater. Eng. 2023, p. 3, https://doi.org/10.1002/mame.202300048}. Copyright {2023} The Authors, Macromolecular Materials and Engineering published by Wiley VCH GmbH]. [141]

5.2.3 Nitroxide Exchange Reaction for the Attachment of Targeting Proteins to the MOF Surface

The ability to perform a nitroxide exchange reaction (NER) when using NMP is ideal for exchanging the end-group on the surface-attached polymers.[142] With this, exchanging the end-group with another functional group for biological purposes is further possible. We reported the NER of TEMPO on a PS-modified particle with the nitroxide 2-lambda1-oxidanyl-1,1,3,3-tetramethylisoindole, known as TMIIO, in 2022.[140] Now, for a biological application, I exchanged the TEMPO with a bioactive group (Figure 38). Binding on the surface is challenging, and a surface protein recognized by receptors on cells makes drug delivery more efficient and increases the effectiveness of a drug. A suitable sequence to model the exchange with a bioactive group in this context is the RGD sequence. First described in 1970, the sequence consists of an Arg-Gly-Asp peptide and connects to integrins (transmembrane receptors) on the cell surface.[143] Figure 38 shows the exchange procedure of SPEGA on the MOF surface with the RGD-nitroxide.

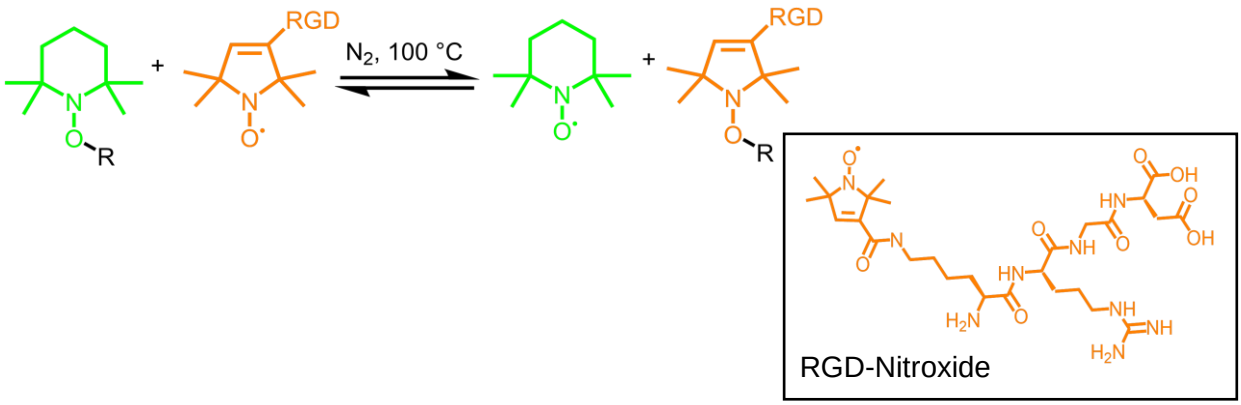

Figure 38: Nitroxide exchange reaction (NER) of the TEMPO-nitroxide (green) with the RGD-nitroxide (orange). The R-group connects the TEMPO- or the RGD-nitroxide to the polymer chain on the metal-organic framework (MOF) surface. The reaction is conducted under the exclusion of oxygen to avoid side reactions. [Figure based on {I. Wagner, S. Spiegel, J. Brückel, M. Schwotzer, A. Welle, M. H. Stenzel, S. Bräse, S. Begum, M. Tsotsalas, "Biofunctionalization of Metal–Organic Framework Nanoparticles via Combined Nitroxide-Mediated Polymerization and Nitroxide Exchange Reaction", Macromol. Mater. Eng. 2023, p. 5}].[141]

After the exchange of TEMPO and the RGD-nitroxide, ToF-SIMS measurements confirmed the success of the reaction (see Figure 39).

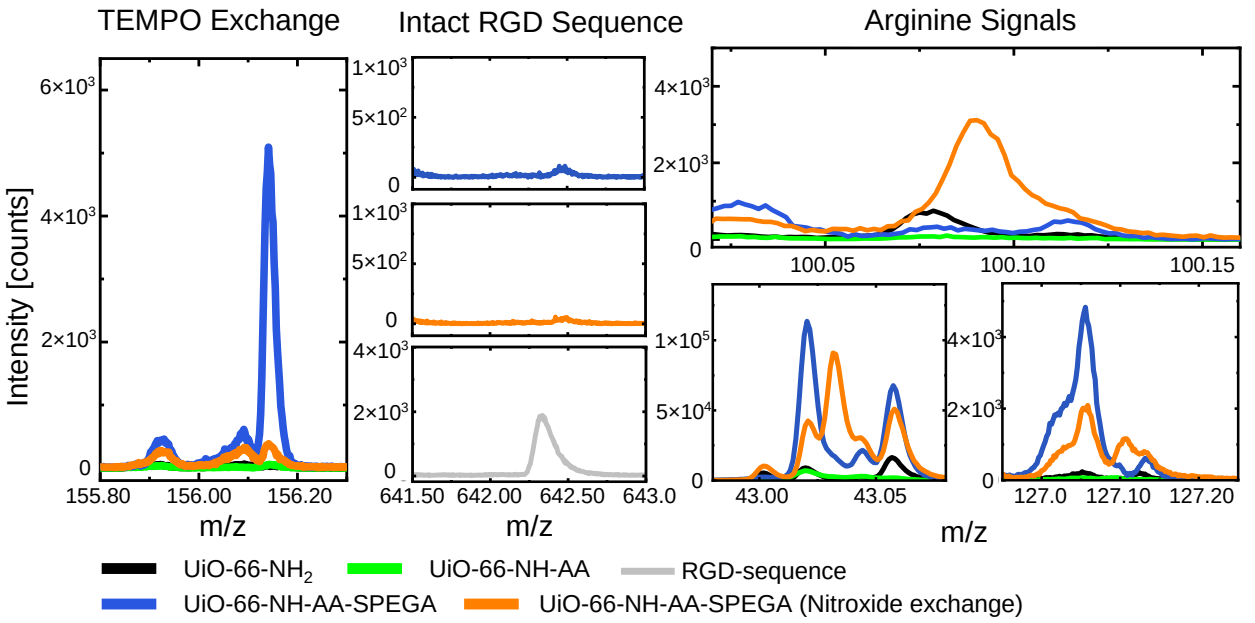

Figure 39: The time-of-flight secondary ion mass spectrometry (ToF-SIMS) measurement verifies the successful nitroxide exchange reaction (NER). The characteristic fragments for the arginine (in the RGD sequence), the TEMPO$^+$ group, and the intact RGD sequence are shown. [Reprinted and adapted with permission from {I. Wagner, S. Spiegel, J. Brückel, M. Schwotzer, A. Welle, M. H. Stenzel, S. Bräse, S. Begum, M. Tsotsalas, "Biofunctionalization of Metal–Organic Framework Nanoparticles via Combined Nitroxide-Mediated Polymerization and Nitroxide Exchange Reaction", Macromol. Mater. Eng. 2023, p. 3, https://doi.org/10.1002/mame.202300048}. Copyright {2023} The Authors, Macromolecular Materials and Engineering published by Wiley VCH GmbH].[141]

The TEMPO signal in Figure 39 confirms the intact TEMPO$^+$ group (*m/z* 156.14) in the SPEGA-modified NPs before the exchange (blue). In orange, the SPEGA-modified NPs do not show any TEMPO$^+$ signal, indicating the success of the end-group exchange. The characteristic arginine signals around *m/z* 43.03, 100.09, and 127.10 are found after the NER (orange) but not before (blue), confirming the successful exchange. In addition, the absence of the intact RGD sequence (*m/z* 642.36) in the SPEGA-modified NPs before (blue) and after (orange) the nitroxide exchange rules out the physisorption of the RGD molecule.

5.2.4 Testing the Suitability of MOF/Polymers for Drug Delivery

After successfully proving the attachment of a PEG molecule and the exchange of the end-group with a bioactive group on UiO-66-NH_2 NPs, I adapted the NMP method on the surface to three other hydrophilic polymers. Afterward, I tried to compare these synthesized MOF/polymer composites in their ability as drug carriers in cells. Therefore, I first synthesized the new MOF/polymer NPs and then tested them with Prof. Martina H. Stenzel during a research exchange in Sydney, Australia, in a model cell environment with MCF-7 breast cancer cells.

5.2.4.1 Applying the MOF/NMP Strategy on Other Monomers

After developing the new NMP grafting-from strategy and using it to graft SPEGA from the UiO-66-NH_2 NP surface (see Chapter 5.2.1), I investigated the same strategy with three other hydrophilic polymers (APEG, HEAA, and DMAA) and UiO-66-NH_2. Figure 40 shows a two-step polymerization reaction with the different monomers. Additionally, I used the NMP initiator MAMA-SG1 instead of the AA for the subsequent polymerization because it performs better with these polymers.

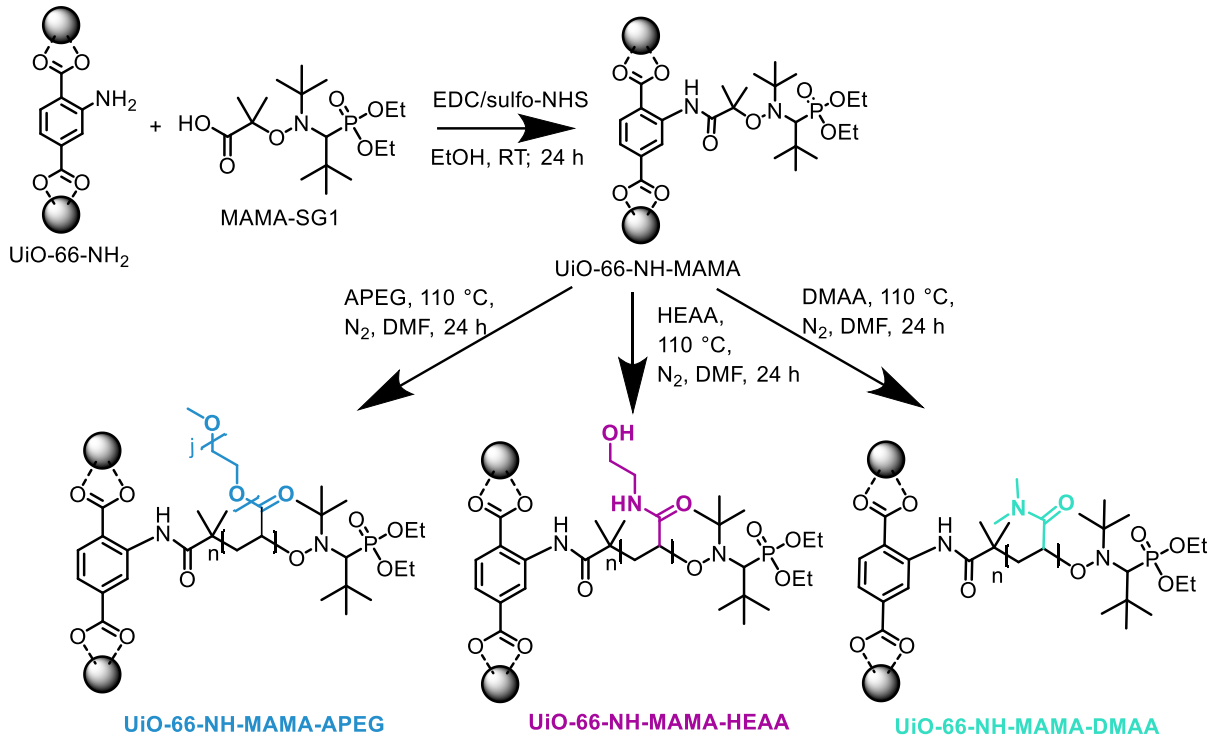

Figure 40: Reaction scheme for the two-step polymerization on the surface of UiO-66-NH_2 nanoparticles (NPs) with poly(ethylene glycol) methyl ether acrylate (APEG), N-hydroxyethylacrylamide (HEAA), and N,N-dimethylacrylamide (DMAA). For the polymerization with MAMA-SG1, the initiator was applied on the surface of UiO-66-NH_2 via an amide bond. In the next step, the polymerization was started in dimethylformamide (DMF) by heating the mixture to 110 °C in the presence of the respective monomers. In the scope of this thesis, the shown process is called two-step synthesis.

Applying hydrophilic polymers should improve the NPs' dispersibility while conserving the crystallinity and nano-size. To confirm the successful polymerization, I conducted ATR-IR and ToF-SIMS measurements. I measured the conserved crystallinity and nano-size with XRD and DLS afterward.

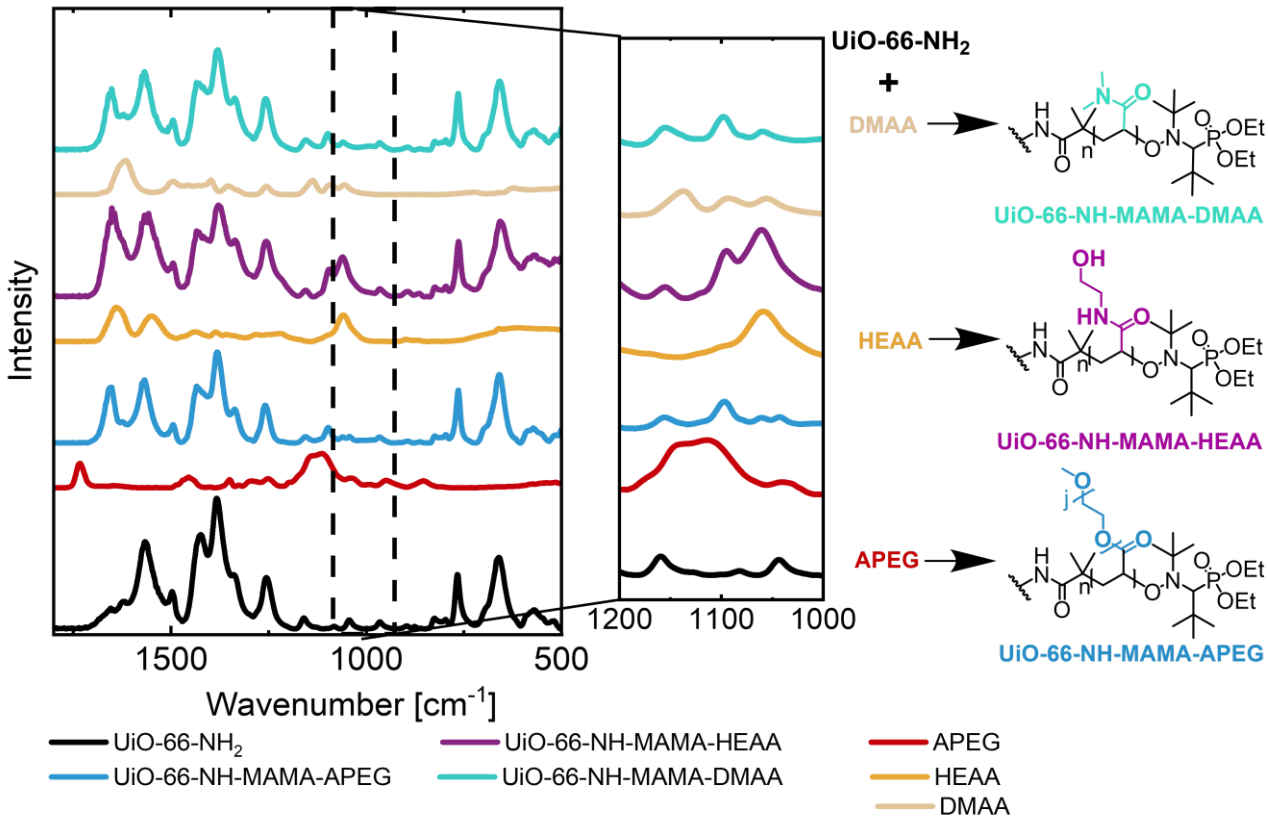

Figure 41: Attenuated total reflection infrared spectroscopy (ATR-IR) results verifying the successful two-step surface polymerization for the UiO-66-NH₂ nanoparticles (NPs) with poly(ethylene glycol) methyl ether acrylate (APEG), N-hydroxyethylacrylamide (HEAA), and N,N-dimethylacrylamide (DMAA). The polymerization reactions were conducted in two steps after a previous initiator (MAMA-SG1) attachment on the surface. The polymerization was carried out at 110 °C in dimethylformamide (DMF).

The ATR-IR, in Figure 41, shows the characteristic bands for UiO-66-NH₂ for all MOFs before and after the polymerization. The O=C-O-C has two vibrations around 1330-1050 cm^{-1}, visible for the APEG-modified MOF NPs (UiO-66-NH-MAMA-APEG).[102] HEAA and DMAA make it more challenging to identify characteristic bands. Although the C=O valence vibration of the amide bond (around 1690 cm^{-1}[102]) is very strong, a band of

the MOFs' basic framework lies in the same area and hides the amide bond. However, in both the reference HEAA and DMAA polymer and the polymer-modified UiO-66-NH-MAMA-HEAA and -DMAA NPs, the band characteristic for the C-N vibration is easily identifiable in the region around 1100 cm^{-1}[102] (see Figure 41 in turquoise and violet). This peak provides a preliminary assessment of the success of the HEAA and DMAA surface polymerization.

To give further eviction of the polymerization on the surface, I evaluated the MOF/polymer NPs with ToF-SIMS. Therefore, the characteristic mass fragments for APEG, HEAA, and DMAA give evidence of the successful synthesis. The fragments typical for APEG: *m/z* 31.02, 43.02, 45.03, and 87.04 (see Figure 42 on top) are all found in the UiO-66-NH-MAMA-APEG NPs (blue). At the same time, they are absent in the pristine UiO-66-NH_2 reference (black). Similarly, the HEAA fragments *m/z* 30.03, 60.04, and 88.04 are all present in the UiO-66-NH-MAMA-HEAA NPs sample (violet) (see Figure 42). The reference (black) shows no peaks in the same area. For DMAA, the characteristic peaks are around *m/z* 56.05 and 57.06. The so-modified UiO-66-NH-MAMA-DMAA NPs show these typical peaks, indicating the successful surface DMAA polymerization. Like the other MOF/polymers, I did not detect peaks for the reference in the same area (see Figure 42 at the bottom). Furthermore, the zirconium peak on the right in Figure 42 displays a decrease from the pristine UiO-66-NH_2 NPs to the polymer-modified ones. The reduced peak results from the polymer surface coating on the MOF NP shielding the zirconium in the framework. In conclusion, ATR-IR and ToF-SIMS prove the successful NMP of the new polymers APEG, HEAA, and DMAA on the UiO-66-NH_2 surface in a two-step synthesis approach with MAMA-SG1.

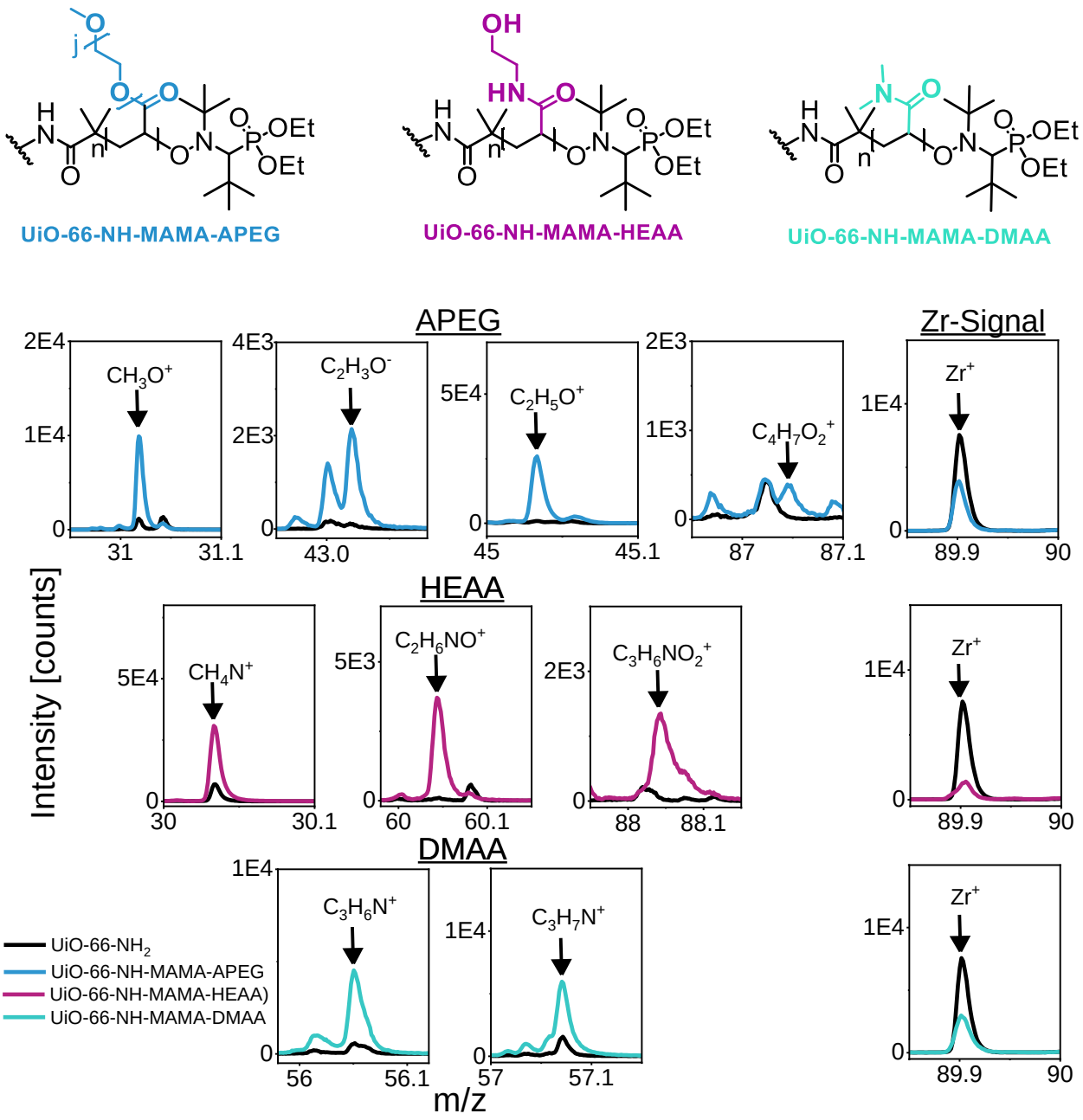

Figure 42: Time-of-flight secondary ion mass spectrometry (ToF-SIMS) results verifying the successful two-step surface polymerization for the UiO-66-NH_2 nanoparticles (NPs) with poly(ethylene glycol) methyl ether acrylate (APEG), N-hydroxyethylacrylamide (HEAA), and N,N-dimethylacrylamide (DMAA). The polymerization reactions were conducted in a two-step procedure after a previous initiator (MAMA-SG1) attachment on the surface. The polymerization was carried out at 110 °C in dimethylformamide (DMF).

When considering a future medication delivery method, the particles must maintain their NP size and crystallinity. Therefore, I conducted XRD and DLS experiments after the surface polymerization. In Figure 43 (left), the peaks of the XRD patterns of all samples show equivalent shapes and intensities. Therefore, I concluded a retention of the crystallinity. Regarding the sizes of the NPs, the DLS in Figure 43 (right) similarly demonstrates a maintained nano-size of approximately 180 to 200 nm. With this outcome, I prove that all of the used hydrophilic polymers respond effectively to the NMP adaptation method and that I was able to create crystalline, nano-sized UiO-66-NH_2 NPs coated with APEG, HEAA, or DMAA polymers.

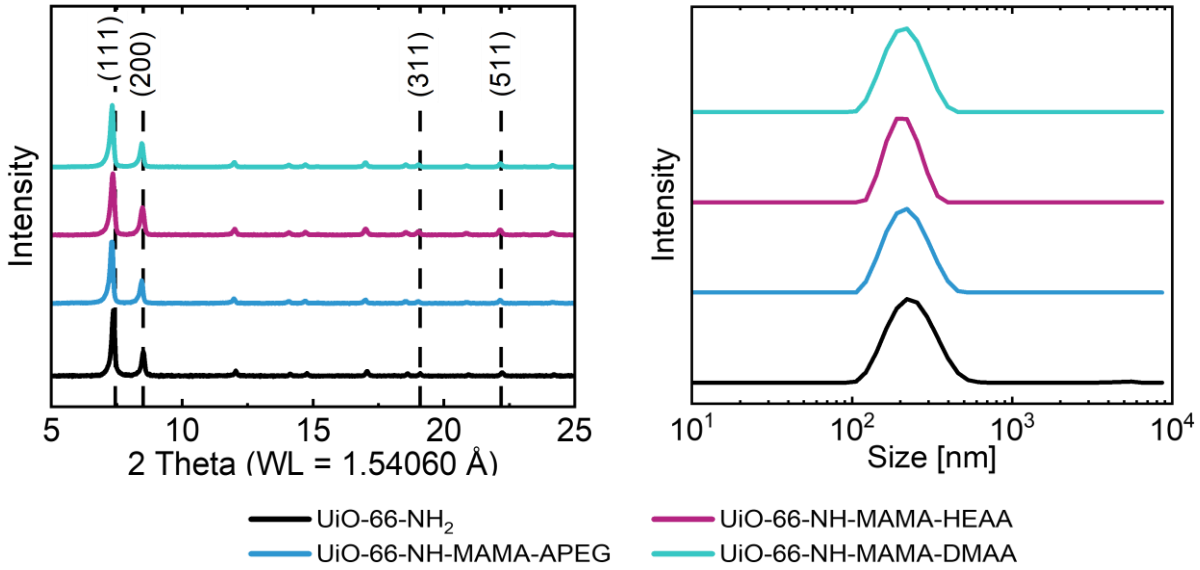

Figure 43: X-ray diffraction (XRD) (left) and dynamic light scattering (DLS) (right) measurements proving the conserved crystallinity and nano-size of the UiO-66-NH_2 nanoparticles (NPs) modified with poly(ethylene glycol) methyl ether acrylate (APEG), N-hydroxyethylacrylamide (HEAA), and N,N-dimethylacrylamide (DMAA) in a two-step synthesis procedure. The polymerization reactions were conducted in a two-step procedure after a previous initiator (MAMA-SG1) attachment on the surface. The polymerization was carried out at 110 °C in dimethylformamide (DMF).

The future potential of the NMP includes a customized strategy for creating a particular MOF/polymer composite material for drug delivery methods, which is highly intriguing. To test if I can use the presented NMP approach for customizing UiO-66-NH_2 NPs with different polymer chain lengths or synthesize different copolymer combinations on the

UiO-66-NH_2 surface, I started an experimental series with four different MOF/polymer or MOF/copolymer combinations using the same monomers (APEG, HEAA, and DMAA) as before.

The polymerization strategy followed the general procedure described previously, with one exception. Instead of first applying the initiator, then washing the NPs, and subsequently polymerizing on the surface, the NPs were mixed with the MAMA-SG1 initiator and the monomers and were heated together in a one-step reaction (see Chapter 8.2.4). The one-step synthesis should help facilitate and shorten the reaction procedure. The four reactions are named as follows: UiO-66-NH-MAMA-APEG/DMAA (6 h), UiO-66-NH-MAMA-HEAA (8 h), UiO-66-NH-MAMA-APEG/HEAA/DMA (23 h), and UiO-66-NH-MAMA-HEAA/DMAA (24 h). Figure 44 displays the reaction scheme with the different polymer and copolymer combinations. I want to point out that the representation of the copolymers is simplified and does not reflect any statement about the statistical distribution of the individual monomer blocks in the polymer.

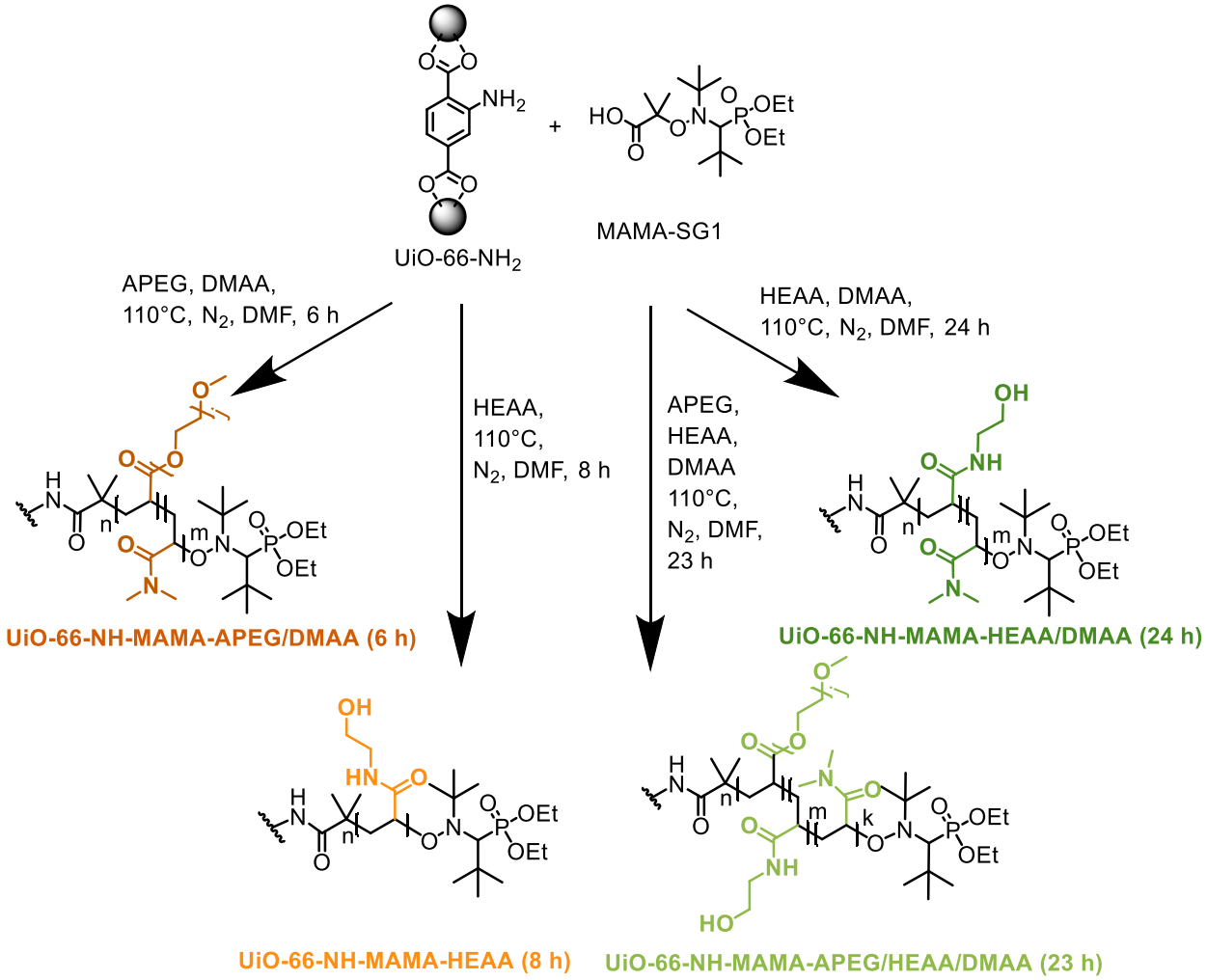

Figure 44: Reaction scheme for the one-step polymerization on the surface of UiO-66-NH_2 nanoparticles (NPs) with poly(ethylene glycol) methyl ether acrylate (APEG), N-hydroxyethylacrylamide (HEAA), and N,N-dimethylacrylamide (DMAA). For the polymerization, the initiator (MAMA-SG1), UiO-66-NH_2, and different amounts of the monomers (APEG, HEAA, and DMAA) were heated at 110 °C in dimethylformamide (DMF) for a specific amount of time. The shown process is called one-step synthesis. The copolymers shown here represent a simple visualization and do not reflect the actual distribution in the polymer.

The same IR bands characteristic of APEG, HEAA, and DMAA described in the previous section for the two-step polymerization process are required for the surface polymer combinations in the one-step process. As previously found, all the characteristic IR for either the O=C-O-C or the C-N vibration in the polymers in the region 1200 to 1000 cm^{-1}[102] are characteristic for APEG, HEAA, and DMAA. In contrast to the

pure UiO-66-NH_2 NPs (black), which do not exhibit any peaks in the desired area, the various MOF/polymers (see Figure 45) all show distinctive peaks in the same area. The ATR-IR result first indicates the successful polymerization on the UiO-66-NH_2 surface with APEG, HEAA, and DMAA.

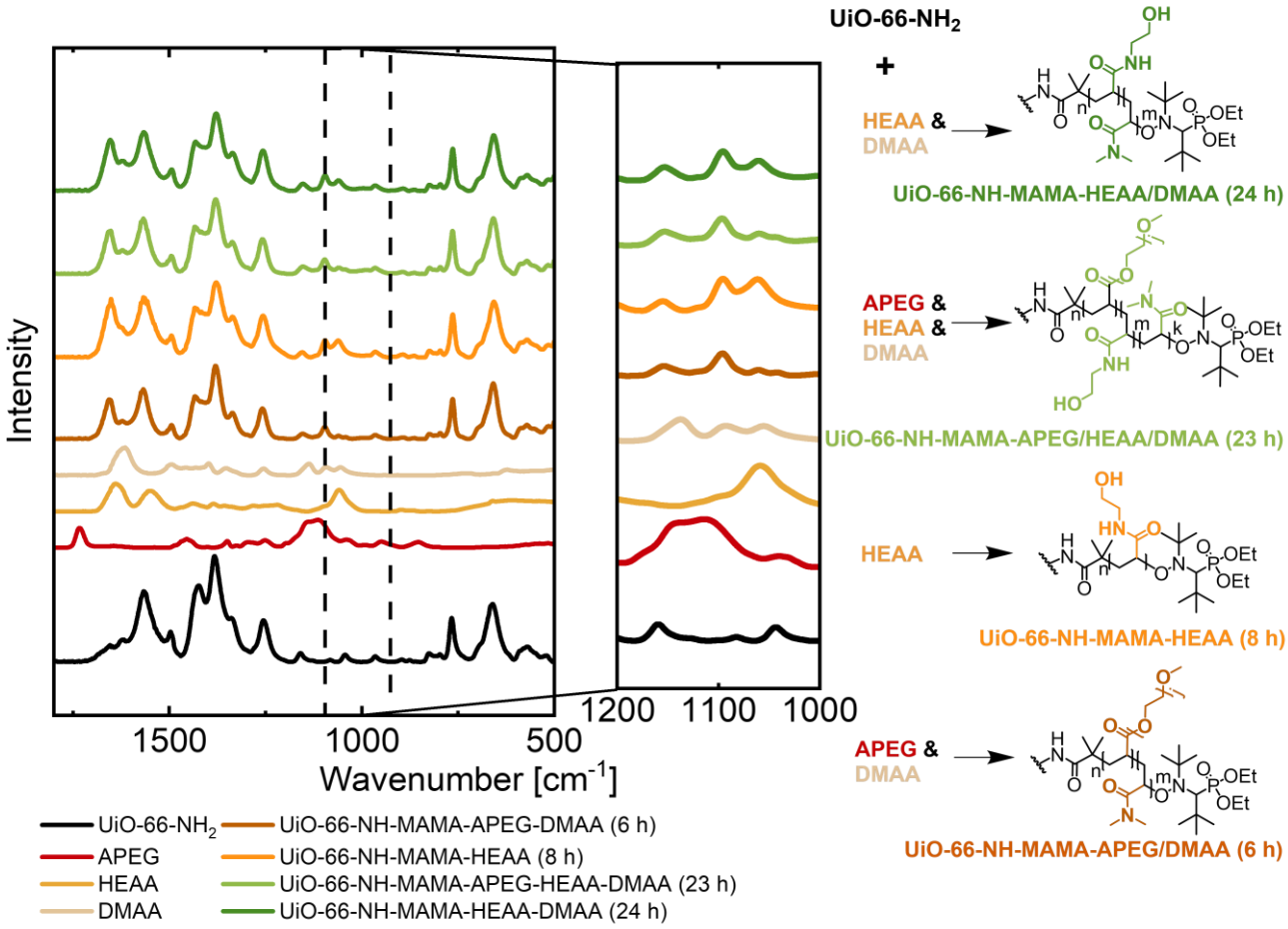

Figure 45: Attenuated total reflection infrared spectroscopy (ATR-IR) verifying the successful surface polymerization of the UiO-66-NH_2 nanoparticles (NPs) with different polymer chain lengths and/or copolymer combinations of poly(ethylene glycol) methyl ether acrylate (APEG), N-hydroxyethylacrylamide (HEAA), and N,N-dimethylacrylamide (DMAA). The polymerization reactions were conducted in a one-step procedure after mixing MAMA-SG1, UiO-66-NH_2 NPs, and the respective monomers (APEG, HEAA, and DMAA) and heating them to 110 °C in dimethylformamide (DMF).

To give further evidence of the effective polymerization on the surface, I evaluated the MOF/polymer NPs with ToF-SIMS. Therefore, the characteristic mass fragments for APEG, HEAA, and DMAA provide proof of the successful synthesis.

The fragments typical for APEG: *m/z* 31.02, 43.02, 45.03, and 87.04 (see Figure 42 on top) are all found in the UiO-66-NH_2 NPs modified with copolymers containing APEG: UiO-66-NH-MAMA-APEG/DMAA (6h) (brown) and UiO-66-NH-MAMA-APEG/HEAA/DMAA (23h) (light green). The pure UiO-66-NH_2 NPs (black) show no signals in the same area.

HEAA is present in three MOF/polymers: UiO-66-NH-MAMA-HEAA (8h) (orange), UiO-66-NH-MAMA-APEG/HEAA/DMAA (8h) (light green), and UiO-66-NH-MAMA-HEAA/DMAA (24 h) (dark green). The typical peaks arise around *m/z* 30.03, 60.04, and 88.04. While all of the HEAA-modified UiO-66-NH_2 NPs show the characteristic peaks, the pure UiO-66-NH_2 NPs (black) show no peaks in the same area (see Figure 46).

During the copolymerization process, one or more monomer-building components compete to be incorporated into the polymer chain. This phenomenon results in different incorporation rates in the chain and, therefore, different relative intensities in the ToF-SIMS spectra. In comparison, during the reaction of the UiO-66-NH-MAMA-HEAA (8h) NP (orange), only one monomer, the HEAA, is present. Since no competing reaction occurs, the UiO-66-NH-MAMA-HEAA (8h) NPs show the highest HEAA peaks in the ToF-SIMs measurement. For all other MOF NPs modified with HEAA, the competitive reaction of the other monomer building blocks leads to a lower HEAA concentration in the final copolymer.

DMAA has the characteristic bands around *m/z* 56.05 and 57.06. While the pure UiO-66-NH_2 NPs (black) show no peaks in the desired area, the UiO-66-NH-MAMA-APEG/DMAA (6 h) NPs (brown) show these characteristic bands, proving the successful polymerization with DMAA. All other MOF/polymers (UiO-66-NH-MAMA-APEG/HEAA/DMAA (23 h) and UiO-66-NH-MAMA-HEAA/DMAA (24 h)), which contain DMAA, also contain HEAA. Since the two polymers have similar chemical structures, they also share the fragments $C_2H_6N^+$ and $C_2H_7N^+$ at *m/z* 56.05 and 57.06, which I used previously for the two-step synthesis to confirm the DMAA grafting (see Figure 42 on the

bottom). This revelation makes it clear that the peaks in Figure 46 result from DMAA and HEAA. DMAA can not be distinguished from HEAA, and ATR-IR is the only proof of the successful DMAA polymerization on the surface for the UiO-66-NH-MAMA-APEG/HEAA/DMAA (23 h) and UiO-66-NH-MAMA-HEAA/DMAA (24 h) NPs.

Additionally, proof of the successful surface polymerization on the UiO-66-NH_2 NPs is given with the zirconium signal at *m/z* 89.9. Figure 46 shows the zirconium peak on the right for all polymer-modified UiO-66-NH_2 NPs. The reduced zirconium peak visible for all polymer-modified NPs, compared to the reference (black), results from the applied polymers. The polymer surface coating shields the zirconium signal, and the peak reduction proves the successful surface modification.

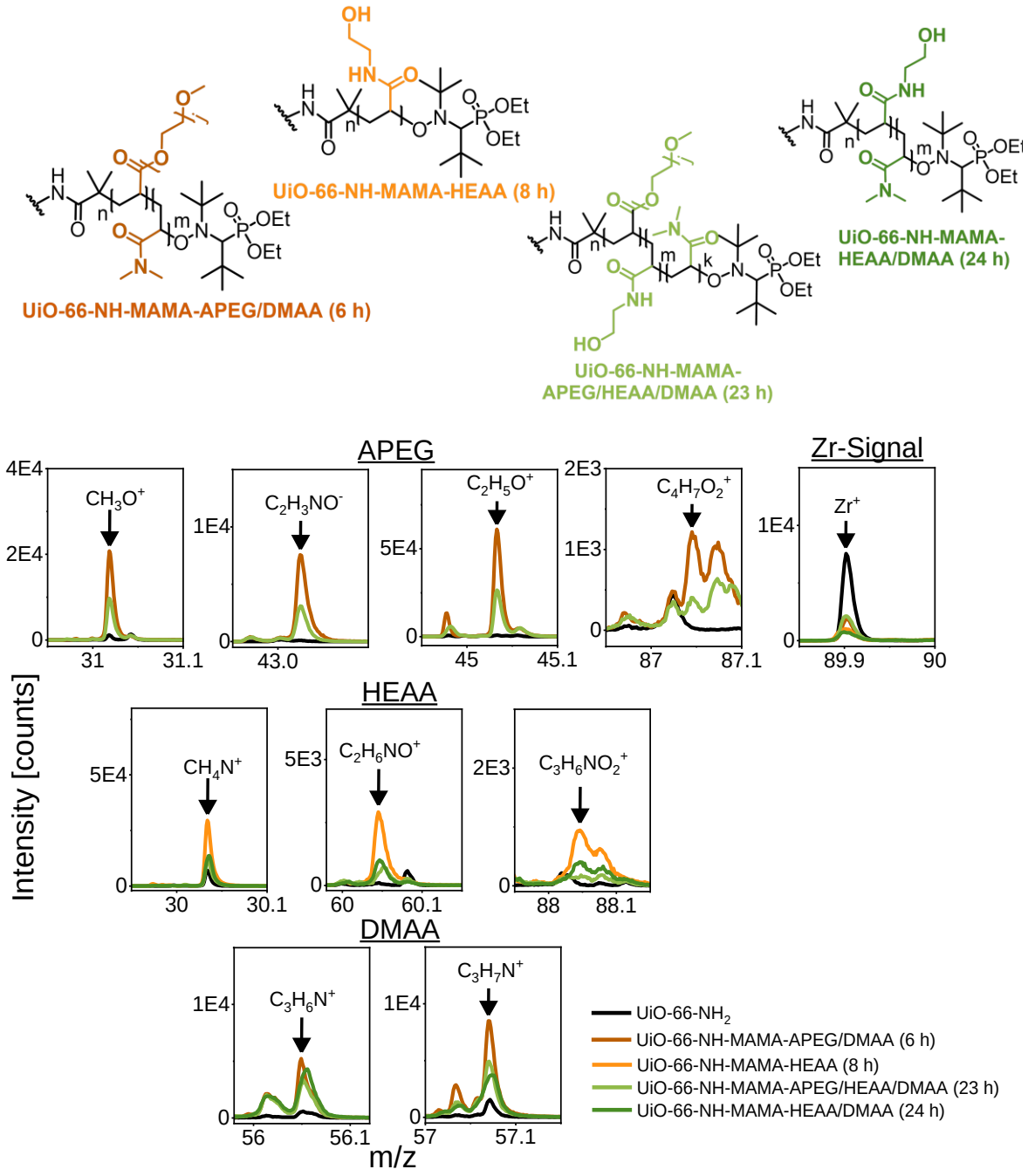

Figure 46: Time-of-flight secondary ion mass spectrometry (ToF-SIMS) results verifying the successful one-step surface modification for the UiO-66-NH_2 nanoparticles (NPs) modified with poly(ethylene glycol) methyl ether acrylate (APEG), N-hydroxyethylacrylamide (HEAA), and N,N-dimethylacrylamide (DMAA) polymers with different chain lengths or copolymers on their surface. The polymerization reactions were conducted in a one-step procedure after mixing MAMA-SG1, UiO-66-NH_2 NPs, and the respective monomers (APEG, HEAA, and DMAA) and heating them to 110 °C in dimethylformamide (DMF).

In summary, the peaks in the desired area for the polymers in ATR-IR (see Figure 45) and the ToF-SIMS characteristic fragments for the different polymers (APEG, HEAA, and DMAA) (see Figure 46) prove the successful surface modification of MOF NPs by NMP for copolymers or homopolymers of different chain length.

Producing crystalline-stable NPs is important for applications in biology and medicine. The NPs used for drug delivery need to be stable to load drugs and transport them into the body. Therefore, I measured the crystallinity and nano-size of the particles after the polymer modification. The XRD peak patterns of the polymer-modified UiO-66-NH_2 NPs in Figure 47 (left) show the same peak position as the pristine UiO-66-NH_2 NPs. This result confirms the conserved crystallinity of the MOF/polymers synthesized with the one-step procedure. Figure 47 (right) shows the DLS measurement of the NPs before and after the polymer modification. The NPs maintain their size around 180 to 200 nm after polymerization.

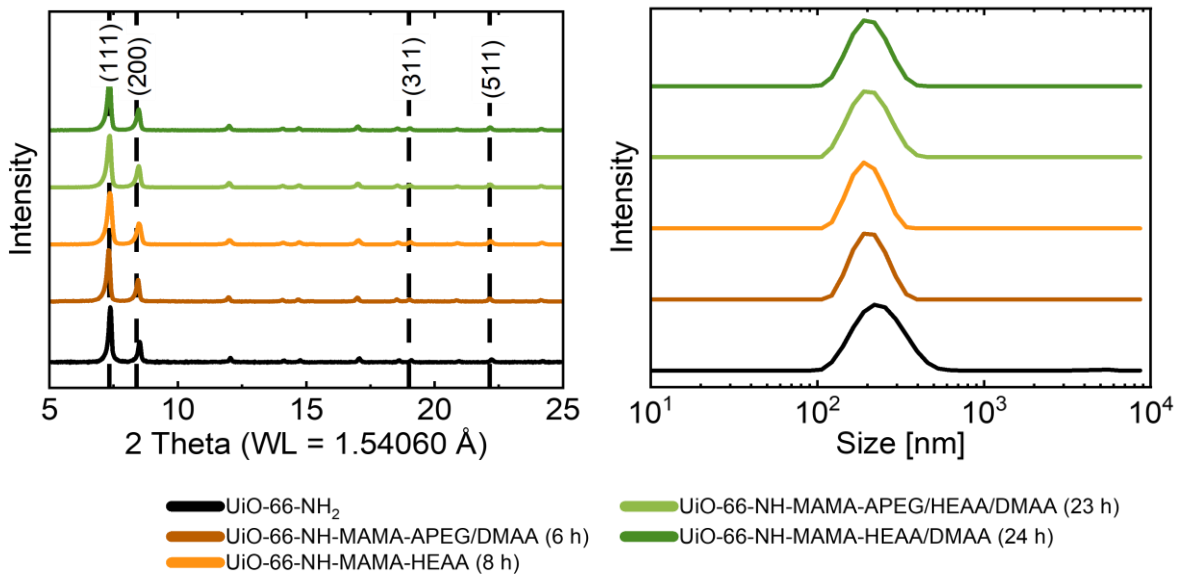

Figure 47: X-ray diffraction (XRD) (left) and dynamic light scattering (DLS) (right) confirm the conserved crystallinity and maintained nano-size of the one-step synthesized metal-organic framework (MOF)/polymer nanoparticles (NPs). The polymerization reactions were conducted in one-step procedures after mixing MAMA-SG1, UiO-66-NH_2 NPs, and the respective monomers (poly(ethylene glycol) methyl ether acrylate (APEG), N-hydroxyethylacrylamide (HEAA), and/or N,N-dimethylacrylamide (DMAA)) and heating them to 110 °C in dimethylformamide (DMF).

A main advantage of NMP and all CRP is the low molar mass dispersity ($Đ_M$) from 1.1 to 1.3 and the controlled chain length.[124] It is essential to control the chain length on the surface, especially for a later application in biology and medicine or the reproduction of polymer-modified MOF NPs. With CRP, it is possible to have a narrow chain length distribution and the possibility of good reproduction of the MOF/polymer composites. I measured the successful polymerization and $Đ_M$ with gel permeation chromatography (GPC) for the MOF/polymers (one-step and two-step procedures) (see Figure 48).

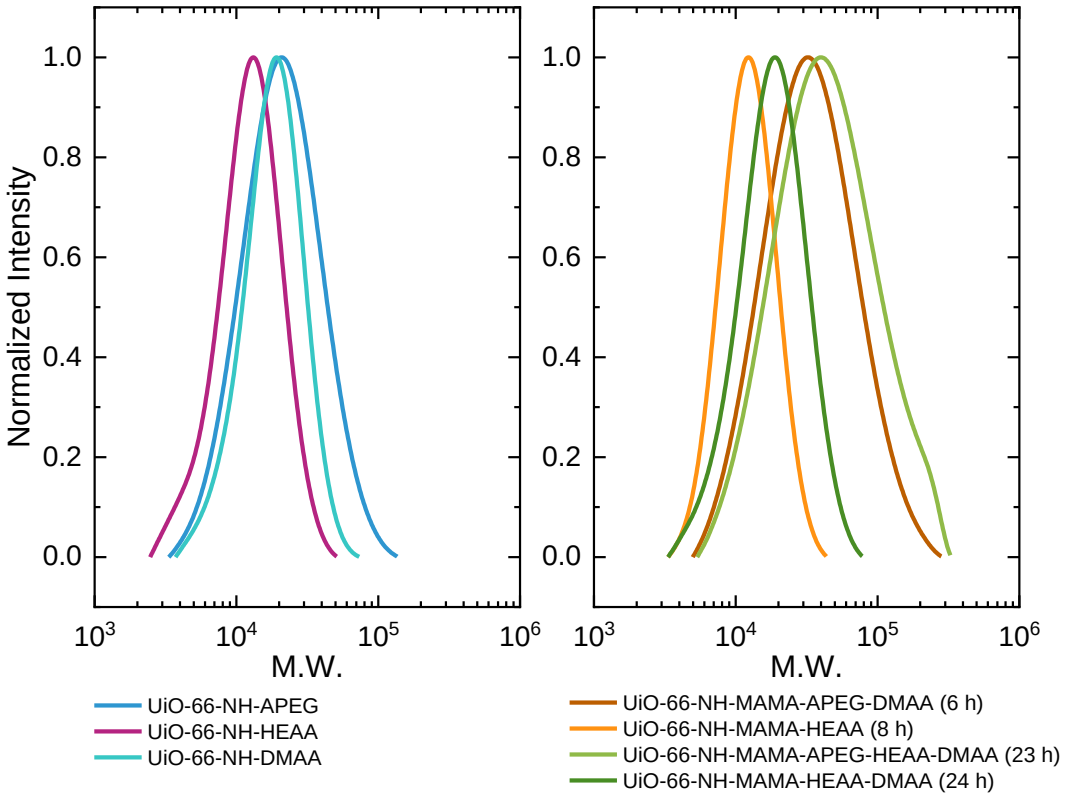

Figure 48: Gel permeation chromatography (GPC) measurement of the polymers grown on the UiO-66-NH_2 nanoparticles (NP) (one- or two-step process). The GPC measurement shows the molecular mass distribution of the individual polymer chains formed in situ in the reaction solution of the polymer-modified metal-organic framework (MOF) NPs and provides information about the molar mass dispersity ($Đ_M$). The GPC experiment was conducted in H_2O+0.5 g/L NaN_3 and a mixture of 40 % acetonitrile (MeCN) and 0.1 % trifluoroacetic acid (TFA).

To encourage polymer formation on the particles, I introduced free MAMA-SG1 during the reaction process in both the one- and two-step reactions. In the solution, this addition

also causes free polymer chains to form. Due to the utilized CRP method, the resulting polymer chains have the same chain length as the polymers on the UiO-66-NH_2 surface.[140] The clear separation of the polymer from the MOF necessitates the decomposition of a substantial sample volume. Even then, the substracted polymer amount from the surface is often too small to be analyzed. Therefore, I used the free polymer chains for the GPC research.

Figure 48 shows the narrow distribution for UiO-66-NH-MAMA-HEAA, -DMAA, -HEAA (8 h), and -HEAA/DMAA (24 h) with $Đ_M$ values from 1.2 to 1.3, proving a controlled polymerization.

The samples UiO-66-NH-MAMA-APEG, UiO-66-NH-MAMA-APEG/DMAA (6 h), and UiO-66-NH-MAMA-APEG/HEAA/DMAA (23 h) show $Đ_M$ values close to 2, similar to the uncontrolled polymerization, which is typical for free radical polymerization.[124]. This performance could result from the high monomer amount in all three mixtures. For the polymerization, APEG and DMAA were present with amounts between 122 and 200 equiv., respectively. The high monomer amount in the reaction solution could lead to an uncontrolled initiation at high temperatures, uncontrolled chain growth, and an undesired wide distribution. Since previous studies have found equal chain lengths in the solution and on the surface of the MOF/polymer NPs in the same reaction solution,[140] I have to assume the same high distribution for the polymer chains on the particle.

The GPC results demonstrate the effective NMP surface modification strategy for low monomer concentrations. At the same time, they also show the limits of the polymers produced and provide strategies for future samples to select the right amount of monomer for a polymerization reaction in NMP. The polymer modification offers great potential for the continued process of modifying MOFs for drug delivery approaches.

Summarized NMP enables surface modification with different hydrophilic polymers of varying chain lengths and copolymers. The crystallinity and nano-size are maintained, and the NPs can be easily applied and tested for drug uptake and their delivery ability in the next chapter.

5.2.4.2 Drug Loading Efficiency in MOF/Polymer Nanoparticles

Taking up drugs is especially important for MOF NPs since the delivery ability strongly depends on the uptake. To try the uptake of an anticancer drug, I decided to monitor the curcumin uptake into UiO-66-NH_2 NPs. Curcumin can target transcription factors, growth factors, cytokinetics, enzymes, and cell genes, influencing their proliferation and apoptosis.[144] Medical and biological studies even suggest the application of curcumin as an anticancer drug.[145,146] It is highly useful in drug delivery for cancer cells and potentially prevents and treats cancer.[145,146] To overcome problems like poor water solubility and low bioavailability, nano-sized delivery methods like NPs have been demonstrated.[145] Especially here, MOF/polymer NPs can help incorporate curcumin, thereby enhancing its bioavailability. An initial experiment about incorporating curcumin into pristine UiO-66-NH_2 was conducted to confirm the suitability of the MOF material for the uptake.

Previous studies have already shown the curcumin uptake into UiO-66-NH_2 particles using chloroform ($CHCl_3$).[147] Curcumin has a good solubility in $CHCl_3$. In cyclohexane (Cyc), however, it is poorly soluble. However, good dispersibility can be a disadvantage for MOF loading, as it is possible that the curcumin stays in solution rather than diffusing in the MOF. To test this solvent influence, I prepared three curcumin solutions in $CHCl_3$, $CHCl_3$/Cyc (2:1, v:v), and $CHCl_3$/Cyc (1:1, v:v) and measured the drug uptake in pristine UiO-66-NH_2 with ultraviolet and visible spectroscopy (UV-Vis) over 180 h (see Chapter 8.2.7). Figure 49 shows the kinetic curcumin uptake measurement.

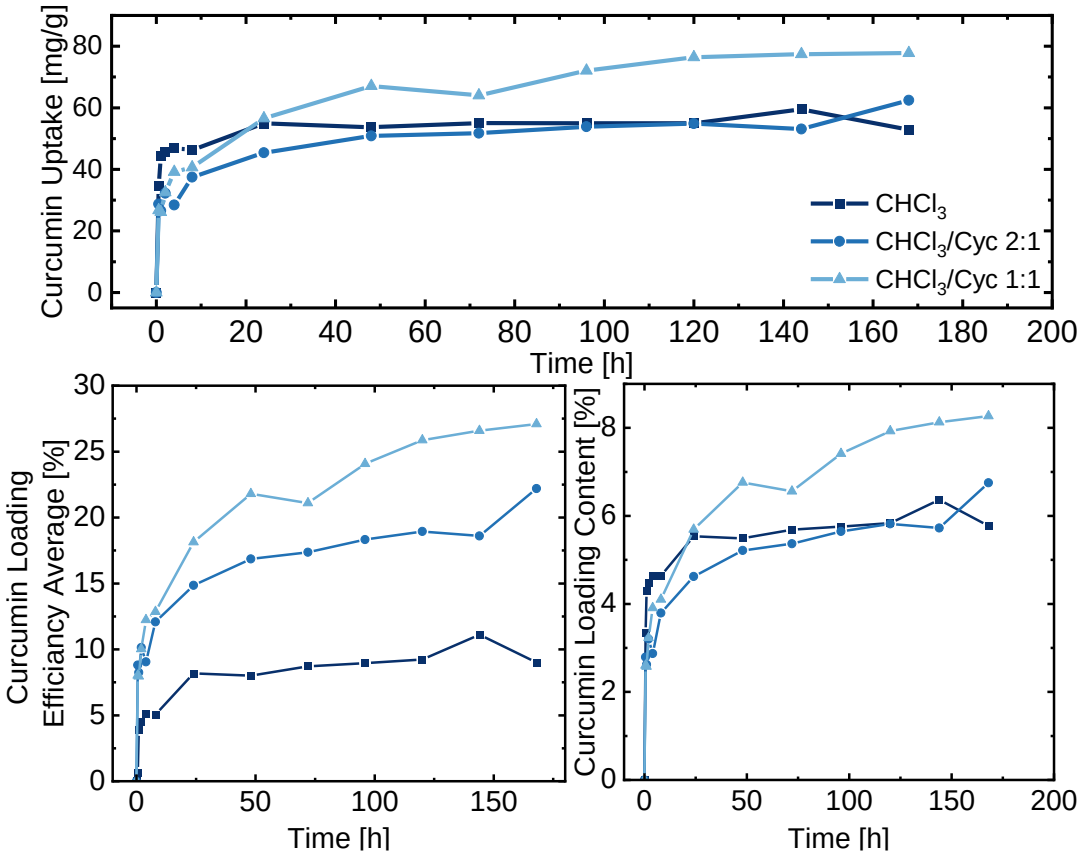

Figure 49: Kinetic study of the curcumin uptake into pristine UiO-66-NH_2 nanoparticles (NPs) over 180 h. Different solvent combinations: chloroform ($CHCl_3$), $CHCl_3$/cyclohexane (Cyc) (2:1, v:v), and $CHCl_3$/Cyc (1:1, v:v) are displayed to determine the highest uptake and correlate different solvent environments with the uptaken drug amount. After 180 h, the NPs in $CHCl_3$/Cyc (1:1, v:v) have the highest uptake. The reaction time is displayed at the bottom, and the concentration is given in mg curcumin per g metal-organic framework (MOF).

Over time, it became clear that the combination of $CHCl_3$ and Cyc (1:1, v:v) led to the most drug uptake after 180 h. Although the uptake was also present in the other solvent combination, there is a clear trend for an increase in drug uptake with an increase in the Cyc concentration (see Figure 49). Unfortunately, I was not able to try higher concentrations of Cyc as the curcumin became insoluble at higher levels of Cyc. The results presented in Figure 49 clearly show that curcumin, which is more soluble in polar solvents, prefers to enter the MOF pores when the solvent's nonpolar component

increases. As a result, the (1:1, v:v) $CHCl_3$/Cyc combination leads to a high absorption of 77.8 mg/g. Compared to that, pure $CHCl_3$ only reaches 52.8 mg/g.

The pristine UiO-66-NH_2 particles proved to be reliable for drug uptake. In a similar experiment, I evaluated the curcumin uptake for the MOF/polymer NPs. Figure 50 shows the curcumin uptake in the MOF/polymer NPs in $CHCl_3$/Cyc (1:1, v:v) after 24 h.

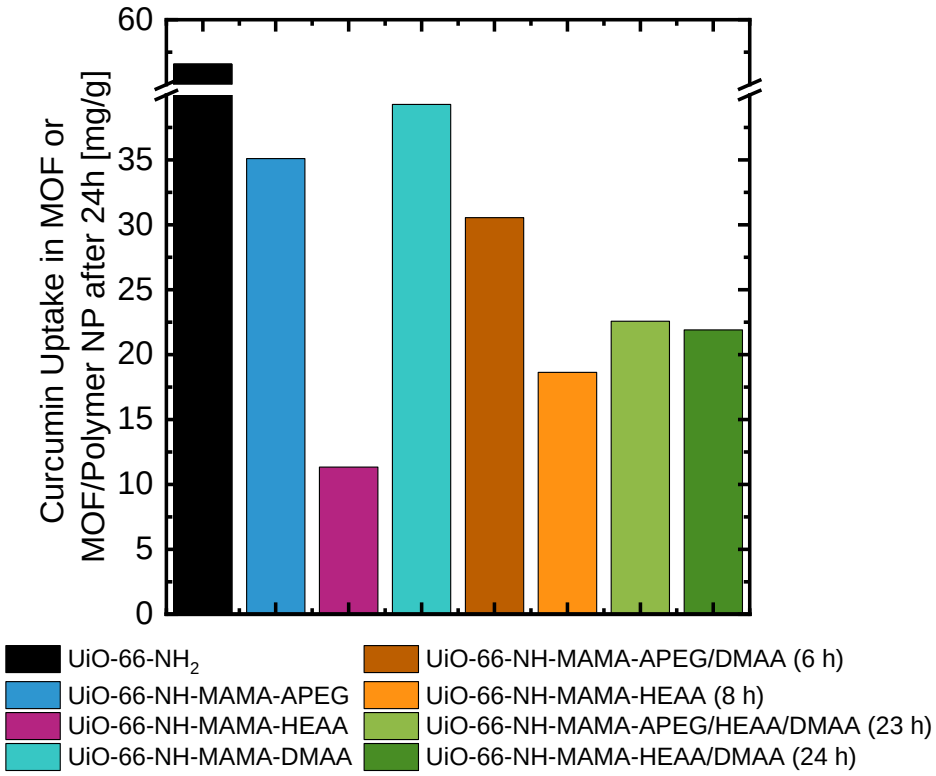

Figure 50: Measuring the curcumin uptake for the different polymer-modified UiO-66-NH_2 nanoparticles (NPs) after 24 h. All NPs show an uptake after 24 h. The curcumin was previously dissolved in chloroform/cyclohexane ($CHCl_3$/Cyc) (1:1, v:v). The time is displayed at the bottom, and the concentration is given in mg curcumin per g metal-organic framework (MOF)/polymer.

The curcumin (dissolved in $CHCl_3$/Cyc (1:1, v:v)) uptake in the different polymer-modified samples was measured after 24 h, and the results were compared (see Figure 50). After 24 h, all polymer-modified NPs show a curcumin uptake. Notably, the highest curcumin uptake for the polymer-modified UiO-66-NH_2 NPs in UiO-66-NH-MAMA-DMAA NPs (around 39.0 mg/g) is lower compared to the pristine UiO-66-NH_2 NPs (around 77.8 mg/g) in $CHCl_3$/Cyc (1:1, v:v) (see Figure 49). A possible explanation is that the formerly

well-dispersed and untangled hydrophilic polymers may collapse in a nonpolar solvent, leading to an aggregation of the NPs. This aggregation would clog the pores and prevent the curcumin from diffusing into them.

I reported the same solvent behavior already with the SPEGA-modified NPs in Chapter 5.2.2. I demonstrated in this chapter that the SPEGA-modified NPs are better dispersed in polar solvents. The same principle applies here, and the polymer-modified UiO-66-NH_2 NPs agglomerate during the uptaking process in a polar/nonpolar solvent mixture like $CHCl_3$/Cyc (1:1, v:v). This phenomenon is especially evident for the UiO-66-NH-HEAA NPs. These HEAA-modified NPs only load 12.0 mg/g of curcumin into their pores. HEAA is the most hydrophilic polymer and tends to agglomerate more in the selected solvent than the other polymers.

The drug loading experiment with the polymer-modified MOF NPs shows that the solvent-to-polymer compatibility influences the drug absorption amount. This phenomenon can be significant for designing a nanocarrier for a specific drug delivery purpose, and the drug-loading solvent has to be appropriately chosen. Furthermore, additional studies still have to be conducted to verify the successful uptake in the pores further and exclude the mere physisorption on the surface.

5.2.4.3 Cell Viability Studies of MOF/Polymers on Breast Cancer Cells

MOF NPs have proven particularly useful for drug delivery. Applying hydrophilic polymers reduces the absorption of unspecific proteins on the surface and increases the dispersibility in aqueous solutions to make them even more biocompatible. Crucial for a later application in biology and medicine is the compatibility of the produced MOF/polymer materials with cells.

Cancer cells are frequently used in research to model the cell environment and to identify new treatments against cancer. MCF-7 breast cancer cells were named after the Michigan Cancer Foundation and are a well-studied cancer cell line that greatly impacted breast cancer research.[148] The cell line is well characterized and can help to find suitable treatment protocols.[149]

Cancer cells normally grow fast and are ideal for modeling the cell environment in the body. A perfect drug delivery system would only destroy the cancer cells but not damage other cells. Therefore, the nanocarrier must not be cytotoxic to body cells. To model the cell environment in the body and mimic the influence of the MOF NPs on cells, I incubated MCF-7 breast cancer cells with the pore-free polymer modified and pristine UiO-66-NH_2 NPs for 72 h. Afterward, I measured the cell viability using the sulforhodamine B (SRB) assay and UV-Vis.

Figure 51 shows the results of the cell viability study. While the pristine UiO-66-NH_2 NPs are very cytotoxic even in low concentrations, around 0.10 mg/ml, the polymer-modified UiO-66-NH_2 NPs show lower cytotoxicity until 1.00 mg/ml. Significantly, the UiO-66-NH-MAMA-HEAA NPs show the lowest cytotoxicity compared to the pristine particles. Regarding this result, I state that the polymer-modified MOF NPs are better suited for drug delivery into the body than the pristine ones, given their reduced cytotoxicity to cells.

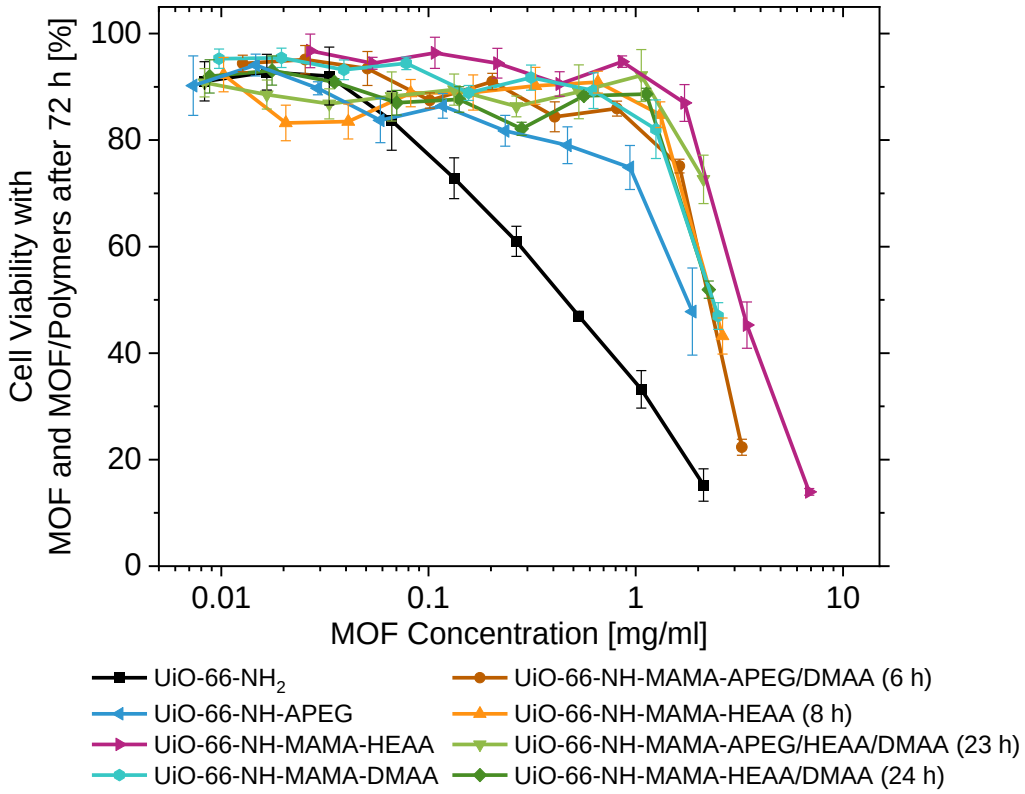

Figure 51: Experimental method for determining the cytotoxicity of drug-free polymer-modified and pristine UiO-66-NH_2 nanoparticles (NPs) for cells. MCF-7 breast cancer cells are used to model the cell environment in the body and provide information on the compatibility of the metal-organic framework (MOF) NPs used with body cells and in the medium. The cells were previously cultured at 37 °C, and the sulforhodamine B (SRB) cytotoxicity assay was used for the analysis.

5.3 Summary

In this chapter, I successfully used NMP on the surface of UiO-66-NH_2 NPs to grow a SPEGA polymer chain. IR and ToF-SIMS verified the successful polymerization, and XRD proved the conserved crystallinity after each surface modification step. SEM images showed the maintained NP sizes around 150 nm. The PEG application on the surface enhanced the dispersibility of the particles, and I could prove that the SPEGA-modified NPs were nicely distributed after two days in EtOH, while the pristine particles settled down quickly. DLS furthermore showed the NP sizes of the polymer-modified and the pristine MOF NPs around 191 ± 73.3 nm and 195 ± 63.7 in water. In EtOH, the polymer-modified NPs showed a lower particle size with 163 ± 55.0 nm compared to 177 ± 54.5 nm for the pristine NPs. On the contrary, the AA-modified NPs showed a high agglomeration and particle sizes in water with two peaks around 761 ± 359 and 236 ± 66.6 nm.

Especially interesting for drug delivery is the reduced “stealth effect” by applying a hydrophilic PEG derivative on the NP surface. With the absorption experiment of HSA on the polymer-modified and the pristine NPs, I could prove a reduced protein absorption by 39 % by applying PEG on the surface.

With NER, I successfully exchanged the TEMPO end-group on the SPEGA-modified UiO-66-NH_2 NPs with a bioactive RGD-nitroxide. The possible modification with a bioactive sequence enables the polymer-modified NPs to directly bind on surface proteins of cells, making a targeted drug delivery more feasible. ToF-SIMS verified the successful exchange with the occurrence of the typical arginine fragments (*m/z* 43.03, 100.09, and 127.10) after the NER. The same signals were absent before. Furthermore, the exchanged $TEMPO^+$ fragment (*m/z* 156.14) was absent after the reaction, verifying the complete conversion during the exchange reaction. Additionally, I excluded the simple physisorption of the RGD sequence on the UiO-66-NH_2 surface since the intact RGD sequence (*m/z* 642.36) fragment was not found after the exchange reaction.

With this newly developed strategy for the NMP on MOF NPs, I tried to transfer it to three other hydrophilic polymers: APEG, HEAA, and DMAA. In the first approach, I synthesized homologous polymers of all three monomers (APEG, HEAA, and DMAA) in a two-step

reaction process after applying the MAMA-SG1 initiator on the UiO-66-NH_2 surface. ATR-IR and ToF-SIMS stated the successful synthesis of the three homopolymers on the MOF surface. XRD confirmed the conserved crystallinity, and the DLS measurement showed maintained NP sizes around 180 to 200 nm after the polymerization.

To shorten and facilitate the reaction procedure, I additionally used the NMP grafting-from method to produce MOF/polymers with different polymer chain lengths and MOF/copolymers in a shorter one-step synthesis process. For this one-step synthesis approach, all reactants are simultaneously in solution, and the bond formation on the MOF happens in situ. I used the same three monomers as before (APEG, HEAA, and DMAA).

The evaluation with ATR-IR and ToF-SIMS showed the successful polymerization with four different polymer and copolymer combinations on the UiO-66-NH_2 NPs surface (UiO-66-NH-MAMA-APEG/DMAA (6 h), UiO-66-NH-MAMA-HEAA (8 h), UiO-66-NH-MAMA-APEG/HEAA/DMAA (23 h), and UiO-66-NH-MAMA-HEAA/DMAA (24 h). All the MOF/polymers showed the characteristic polymer-specific bands in IR and respective fragments in ToF-SIMS. Additionally, XRD and DLS confirmed their conserved crystallinity and nano-size after the polymerization.

NMP is a CRP method in which initiator molecules control the polymerization throughout the synthesis, resulting in narrow chain distribution with a low $Đ_M$ of around 1.1 to 1.3. With GPC, I confirmed that four of the seven MOF/polymers synthesized with MAMA-SG1 (two-step and one-step) showed low $Đ_M$ values from 1.2 to 1.3. This finding proves the efficiency of CRP for these polymerization strategies. The other three polymer-modified UiO-66-NH_2 NPs showed high $Đ_M$ values close to 2, similar to free radical polymerization, displaying uncontrolled polymerization behaviors. The high monomer amounts (around 122 to 200 equiv.) in these reactions could be responsible for initiating self-polymerization and uncontrolled chain growth. The GPC results showed that the polymerization conditions play a decisive role in synthesizing customized MOF/polymer materials and, above all, in successfully reproducing the most successful materials.

To test whether the synthesized MOF/polymers are suitable for drug delivery, I first tested the uptake of curcumin, an anticancer drug, into the polymer-modified MOF NPs.

Curcumin is quite soluble in $CHCl_3$, and studies have already used $CHCl_3$ to uptake curcumin into UiO-66-NH_2 NPs. To investigate the possibility of increasing the curcumin absorption, I experimented with three different $CHCl_3$ and Cyc concentrations ($CHCl_3$, $CHCl_3$/Cyc (2:1, v:v), and $CHCl_3$/Cyc (1:1, v:v)). The solvent combination $CHCl_3$/Cyc (1:1, v:v) indeed increased the uptake to 77.8 mg/g curcumin in pristine UiO-66-NH_2 NPs. Compared to that, the uptake was only 52.8 mg/g for curcumin in $CHCl_3$. Therefore, I assumed that the diffusion into the MOF is faster when it protects the curcumin from a nonpolar environment, as is the case in $CHCl_3$/Cyc (1:1, v:v).

With the presented study, I continued to test the curcumin uptake for all the before-synthesized MOF/polymer NPs after 24 h. Interestingly, some polymer-modified UiO-66-NH_2 NPs, especially the UiO-66-NH-MAMA-HEAA, showed low absorption of around 12.0 mg/g. A possible explanation is the nonpolar character of the used $CHCl_3$/Cyc (1:1, v:v) solvent. The particles probably agglomerate because of the hydrophilic polymers on the MOF surface, blocking the curcumin uptake in the MOF. Although successful drug uptake was achieved for the MOF/polymer NPs, it is important to consider that the solvent to polymer compatibility influences the drug absorption amount.

Loading curcumin into the pores of the MOF/polymer NPs is crucial for a later drug delivery application. The previously described curcumin uptake experiments first proved successful drug loading into the polymer-modified MOF NPs. Additional studies still have to be conducted to verify the successful uptake in the pores further and exclude the mere physisorption on the surface.

The customization of MOF/polymer materials for higher biocompatibility is significant for their compatibility with cells and, therefore, the later drug delivery applications. The drug released by MOF nanocarriers must harm malign cancer cells. The nanocarrier alone should not harm the cells. To model the cell environment in the body and provide information on the compatibility of the MOF NPs used with body cells and in the medium, I incubated MCF-7 cells with the pore-free polymer-modified and pristine UiO-66-NH_2 NPs for 72 h.

The experiment demonstrated high toxicity values for 0.10 mg/ml of the pristine particles. Compared to that, the polymers on the surface reduced the cell toxicity by ten, and the MOF/polymer materials were not toxic up to 1.00 mg/ml. With this, I showed both the enhanced biocompatibility of the synthesized MOF/polymer NPs and the efficiency of our NMP technique of surface-based polymerization in finding highly specialized MOF/polymer systems for drug delivery in various cell systems.

This chapter described modifying UiO-66-NH_2 NPs precisely for a tailored application in biology and medicine. I showed how we can use the NMP grafting-from approach to apply different polymers on the surface while maintaining the NP size. Furthermore, I demonstrated the reduced unspecific protein adsorption and the exchange of the polymer end-chain in favor of a bioactive group. In the second part of the chapter, I successfully proved the effective transfer of the NMP method to other polymers while conserving the crystallinity and size of the UiO-66-NH_2 NPs. Additionally, I showed the maintained drug uptake for the anticancer uptake of curcumin with the MOF/polymer NPs. Finally, I demonstrated the effectiveness of the polymer coating with the reduced cell cytotoxicity of the polymer-modified compared to pristine UiO-66-NH_2 NPs.

6. Machine Learning supporting MOF Synthesis

The previous two chapters explained how to tailor and modify metal-organic framework (MOF) materials for specific applications in biology and medicine (enzyme incorporation and drug delivery). In both of these examples, I adjusted different MOF materials for a particular application. In general, this modification or customization requires many experiments, and finding the most suitable reaction conditions for a tailored material is time-consuming. Therefore, new synthesis methods have been developed recently using machine learning (ML) algorithms to find optimized synthesis approaches quickly and efficiently (see Chapter 2.2.3). These algorithm-based optimization strategies save resources and experimentation time by combining chemical expertise with ML techniques. Hence, applying an ML algorithm is very useful in daily synthesis approaches, and the next chapter shows how I used ML algorithms to optimize a MOF thin film synthesis.

6.1 Introduction

ML approaches have proven helpful in saving time and increasing the efficiency of finding optimized reaction conditions for a particular synthesis. Many researchers in the last decade have already benefited from ML and have been able to utilize optimization algorithms in their work.[85,87] While scientists are beginning to integrate ML techniques into their daily routines, a significant problem still exists: How to select an appropriate ML strategy for a particular optimization? In the upcoming chapter, I'll give an example of how to accomplish this task for a specific chemical problem. Therefore, I applied two distinct ML algorithms to the same chemical optimization issue and assessed their respective performances in reaching the targeted optimization.

To assess the reaction optimization, I first defined the relevant parameter set. Both ML algorithms start with the same parameter set. After conducting the experiments, I assessed their performance with a previously established fitness function. In the next step, I used the reaction parameters and their corresponding fitness values as input to develop the prediction of the ML algorithms further. The following paragraphs provide an

overview of the two methods employed for the optimization: the genetic algorithm (GA) and the Bayesian optimization (BO).

The BO is a global optimization technique appropriate for complex, noisy black-box functions that are expensive to evaluate.[150] BO builds a probabilistic objective function model to direct the search toward optimal solutions.[151] It then uses Bayes' theorem to update the model's belief about the objective as it gathers more data.[83]

The optimization process begins with the initial experiments for any given parameter set. Afterward, a probabilistic model is trained on these initial parameters and utilized as a surrogate model for the objective function.[151] The applied surrogate model then helps identify new experimental candidates by using an acquisition function that quantifies the informativeness of new data based on the predicted objective function while balancing exploitation and exploration behaviors according to predefined criteria.[150,152] The surrogate model is consistently updated with new data, and the acquisition function predicts improved parameters for the next experiments.

Summarized, the surrogate model modeling the objective function and the acquisitions function that forecasts further sampling make up the two fundamental components of BO.[151,152] The constant update of the surrogate models with new data makes the BO a widely used optimization algorithm.[150] Especially for nonexperts, the advantage of BO is that they can improve the performance only by describing an objective function and not a solution algorithm.[151]

GAs are another (global) optimization technique applied for synthesis optimization.[153] A basic set of genes, which in this case correspond to a set of synthesis parameters, regulate the GAs following natural selection.[153] Successful genes are inherited, similar to evolutionary development, and GAs employ them to drive a population of genes toward their regional or global optimum.[153] The fitness function improves during the selection procedure.[153] The "survival rate" of a particular gene and its likelihood of being reproduced in the following generation are both improved by higher fitness values.[153] In a GA, new experiments are produced not only by crossover but also by random mutation.[153] This method helps restore lost information, much like in nature.[153]

Both algorithms show unique optimization methods: the BO modeling the objective function and the GA testing the evolution technique. Given that GAs have already been effectively utilized to enhance MOF synthesis, [85,87] it will be interesting to discover if the BO approach can produce equal or better results. To investigate that, I developed a BO algorithm in AX and employed the already-existing Synthesis Condition Finder (SyCoFinder)[85] tool for GA. I used both ML algorithms to optimize the production of a MOF film over three generations with ten experiments per generation.

MOF films are useful in biological applications for drug delivery or sensing. Customizing a uniformly covered crystalline MOF on a glass wafer, especially for drug delivery, is a huge advantage[154], and the two ML algorithms will show how to facilitate the optimization.

6.2 Results and Discussions

The following chapter describes the results and insights of the ML approaches for optimizing the MOF film synthesis on a glass wafer. Furthermore, I will outline how the two algorithms perform differently and assess each one concerning the particular goals of this work.

6.2.1 Genetic Algorithm vs. Bayesian Optimization: A Comparative Study

I tested the efficiency of both ML approaches by coating a glass wafer with a UiO-66-NH_2 film. The chemical vapor-assisted method (VAC) was the reaction method I optimized for the film production (see Chapter 8.3.1). The optimization over three generations (initial set, the 1^{st,} and 2nd generation) should lead to a crystalline MOF film on the glass wafer that covers the substrate completely and evenly. After each reaction, I evaluated the material produced with X-ray diffraction (XRD) and scanning electron microscopy (SEM) and classified it with a previously created fitness function (see Equation 8).

Figure 52 displays the optimized results for the SyCoFinder with the GA on the left. The starting set has an average fitness of only 19 %. Throughout three generations, the performance improved, reaching 54 % in the 2nd generation. The GA received its best result in the 2nd generation from a single experiment at 95 %.

The crystallinity progressively increased throughout three generations. Only four out of ten products in the initial set were crystalline, as opposed to six out of ten in the 2nd generation. The coating also improved throughout the three generations. Figure 52 on the bottom left shows SEM images of the samples with the highest fitness from each generation. While the initial set shows a poorly coated wafer, the coating in the 2nd generation significantly improved with a complete and thick layer. In summary, the GA increased its results from the initial set to the 2nd generation by 35 %.

In the BO, shown in Figure 52 on the right, the initial set starts with a fitness of 29 %, increases to 49 % during the 1st generation, and decreases to 41 % during the 2nd. I obtained the best individual fitness for a single product, optimized with BO, in the 1st generation with 92 %.

In terms of crystallinity, the BO shows only nine crystalline samples in the initial set, but its performance increased to ten in both the 1st and 2nd generation. With each new generation, the coating also improves for the BO (see Figure 52, bottom right).

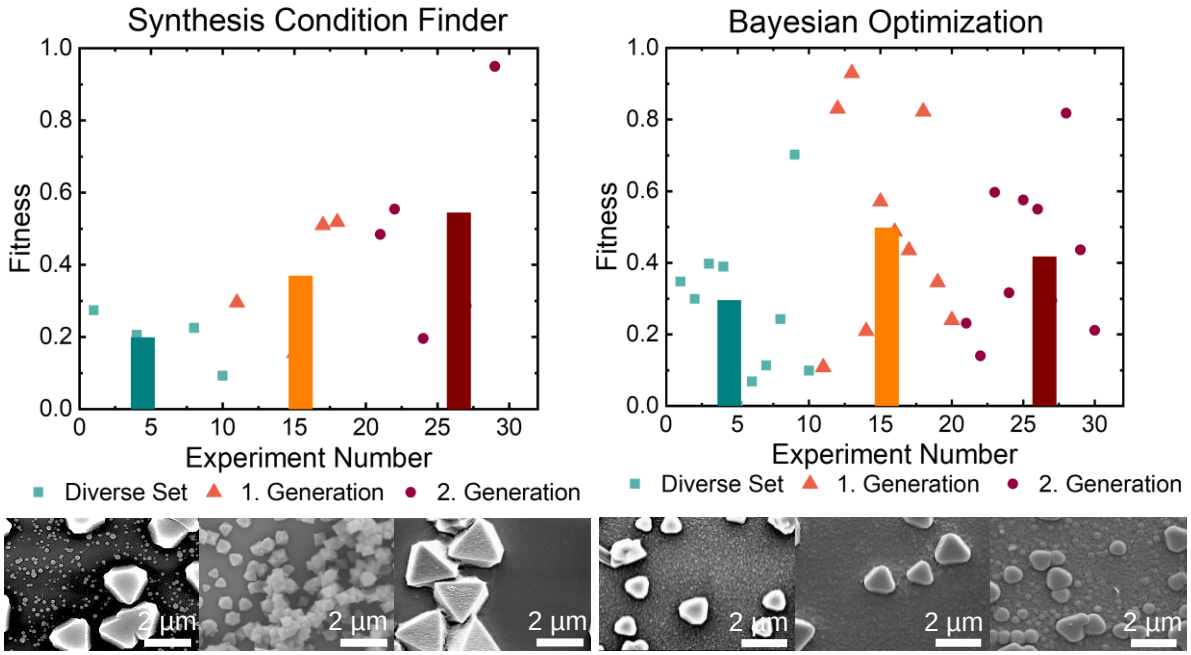

Figure 52: The fitness values of the three generations for the Synthesis Condition Finder (SyCoFinder) with the genetic algorithm (GA) (left) and the Bayesian optimization (BO) (right). All generations consist of ten experiments, and the average fitness was calculated from all the successful reactions. The scanning electron microscopy (SEM) pictures at the bottom show one surface picture of the single best results in each generation for both algorithms.

In summary, both optimization techniques increased the fitness and, therefore, the coating and crystallinity of the UiO-66-NH_2 film over three generations. However, differences exist between the two ML approaches in determining the experiments for the initial set. While the GA starts with the MaxMin method, which takes in all the possible parameter sets, the BO starts with a random approach. Each approach has its advantages. The MaxMin method helps gain an overall picture of the parameter space initially. One drawback is the possibility that none of the experiments might result in a successful outcome in the first place. Opposed to that, the random technique used in the BO has a higher likelihood of generating at least one successful result.

When examining the algorithms for the previously described synthesis optimization, both proved effective; however, the choice of the algorithm depends on the given data set. In our example, both approaches increased the fitness and synthesis reaction over three generations. While the BO improved in the 1st generation and slightly decreased by around 8 % in the 2nd, the GA improved gradually over the three generations. I continued testing all three generations to investigate if I might improve the outcome with the BO even further. Overall, I achieved the best result for the GA with 95 % (2nd generation). The BO also yielded a good result with 92 % (1st generation). Both optimization techniques generally yield 90 % of the desired outcome and proved valuable for optimizing the MOF film synthesis.

It is important to highlight that starting both optimization procedures with the same initial data set would have improved procedure comparability. However, this was not feasible for technical reasons. I further point out that although BO-based optimization would have benefitted from a strictly sequential method, I executed it in batches of ten samples per generation to be similar to the SyCoFinder-based strategy.

6.2.2 Reproducing the Optimized Reactions

Replicating the most successful reactions found with the ML algorithms is essential to ensure reproducibility. Therefore, I repeated the synthesis procedures for the reactions with the best fitness values discovered with the ML approaches in the previous paragraph (see Chapter 6.2.1). Figure 53 (blue) shows good fitness values of 79 % for the SyCoFinder replicates and 80 % for the BO replicates. Compared to the original fitness for both optimized procedures, 95 % for GA and 92 % for BA, I observed a minor decrease (see Figure 53 (black)). Although I successfully replicated the procedure and created a highly crystalline and complete UiO-66-NH_2 layer on the substrate, this experiment demonstrates the natural noise level of the measurements and, therefore, the data.

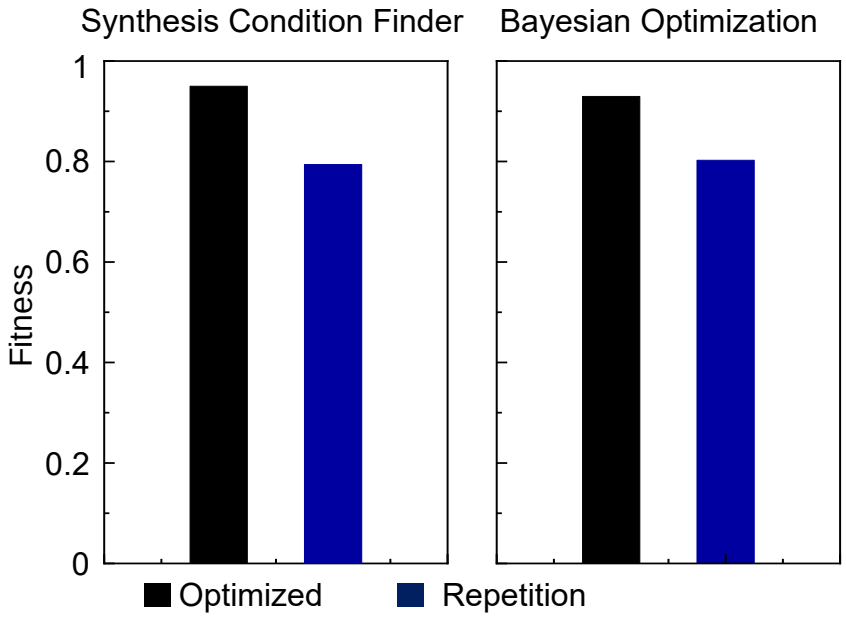

Figure 53: Repetition of the reactions with the best fitness values found by the two machine learning (ML) algorithms over three generations. The fitness values of the Synthesis Condition Finder (SyCoFinder) with the genetic algorithm (GA) are on the right, and the Bayesian optimization (BO) algorithm is on the left. Both experiments show comparably good fitness values concerning the original results. The fitness for the optimized results is shown in black, and the fitness of the repeated reactions is shown in blue.

6.2.3 Scientific Application Potentials

This chapter considers the scientific application potential for the two ML approaches to optimize a chemical reaction. Even though ML has become increasingly attractive for scientific reaction approaches, applying it for particular optimizations commonly requires a certain level of prior computer science understanding. For this reason, the accessibility of the methods plays an essential role in their broad application.

The SyCoFinder is an online tool available in the Materials Cloud. The Materials Cloud is a platform sharing computational science.[155] The SyCoFinder is easy to handle, and the online tool allows one to manually fill in the ranges of the used variables and choose a weighting. The program then automatically calculates the first experiments. This process makes it easy for scientists who have never worked with ML techniques.

Starting to set up the BO algorithms, simple code examples are available online, for instance, in libraries like AX. Nevertheless, choosing the correct surrogate model and acquisition function can make it challenging for nonexperts to utilize BO. However, adjusting and modifying the surrogate model and acquisition function makes the BO great for customizing the ML algorithm to a specific experimental setting. The SyCoFinder, in contrast, is easy to handle, but a nonexpert may find it hard to change code independently.

6.3 Summary

In this chapter, I tested and evaluated the functionalities of two different ML optimization techniques to optimize MOF thin film growth. Using both ML techniques, I demonstrated that I could create a complete crystalline UiO-66-NH_2 layer on a glass wafer. Based on a GA, the SyCoFinder reached the best fitness of about 95 %. The BO algorithm achieved a similarly high fitness of 92 % within the experimental uncertainty. By repeating these optimized synthesis procedures, I confirmed the successful reproduction of the experiments with a fitness of roughly 79 % for the GA and 80 % for the BO. Based on the indicated results, I demonstrated that both ML algorithms improved the formation of a complete crystalline MOF film on the glass surface.

Furthermore, I evaluated both ML algorithms concerning scientific application potentials. The SyCoFinder proved easy to work with and is especially good for scientists who have never worked with ML techniques. Unfortunately, it is an online application in the Materials Cloud, and modifying its code to a given scenario is difficult for a nonexpert. The BO works with a surrogate model and acquisition function, which can be difficult for an inexperienced user to choose. However, the customization and modification possibilities for both the surrogate model and the acquisition function make the BO valuable for optimizing complex and specific experimental procedures.

The optimization approaches show how I effectively applied ML algorithms in a daily synthesis approach. When we think about the future and potential applications, ML algorithms can help reduce the time to find optimized synthesis routes and drive the effectiveness of producing targeted materials. The ability to customize synthesis reactions to produce products for specific applications can help us, for example, in synthesizing particular biological and medical materials.

7. Summary and Outlook

This Ph.D. thesis provided an overview of several methods and approaches to prepare customized metal-organic framework (MOF) materials for biological and medical purposes. In this context, I developed tailored synthesis approaches to modify MOF materials for a particular purpose and applied them in various ways.

In the first project, I developed MOF particles for the encapsulation of the wild type (wT) and a mutant (m) form of the phenacrylate decarboxylase (PAD). The PAD catalyzes the production of p-coumaric acid (pCA) to p-hydroxystyrene (pHS). Therefore, I investigated a compatible MOF system to encapsulate the enzyme to protect it from harsh conditions, such as organic solvents.

It is essential that the enzymatic activity must not be affected by the encapsulation. Hence, I tested four different MOFs (ZIF-8 (ZIF-CO_3-1), ZIF-90, MIL-53(Al), and Ca(BDC)) that were all synthesized in water. The subsequent X-ray diffraction (XRD) and scanning electron microscopy (SEM) tests showed the successful formation of ZIF-8 (ZIF-CO_3-1) (wt and m), ZIF-90 (without enzyme (woE), wT, and m), and Ca(BDC) (woE, wT, and m). At the same time, I could not definitively confirm the successful synthesis of ZIF-8 (ZIF-CO_3-1) (woE) and MIL 53(Al) (woE, wT, and m).

Still, only the PAD@Ca(BDC) (wT and m) have proven to preserve the enzymatic activity after the synthesis. The limitation for ZIF-8 (ZIF-CO_3-1), ZIF-90, and MIL-53(Al) was the high toxicity of the used metals and linkers in the solution, causing the loss of enzymatic activity even before the MOFs were synthesized.

By the later encapsulation of PAD (wT and m) in Ca(BDC), the MOF successfully protected the enzymatic activity against organic solvents, like cyclohexane (Cyc), toluene (Tol), tetrahydrofuran (THF), ethyl acetate (EtOAc), dimethylformamide (DMF), acetonitrile (MeCN), ethanol (EtOH), H_2O, and aqueous solutions of pH 7, and pH 6. Additionally, the MOF conserved their crystallinity. In summary, the optimized PAD@Ca(BDC) particles are stable in various organic solvents for up to two weeks.

Another exciting application in medicine and biology is the utilization of MOF nanoparticles (NPs) in drug delivery systems. Unfortunately, limiting factors for using

MOFs as nanocarriers are the poor dispersion in polar solvents and the unspecific protein adsorption in the blood. A surface modification with biocompatible groups is often necessary to circumvent these limitations and efficiently use the NPs for drug delivery.

Therefore, in the second project described in this thesis, I adjusted different hydrophilic polymers on UiO-66-NH_2 NPs. First, I implemented a grafting-from approach with nitroxide-mediated polymerization (NMP). In the initial approach, I successfully used NMP to apply a hydrophilic styrene-PEG derivative (poly(ethylene oxide) methyl-p-vinylbenzyl-ether (SPEGA)) on the NP surface. Attenuated total reflection infrared spectroscopy (ATR-IR) and time-of-flight secondary ion mass spectrometry (ToF-SIMS) proved the successful surface polymerization.

Furthermore, XRD and dynamic light scattering (DLS) measurements confirmed the conserved crystallinity and nano-size of the particles. The SPEGA-modified NPs were less aggregated in a polar solvent such as EtOH and showed 39 % less protein (human serum albumin (HSA)) adsorption than pristine UiO-66-NH_2 NPs. Additionally, I enhanced the biocompatibility for drug delivery by proving the successful attachment of a bioactive peptide sequence (RGD) in a nitroxide exchange reaction (NER) verified by ToF-SIMS. The RGD sequence consists of arginine, glycyl, and aspartic acid and models the possibility of an end-group modification. In the future, NER reactions can help to modify the MOF/polymer NPs with other bioactive end-groups for targeted drug delivery.

Especially for medical administration into various cells, the attachment of different hydrophilic polymers using the NMP approach is useful since the polymers can be chosen or modified depending on the targeted tissue or the drug employed. In this regard, my thesis aimed to prove that different MOF/polymer NPs can be synthesized for drug delivery using the NMP method. To demonstrate this potential, I synthesized seven distinct biocompatible polymers and copolymers on UiO-66-NH_2 NPs using poly(ethylene glycol) methyl ether acrylate (APEG), N-hydroxyethylacrylamide (HEAA), and N,N-dimethylacrylamide (DMAA).

Three of these reactions were conducted similarly to the SPEGA-modified MOF NPs. In this two-step reaction, the initiator MAMA-SG1 was first applied on the surface, and then the polymerization was initiated on the MOF surface.

To shorten and facilitate the reaction procedure, I additionally used the NMP grafting-from method to produce four MOF/polymer NPs with different polymer chain lengths and MOF/copolymers in a shorter one-step synthesis process. For this one-step synthesis, all reactants were simultaneously in solution, and the bond formation on the MOF happened in situ. I used the same three monomers as before (APEG, HEAA, and DMAA).

ATR-IR and ToF-SIMS proved the successful surface polymerization for all MOF/polymer NPs synthesized with the two- or one-step method. XRD and DLS measurements confirmed the conserved crystallinity and preserved nano-size of the polymer-modified MOF NPs around 180 to 200 nm. The successful polymerization for the one-step procedure verifies that it is possible to polymerize directly in the solution without applying the initiator on the MOF surface beforehand.

In biology and medicine, it is crucial to replicate the generated and evaluated MOF/polymer NPs with identical properties to obtain comparable reaction behaviors. To ensure similar polymer chain lengths and narrow chain length distribution with molar mass dispersity ($Đ_M$) values of 1.1 to 1.3, I used NMP, a controlled radical polymerization (CRP).

Measuring gel permeation chromatography (GPC), I confirmed that four of the seven polymerization approaches on the surface yielded controlled chain growth with $Đ_M$ values from 1.2 to 1.4. The three other MOF/polymer or MOF/copolymer combinations with high conversion times around 23 h and 24 h and high monomer amounts (122 and 200 equiv.) showed uncontrolled polymerization behavior with $Đ_M$ values around 2. These findings prove the importance of monitoring the reaction time and monomer concentration for reproducing a material with a desired and uniform chain length.

After examining the polymers' $Đ_M$ values, I studied the MOF/polymers' drug uptake accessibility for a future drug delivery application. Therefore, I first examined the uptake of the anticancer drug curcumin with pristine UiO-66-NH_2 particles. Upon testing various solvent combinations of chloroform ($CHCl_3$) and Cyc ($CHCl_3$, $CHCl_3$/Cyc (2:1, v:v), and (1:1, v:v)), I discovered that the solvent mixture comprising of $CHCl_3$/Cyc (1:1, v:v) had the best uptake of 77.8 mg curcumin with 1.00 g UiO-66-NH_2 NPs. Since Curcumin is highly soluble in polar solvents such as $CHCl_3$, adding a nonpolar solvent reduces the

solubility. As a result, the curcumin diffuses into the MOF rather than staying in the solution.

Afterward, I tested the curcumin uptake of the MOF/polymer NPs in $CHCl_3$/Cyc (1:1, v:v). Although I found a high curcumin uptake with pristine particles (77.8 mg/g), the MOF/polymer NPs displayed a reduced but still effective uptake. The reduced uptake mainly resulted from the chosen solvent. While the pristine UiO-66-NH_2 NPs showed the highest uptake in $CHCl_3$/Cyc (1:1, v:v), the nonpolar component could have been a limitation for the hydrophilic polymers on the MOF surface. As previously demonstrated with the SPEGA-modified NPs, the solvent selection significantly impacts the NPs' dispersity. Because the chosen polymers are hydrophilic, a nonpolar solvent likely caused greater aggregation and decreased dispersibility. Therefore, the polymers on the surface collapse, and the pore accessibility is restricted. The described effect needs to be monitored for future reactions, and, in particular, a suitable solvent needs to be selected for the incorporation of drugs into MOF/polymers for a specific drug delivery or cell line.

Loading curcumin into the pores of the MOF/polymer NPs is crucial for a later drug delivery application. The previously described curcumin uptake experiments first prove the successful loading of drugs into the polymer-modified MOF NPs. Additional studies still have to be conducted to verify the successful uptake in the pores further and exclude the mere physisorption on the surface.

The compatibility of the MOF/polymer materials with cells is significant for the subsequent delivery of drugs in the body. The drug released by MOF nanocarriers must harm malign cancer cells. The nanocarrier itself should not damage the cells. To model the cell environment in the body and mimic the influence of the MOF/polymer NPs on cells, I incubated MCF-7 breast cancer cells with the pore-free polymer-modified and pristine UiO-66-NH_2 NPs for 72 h.

The experiment demonstrated high toxicity values for 0.10 mg/ml of the pristine particles. Compared to that, the polymers on the surface reduced the cell toxicity by ten, and the MOF/polymer materials were not toxic up to 1.00 mg/ml. This result demonstrated both the improved biocompatibility of the synthesized MOF/polymer NPs and the efficiency of

our NMP surface-based polymerization technique in the development of compatible MOF/polymer systems for drug delivery in cell systems.

Adapting MOF systems to a specific application can be challenging and usually takes a long time. Addressing this challenge, recent attempts have been made in the application of machine learning (ML) optimization techniques in chemistry. Therefore, in my last project, I focused on ML techniques to support the optimized synthesis approach of a crystalline MOF film system covering the complete surface of a glass wafer. In biology, MOF thin films can be used for sensing biomolecules or be converted to gels as SURGELS without metals for cell culture studies to deliver bioactive molecules or drugs.

In all these applications, a crystalline MOF film that completely covers the wafer is preferred. However, accomplishing this is challenging and requires extensive experimentation and synthesis. Furthermore, reproducibility is often poor. Yet, a quick but still accurate technique to find optimized reaction conditions to create MOFs with a complete surface coverage and high crystallinity is required to synthesize diverse MOF films for various biomolecules.

In this last project, I compared two ML algorithms in their ability to find the most suitable synthesis method to cover the complete surface of a glass wafer with crystalline UiO-66-NH_2 particles. This approach employs the chemical vapor-assisted method (VAC) to coat a wafer. During the experiments, six reaction parameters were varied simultaneously. The ML algorithms applied were the Synthesis Condition Finder (SyCoFinder) equipped with a genetic algorithm (GA) and the Bayesian optimization (BO). Both algorithms were used for three generations with ten experiments each. After each generation, I classified the experiments with a previously described fitness function based on the crystallinity of the MOF material and surface coverage on the glass wafer, using XRD and SEM measurements.

After conducting the experiments, it was clear that both ML methods helped to achieve valuable results with a high fitness value of 95 % and 92 %, respectively. This statement became apparent when, after only 30 experiments, I confirmed that I obtained optimized reaction conditions for synthesizing a high crystalline MOF film covering the whole surface of a glass wafer. By repeating these optimized synthesis procedures, I confirmed the

successful reproduction of the experiments with a fitness of roughly 79 % for the GA and 80 % for the BO. In conclusion, both ML algorithms showed promising results, especially for optimizing the reaction parameters for synthesizing a particular MOF system on a wafer.

Comparing the scientific approach of both ML algorithms, I discovered that the SyCoFinder is easy to use and especially good for scientists who have never worked with ML techniques. On the other hand, the BO uses surrogate models and acquisition functions, and it can be challenging for nonexperts to choose the best-suited one for a given experimental setup. However, adjusting and modifying the surrogate model and acquisition function makes the BO great for customizing the ML algorithm to a specific experimental setting. The SyCoFinder, in contrast, is easy to handle, but a nonexpert may find it hard to change code independently.

Summarizing this thesis, I showed how to modify and adapt MOF systems for particular biological problems. The encapsulation of enzymes in MOFs proved to protect them against harsh conditions. In addition, I enhanced the biocompatibility for MOFs as drug delivery carriers by attaching hydrophilic polymers on UiO-66-NH_2 NP using a new NMP grafting-from approach. Furthermore, I showed how to add a bioactive component to the MOF/polymer end chain in an NER experiment for targeted drug delivery. The ability to specifically modify MOFs with various hydrophilic polymers and improve their biocompatibility with cell systems was another benefit of the novel NMP technique. The developed polymerization method makes employing it in many medical applications possible. Finally, I demonstrated how different ML techniques optimize synthesis approaches for MOFs or MOF film syntheses for specific biological applications.

In the future, the PAD@CaDBC can be used in flow catalysis to make the PAD more persistent. In addition, the knowledge gained will help to find new encapsulation methods for specific enzymes. The tested and successfully developed NMP grafting-from process can be used to synthesize various MOF/polymer hybrid materials. The next step for these synthesized materials would be to use them for drug delivery into cancer cells and to evaluate their efficacy. In addition, the NER approach should be used to apply different bioactive groups on the MOF/polymer end-chain, and their effectiveness for enhancing

targeted drug delivery must be studied. Furthermore, ML approaches for the presented MOF customization strategies should be tested to support the synthesis optimization of functional materials.

8. Experimental Section

The chemicals used in this section were bought from Sigma Aldrich and, except for the monomers, were all used without purification. The monomers were purified by passing through a basic aluminum oxide column to remove the stabilizer. Afterward, they were stored at -22 °C under nitrogen atmosphere to prevent self-polymerization. All other used chemicals received from external collaborators are listed as follows: The MAMA-SG1 (BlocBuilder®) was kindly provided by Prof. Guillaume Delaittre from the University of Wuppertal, Julian Brückel specially synthesized the RGD-nitroxide in the group of Prof. Stefan Bräse at Karlsruhe Institute of Technology (KIT),[141] and Prof. Martina H. Stenzel from the University of New South Wales (UNSW) provided the curcumin. Prof. Martina H. Stenzel also provided the MCF-7 cells (from the American Type Culture Collection) used in this study. The phenacrylate decarboxylase (PAD) enzymes (wild type (wT) and mutant (m)) were provided by Esther Mittmann and Kersten Rabe from the Insitute for Biological Interfaces (IBG-1).

8.1 MOF-Shell Protection of Enzymes

The following paragraphs describe the synthesis procedures for the different metal-organic framework (MOF) systems used for enzyme protection in Chapter 4.

8.1.1 ZIF-8 (ZIF-CO_3-1) – Synthesis

The ZIF-8 (ZIF-CO_3-1) (zeolitic imidazolate framework) MOF particles were synthesized following a modified reaction procedure.[6] Three similar metal solutions were prepared beforehand in 20 ml scintillation vials. Therefore, 3 × 0.03 g (40.0 mM) $Zn(OAc)_2 \times 2H_2O$ was dissolved in 1.50 ml Milli-Q water. For the linker solution, three samples were prepared with 3 × 0.04 g (160 mM) 2-methylimidazole (HmIM), dissolved in 1.50, 1.47 ml, and 1.47 ml Milli-Q water, respectively. Afterward, one linker solution was displaced with 26.0 µl (wT) and another with 25.0 µl (m) PAD enzyme. The third sample was used without any further additions and was used as a reference. The metal solutions were then dropwise added to the linker solutions, and the vials were left to react for 12 h. The formed precipitates were washed three times with 3 ml Milli-Q water and placed to dry overnight

at RT. The particles were analyzed using X-ray diffraction (XRD) and scanning electron microscopy (SEM).

8.1.2 ZIF-90 – Synthesis

ZIF-90 was synthesized according to a modified synthesis approach.[7] First, three solutions of $Zn(NO_3)_2 \times 6H_2O$ were prepared by dissolving 3 × 0.04 g (40.0 mM) in 1.50 ml Milli-Q water in 20 ml scintillation vials. Then three linker solutions were produced by dissolving 3 × 0.05 g (160 mM) of 2-imidazolecarboxaldehyde (HICA) in 1.50, 1.47, and 1.47 ml Milli-Q water in 20 ml scintillation vials. All solutions were sonicated for 20 minutes until they were fully dissolved. Then, 26.0 µl of the PAD enzyme (wT) and 25.0 µl of the PAD enzyme (m) were given to the respective linker solution to reach 1.50 ml. Additionally, one sample was spared with enzymes as a reference. Then, the metal solutions were slowly added to the linker solutions, and the reaction was left to react for 24 h at room temperature (RT). The precipitates were washed three times with 3 ml Milli-Q water and centrifuged at 5000 rpm. Afterward, the precipitates were dried at RT overnight. The particles were analyzed using XRD and SEM.

8.1.3 Disodium Terephthalate Synthesis

The disodium terephthalate (Na_2BDC) was prepared according to a modified synthesis procedure.[9] 4.16 g (25.0 mM) of terephthalic acid (BDC) was dispersed in 20 ml Milli-Q water in a 50 ml beaker, and 2.00 g (50.0 mM) NaOH was added. The mixture was stirred at RT for 1 h, after which a white precipitate was received. The white precipitate was dropwise added to a stirring solution of 400 ml cold isopropanol in a 600 ml beaker and afterward filtered and washed with cold isopropanol. After washing, the solution reached a pH of 7, and the powder was dried in an oven at 75 °C.

8.1.4 MIL-53(Al) – Synthesis

MIL-53(Al) (Matériaux de l'Institut Lavoisier) was synthesized following a modified reaction procedure.[8] Three solutions with the wild type (wT), the mutant (m), and without any (woE) addition of the PAD enzyme were prepared in 20 ml scintillation vials. First, three metal solutions were prepared by dissolving 3 × 1.56 g (1390 mM) $Al(NO_3) \times 9H_2O$ in 1.50 ml Milli-Q water. Three linker solutions were prepared by dissolving 3 × 0.44 g

(700 mM) Na_2BDC in 1.50, 1.47, and 1.48 ml Milli-Q water. All solutions were placed in a sonicator for 15 to 20 minutes to dissolve completely. The linker solution was displaced with 26.0 µl (wT) or 25.0 µl (m) PAD enzyme. One of the linker solutions remained untreated and served as a reference sample. Afterward, the metal solutions were dropwise added into the linker solutions, and the vials were left to react at RT for 24 h. The precipitates were centrifuged and washed three times with 3.00 ml Milli-Q water. They were then placed at RT overnight to dry. The particles were analyzed using XRD and SEM.

8.1.5 Ca(BDC) – Synthesis

The synthesis of Ca(BDC) MOF particles was implemented by a modified reaction procedure in 20 ml scintillation vials.[9] Three solutions were prepared for the Ca(BDC) without (woE), with the (wT), and with the (m) PAD enzyme. The concentration in the final solution (10.0 ml) was 600 mM for the metal and the linker, respectively. For the metal solution, 3 × 0.33 g $CaCl_2$ (600 mM) was dissolved in 3 x 5.00 ml Milli-Q water. Meanwhile, 3 × 0.63 g (600 mM) (Na_2BDC) was dissolved in 4.74 ml, 4.75 ml, or 5.00 ml Milli-Q water for the linker solution. Both solutions were sonicated for 15 to 20 minutes until the metal or linker was dissolved entirely. 250 µl (wT) and 260 µl (m) PAD enzyme were given to the linker solutions, respectively. The metal solution was then slowly introduced into the linker solution, and after complete addition, the reaction vial was shaken at low speed for 15 seconds. Then, the reaction was left to react for 16 h at RT. Afterward, the precipitate was washed 4 to 5 times with 5.00 ml Milli-Q water and centrifuged at 5000 rpm. The finished precipitate was then air-dried at RT overnight. The particles were analyzed using XRD and SEM.

8.1.6 Ca(BDC) – Tests in Different Solvents

For the solvent tests, 30.0 mg of the before-prepared dry Ca(BDC) MOF was dispersed in different solvents: ethyl acetate (EtOAc), toluene (Tol), ethanol (EtOH), acetonitrile (MeCN), methanol (MeOH), H_2O, dimethylformamide (DMF), tetrahydrofuran (THF), H_2O (100 °C), cyclohexane (Cyc). Additionally, several aqueous pHs (4, 6, and 7) were examined. Therefore, the pHs were adjusted using citric acid and sodium hydroxide. As a reference, one sample was prepared on air. The samples were all kept in their

respective solvents for two weeks. After that, the precipitates were washed three times with water and then dried at RT. The particles were analyzed using XRD and SEM. All reactions were carried out in 20 ml scintillation vials.

8.2 MOF/Polymer Nanoparticles for Drug Delivery

The following paragraphs describe the synthesis and test procedures for the MOF and MOF/polymer nanoparticles (NPs) introduced in Chapter 5.

8.2.1 UiO-66-NH_2 – Synthesis

The UiO-66-NH_2 synthesis was implemented using a modified reaction procedure.[140,141,156] 0.24 g $ZrCl_4$ (1.03 mmol, 1.00 equiv.), 1.77 ml acetic acid (AcOH) (30.9 mmol, 30.0 equiv.) and 75.0 µl Milli-Q water (4.12 mmol) in a 100 ml crimp vial with an aluminum cap equipped with a Teflon septum, were dissolved in 20 ml DMF by sonication for 5 minutes. Meanwhile, the linker solution was prepared in a 100 ml crimp vial with an aluminum cap equipped with a Teflon septum by dissolving 0.19 g 2-aminoterephthalic acid (BDC-NH_2) (1.03 mmol, 1.00 equiv.) in 40 ml DMF by sonication for 5 minutes. Both solutions were mixed and placed in a preheated oven at 120 °C for 24 h and then cooled down. The obtained precipitate was then washed three times with 10 ml DMF by centrifugation for 10 minutes at 8000 rpm. The washed particles were kept in DMF until further use. The particles were analyzed using attenuated total reflection infrared spectroscopy (ATR-IR), time-of-flight secondary ion mass spectrometry (ToF-SIMS), XRD, dynamic light scattering (DLS), and SEM. Additional data supporting the chemical synthesis results is available via the Chemotion repository: https://doi.org/10.14272/reaction/SA-FUHFF-UHFFFADPSC-YJAIWVDPLY-UHFFFADPSC-NUHFF-BUHFF-NUHFF-ZZZ.

8.2.2 TEMPO-Alkoxyamine – Synthesis

The TEMPO-alkoxyamine (((4-(1-((2,2,6,6-tetramethylpiperidin-1-yl)oxy)ethyl) benzoic acid)) synthesis was prepared according to a modified synthesis method.[140,141,157] 1.00 g TEMPO (6.40 mmol, 1.00 equiv.), 4-(1-bromoethyl)benzoic acid (1.20 equiv.), copper powder (1.20 equiv.), and CuBr (1.20 equiv.) were added into a three neck round flask. The flask was closed, degassed, and refilled with nitrogen (N_2). Then, 30 ml THF in

a 50 ml Schlenk flask and bis(2-dimethylaminoethyl)-methylamine (PMDETA) (2.40 equiv.) in a 20 ml Schlenk flask were separately degassed using the freeze-pump-thaw method. Afterward, the oxygen-free THF was added to the flask, the mixture was stirred for 10 minutes, and the PMDETA was added. The reaction mixture was then stirred for an additional 24 h at RT. After the reaction was finished, the mixture was diluted with 100 ml dichloromethane (DCM) and washed with 5 x 100 ml of an aqueous disodium ethylenediamine-tetraacetate solution to remove the catalyst. This procedure was repeated until the supernatant was clear. The organic layer was then dried over $MgSO_4$, filtered, and evaporated. A recrystallization in MeOH at RT was conducted, after which a white/light yellow powder was received. (yield: 3.00 g, 3.20 mmol, 51.0 %). 1H NMR (400 MHz, CDCl3): δ (ppm) = 8.07 (d, J = 8.05 Hz, 2H), 7.43 (d, J = 8.0 Hz, 2H), 4.86 (q, J = 6.94 Hz, 1H), 1.50 (d, J = 6.48 Hz, 3H), 1.30-0.56 (m, 18H). 13C NMR (CDCl3): δ (ppm) = 171.77 (1C), 152.12 (1C), 130.18 (2C), 127.76 (1C), 126.59 (2C), 83.00 (1C), 59.80 (2C), 40.32 (1C), 34.19, 23.60 (2C), 20.36 (4C), 17.18 (1C) (see Attachment F). Additional data supporting the analysis of the target compound is available via the Chemotion repository: https://doi.org/10.14272/reaction/SA-FUHFF-UHFFFADPSC-IXIHDVSFIR-UHFFFADPSC-NUHFF-NUHFF-NUHFF-ZZZ.

8.2.3 MOF Surface Modification

With TEMPO-Alkoxyamine (AA):

The MOF surface functionalization via the amide bond on the MOF surface was realized using a modified reaction procedure.[140,141,158] 30.0 mg of the synthesized UiO-66-NH_2 NP (0.02 mmol, 1.00 equiv.) in a 30 ml round bottom flask were washed three times with 3 ml EtOH. Then, around 110 mg of N(3-dimethylaminopropyl)N'ethyl-carbodiimide hydrochloride (EDC×HCl) (0.57 mmol, 36.0 equiv.) and a catalytic amount of N-hydroxysulfosuccinimide sodium salt (sulfo-NHS) was added. Then, 30.0 mg of the TEMPO-alkoxyamine (AA) (0.10 mmol, 0.61 equiv.) was added before the suspension was stirred overnight at RT. Afterward, the precipitate was washed three times with 5 ml EtOH and stored in EtOH. The surface-coated particles are further referred to as UiO-66-NH-AA. The particles were analyzed using ATR-IR, ToF-SIMS, XRD, DLS, and SEM. Additional data supporting the chemical synthesis results is available via the Chemotion

repository: https://doi.org/10.14272/reaction/SA-FUHFF-UHFFFADPSC-ABCUGETYYU-UHFFFADPSC-NUHFF-NUHFF-NUHFF-ZZZ.

With MAMA-SG1:

In a separate synthesis, the nitroxide-mediated polymerization (NMP)-initiator, MAMA-SG1, also called BlocBuilder®, was attached to the surface of UiO-66-NH_2 NPs. The synthesis reaction followed a modified synthesis procedure.[140,141,158] Since MAMA-SG1 is very sensitive to oxygen, all of the synthesis steps were performed under nitrogen. 150 mg of the synthesized UiO-66-NH_2 NPs (0.08 mmol, 1.00 equiv.) were washed three times with 3 ml EtOH, given in 9 ml of DMF in a 20 ml Schlenk flask, and then degassed with the freeze-pump-thaw procedure. In a separate 30 ml Schlenk flask, 69.0 mg of EDC×HCl (0.36 mmol, 4.00 equiv.), a catalytic amount of sulfo-NHS, and 22.9 mg MAMA-SG1 (0.06 mmol, 1.00 equiv.) were dissolved in 9 ml of dry DMF. The mixture was degassed using the freeze-pump-thaw method, and the reaction was stirred for 20 minutes. Then, the MOF suspension in DMF was introduced into the reaction solution under the exclusion of oxygen and stirred at RT for 24 h. Afterward, the reaction vessel was opened, and the received precipitate was washed three times with 5 ml DMF and stored in DMF afterward. The surface-coated particles are further referred to as UiO-66-NH-MAMA. The particles were analyzed using ATR-IR, ToF-SIMS, XRD, and SEM.

8.2.4 Nitroxide-Mediated Polymerization on the MOF Surface

With TEMPO-Alkoxyamine (AA):

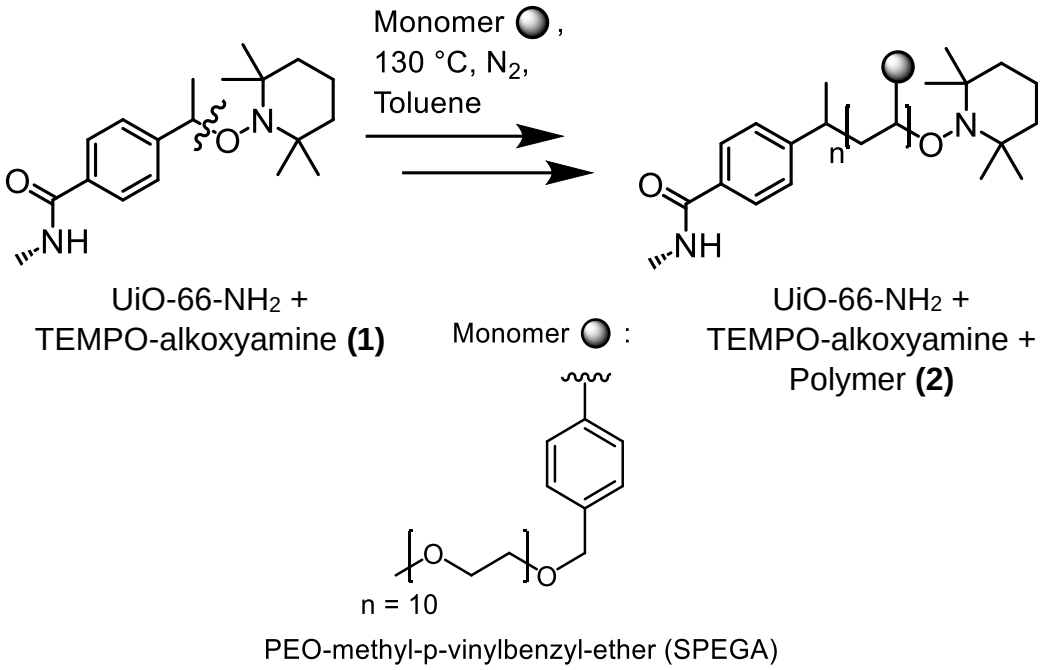

*Figure 54: Reaction scheme of nitroxide-mediated polymerization (NMP) on the surface of UiO-66-NH_2 nanoparticles (NP). After the initiator (TEMPO-alkoxyamine) has been applied to the NP, the molecule **(1)** is heated. The heating of the surface-bound initiator results in a bond break between C and O. The resulting carbon radical can react with the double bond of the monomer, forming the polymer chain on the surface **(2)**. The reaction was carried out in toluene (Tol) under the exclusion of oxygen.*

The NMP on the UiO-66-NH_2 surface was carried out by washing 100 mg of the UiO-66-NH-AA NP (1.00 equiv.) three times with 2 ml of Tol and then dispersed them in 5 ml Tol in a 20 ml Schlenk flask. Then 4 ml of the monomer poly(ethylene oxide) methyl-p-vinylbenzyl-ether (SPEGA) (6.55 mmol, 20.0 equiv.) and 100 mg of free TEMPO-alkoxyamine (AA) (0.33 mmol, 1.00 equiv.) was added. The mixture was freeze-pump-thawed three times until no further gas evolution occurred. Afterward, the reaction flask was placed in a preheated oil bath at 130 °C and was stirred for 24 h. After the flask was cooled down to RT, it was washed three times with 5 ml THF/EtOH (2:1, v:v) to remove free monomer and polymer from the solution. The surface-coated MOF/polymer NPs (UiO-66-NH-AA-SPEGA) were stored in EtOH and characterized with DLS, SEM,

XRD, ToF-SIMS, and ATR-IR. Additional data supporting the chemical synthesis results is available via the Chemotion repository: https://doi.org/10.14272/reaction/SA-FUHFF-UHFFFADPSC-UHTPHSRMIL-UHFFFADPSC-NUHFF-NUHFF-NUHFF-ZZZ.

With MAMA-SG1:

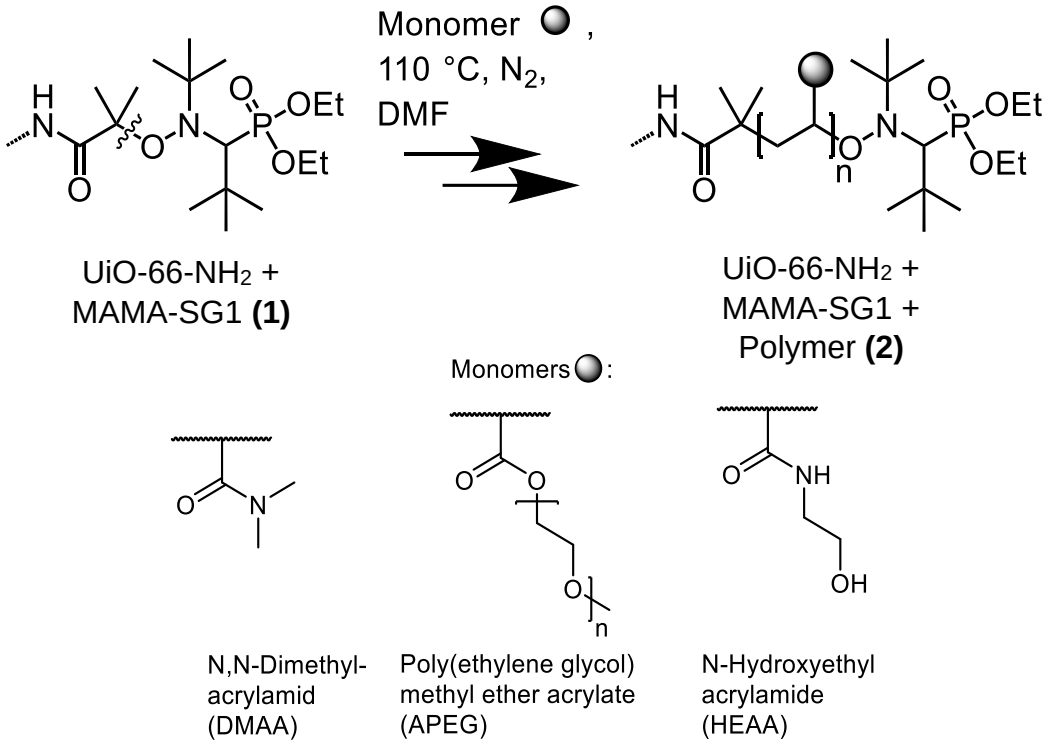

*Figure 55: Reaction scheme of the nitroxide-mediated polymerization (NMP) on the surface of UiO-66-NH_2 nanoparticles (NPs) with the initiator MAMA-SG1. After the initiator has been applied to the NPs, the molecule **(1)** is heated. The heating of the surface-bound initiator results in a bond break between C and O. The resulting carbon radical can react with the double bond of the monomer, forming the polymer chain **(2)** (two-step synthesis). Additionally, the UiO-66-NH_2 NPs are heated in the presence of the initiator MAMA-SG1 and the respective monomer. In this case, the bond formation on the metal-organic framework (MOF) surface happens simultaneously with polymerization (one-step synthesis). The reaction was carried out in dimethylformamide (DMF) under the exclusion of oxygen.*

I tested two different reaction procedures for the polymerization on the MOF surface with MAMA-SG1. First is the two-step polymerization on the previously synthesized UiO-66-NH-MAMA NP, and the second is the polymerization with free MAMA-SG1 and monomer directly on the surface of pristine UiO-66-NH_2 particles in a one-step reaction.

For the two-step polymerization with the previously synthesized UiO-66-NH-MAMA NP, first 25.0 mg of free MAMA-SG1 was filled into a Schlenk vial and degassed three times until it was oxygen-free. Meanwhile, 50.0 mg of a 10.0 mg/ml suspension of UiO-66-NH-MAMA was filled into a Schlenk tube, and freeze-pump-thawed three times until it was oxygen-free. Then, one of the respective oxygen-free monomers (poly(ethylene glycol) methyl ether acrylate (APEG), N-hydroxyethylacrylamide (HEAA), or N,N-dimethylacrylamide (DMAA)) was added, and the solution was freeze-pump-thawed again. Afterward, the suspension was combined with the degassed MAMA-SG1, heated to 110 °C, and stirred for a respective amount of time. Table 2 gives the exact monomer amount [equiv.] and time for each polymerization.

Table 2: Two-step procedure for three different metal-organic framework (MOF)/polymer nanoparticles (NPs) using poly(ethylene glycol) methyl ether acrylate (APEG), N-hydroxyethylacrylamide (HEAA), or N,N-dimethylacrylamide (DMAA). The synthesis was carried out with the pristine UiO-66-NH-MAMA modified MOF NP and the free MAMA-SG1 nitroxide-mediated polymerization (NMP) initiator in a dimethylformamide (DMF) solution. The table gives an overview of the monomer amounts used [equiv.] and the polymerization time.

Sample	Time[h]	APEG [equiv.]	HEAA [equiv.]	DMAA [equiv.]
UiO-66-NH-APEG	24	200	0	0
UiO-66-NH-HEAA	24	0	200	0
UiO-66-NH-DMAA	24	0	0	200

For the one-step polymerization on the pristine UiO-66-NH_2 NPs, 5 ml of a UiO-66-NH_2 suspension (150 mg, 30.0 mg/ml) in DMF was filled into a 20 ml Schlenk vial and degassed with the freeze-pump-thaw method. Then the respective oxygen-free monomers (APEG, HEAA, and DMAA) were added, and the solution was freeze-pump-thawed again. Meanwhile, 25 mg of the MAMA-SG1 was filled into a 30 ml Schlenk vial and degassed three times until it was oxygen free. The MOF and monomer suspension was then added to the MAMA-SG1 powder (under the exclusion of oxygen), and the suspension was heated to 110 °C and stirred for a respective amount of time. Table 3 gives the exact monomer amount [equiv.] and time for each polymerization:

Table 3: One-step procedure for four different metal-organic framework (MOF)/polymer or MOF/copolymer nanoparticles (NPs) using poly(ethylene glycol) methyl ether acrylate (APEG), N-hydroxyethylacrylamide (HEAA), and/or N,N-dimethylacrylamide (DMAA). The synthesis was carried out with the pristine UiO-66-NH_2 NP and the free MAMA-SG1 nitroxide-mediated polymerization (NMP) initiator in a dimethylformamide (DMF) solution. The table gives an overview of the monomer amounts used [equiv.] and the polymerization time.

Sample	Time[h]	APEG [equiv.]	HEAA [equiv.]	DMAA [equiv.]
UiO-66-NH-MAMA-APEG/DMAA (6 h)	6	200	0	122.4
UiO-66-NH-MAMA-HEAA (8 h)	8.15	0	200	0
UiO-66-NH-MAMA-APEG/HEAA/DMAA (23 h)	23	149.8	0.42	199.6
UiO-66-NH-MAMA-HEAA/DMAA (24 h)	24	0	128.5	130.4

After the two-step and one-step polymerization on the surface, the MOF/polymer precipitates were washed with a diethyl ether and DMF mixture and centrifuged. Free polymer chains were present in the solution because free MAMA-SG1 was added to the reaction mixture. Therefore, care was taken to ensure that the volume ratio of the two washing solvents was adjusted so that the polymer-modified particles precipitated, but the free polymer remained in the solution. To ensure this, an NMR experiment of the supernatant after every washing step was conducted to monitor the remaining polymer in

suspension. The precipitated MOF/polymer NPs were washed until the supernatant was polymer-free.

After removing the free polymer, the MOF/polymer NPs were dried in a vacuum oven at 30 °C for 24 h. The free polymer in the withheld supernatant from the washing steps was precipitated in diethyl ether and dried in a vacuum oven at 30 °C for 24 h. The MOF/polymer NPs were characterized using ATR-IR, ToF-SIMS, XRD, and DLS. The free polymer in the solution was analyzed using gel permeation chromatography (GPC).

8.2.5 Protein Adsorption Test

The protein adsorption test was carried out using the UiO-66-NH-SPEGA particles. Therefore, 300 µg of the UiO-66-NH-SPEGA NPs were washed three times with 1 ml of an ammonium acetate (CH_3COONH_4) (7.07 mg/ml) solution in water in a 1 ml Eppendorf tube. Then, the supernatant was removed, and the NPs were dispersed in a 100 µg/ml human serum albumin (HSA) solution in 77.0 mg/ml $NH_4CH_3CO_2$. This procedure was implemented for the pristine and the UiO-66-NH-AA-SPEGA particles. The suspensions were incubated for 4 h at 37 °C and centrifuged for 10 minutes at 10,000 rpm. The precipitate was discarded, and 25 µl of the supernatant was mixed with 200 µl of the bicinochinic (BCA) reagent (50:1 reagent A to B) in a 96-well plate. For every sample, three replicates were produced. The plate was incubated for 30 minutes at 37 °C, and the absorbance was then measured at 532 nm.

8.2.6 Nitroxide Exchange Reaction of TEMPO with RGD-Nitroxide

The RGD-nitroxide used in this reaction was synthesized by Julian Brückel in the group of Prof. Stefan Bräse at KIT. For the nitroxide exchange reaction (NER), 2.00 mg of the UiO-66-NH-SPEGA NP was dissolved in 2 ml DMF in a 10 ml Schlenk tube. Then, around 1.00 mg of the previously synthesized RGD-nitroxide was added, and the mixture was freeze-pump-thawed three times to remove oxygen from the solution. After that, the suspension was placed in a preheated oil bath at 100 °C and stirred for 24 h. After cooling the flask, the received precipitate (UiO-66-NH-SPEGA-RGD) was washed three times with 1 ml DMF, dried under reduced pressure, and analyzed using ToF-SIMS. Additional data supporting the analysis of the target compound is available via the Chemotion

repository: https://doi.org/10.14272/reaction/SA-FUHFF-UHFFFADPSC-UHFFFADPSC-UHFFFADPSC-NUHFF-NUHFF-NUHFF-ZAZ.7.

8.2.7 Drug Loading

In Pristine MOF Nanoparticles

Different solvent combinations of chloroform ($CHCl_3$) and Cyc were prepared for the kinetic study of the curcumin uptake. Therefore, stock solutions of 0.90 mg/ml curcumin were prepared in $CHCl_3$, $CHCl_3$/Cyc (2:1, v:v), and $CHCl_3$/Cyc (1:1, v:v). Then, three suspensions of 1.00 mg of the pristine MOF (UiO-66-NH_2) NP were prepared in 4 ml of the respective $CHCl_3$/Cyc solution in 20 ml scintillation vials. The uptake of curcumin was monitored by measuring the supernatant at specific time steps over 168 h using ultraviolet and visible spectroscopy (UV-Vis). Three measurements of the same sample were carried out for each time step, and the average was formed.

In MOF/Polymer Nanoparticles

For the drug loading into the pores of the MOF/polymer NP, a stock solution of 0.13 mg/ml curcumin in $CHCl_3$/Cyc was prepared. Then 4-7 mg of every MOF/polymer was given into 4 ml of the curcumin solution in 20 ml scintillation vials and left standing for 24 h. Afterward, the reduced curcumin concentration in the supernatant was measured with UV-Vis, and the absorption in the particles was calculated. Three measurements of the same sample were carried out, and the average was formed.

8.2.8 Cell Cytotoxicity Tests

A respective amount of the MOF/polymer NPs was dispersed in 1 ml sterilized water in Eppendorf tubes for the cell cytotoxicity tests. The MCF-7 cells were cultivated in Dulbecco's Modified Eagle Medium (DMEM) with 10 % fetal bovine serum (FBS), 1 % GlutaMAX™, and 1 % Penicillin in a 5 % CO_2 incubator at 37 °C. The media was changed every two days, and the cells were sub-cultured every 4 days. A 96-well plate was used for the cell study. Around 4000 cells in 200 µl cell growth media were seeded into every well. The plate was incubated for 24 h at 37 °C. Then, the media was removed, and the wells were filled with 100 µl double media (double DMEM, 20 % FBS, 2 % GlutaMAX™, and 2 % Penicillin). 100 µl of the MOF/polymer dispersions were added

to the wells. Every sample was placed in at least 3 different wells (3 replicates), and additionally, 3 wells with 100 µl sterilized water were prepared as a reference. The well-plate was incubated at 37 °C for 72 h. Afterward, the cells were washed and treated according to the Sulforhodamine B (SRB) assay procedure.[159] The absorption was then measured at 490 and 570 nm.

8.3 Machine Learning supporting MOF Synthesis

The following paragraphs describe the synthesis and test approaches for the machine learning (ML) support for MOF films in Chapter 6.

8.3.1 MOF Thin Film Synthesis – Chemical Vapor-Assisted Conversion

The chemical vapor-assisted conversion method (VAC) was carried out using a modified synthesis method to produce a UiO-66-NH_2 film.[29] First, the precursor solution was prepared. Therefore, a 20.0 mg/ml solution with 11.6 mg $ZrOCl_2$ (0.65 mmol, 1.00 equiv.) and 6.52 mg BDC-NH_2 (0.043 mmol, 1.00 equiv.) was prepared in a 20 ml crimp vial with an aluminum cap equipped with a Teflon septum and sonicated for 5 minutes until a clear solution was obtained. Then 300 µl were removed and filled with DMF until the desired concentration was reached. Additionally, a specific amount of AcOH was added. Meanwhile, the bottom of a wide neck 250 ml DURAN glass was filled with Raschig rings, and a specific amount of the vapor source, consisting of DMF and AcOH, was filled into the vial. The ratio of DMF to AcOH in the vapor source was varied during the synthesis. A glass wafer (1.3 cm diameter and 1 mm thickness) was cleaned using a UV-Ozone cleaner for 30 minutes and stored in DMF. The wafer was placed on top of the Raschig rings in the glass reaction vial, and a specific amount of the precursor solution was placed on top. The reaction vial was closed, put into a preheated oven at 120 °C, and left there for a specific time. Figure 56 shows the experimental setup. After the reaction, the glass wafer was dried under reduced pressure and analyzed with XRD and SEM.

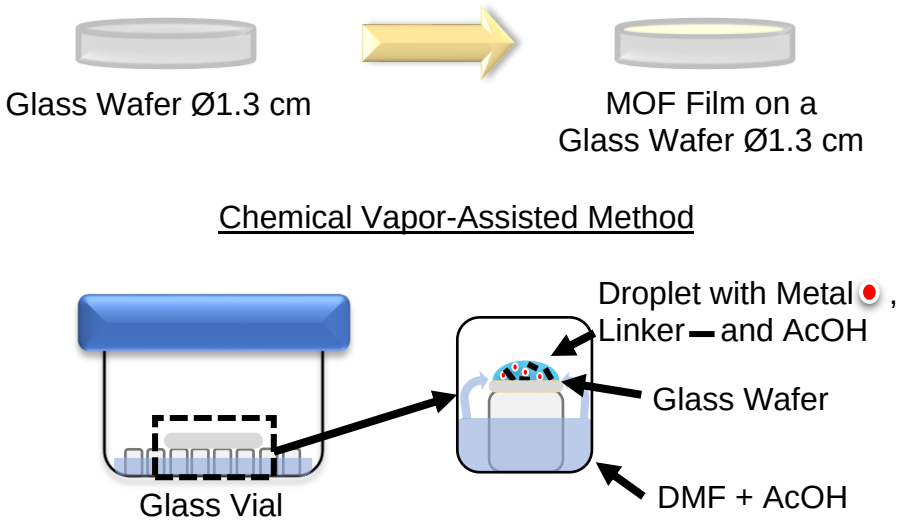

Figure 56: General principle of the chemical vapor-assisted method (VAC). A substrate is placed on top of Raschig rings over a vapor source. Carefully, a drop of the precursor solution (containing metal, linker, and modulator) is placed on top of the wafer. The reaction vessel is closed and heated up for a defined time. During that time, a metal-organic framework (MOF) film forms on the wafer's surface.

The two employed algorithms predicted the parameters used for the synthesis procedure within specific previously established ranges throughout the experiments. Table 4 shows the parameters' corresponding ranges. The exact reaction conditions for all generations carried out can be found in Appendix F.

8.3.2 Machine Learning Setup

The VAC provides the parameter space for the optimization carried out by the two ML algorithms. During the optimization, the concentration of metal and linker [mmol/l], the amount of AcOH as a modulator in the precursor [µl], the DMF ratio to AcOH in the vapor source [0,1], the reaction time [h], the volume of the surface drop on the wafer [µl], and the vapor source volume [ml] were varied. Table 4 shows the parameters and corresponding ranges.

Table 4: The parameter sets for the optimization strategy with the two machine learning (ML) algorithms. The parameters were adjusted according to the user-provided range values.

Parameter	Ranges
Concentration of metal and linker [mmol/l]	1-20
Amount of modulator [µl]	0-26
DMF ratio to AcOH in the vapor source	0-1
Reaction time [h]	1-5
Volume surface drop [µl]	20-50
Vapor source volume [ml]	1-10

The two ML algorithms used in this thesis are shown below. Both were used for the specific purpose described above and are openly available.

Bayesian Optimization Algorithm

The Bayesian optimization (BO) algorithm was implemented using the platform AX. A random search in the parameter space was used to create the initial set. For the hyperparameters of the algorithm, I chose a Gaussian model as the surrogate model and the expected improvement (EI) method as the acquisition function.

Synthesis Condition Finder – Genetic Algorithm

For the genetic algorithm (GA), I used the open available Synthesis Condition Finder (SyCoFinder).[85] The SyCoFinder predicts the initial set via a MaxMin approach.[85] Based on the first experiments, it then predicts the next round of experiments using a GA.

8.3.3 Fitness Calculation

For the evaluation of the experiments, the crystallinity was measured via XRD, and the surface coverage was determined using SEM pictures. XRD was measured for every sample, and the crystallinity [%] was determined using the software DIFFRAC.EVA Version 5.2.0.3 (32-bit) after background correction. The surface coverage was determined using SEM pictures. Therefore, images with the magnification 2400x and 15000x were recorded on eight different positions on the surface at 0°, 45°, 90°, 135°, 180°, 225°, 270°, and 315° (see Figure 57 (A)). The received images were then processed using a Python script to calculate the ratio of particles from the picture (see Figure 57 (B)). This procedure was repeated for all 16 images on one sample, and the average was generated, reflecting the surface coverage [%].

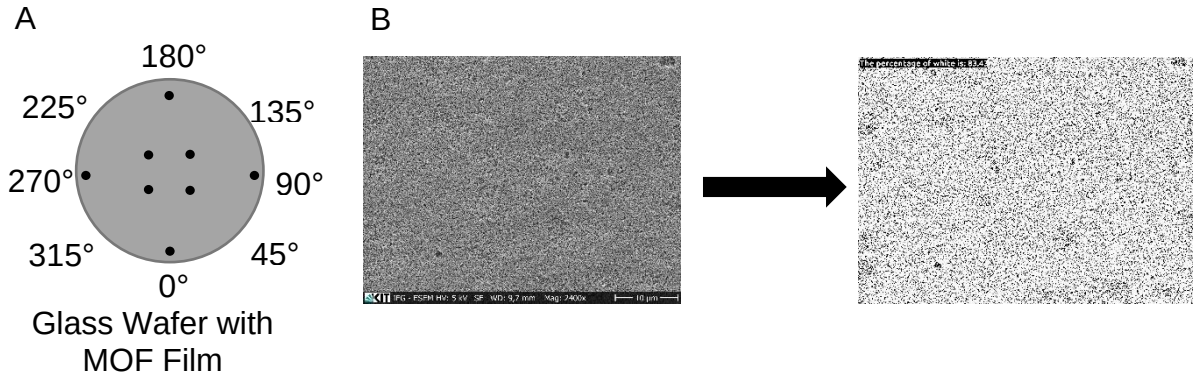

Figure 57: Scanning electron microscopy (SEM) evaluation of the experiments predicted with the two machine learning (ML) algorithms. The illustration in A shows the positions on which SEM images were taken to evaluate the surface coverage on a glass wafer. Additionally, B shows the process of determining the particle ratio in the pictures. A Python script was used to calculate the particle coverage on the surface [%].

The crystallinity and the surface coverage were used to form a fitness function to assess the quality of a sample (see Equation 8).

$$Fitness = Crystallinity\ [\%] * Surface\ Coverage\ [\%]$$

Equation 8: The shown fitness formula reflects the criteria for the quality of a produced sample. All produced samples were classified with the fitness formula, and the experiments and their fitness were used to train the algorithms.

9. Abbreviations

General

AA	TEMPO-alkoxyamine
MeCN	Acetonitrile
AcOH	Acetic acid
APEG	Poly(ethylene glycol) methyl ether acrylate
ATRP	Atom transfer radical polymerization
BDC	Terephthalic acid
BDC-Br	2-Bromoterephthalic acid
BDC-NH_2	2-Aminoterephthalic acid
BDC-NO_2	2-Nitroterephthalic acid
BO	Bayesian optimization
BSE	Backscattered electrons
δ	Chemical shift
$CHCl_3$	Chloroform
CRP	Controlled radical polymerization
Cyc	Cyclohexane
dia	diamondoid
$Đ_M$	Molar mass dispersity
DMAA	N,N-dimethylacrylamide
DMEM	Dulbecco's Modified Eagle Medium
DMF	Dimethylformamide
Na_2BDC	Disodium terephthalate
EDC×HCl	N(3-dimethylaminopropyl)N’ethylcarbodiimide hydrochloride
EI	Expected improvement
equiv.	equivalent
EtOAc	Ethyl acetate
EtOH	Ethanol

FBS	Fetal bovine serum
GA	Genetic algorithm
HEAA	N-hydroxyethylacrylamide
HICA	2-Imidazolecarboxaldehyde
HKUST-1	Hong Kong University [$Cu_3(btc)_2$]
HmIM	2-Methylimidazole
HSA	Human serum albumin
LBL	Layer-by-Layer
m	mutant
MeOH	Methanol
MIL	Matériaux de l'Institut Lavoisier
ML	Machine learning
MOF	Metal-organic framework
NER	Nitroxide exchange reaction
NMP	Nitroxide-mediated polymerization
NP	Nanoparticle
OM	Optical microscopy
PAD	Phenacrylate decarboxylase
pCA	p-coumaric acid
pHS	p-hydroxystyrene
QCM-D	Quartz Crystal Microbalance and Dissipation
RAFT	Reversible addition-fragmentation chain-transfer polymerization
RT	room temperature
SAM	Self-assembled monolayer
SBU	Secondary building unit
SE	Secondary electrons
sod	sodalite
SPEGA	Poly(ethylene oxide) methyl-p-vinylbenzyl-ether

sulfo-NHS	N-hydroxysulfosuccinimide sodium salt
SURMOF	Surface-anchored metal-organic framework
SyCoFinder	Synthesis Condition Finder
TEMPO	2,2,6,6-Tetramethylpiperidin-1-yl)oxyl
TFA	Trifluoroacetic acid
THF	Tetrahydrofuran
Tol	Toluene
UiO	Universitetet i Oslo
VAC	Chemical vapor-assisted method
WL	wavelength
woE	without enzyme
wT	wild type
ZIF	Zeolitic imidazole framework

Characterization Techniques

ATR-IR	Attenuated total reflection infrared spectroscopy
DLS	Dynamic light scattering
GPC	Gel permeation chromatography
IR	Infrared spectroscopy
NMR	Nuclear magnetic resonance
SEM	Scanning electron microscopy
ToF-SIMS	Time-of-flight secondary ion mass spectrometry
UV-Vis	Ultraviolet and visible spectroscopy
XRD	X-ray diffraction

10. References

[1] C. R. Groom, I. J. Bruno, M. P. Lightfoot, S. C. Ward, *Acta Crystallogr., Sect. B: Struct. Sci., Cryst. Eng. Mater.* **2016**, *72*, 171.

[2] H. Furukawa, K. E. Cordova, M. O'Keeffe, O. M. Yaghi, *Science* **2013**, *341*, 1230444.

[3] H. Furukawa, N. Ko, Y. B. Go, N. Aratani, S. B. Choi, E. Choi, A. O. Yazaydin, R. Q. Snurr, M. O'Keeffe, J. Kim et al., *Science* **2010**, *329*, 424.

[4] Z. Wang, A. Bilegsaikhan, R. T. Jerozal, T. A. Pitt, P. J. Milner, *ACS Appl. Mater. Interfaces* **2021**, *13*, 17517.

[5] M. Kalaj, K. C. Bentz, S. Ayala, J. M. Palomba, K. S. Barcus, Y. Katayama, S. M. Cohen, *Chem. Rev.* **2020**, *120*, 8267.

[6] N. K. Maddigan, A. Tarzia, D. M. Huang, C. J. Sumby, S. G. Bell, P. Falcaro, C. J. Doonan, *Chem. Sci.* **2018**, *9*, 4217.

[7] W. Liang, H. Xu, F. Carraro, N. K. Maddigan, Q. Li, S. G. Bell, D. M. Huang, A. Tarzia, M. B. Solomon, H. Amenitsch et al., *J. Am. Chem. Soc.* **2019**, *141*, 2348.

[8] M. Sánchez-Sánchez, N. Getachew, K. Díaz, M. Díaz-García, Y. Chebude, I. Díaz, *Green Chem.* **2015**, *17*, 1500.

[9] Q. Li, Y. Pan, H. Li, L. Alhalhooly, Y. Li, B. Chen, Y. Choi, Z. Yang, *ACS Appl. Mater. Interfaces* **2020**, *12*, 41794.

[10] A. C. McKinlay, R. E. Morris, P. Horcajada, G. Férey, R. Gref, P. Couvreur, C. Serre, *Angew. Chem., Int. Ed.* **2010**, *49*, 6260.

[11] H.-C. Zhou, J. R. Long, O. M. Yaghi, *Chem. Rev.* **2012**, *112*, 673.

[12] J.-P. Zhang, Y.-B. Zhang, J.-B. Lin, X.-M. Chen, *Chem. Rev.* **2012**, *112*, 1001.

[13] O. M. Yaghi, H. Li, *J. Am. Chem. Soc.* **1995**, *117*, 10401.

[14] H. Li, M. Eddaoudi, M. O'Keeffe, O. M. Yaghi, *Nature* **1999**, *402*, 276.

[15] D. Farrusseng, *Metal-organic frameworks*. *Applications from catalysis to gas storage*, WILEY-VCH Verlag GmbH & Co. KGaA, Weinheim, Germany, **2011**.

[16] S. R. Batten, N. R. Champness, X.-M. Chen, J. Garcia-Martinez, S. Kitagawa, L. Öhrström, M. O'Keeffe, M. Paik Suh, J. Reedijk, *Pure and Appl. Chem.* **2013**, *85*, 1715.

[17] H. Furukawa, O. M. Yaghi, *J. Am. Chem. Soc.* **2009**, *131*, 8875.

[18] O. K. Farha, I. Eryazici, N. C. Jeong, B. G. Hauser, C. E. Wilmer, A. A. Sarjeant, R. Q. Snurr, S. T. Nguyen, A. Ö. Yazaydın, J. T. Hupp, *J. Am. Chem. Soc.* **2012**, *134*, 15016.

[19] H. K. Chae, D. Y. Siberio-Pérez, J. Kim, Y. Go, M. Eddaoudi, A. J. Matzger, M. O'Keeffe, O. M. Yaghi, *Nature* **2004**, *427*, 523.

[20] H.-C. ". Zhou, S. Kitagawa, *Chem. Soc. Rev.* **2014**, *43*, 5415.

[21] R. J. Kuppler, D. J. Timmons, Q.-R. Fang, J.-R. Li, T. A. Makal, M. D. Young, D. Yuan, D. Zhao, W. Zhuang, H.-C. Zhou, *Coord. Chem. Rev.* **2009**, *253*, 3042.

[22] C. P. Raptopoulou, *Materials* **2021**, *14*, 310.

[23] M. Eddaoudi, D. B. Moler, H. Li, B. Chen, T. M. Reineke, M. O'Keeffe, O. M. Yaghi, *Acc. Chem. Res.* **2001**, *34*, 319.

[24] A. Schoedel, S. Rajeh, *Top. Curr. Chem.* **2020**, *378*, 19.

[25] D. Zacher, O. Shekhah, C. Wöll, R. A. Fischer, *Chem. Soc. Rev.* **2009**, *38*, 1418.

[26] O. Shekhah, H. Wang, S. Kowarik, F. Schreiber, M. Paulus, M. Tolan, C. Sternemann, F. Evers, D. Zacher, R. A. Fischer et al., *J. Am. Chem. Soc.* **2007**, *129*, 15118.

[27] H. K. Arslan, O. Shekhah, J. Wohlgemuth, M. Franzreb, R. A. Fischer, C. Wöll, *Adv. Funct. Mater.* **2011**, *21*, 4228.

[28] H. Gliemann, C. Wöll, *Mater. Today* **2012**, *15*, 110.

[29] E. Virmani, J. M. Rotter, A. Mähringer, T. von Zons, A. Godt, T. Bein, S. Wuttke, D. D. Medina, *J. Am. Chem. Soc.* **2018**, *140*, 4812.

[30] N. L. Rosi, J. Eckert, M. Eddaoudi, D. T. Vodak, J. Kim, M. O'Keeffe, O. M. Yaghi, *Science* **2003**, *300*, 1127.

[31] A. G. Wong-Foy, A. J. Matzger, O. M. Yaghi, *J. Am. Chem. Soc.* **2006**, *128*, 3494.

[32] D. Zhao, D. Yuan, H.-C. Zhou, *Energy Environ. Sci.* **2008**, *1*, 222.

[33] S. Ma, D. Sun, X.-S. Wang, H.-C. Zhou, *Angew. Chem., Int. Ed.* **2007**, *46*, 2458.

[34] a) S. Ma, X.-S. Wang, C. D. Collier, E. S. Manis, H.-C. Zhou, *Inorg. Chem.* **2007**, *46*, 8499; b) M. Dinca, J. R. Long, *J. Am. Chem. Soc.* **2005**, *127*, 9376.

[35] X. Lian, Y. Fang, E. Joseph, Q. Wang, J. Li, S. Banerjee, C. Lollar, X. Wang, H.-C. Zhou, *Chem. Soc. Rev.* **2017**, *46*, 3386.

[36] S. Okur, Z. Zhang, M. Sarheed, P. Nick, U. Lemmer, L. Heinke, *Sens. Actuators, B* **2020**, *306*, 127502.

[37] M. B. Majewski, A. J. Howarth, P. Li, M. R. Wasielewski, J. T. Hupp, O. K. Farha, *CrystEngComm* **2017**, *19*, 4082.

[38] F. Lyu, Y. Zhang, R. N. Zare, J. Ge, Z. Liu, *Nano Lett.* **2014**, *14*, 5761.

[39] F.-K. Shieh, S.-C. Wang, C.-I. Yen, C.-C. Wu, S. Dutta, L.-Y. Chou, J. V. Morabito, P. Hu, M.-H. Hsu, K. C.-W. Wu et al., *J. Am. Chem. Soc.* **2015**, *137*, 4276.

[40] a) K. S. Soppimath, T. M. Aminabhavi, A. R. Kulkarni, W. E. Rudzinski, *J. Controlled Release* **2001**, *70*, 1; b) P. Horcajada, C. Márquez-Alvarez, A. Rámila, J. Pérez-Pariente, M. Vallet-Regí, *Solid State Sci.* **2006**, *8*, 1459; c) B. Muñoz, A. Rámila, J. Pérez-Pariente, I. Díaz, M. Vallet-Regí, *Chem. Mater.* **2003**, *15*, 500.

[41] P. Horcajada, C. Serre, M. Vallet-Regí, M. Sebban, F. Taulelle, G. Férey, *Angew. Chem., Int. Ed.* **2006**, *45*, 5974.

[42] J. An, S. J. Geib, N. L. Rosi, *J. Am. Chem. Soc.* **2009**, *131*, 8376.

[43] Z. Moussa, M. Hmadeh, M. G. Abiad, O. H. Dib, D. Patra, *Food Chem.* **2016**, *212*, 485.

[44] S. Burt, *Int. J. Food Microbiol.* **2004**, *94*, 223.

[45] M. Tsotsalas, J. Liu, B. Tettmann, S. Grosjean, A. Shahnas, Z. Wang, C. Azucena, M. Addicoat, T. Heine, J. Lahann et al., *J. Am. Chem. Soc.* **2014**, *136*, 8.

[46] G. Hills, *Eur. J. Lipid Sci. Technol.* **2003**, *105*, 601.

[47] T. Nagasawa, T. Nakamura, H. Yamada, *Appl. Microbiol. Biotechnol.* **1990**, *34*, 322.

[48] J.-M. Choi, S.-S. Han, H.-S. Kim, *Biotechnol. Adv.* **2015**, *33*, 1443.

[49] R. DiCosimo, J. McAuliffe, A. J. Poulose, G. Bohlmann, *Chem. Soc. Rev.* **2013**, *42*, 6437.

[50] W. Liang, P. Wied, F. Carraro, C. J. Sumby, B. Nidetzky, C.-K. Tsung, P. Falcaro, C. J. Doonan, *Chem. Rev.* **2021**, *121*, 1077.

[51] a) A. Küchler, J. N. Bleich, B. Sebastian, P. S. Dittrich, P. Walde, *ACS Appl. Mater. Interfaces* **2015**, *7*, 25970; b) S. Fornera, T. Bauer, A. D. Schlüter, P. Walde, *J. Mater. Chem.* **2012**, *22*, 502.

[52] W. Feng, P. Ji, *Biotechnol. Adv.* **2011**, *29*, 889.

[53] J. Mehta, N. Bhardwaj, S. K. Bhardwaj, K.-H. Kim, A. Deep, *Coord. Chem. Rev.* **2016**, *322*, 30.

[54] D. S. Raja, W.-L. Liu, H.-Y. Huang, C.-H. Lin, *Comments Inorg. Chem.* **2015**, *35*, 331.

[55] A. Phan, C. J. Doonan, F. J. Uribe-Romo, C. B. Knobler, M. O'Keeffe, O. M. Yaghi, *Acc. Chem. Res.* **2010**, *43*, 58.

[56] K. S. Park, Z. Ni, A. P. Côté, J. Y. Choi, R. Huang, F. J. Uribe-Romo, H. K. Chae, M. O'Keeffe, O. M. Yaghi, *Proc. Natl. Acad. Sci. U. S. A.* **2006**, *103*, 10186.

[57] M. Gao, J. Wang, Z. Rong, Q. Shi, J. Dong, *RSC Adv.* **2018**, *8*, 39627.

[58] K. Zhang, R. P. Lively, M. E. Dose, A. J. Brown, C. Zhang, J. Chung, S. Nair, W. J. Koros, R. R. Chance, *Chem. Commun.* **2013**, *49*, 3245.

[59] F. Carraro, M. d. J. Velásquez-Hernández, E. Astria, W. Liang, L. Twight, C. Parise, M. Ge, Z. Huang, R. Ricco, X. Zou et al., *Chem. Sci.* **2020**, *11*, 3397.

[60] W. Liang, R. Ricco, N. K. Maddigan, R. P. Dickinson, H. Xu, Q. Li, C. J. Sumby, S. G. Bell, P. Falcaro, C. J. Doonan, *Chem. Mater.* **2018**, *30*, 1069.

[61] P. Küsgens, M. Rose, I. Senkovska, H. Fröde, A. Henschel, S. Siegle, S. Kaskel, *Microporous Mesoporous Mater.* **2009**, *120*, 325.

[62] P. Horcajada, C. Serre, G. Maurin, N. A. Ramsahye, F. Balas, M. Vallet-Regí, M. Sebban, F. Taulelle, G. Férey, *J. Am. Chem. Soc.* **2008**, *130*, 6774.

[63] T. Loiseau, C. Serre, C. Huguenard, G. Fink, F. Taulelle, M. Henry, T. Bataille, G. Férey, *Chem. - Eur. J.* **2004**, *10*, 1373.

[64] J. O. Hsieh, K. J. Balkus, J. P. Ferraris, I. H. Musselman, *Microporous Mesoporous Mater.* **2014**, *196*, 165.

[65] H. T. Nguyen, L. H. Thuy Nguyen, T. Le Hoang Doan, P. H. Tran, *RSC Adv.* **2019**, *9*, 9093.

[66] P. George, R. K. Das, P. Chowdhury, *Microporous Mesoporous Mater.* **2019**, *281*, 161.

[67] S. H. Dale, M. R. J. Elsegood, *Acta Crystallogr., Sect. E: Struct. Rep. Online* **2003**, *59*, m586.

[68] A. Hoshi, R. Yanai, K. Kuretani, *Chem. Pharm. Bull.* **1968**, *16*, 1655.

[69] M. Giménez-Marqués, T. Hidalgo, C. Serre, P. Horcajada, *Coord. Chem. Rev.* **2016**, *307*, 342.

[70] D. Peer, J. M. Karp, S. Hong, O. C. Farokhzad, R. Margalit, R. Langer, *Nat. Nanotechnol.* **2007**, *2*, 751.

[71] M. Manzano, M. Colilla, M. Vallet-Regí, *Expert Opin. Drug Delivery* **2009**, *6*, 1383.

[72] P. Yang, S. Gai, J. Lin, *Chem. Soc. Rev.* **2012**, *41*, 3679.

[73] P. Horcajada, T. Chalati, C. Serre, B. Gillet, C. Sebrie, T. Baati, J. F. Eubank, D. Heurtaux, P. Clayette, C. Kreuz et al., *Nat. Mater.* **2010**, *9*, 172.

[74] T. Hashem, E. P. V. Sanchez, E. Bogdanova, A. Ugodchikova, A. Mohamed, M. Schwotzer, M. H. Alkordi, C. Wöll, *Membranes* **2021**, *11*, 207.

[75] J. H. Cavka, S. Jakobsen, U. Olsbye, N. Guillou, C. Lamberti, S. Bordiga, K. P. Lillerud, *J. Am. Chem. Soc.* **2008**, *130*, 13850.

[76] M. Kandiah, M. H. Nilsen, S. Usseglio, S. Jakobsen, U. Olsbye, M. Tilset, C. Larabi, E. A. Quadrelli, F. Bonino, K. P. Lillerud, *Chem. Mater.* **2010**, *22*, 6632.

[77] A. P. Nelson, O. K. Farha, K. L. Mulfort, J. T. Hupp, *J. Am. Chem. Soc.* **2009**, *131*, 458.

[78] A. P. Nelson, D. A. Parrish, L. R. Cambrea, L. C. Baldwin, N. J. Trivedi, K. L. Mulfort, O. K. Farha, J. T. Hupp, *Cryst. Growth Des.* **2009**, *9*, 4588.

[79] T. U. Wani, S. N. Raza, N. A. Khan, *Polym. Bull.* **2020**, *77*, 3865.

[80] N. J. Butcher, G. M. Mortimer, R. F. Minchin, *Nat. Nanotechnol.* **2016**, *11*, 310.

[81] L. Shi, J. Zhang, M. Zhao, S. Tang, X. Cheng, W. Zhang, W. Li, X. Liu, H. Peng, Q. Wang, *Nanoscale* **2021**, *13*, 10748.

[82] K. Xie, Q. Fu, Y. He, J. Kim, S. J. Goh, E. Nam, G. G. Qiao, P. A. Webley, *Chem. Commun.* **2015**, *51*, 15566.

[83] K. T. Butler, D. W. Davies, H. Cartwright, O. Isayev, A. Walsh, *Nature* **2018**, *559*, 547.

[84] C. W. Coley, W. H. Green, K. F. Jensen, *Acc. Chem. Res.* **2018**, *51*, 1281.

[85] S. M. Moosavi, A. Chidambaram, L. Talirz, M. Haranczyk, K. C. Stylianou, B. Smit, *Nat. Commun.* **2019**, *10*, 539.

[86] Y. Luo, S. Bag, O. Zaremba, A. Cierpka, J. Andreo, S. Wuttke, P. Friederich, M. Tsotsalas, *Angew. Chem., Int. Ed.* **2022**, *61*, e202200242.

[87] L. Pilz, C. Natzeck, J. Wohlgemuth, N. Scheuermann, P. G. Weidler, I. Wagner, C. Wöll, M. Tsotsalas, *Adv. Mater. Interfaces* **2023**, *10*, 2201771.

[88] L. Spieß, G. Teichert, R. Schwarzer, H. Behnken, C. Genzel, *Moderne Röntgenbeugung*. *Röntgendiffraktometrie für Materialwissenschaftler, Physiker und Chemiker*, Springer Spektrum, Wiesbaden, Germany, **2019**.

[89] H.-J. Bautsch, J. Bohm, W. Kleber, *Einführung in die Kristallographie*, Oldenbourg Verlag München, München, Germany, **2010**.

[90] T. Oeser, *Kristallstrukturanalyse durch Röntgenbeugung*. *Spektroskopiekurs kompakt*, Springer Spektrum, Wiesbaden, Germany, **2019**.

[91] H. P. Klug, L. E. Alexander, *X-ray diffraction procedures : for polycrystalline and amorphous materials*, John Wiley & Sons, Ltd., New York, NY, USA, **1954**.

[92] D. L. Bish, J. E. Post, *Modern powder diffraction*, Mineralogical Society of America, Washington, D.C., USA, **1989**.

[93] Q. Yang, H.-Y. Zhang, L. Wang, Y. Zhang, J. Zhao, *ACS omega* **2018**, *3*, 4199.

[94] Z. Huang, M. Ge, F. Carraro, C. Doonan, P. Falcaro, X. Zou, *Faraday Discuss.* **2021**, *225*, 118.

[95] Z. Huang, M. Ge, F. Carraro, C. Doonan, P. Falcaro, X. Zou, *CCDC 1979160: Experimental Crystal Structure Determination*, Cambridge Crystallographic Data Centre, **2020**.

[96] C. L. Hobday, T. D. Bennett, D. Fairen-Jimenez, A. J. Graham, C. A. Morrison, D. R. Allan, T. Düren, S. A. Moggach, *CCDC 1566959: Experimental Crystal Structure Determination*, Cambridge Crystallographic Data Centre, **2018**.

[97] J. Stetefeld, S. A. McKenna, T. R. Patel, *Biophys. Rev.* **2016**, *8*, 409.

[98] B. J. Berne, R. Pecora, *Dynamic light scattering*. *With applications to chemistry, biology, and physics*, Dover Publications, Mineola, NY, USA, **2000**.

[99] C. Bellmann, A. Caspari, C. Moitzi, F. Babick, *Dynamische und elektrophoretische Lichtstreuung*. *Leitfaden zur Partikelgrößenanalyse und Zetapotenzialbestimmung*, Anton Paar GmbH, Graz, Austria, **2018**.

[100] H. Günzler, H.-U. Gremlich, *IR-Spektroskopie*. *Eine Einführung*, WILEY-VCH Verlag GmbH & Co. KGaA, Weinheim, **2003**.

[101] Y. Ozaki, C. Huck, S. Tsuchikawa, S. B. Engelsen (Eds.) *Near-infrared spectroscopy*. *Theory, spectral analysis, instrumentation, and applications*, Springer Nature, Singapore, Singapore, **2021**.

[102] M. Hesse, S. Bienz, H. Meier, L. Bigler, T. Fox, *Spektroskopische Methoden in der organischen Chemie*, Georg Thieme Verlag KG, Stuttgart, Germany, New York, NY, USA, **2016**.

[103] P. Larkin, *Infrared and Raman spectroscopy*. *Principles and spectral interpretation*, Elsevier, Amsterdam, Netherlands, Oxford, UK, Cambridge, MA, USA, **2018**.

[104] H. K. V. Lotsch, *Optik* **1970**, *32*, 116.

[105] F. Goos, H. Hänchen, *Ann. Phys.* **1943**, *435*, 383.

[106] A. Bogner, P.-H. Jouneau, G. Thollet, D. Basset, C. Gauthier, *Micron* **2007**, *38*, 390.

[107] J. Goldstein, D. E. Newbury, J. R. Michael, N. W. M. Ritchie, J. H. J. Scott, D. C. Joy, *Scanning electron microscopy and x-ray microanalysis*, Springer, New York, NY, USA, **2018**.

[108] K. Akhtar, S. A. Khan, S. B. Khan, A. M. Asiri in *Handbook of Materials Characterization* (Ed.: S. K. Sharma), Springer Nature Switzerland AG, Cham, Switzerland, **2018**, pp. 113–145.

[109] A. Ul-Hamid in *A Beginners' Guide to Scanning Electron Microscopy* (Ed.: A. Ul-Hamid), Springer Nature Switzerland AG, Cham, Switzerland, **2023**, pp. 1–14.

[110] K. D. Vernon-Parry, *III-Vs rev.* **2000**, *13*, 40.

[111] A. Ul-Hamid in *A Beginners' Guide to Scanning Electron Microscopy* (Ed.: A. Ul-Hamid), Springer Nature Switzerland AG, Cham, Switzerland, **2023**, pp. 15–76.

[112] A. Ul-Hamid in *A Beginners' Guide to Scanning Electron Microscopy* (Ed.: A. Ul-Hamid), Springer Nature Switzerland AG, Cham, Switzerland, **2023**, pp. 129–180.

[113] H. Friebolin, J. K. Becconsall, *Basic one- and two-dimensional NMR spectroscopy*, WILEY-VCH Verlag GmbH & Co. KGaA, Weinheim, Germany, **2011**.

[114] H. Friebolin, C. M. Thiele, *Ein- und zweidimensionale NMR-Spektroskopie*. *Eine Einführung*, WILEY-VCH Verlag GmbH & Co. KGaA, Weinheim, Germany, **2013**.

[115] J. B. Lambert, S. Gronert, H. F. Shurvell, *Spektroskopie*. *Strukturaufklärung in der organischen Chemie*, Pearson Education Deutschland GmbH, München, Germany, **2012**.

[116] P. J. Hore, *Nuclear magnetic resonance*, Oxford University Press, Inc., New York, NY, USA, **1995**.

[117] K. Cammann, *Instrumentelle analytische Chemie*. *Verfahren, Anwendungen und Qualitätssicherung*, Spektrum Akademischer Verlag, Heidelberg, Germany, **2010**.

[118] E. de Hoffmann, V. Stroobant, *Mass spectrometry*. *Principles and applications*, John Wiley & Sons, Ltd, Chichester, UK, **2007**.

[119] H. Budzikiewicz, M. Schäfer, *Massenspektrometrie*. *Eine Einführung*, WILEY-VCH Verlag GmbH & Co. KGaA, Weinheim, Germany, **2012**.

[120] J. C. Vickerman, D. Briggs, *ToF-SIMS*. *Materials analysis by mass spectrometry*, IM Publications, Chichester, UK, **2013**.

[121] J. Grams, *New trends and potentialities of ToF-SIMS in surface studies*, Nova Science Publishers, Inc., New York, NY, USA, **2007**.

[122] R. J. Young, P. A. Lovell, *Introduction to polymers*, CRC Press, Boca Raton, FL, USA, **2011**.

[123] M. D. Lechner, K. Gehrke, E. H. Nordmeier, *Makromolekulare Chemie*. *Ein Lehrbuch für Chemiker, Physiker, Materialwissenschaftler und Verfahrenstechniker*, Springer Spektrum, Berlin, Heidelberg, Germany, **2014**.

[124] B. Tieke, *Makromolekulare chemie*. *Eine Einführung*, WILEY-VCH Verlag GmbH & Co. KGaA, Weinheim, Germany, **2014**.

[125] P. F. W. Simon, A. Fahmi, *Polymere - Chemie und Strukturen*. *Herstellung, Charakterisierung und Werkstoffe*, WILEY-VCH Verlag GmbH & Co. KGaA, Weinheim, Germany, **2020**.

[126] L. K. Kostanski, D. M. Keller, A. E. Hamielec, *J. Biochem. Biophys. Methods* **2004**, *58*, 159.

[127] H.-H. Perkampus, *UV-VIS Spectroscopy and Its Applications*, Springer-Verlag, Berlin, Heidelberg, Germany, **1992**.

[128] a) H. Rodríguez, I. Angulo, B. de Las Rivas, N. Campillo, J. A. Páez, R. Muñoz, J. M. Mancheño, *Proteins* **2010**, *78*, 1662; b) J.-F. Cavin, L. Barthelmebs, J. Guzzo, J.

Beeumen, B. Samyn, J.-F. Travers, C. Diviès, *FEMS Microbiol. Lett.* **1997**, *147*, 291; c) J. M. Landete, H. Rodríguez, J. A. Curiel, B. de Las Rivas, J. M. Mancheño, R. Muñoz, *J. Ind. Microbiol. Biotechnol.* **2010**, *37*, 617.

[129] S. Gao, H.-N. Yu, Y.-F. Wu, X.-Y. Liu, A.-X. Cheng, H.-X. Lou, *Biochem. Biophys. Res. Commun.* **2016**, *481*, 239.

[130] M. Peng, E. Mittmann, L. Wenger, J. Hubbuch, M. K. M. Engqvist, C. M. Niemeyer, K. S. Rabe, *Chem. - Eur. J.* **2019**, *25*, 15998.

[131] D.-H. Jung, W. Choi, K.-Y. Choi, E. Jung, H. Yun, R. J. Kazlauskas, B.-G. Kim, *Appl. Microbiol. Biotechnol.* **2013**, *97*, 1501.

[132] K. Kunitsky, C. Mukesh, S. Hockessin, S. W. Shuey, B. M. Los Altos Hills Trost, M. E. Wilmington Wagman, WO2005097719A, 2005.

[133] E. Nomura, A. Hosoda, H. Mori, H. Taniguchi, *Green Chem.* **2005**, *7*, 863.

[134] S. A. Basnayake, J. Su, X. Zou, K. J. Balkus, *Inorg. Chem.* **2015**, *54*, 1816.

[135] K. Liang, R. Ricco, C. M. Doherty, M. J. Styles, S. Bell, N. Kirby, S. Mudie, D. Haylock, A. J. Hill, C. J. Doonan et al., *Nat. Commun.* **2015**, *6*, 7240.

[136] A. Z. Wilczewska, K. Niemirowicz, K. H. Markiewicz, H. Car, *Pharmacol. Rep.* **2012**, *64*, 1020.

[137] a) K. Li, Z. Yu, I. Dovgaliuk, C. Le Coeur, V. Lütz-Bueno, E. Leroy, B. Brissault, Y. de Rancourt Mimerand, M. Lepoitevin, C. Serre et al., *Chem. Commun.* **2023**, *59*, 4923; b) C. Boyer, V. Bulmus, T. P. Davis, V. Ladmiral, J. Liu, S. Perrier, *Chem. Rev.* **2009**, *109*, 5402.

[138] R. B. Grubbs, *Polym. Rev.* **2011**, *51*, 104.

[139] a) I. Wessely, V. Mugnaini, A. Bihlmeier, G. Jeschke, S. Bräse, M. Tsotsalas, *RSC Adv.* **2016**, *6*, 55715; b) C. J. Hawker, G. G. Barclay, J. Dao, *J. Am. Chem. Soc.* **1996**, *118*, 11467.

[140] S. Spiegel, I. Wagner, S. Begum, M. Schwotzer, I. Wessely, S. Bräse, M. Tsotsalas, *Langmuir* **2022**, *38*, 6531.

[141] I. Wagner, S. Spiegel, J. Brückel, M. Schwotzer, A. Welle, M. H. Stenzel, S. Bräse, S. Begum, M. Tsotsalas, *Macromol. Mater. Eng.* **2023**, *308*, 2300048.

[142] a) J. P. Blinco, K. E. Fairfull-Smith, A. S. Micallef, S. E. Bottle*, *Polym. Chem.* **2010**, *1*, 1009; b) Y. Jia, Y. Matt, Q. An, I. Wessely, H. Mutlu, P. Theato, S. Bräse, A. Llevot, M. Tsotsalas, *Polym. Chem.* **2020**, *11*, 2502.

[143] E. Ruoslahti, M. D. Pierschbacher, *Science* **1987**, *238*, 491.

[144] A. Goel, A. B. Kunnumakkara, B. B. Aggarwal, *Biochem. Pharmacol.* **2008**, *75*, 787.

[145] J. Chen, Z.-M. He, F.-L. Wang, Z.-S. Zhang, X. Liu, D.-D. Zhai, W.-D. Chen, *Eur. J. Pharmacol.* **2016**, *772*, 33.

[146] B. B. Aggarwal, A. Kumar, A. C. Bharti, *Anticancer Res.* **2003**, *23*, 363.

[147] A. A. M. El-Shafey, M. H. A. Hegab, M. M. E. Seliem, A. M. A. Barakat, N. E. Mostafa, H. A. Abdel-Maksoud, R. M. Abdelhameed, *J. Mater Sci.: Mater. Med.* **2020**, *31*, 90.

[148] A. V. Lee, S. Oesterreich, N. E. Davidson, *J. Natl. Cancer Inst.* **2015**, *107*, djv073.

[149] Ş. Comşa, A. M. Cîmpean, M. Raica, *Anticancer Res.* **2015**, *35*, 3147.

[150] M. A. Gelbart, J. Snoek, Adams, Ryan P., **2014**, arXiv preprint DOI: 10.48550/arXiv.1403.5607.

[151] D. J. Lizotte, Practical Bayesian Optimization, Dissertation, Departement of Computer Science, Edmonton, Alberta, Canada, **2008**.

[152] Frazier, Peter I., **2018**, arXiv preprint DOI: 10.48550/arXiv.1807.02811.

[153] M. Srinivas, L. M. Patnaik, *Computer* **1994**, *27*, 17.

[154] S. G. Guillen, J. Parres-Gold, A. Ruiz, E. Lucsik, B. Dao, T. K. L. Hang, M. Chang, A. O. Garcia, Y. Wang, F. Tian, *Langmuir* **2022**, *38*, 16014.

[155] L. Talirz, S. Kumbhar, E. Passaro, A. V. Yakutovich, V. Granata, F. Gargiulo, M. Borelli, M. Uhrin, S. P. Huber, S. Zoupanos et al., *Sci. Data* **2020**, *7*, 299.

[156] A. Schaate, P. Roy, A. Godt, J. Lippke, F. Waltz, M. Wiebcke, P. Behrens, *Chem. - Eur. J.* **2011**, *17*, 6643.

[157] D. Le, T. N. T. Phan, L. Autissier, L. Charles, D. Gigmes, *Polym. Chem.* **2016**, *7*, 1659.

[158] A. Zimpel, T. Preiß, R. Röder, H. Engelke, M. Ingrisch, M. Peller, J. O. Rädler, E. Wagner, T. Bein, U. Lächelt et al., *Chem. Mater.* **2016**, *28*, 3318.

[159] V. Vichai, K. Kirtikara, *Nat. Protoc.* **2006**, *1*, 1112.

11. Appendix

A. Publications

S. Spiegel, I. Wagner, S. Begum, M. Schwotzer, I. Wessely, S. Bräse, M. Tsotsalas, *Langmuir* **2022**, 38, 6531.

L. Pilz, C. Natzeck, J. Wohlgemuth, N. Scheuermann, P. G. Weidler, I. Wagner, C. Wöll, M. Tsotsalas, *Adv. Mater. Interfaces* **2023**, 10, 2201771.

I. Wagner, S. Spiegel, J. Brückel, M. Schwotzer, A. Welle, M. H. Stenzel, S. Bräse, S. Begum, M. Tsotsalas, *Macromol. Mater. Eng.* **2023**, 308, 2300048.

I. Wagner, E. Bevier, M. Krause, L. Torresi, P. Friederich, M. Tsotsalas; “Bayesian Optimization vs. Genetic Algorithm: A Comparison at the Use Case of MOF Film Growth Optimization” [in preparation]

E. Mittmann, I. Wagner, E. Bevier, K. Rabe, and M. Totsalas, „Using Metal-Organic Frameworks to Retaine the Enzymatic Activity for the Phenacrylate Decarboxylase for two Weeks in Organic Solvents“ [in preparation]

I. Wagner, A. Welle, M. H. Stenzel, S. Begum, M. Tsotsalas, „MOF/Polymer Nanoparticles and their Applicability for Drug Delivery in Cancer Cells“ [in preparation]

B. Conference Contributions

Poster presentation:

Ilona Wagner, Simon Spiegel, Salma Begum, Frank Kirschhöfer, Guillaume Delaittre, Manuel Tsotsalas “From Polyethylene glycol coated MOF Nanoparticles to a new Screening Method for Optimized Polymer MOF Hybrid Materials - Reducing Stealth Effects and Enhancing Drug Delivery Processes” **33. Deutsche Zeolith-Tagung**, Frankfurt, Germany 2022

Poster presentation:

Ilona Wagner, Simon Spiegel, Salma Begum, Frank Kirschhöfer, Guillaume Delaittre, Manuel Tsotsalas, “From Polyethylene glycol coated MOF Nanoparticles to a new Screening Method for Optimized Polymer MOF Hybrid Materials - Reducing Stealth Effects and Enhancing Drug Delivery Processes”, **Material Research Society (MRS) Spring Meeting 2022**, Hawaii, USA, 2022

Poster presentation:

Ilona Wagner, Simon Spiegel, Salma Begum, Frank Kirschhöfer, Guillaume Delaittre, Manuel Tsotsalas “Optimizing the Synthesis of MOF-Polymer-Hybrid Materials with a New Machine Learning-Based Screening Method – to Improve Drug Delivery Processes”, **8th International Conference on Metal-Organic Frameworks and Open Framework Compounds,** Dresden, Germany, 2022

Poster presentation:

Ilona Wagner, Simon Spiegel, Julian Brückel, Matthias Schwotzer, Alexander Welle, Martina Stenzel, Stefan Bräse, Salma Begum, Manuel Tsotsalas “MOF-Polymer Nanoparticle - Synthesis via Nitroxide Mediated Polymerization - for Improved Drug Delivery into Cancer Cells”, **5th European Conference on Metal-Organic Frameworks and Porous Polymers**, Granada, Spain, 2023

C. Awards

BIF-IGS Travel Competitions Award over 1000 € for the Material Research Society (MRS) Spring Meeting 2022, Hawaii, USA, 2022

KHYS Research Travel Grant over 9570 € for the Research Stay in the group of Martina Stenzel at the University of New South Wales (UNSW) from January to June 2023, Sydney, Australia, 2023

Otto Bayer Fellowships in Drug Discovery over 9870 €, for the Research Stay in the group of Martina Stenzel at the University of New South Wales (UNSW) from January to June 2023, Sydney, Australia, 2023

Travel Grant of the Max-Buchner-Forschungsstiftung over 500 € for the "5th European Conference on Metal-Organic Frameworks and Porous Polymers" (24. - 27. September 2023) in Granda, Spain, 2023

D. Societies

BioInterfaces International Graduate School (BIF-IGS)

since 2021

CDI Collège des Ingénieurs (Munich) – MBA for Engineers and Scientists

Science and Management Program since 2021

E. Curriculum Vitae

Personal Details

Name:	Ilona Wagner
Date of Birth:	December 05, 1994
Place of Birth:	Waldkirch

Work Experience

since 2021	**CDI Collège des Ingénieurs, Munich** Science and Management Program
03/2021 – 02/2024	**KIT (Karlsruhe Institute of Technology)** Ph.D. Student
01/2023 – 06/2023	**University of New South Wales: Research Exchange** International Exchange with Prof. Martina Stenzel at the University of New South Wales (UNSW) in Sydney, Australia
01/2020 – 06/2020	**BASF (Explore Together)** Intercultural Internship at BASF in Tarrytown, NY, USA
09/2018 – 02/2019	**KIT (Karlsruhe Institute of Technology)** Research Assistant at Aquarray (Startup at KIT Campus North)
01/2018 – 03/2018	**KIT (Karlsruhe Institute of Technology)** Research Assistant at the Institute for Chemical Technology and Polymerchemistry
10/2017 – 09/2018	**KIT (Karlsruhe Institute of Technology)** Research Assistant at the Institute for Food Chemistry and Toxicology

Academic Career

2018 – 2021	**Karlsruher Institute of Technology (KIT)** Master of Chemistry | 1.2
2014 – 2018	**Karlsruher Institute of Technology (KIT)** Bachelor of Chemistry | 1.7

Extracurricular Activities

since 05/2019	**Social Engagement** Board member of DLRG Stadtgruppe Karlsruhe eV.
since 10/2017	**Social Engagement** DLRG Stadtgruppe Karlsruhe eV.
12/2011 – 06/2014	**Social Engagement** DLRG Freiamt

F. Appendix

TEMPO-alkoxyamine (AA) NMR

^{1}H NMR of TEMPO-alkoxyamine (4-(1-((2,2,6,6-Tetramethylpiperidin-1-yl)oxy)ethyl) benzoic acid):

1H NMR (400 MHz, $CDCl_3$): δ (ppm) = 8.07 (d, J = 8.05 Hz, 2H), 7.43 (d, J = 8.0 Hz, 2H), 4.86 (q, J = 6.94 Hz, 1H), 1.50 (d, J = 6.48 Hz, 3H), 1.30-0.56 (m, 18H).

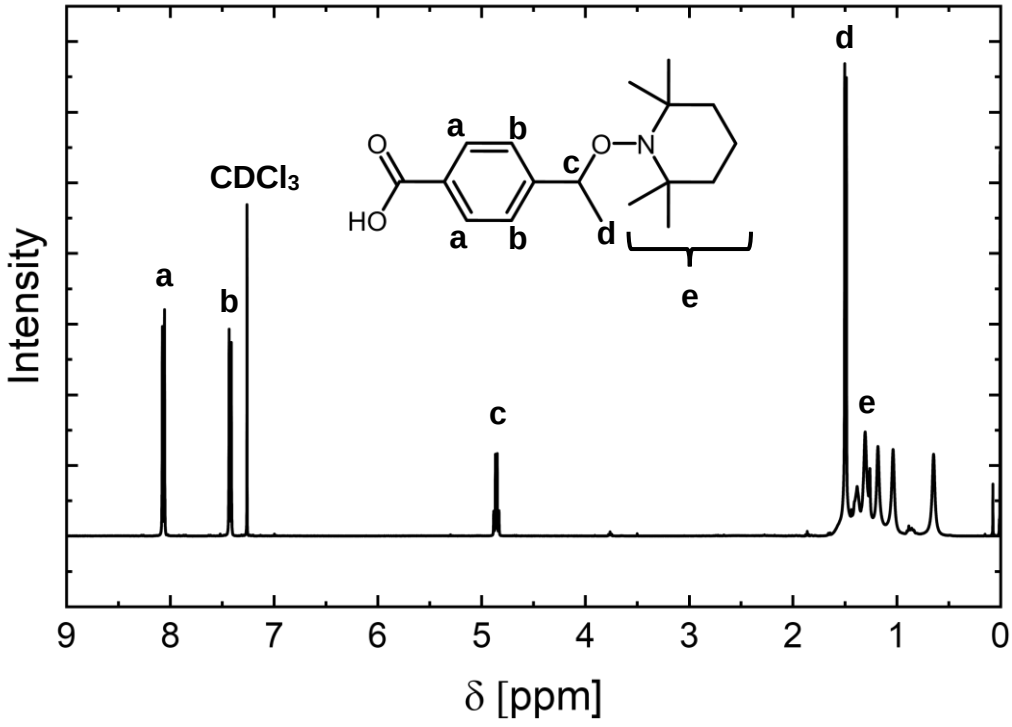

Figure A 1: 1H nuclear magnetic resonance (NMR) measurement of TEMPO-alkoxyamine (AA).

^{13}C NMR of TEMPO-alkoxyamine (4-(1-((2,2,6,6-Tetramethylpiperidin-1-yl)oxy)ethyl) benzoic acid):

13C NMR ($CDCl_3$): δ (ppm) = 171.77 (1C), 152.12 (1C), 130.18 (2C), 127.76 (1C), 126.59 (2C), 83.00 (1C), 59.80 (2C), 40.32 (1C), 34.19, 23.60 (2C), 20.36 (4C), 17.18 (1C).

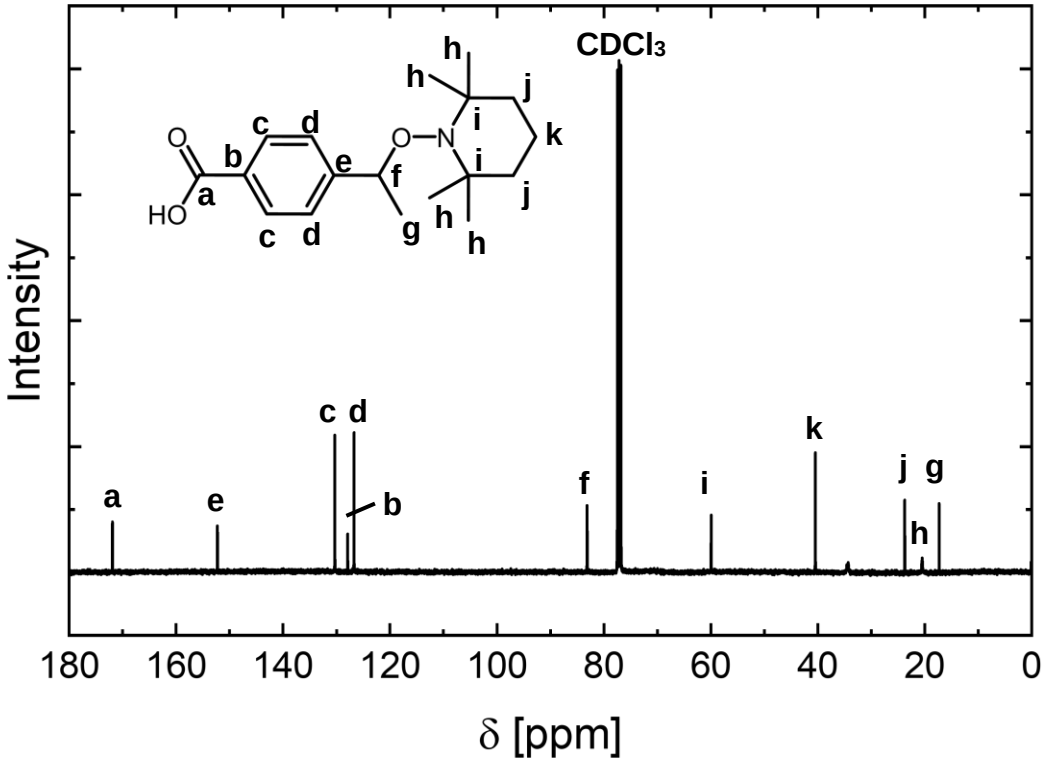

Figure A 2: 13C NMR nuclear magnetic resonance (NMR) measurement of TEMPO-alkoxyamine (AA).

Machine-Learning Parameter Sets from the Genetic Algorithm

Table A 1: Initial set of the genetic algorithm (GA), defined with the Synthesis Condition Finder (SyCoFinder).

Label	Reaction time [h]	Vapor source volume [ml]	Amount of modulator [µl]	Concentration of metal and linker [mmol/L]	Volume surface drop [uL]	DMF ratio to AcOH in the vapor source
EB-SUR-1	5.00	1.00	6.15	19.6	20.0	0.00
EB-SUR-2	1.16	10.0	0.00	1.00	50.0	1.00
EB-SUR-3	1.00	4.65	0.08	20.0	50.0	0.00
EB-SUR-4	1.00	1.00	0.00	11.9	20.0	1.00
EB-SUR-5	1.00	10.0	15.0	20.0	20.0	0.07
EB-SUR-6	5.00	9.96	13.2	8.58	50.0	0.00
EB-SUR-7	3.30	8.33	15.0	1.00	20.0	1.00
EB-SUR-8	5.00	10.0	0.00	20.0	32.5	1.00
EB-SUR-9	1.00	1.00	15.0	1.01	37.5	0.00
EB-SUR-10	3.30	1.16	14.8	19.6	49.5	0.99

Table A 2: First generation of the genetic algorithm (GA), defined with the Synthesis Condition Finder (SyCoFinder.

Label	Reaction time [h]	Vapor source volume [ml]	Amount of modulator [µl]	Concentration of metal and linker [mmol/L]	Volume surface drop [uL]	DMF ratio to AcOH in the vapor source
EB-SUR-11	5.00	1.00	6.15	19.6	20.0	0.00
EB-SUR-12	1.57	7.76	0.97	10.8	33.9	0.15
EB-SUR-13	1.42	8.73	1.55	5.67	49.6	1.00
EB-SUR-14	2.35	9.58	1.79	4.21	34.7	0.39
EB-SUR-15	4.39	7.04	13.3	7.88	20.0	0.97
EB-SUR-16	1.69	9.15	4.45	18.5	50.0	0.00
EB-SUR-17	1.00	9.95	17.4	20.0	43.0	0.81
EB-SUR-18	1.02	7.27	0.06	7.88	50.0	0.66
EB-SUR-19	1.00	3.53	3.35	1.00	43.3	0.28
EB-SUR-20	1.61	1.29	2.40	3.87	3.00	0.81

Table A 3: Second generation of the genetic algorithm (GA), defined with the Synthesis Condition Finder (SyCoFinder).

Label	Reaction time [h]	Vapor source volume [ml]	Amount of modulator [µl]	Concentration of metal and linker [mmol/L]	Volume surface drop [uL]	DMF ratio to AcOH in the vapor source
EB-SUR-21	1.38	12.1	0.23	20.0	38.5	0.69
EB-SUR-22	1.22	6.12	0.50	6.22	32.7	0.80
EB-SUR-23	3.38	3.03	1.46	12.5	32.4	0.10
EB-SUR-24	1.28	9.15	9.67	10.9	47.9	0.93
EB-SUR-25	1.59	7.16	1.52	4.20	8.14	0.33
EB-SUR-26	1.14	8.37	0.39	5.86	49.8	0.86
EB-SUR-27	1.00	8.24	4.33	14.9	43.1	0.74
EB-SUR-28	1.87	4.79	1.95	3.98	10.9	0.43
EB-SUR-29	5.00	1.00	6.15	19.6	20.0	0.00
EB-SUR-30	1.00	3.53	3.35	1.00	43.3	0.28

Fitness for the Samples Predicted with the Synthesis Condition Finder

Table A 4: Fitness values of all samples predicted with the Synthesis Condition Finder (SyCoFinder).

Label	Fitness
EB-SUR-1	0.27
EB-SUR-2	0.00
EB-SUR-3	0.00
EB-SUR-4	0.21
EB-SUR-5	0.00
EB-SUR-6	0.00
EB-SUR-7	0.00
EB-SUR-8	0.23
EB-SUR-9	0.00
EB-SUR-10	0.09
EB-SUR-11	0.30
EB-SUR-12	0.00
EB-SUR-13	0.00
EB-SUR-14	0.00
EB-SUR-15	0.16

Label	Fitness
EB-SUR-16	0.00
EB-SUR-17	0.51
EB-SUR-18	0.52
EB-SUR-19	0.00
EB-SUR-20	0.00
EB-SUR-21	0.48
EB-SUR-22	0.55
EB-SUR-23	0.00
EB-SUR-24	0.20
EB-SUR-25	0.00
EB-SUR-26	0.00
EB-SUR-27	0.29
EB-SUR-28	0.00
EB-SUR-29	0.95
EB-SUR-30	0.00

Machine-Learning Parameter Sets from the Bayesian Optimization

Table A 5: Initial set of the Bayesian optimization (BO).

Label	Reaction time [h]	Vapor source volume [ml]	Amount of modulator [µl]	Concentration of metal and linker [mmol/L]	Volume surface drop [uL]	DMF ratio to AcOH in the vapor source
EBB-SUR-1	4.00	8.00	0.00	20.0	20.0	0.40
EBB-SUR-2	5.00	5.00	20.0	10.0	40.0	1.00
EBB-SUR-3	5.00	6.00	10.0	20.0	50.0	0.40
EBB-SUR-4	5.00	10.0	0.00	15.0	50.0	0.80
EBB-SUR-5	4.00	5.00	6.00	5.00	40.0	0.00
EBB-SUR-6	1.00	2.00	16.0	5.00	30.0	1.00
EBB-SUR-7	1.00	5.00	16.0	10.0	50.0	0.00
EBB-SUR-8	2.00	6.00	0.00	15.0	50.0	0.00
EBB-SUR-9	2.00	5.00	26.0	20.0	30.0	0.80
EBB-SUR-10	3.00	7.00	6.00	5.00	40.0	0.80

Table A 6: First generation of the Bayesian optimization (BO).

Label	Reaction time [h]	Vapor source volume [ml]	Amount of modulator [µl]	Concentration of metal and linker [mmol/L]	Volume surface drop [uL]	DMF ratio to AcOH in the vapor source
EBB-SUR-11	2.62	5.58	25.9	20.0	30.9	0.78
EBB-SUR-12	1.37	4.56	26.0	20.0	30.0	0.82
EBB-SUR-13	2.23	4.17	23.3	20.0	27.3	0.76
EBB-SUR-14	2.05	5.08	25.8	20.0	29.8	1.00
EBB-SUR-15	1.87	6.45	26.0	20.0	30.0	0.89
EBB-SUR-16	2.00	4.58	26.0	20.0	35.4	0.77
EBB-SUR-17	2.37	4.30	26.0	20.0	30.0	0.97
EBB-SUR-18	2.05	5.95	26.0	20.0	30.0	0.62
EBB-SUR-19	2.23	3.88	26.0	20.0	30.0	0.96
EBB-SUR-20	2.00	5.85	22.2	20.0	26.2	0.82

Table A 7: Second generation of the Bayesian optimization (BO).

Label	Reaction time [h]	Vapor source volume [ml]	Amount of modulator [µl]	Concentration of metal and linker [mmol/L]	Volume surface drop [uL]	DMF ratio to AcOH in the vapor source
EBB-SUR-21	1.65	4.00	24.9	20.0	28.9	0.64
EBB-SUR-22	1.23	5.47	26.0	20.0	30.0	0.66
EBB-SUR-23	1.28	5.63	26.0	20.0	30.0	0.65
EBB-SUR-24	1.65	4.42	25.8	16.8	29.8	0.67
EBB-SUR-25	1.95	2.87	23.3	20.0	27.3	0.68
EBB-SUR-26	2.09	3.03	23.2	20.0	27.2	0.64
EBB-SUR-27	1.45	2.53	25.9	20.0	29.9	0.73
EBB-SUR-28	1.11	3.24	26.0	20.0	30.9	0.71
EBB-SUR-29	1.33	3.68	23.0	20.0	27.0	0.73
EBB-SUR-30	1.88	4.98	26.0	19.7	30.0	0.49

Fitness for the Samples Predicted with the Bayesian Optimization

Table A 8: Fitness values of all samples predicted with the Bayesian optimization (BO).

Label	Fitness
EBB-SUR-1	0.35
EBB-SUR-2	0.30
EBB-SUR-3	0.40
EBB-SUR-4	0.39
EBB-SUR-5	0.00
EBB-SUR-6	0.07
EBB-SUR-7	0.11
EBB-SUR-8	0.24
EBB-SUR-9	0.70
EBB-SUR-10	0.10
EBB-SUR-11	0.11
EBB-SUR-12	0.83
EBB-SUR-13	0.93
EBB-SUR-14	0.21
EBB-SUR-15	0.57

Label	Fitness
EBB-SUR-16	0.49
EBB-SUR-17	0.43
EBB-SUR-18	0.82
EBB-SUR-19	0.35
EBB-SUR-20	0.24
EBB-SUR-21	0.23
EBB-SUR-22	0.14
EBB-SUR-23	0.60
EBB-SUR-24	0.32
EBB-SUR-25	0.58
EBB-SUR-26	0.55
EBB-SUR-27	0.29
EBB-SUR-28	0.82
EBB-SUR-29	0.44
EBB-SUR-30	0.21

Fitness for the Repeated Samples with the Optimized Conditions from the Synthesis Condition Finder (SyCoFinder) and the Bayesian Optimization (BO)

Based on	Label	Fitness
EB-SUR-29	**EBB-SUR-31**	0.79
EBB-SUR-13	**EBB-SUR-32**	0.80

Acknowledgment

First of all, I want to thank my supervisor, PD. Manuel Tsotsalas, for the support, the helpful discussions, the always motivating words, and the fascinating subject. Furthermore, I want to thank Prof. Patrick Théato for taking over the coreferat of my thesis. Additionally, I want to thank Prof. Christof Wöll for welcoming me to the Institute of Functional Interfaces (IFG) and for providing the infrastructure in the lab.

Besides, special thanks go to Dr. Salma Begum, who always supported me and showed me how to spend my time on projects and write papers effectively. Furthermore, I want to thank my supportive colleagues who made learning and working in the lab fun. So, I want to thank Simon Spiegel, Lena Pilz, Dr. Yi Luo, Dr. Yixuan Jia, Dr. Alexander Welle, Dr. Hartmut Gliemann, Dr. Matthias Schwotzer, Dr. Peter Weidler, Stefan Heißler, Birgit Huber, Frank Kirschhöfer, Dr. Gerald Brenner-Weiß and Henry Unger. Additionally, I want to thank all members of the IFG for a great time and help in the lab.

Cooperation partners are an essential part of the life of a scientist, and I am delighted that I had some great collaborators in Dr. Esther Mittmann, Dr. Kersten Rabe, Cordula Nies, Prof. Eric Gottwald, Prof. Pascal Friederich, Lucca Torressi, Julian Brückel, Prof. Stefan Bräse, Prof. Martina H. Stenzel, Dr. Seçkin Altuncu and Prof. Guillaume Delaittre whom I want to thank for their fruitful collaborative work.

Furthermore, I want to special thank Esther Mittmann for the performance of the enzyme activity tests and the western blots, Dr. Nicole Jung together with Pei-Chi Huang and Chia-Lin Lin for their help with Chemotion, and Dr. Alexander Welle for all the ToF-SIMS measurements. I also want to thank PD. Manuel Tostsalas, Lena Pilz, Simon Spiegel, Dr. Yi Luo, Nils Holz, Dr. Peter Weidler, Birgit Huber, Max Krause, Fabian Hoffmann, Stefan Heißler, Dr. Matthias Schwotzer, and Dr. Alexander Welle for proofreading my thesis.

Special thanks also go to the graduate school BIF-IGS for the interesting courses on presentation skills, stress management, python courses, etc., over the years. I also want to thank my retreat organization team, especially Christina Cramer von Clausbruch, for the fun meetings and helpful talks. My TAC team: Prof. Markus Reischl, Prof. Eric

Gottwald and PD. Manuel Tsotsalas, I especially want to thank you for all the supportive discussions and evaluations of my doctoral thesis over the years.

An exchange is not always easy, especially not without the support of the people staying at home. So, I want to thank Emily Bevier, who was a great help in the lab and even more essential during my time in Australia. For the time I stayed in Australia, I want to particularly thank Prof. Martina H. Stenzel, who invited me to her group in Sydney and supported me and my project. Furthermore, I want to thank Dr. Radhika Raveendran for all the organizational help and Miriam, Jarrod, Evie, and Clélia, who became good friends during my time abroad. Moreover, I want to thank the whole team in Australia for the warm and supportive welcome.

For the financial support during my Ph.D., I want to thank the BIF-IGS Graduate School for the Travel Grand for the Material Research Society (MRS) conference in 2022 in Hawaii. The KHYS for the Research Travel Grant and the Bayer Foundation for the Otto Bayer Fellowships in Drug Discovery for the Research Exchange with Australia in 2023. Additionally, I want to thank the DECHEMA for the Max-Buchner Travel Grant for the 5th European Conference on Metal-Organic Frameworks and Porous Materials in 2023 in Spain.

Finally, a Ph.D. is nothing without a supportive circle of friends and family. So, I thank my friends. Especially Franzi and Verena. Without you, my time in Karlsruhe would not have been the same and I would not have survived the first few semesters. André, Steffen, Timo, Vivi, and Elena, I would like to thank you for the bars and the late-night chats away from chemistry to take my mind off university. Alexios for the best Greek food I ever had. Nicola, Sarah, Saskia, Tobi, Jerome, Fabian, and Anna for proving that you can make good friends through university practical courses. Nicole and Marc for being the best neighbors I ever had. Lena, Melissa, Chiara, and Anna for sticking by me even after school. I also want to thank the DLRG team, especially Maike, Hanna, and Patrick, who are good friends and share a wonderful hobby with me.

Furthermore, I would like to thank my family: Wolfgang, Dagmar, Rolf-Dieter, Martha, Brigitte, and Andreas for their support during my studies. My special thanks go to my uncle Ernst, who was always interested in my topic and supported me in my dissertation

project with his birthday and Christmas presents, consisting of interesting research literature.

In particular, I would like to thank my sister, Caroline, and my parents, Fritz and Cornelia. I am forever grateful for your support and kind words throughout the whole time. I also love that you were always there for me and visited me when I was abroad.

Last but not least, I want to thank Max. I cannot even try to express how happy I am to have you in my life. You accompanied me on more than one adventure, and I hope for many more to come.